Acoustic shock wave propagation through uncertain atmospheres

Roman Leconte


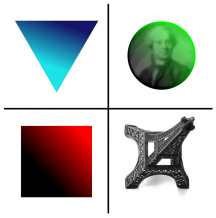


SORBONNE UNIVERSITÉ

ÉCOLE DOCTORALE 391 : SCIENCES MÉCANIQUES, ACOUSTIQUE, ELECTRONIQUE ET ROBOTIQUE DE PARIS

THÈSE DE DOCTORAT
Spécialité Acoustique

Acoustic shock wave propagation through uncertain atmospheres

Roman Leconte

Écrite sous la direction de :

Régis Marchiano, *Professeur Sorbonne Université*,
François Coulouvrat, *Directeur de recherche CNRS*,

à l'Institut Jean Le Rond ∂'Alembert, Sorbonne Université, CNRS, UMR 7190.

Jury composé de :

Sylvain Cheinet	Directeur de recherche ISL	*Rapporteur*
Benoit Gauvreau	Directeur de recherche Université G. Eiffel	*Rapporteur*
Quentin Grimal	Professeur Sorbonne Université	*Examinateur*
Joël Gilbert	Directeur de recherche CNRS	*Examinateur*
Alexandra Loubeau	Ingénieur de recherche NASA	*Invitée*
Olaf Gainville	Ingénieur de recherche CEA, DAM, DIF	*Invité*
Jean-Camille Chassaing	Professeur Sorbonne Université	*Invité*
Franck Hervy	Docteur DGA	*Invité*
Régis Marchiano	Professeur Sorbonne Université	*Directeur de thèse*
François Coulouvrat	Directeur de recherche CNRS	*Directeur de thèse*

Contents

List of Figures

List of Tables

Chapter 1

Introduction

1.1 Context

This work is a contribution to the development of numerical tools for a better prediction of the propagation of acoustic shock waves through media with uncertain physical properties. Acoustic shock waves are characterized by an abrupt, nearly discontinuous, change in waves characteristics (pressure, density, speed,...). These shock waves can propagate in different media, such as air or water. There exist many sources of shock waves: they can be natural, for instance the thunder [45, 46, 85] or the meteorites entering in the atmosphere [140, 65, 185], or man-made such as shock waves used for lithotripsy [91], sonic boom generated by supersonic aircraft [164], or explosions due to industrial processes [116], accidents [157] or military activities [35].

The works presented in this thesis focus on the latter: sonic boom and blast waves. The guideline is how to simulate and quantify the effects on acoustic shock waves of the atmosphere whose description is uncertain, because of meteorological and turbulence effects. This work has been done in the framework of the European project RUMBLE (RegUlation and norM for low sonic-Boom LEvel) [143] for sonic boom and in collaboration with CEA (Commissariat à l'énergie atomique et aux énergies alternatives) for blast waves.

1.2 State of the art

1.2.1 Sonic boom

Sonic boom occurs when the speed of an aircraft (or of any object with a supersonic speed) exceeds the local sound speed. This creates a conic shock front near the aircraft [164, 102, 136], whose angle depends on the speed, the famous Mach cone (see figure 1.1 for a picture of Mach cones). Then, shocks propagate from the aircraft to the ground through the atmosphere. In a homogeneous atmosphere, the geometrical spreading of a lineal source is cylindrical, and therefore its amplitude would decrease as power $-1/2$ of the distance (much slower than for spherical spreading). Moreover, important nonlinear cumulative effects take place and modify dramatically the sonic boom signature during its propagation with the coalescence of the shocks (see figure 1.1). After a sufficient long distance of propagation, the signature becomes an N-wave which is the classic signature

for a sonic boom [167] (see figure 1.2). With nonlinear effects taken into account, sonic boom amplitude decays as power $-3/4$ of the distance [166, 165]. In realistic atmospheres, refraction makes this decay slower, depending on the local meteorological temperature and wind vertical profile [96, 136, 15, 61]. Sonic boom has been an intensive topic of research since the 60's and the development of Concorde [102]. Because of sonic boom, supersonic overland flights are still prohibited. Nevertheless, there is a renewed interest in supersonic civil aviation and one of its main challenges is the mitigation of the annoyance due to sonic boom at ground [29]. A way to develop a quiet supersonic aircraft is to design its shape to produce a signature different from the N-wave at the ground [102]. Such low boom signatures have a reduced peak pressure and a longer rise time, which make them more acceptable for people. Multiple designs and concepts have been proposed and improved for low sonic booms aircraft [7, 151, 127]. Nevertheless, there is currently no consensus on acceptable levels, and further knowledge is expected about effects of the atmosphere [18], ground topography [43], transmission into structures [119] and human response [159, 98, 88].

As mentioned earlier, this work on sonic boom has been done in the context of the European project RUMBLE [143], which aims to contribute to the determination of acceptable level of overland sonic booms and to the appropriate ways to comply with it. The work done during this thesis is included in Work Package 2 (WP2) "Sonic Boom Prediction Capabilities" and in particular the studies on far field modeling. It is also linked to the WP3 which focuses on the human response to sonic boom, and especially the development of a low-boom simulator for perception studies [159, 107].

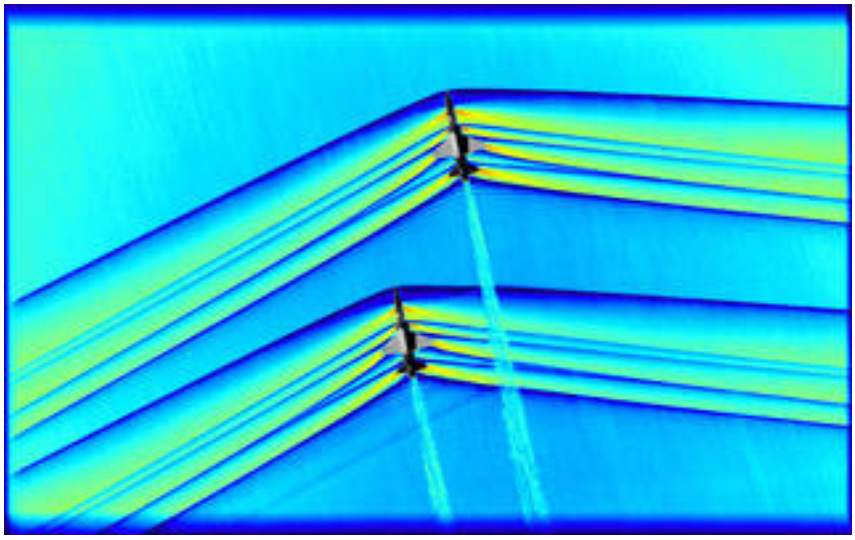

Figure 1.1: Schlieren in-flight mach cones formed by supersonic aircraft. Figure realized by NASA, extracted from [113].

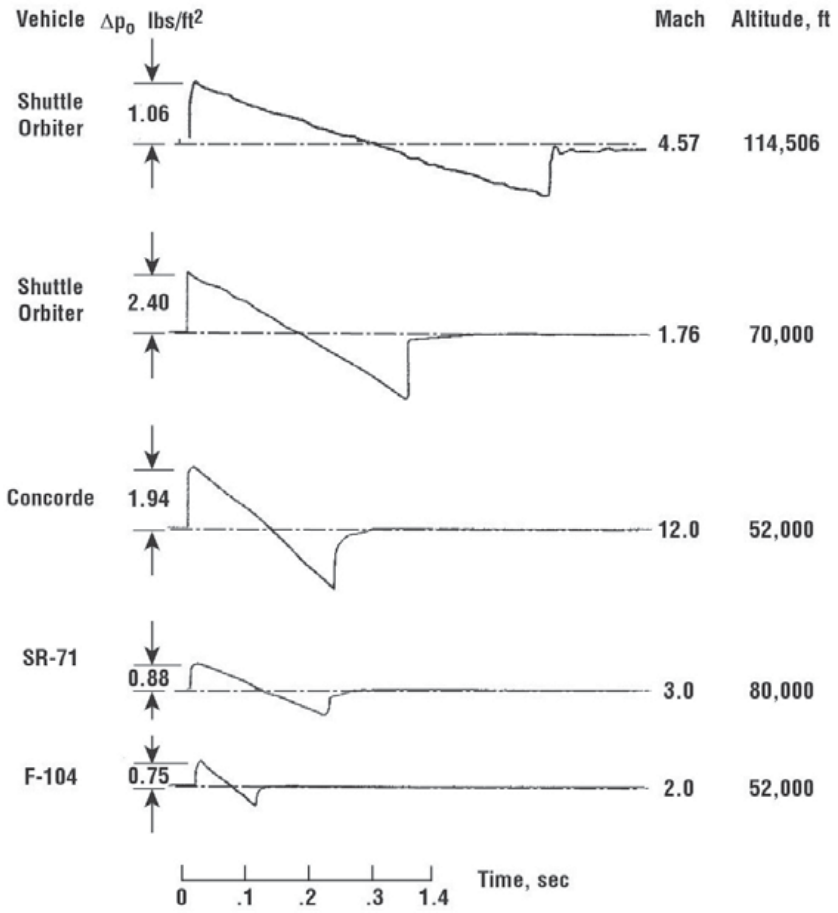

Figure 1.2: Measured sonic booms in a quiescent atmosphere, for different types of supersonic vehicles. Extracted from *Maglieri et al.* [102].

1.2.2 Blast waves

Blast waves are shock waves produced by explosions. Generally, explosions release an important amount of energy E_0 in a short time, resulting in an impulsive point source. This causes a shock wave to develop in the medium of propagation. Close to the source the geometrical spreading is spherical. In the strong shock regime nearest the source, the pressure is much larger than the unperturbed atmospheric pressure p_0 and decreases very quickly as power -3 of the distance. It is governed by an equivalent characteristic radius R_0 proportional to $(E_0/p_0)^{1/3}$ [158]. At distances larger than R_0, the waveform is modified and tends progressively to a weak shock according to a process described numerically in [19, 20]. In this weak shock regime, the amplitude of the blast wave decreases almost as a linear point source (inversely proportional to the distance). A picture of an explosion is shown figure 1.3. This explosion was conducted in 1987 by the United States Defense Nuclear Agency, and data from the blast wave were used to collect explosive environmental data. Other sources of blast waves include accidental explosions like the explosion in Beirut port in 2020 [114], or natural explosions like the eruption of the volcano Hunga Tonga-Hunga Ha'apai in January 2022 [63]. The study of their blast waves can give important information on the source, and be used to predict the damages caused by explosions. Blast wave study can also be used to detect nuclear explosions in

the context of the Comprehensive Nuclear Test Ban Treaty [34].

A model of blast wave signature can be seen on figure 1.4. It outlines the characteristic near discontinuous variation of pressure of the shock wave, and the unsymmetrical (unlike the N-wave) positive and negative pressure phases. There is a nonlinear strong shock regime in near field where the amplitude is still high, and a linear regime in the far field. During the thesis, we had the opportunity to collaborate with CEA on the impacts of meteorological effects on the propagation of blast waves produced by an industrial process [117].

To have a better understanding on shock wave influence on the population, it is important to have indicators which reflect the effect of these shock waves on people. These indicators are called metrics.

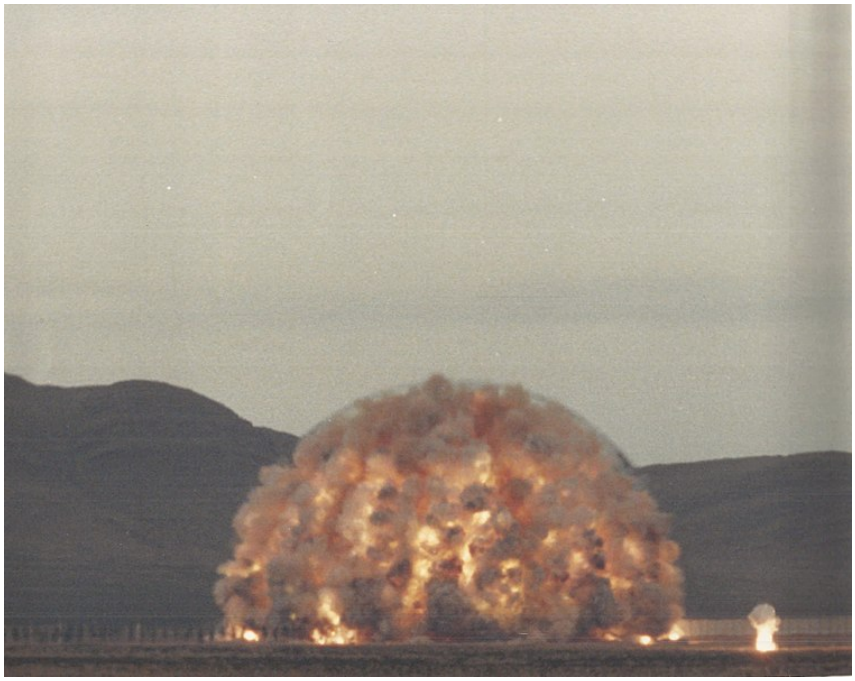

Figure 1.3: Picture of the misty picture test conducted in 1987. Extracted from [2].

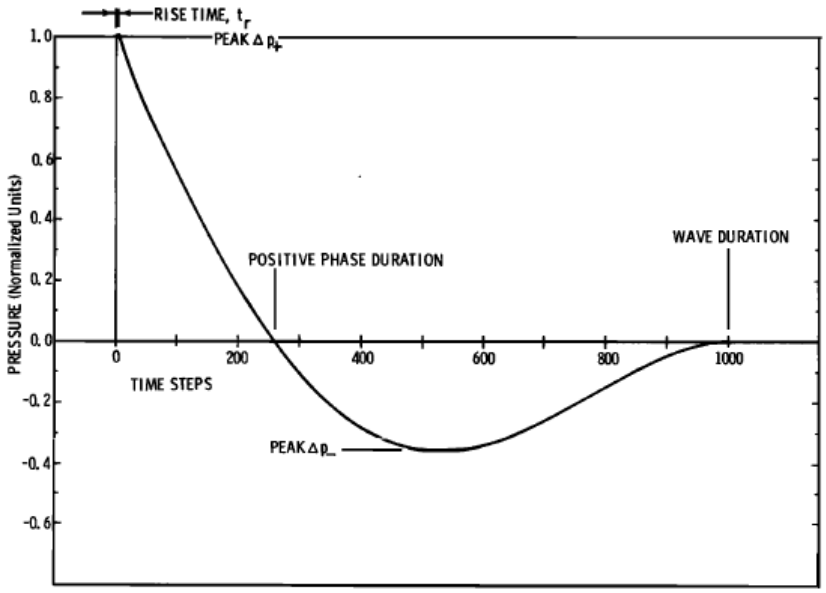

Figure 1.4: Theoretical blast wave. Extracted from *Reed* [139].

1.2.3 Metrics

Metrics are indicators used to characterize the disturbance caused by sound. It is difficult to have a single indicator, because disturbances come from a wide array of factors [22], like the sound level, the signal spectral components, its variations, its duration,... Furthermore, there are different sorts of disturbances, like sleep or activity interference, or simply annoyance [122]. For urban noise, a European directive in 2002 chose the L_{den} metric [23] where L_{den} stands for day-evening-night level. It is a descriptor of noise level based on energy equivalent noise level (Leq) over a whole day with a penalty of 10 dB(A) for night time noise and an additive penalty of 5 dB(A) for evening night. This metric obviously does not take into account the variations in the noise, as well as its spectral properties. A lot of different metrics have been developed, to answer different problems [23]. In [22], three metrics are chosen for the sound structure: $L_{50,A}$, $\sigma_{Leq,A}$ and $SGC_{[50Hz-10kHz]}$, and three metrics are chosen for the sound events (calculated at specific stop points): $L_{1,A}$, $MI_{LA50+10}$ and $MI_{LLF50+15}$. $L_{50,A}$ corresponds to the median of the energy level with the A-weighting, $L_{1,A}$ to the level exceeded by only 1 % of the measured levels. $\sigma_{Leq,A}$ is the standard deviation, and $SGC_{[50Hz-10kHz]}$ an indicator showing the contribution of the energy bands to the pressure levels. Finally, $MI_{LA50+10}$ is the percentage of the cumulative time where the level exceeds $L_{50,A} + 10$ dB and $MI_{LLF50+15}$ is calculated the same way, but for low frequencies. In conclusion, there exists a lot of different metrics, which correspond to different disturbance causes, but there is no single metric adapted to all situations.

In the case of shock waves and especially sonic boom, the signature is characterized by a short duration, a small rise time and a high pressure level. Simple indicators like the peak pressure are not fully relevant. There is a need to select metrics which can describe the sensorial response of the population. Six metrics have been preselected by ICAO (International Civil Aviation Organisation) as the most promising ones [70]: Sound Exposure Level (SEL) with A, B, D and E weighting, Stevens Mark VII Perceived Level

(PL) and ISBAP which is a combination of PL, A-SEL and C-SEL [153, 97]. These metrics are calculated from the raw signature of the boom, and like the pressure waveform, they can be significantly affected by the meteorological conditions. The quantification of their uncertainty is an important part of the RUMBLE project, especially for low-booms, whose metrics uncertainty due to turbulence remains to be better quantified.

1.2.4 Influence of the medium of propagation

It is well-known that the waveform is strongly affected by the medium of the propagation. Experiments and measures of shock wave signatures have been done extensively, for sonic booms as well as for blast waves. For sonic booms, a large variety of waveforms has been observed during flight tests campaigns [67, 56, 103, 89, 168] showing N-waves more or less rounded or peaked with significant differences for the amplitude and the rise-time. Qualitative models [131, 132, 133, 33, 57, 66, 74, 138] concluded that these variations are mainly due to atmospheric turbulence in the Planetary Boundary Layer and that statistical studies are necessary to quantify them. The observations have been reproduced with experiments at laboratory scale [9, 39, 94, 93, 92, 141, 160, 12, 55, 5, 3, 130, 147]. In some cases, simulations with ray tracing methods [66, 14] non-linear parabolic methods [55, 3, 77, 14] have been performed, and gave results comparable with observations. However, laboratory experiments have 1) a controlled source different from an aircraft (generally a fixed source of shock wave), and 2) frequently a deterministic propagation medium. These limitations and the difficulty to reproduce in the laboratory the complexity of the atmosphere and an exact similitude, make it necessary to rely also on a numerical and statistical approach. For sonic boom, the influence of the medium of propagation has been recognized as a priority. Recently, the NASA program "Sonic Booms in Atmospheric Turbulence" (SonicBAT) has been conducted to increase the knowledge on the influence of turbulence on sonic boom. In the final report [18], it is explicitly written that "Prediction code that accounts for turbulence was not existent".

For blast waves, in [161], experimental explosions have been detonated in areas with mild or desert climate, under a variety of meteorological conditions. The variability in sound levels was studied between 4 and 16 km. Over 200 charges were detonated and around 20,000 waveforms were recorded. High variability in peak pressure and C-weighted metric was observed. In [115, 117, 116], measures of blast waves signals are compared with numerical propagations realized with Euler simulations or a parabolic equation, and a qualitative agreement is observed. However the simulations were deterministic, and the uncertainty still needs to be quantified. In [81], acoustic data for a series of controlled truck bomb explosions are analyzed, in order to develop scaling laws, used to extrapolate the initial charge of explosions from waveforms properties at different distances from the source. However, because of a low number of experiments (4 explosions), the variability in the waveforms was not properly observed. In [80], data from an explosion experiment in New Mexico in 2012 are compared to a 3D finite-difference linear model. Topography and wind and temperature profiles are taken into account. In the case of weak wind, simulated peak pressures were found close to experiments, while the peak pressure was poorly reproduced in case of a strong wind. One of the reasons is because the variability in the meteorological profiles was poorly characterized. In conclusion, despite numerical models which show for some configurations a good agreement with measurements, the

variability in the signature remains generally poorly understood.

This variability is illustrated for two different situations on figures 1.5 and 1.6. Figure 1.5, extracted from [67], shows measured sonic boom waveforms on the ground for a B-58 flight test in 1965, with low-wind conditions and high-wind conditions. On the left, the signatures measured for the low wind conditions are close to the theoretical N-wave, while on the right the signatures are strongly affected. Figure 1.6 shows the waveforms and their spectra for a series of canon shots. The blue curves are the individual shots and the black line is the average. We can see large fluctuations due to the different realizations of the atmosphere. In these two examples, distances of propagation are very different (tens of kilometers vs tens of meters) but the effects of the medium of propagation and the uncertainty of the observation are clearly visible. Effects due to atmosphere on the propagation of the shock waves and in particular the way to simulate and quantify them, is at the heart of this thesis.

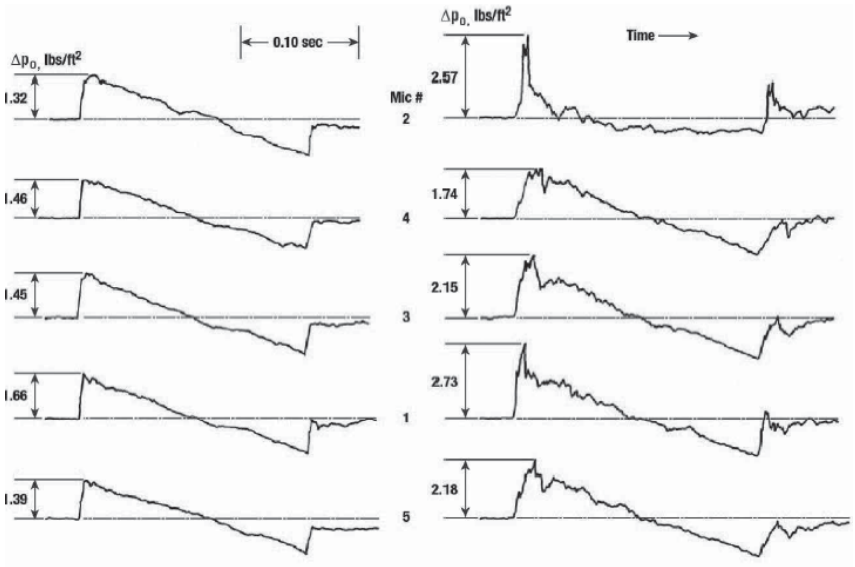

Figure 1.5: Measured boom waveforms on the ground for a B-58 flight test in 1965, with low-wind conditions (left) and high-wind conditions (right). Extracted from *Hilton et al.* [67].

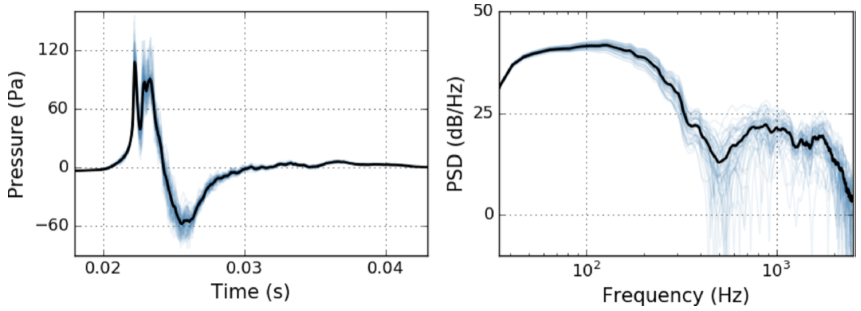

Figure 1.6: Acoustic recordings of 56 cannon shots measured at 7.5 m, with (left) the pressure with time (relative to emission), and (right) the power spectral densities. The blue lines are for individual shots, the black line is the average. Extracted from *Cheinet et al.* [24].

1.2.5 Atmospheric models for acoustic propagation

Previous paragraph outlines the major role of the atmosphere on the shape and amplitude of waveforms during the propagation of shock waves. Schematically, we can split its influence between the macro effects due to the vertical gradients of atmospheric pressure, temperature and wind, and the micro effects due mainly to small scale turbulence.

Macro effects cause refraction effects and impact the location of the shock wave, as well as its intensity. Mean vertical gradients of pressure, density or temperature are given by the ICAO Standard Atmosphere [121] (see figure 1.7 for a representation of standard profiles) and are often used as reference. Of course, real profiles are always different from the idealized ICAO Standard atmosphere.

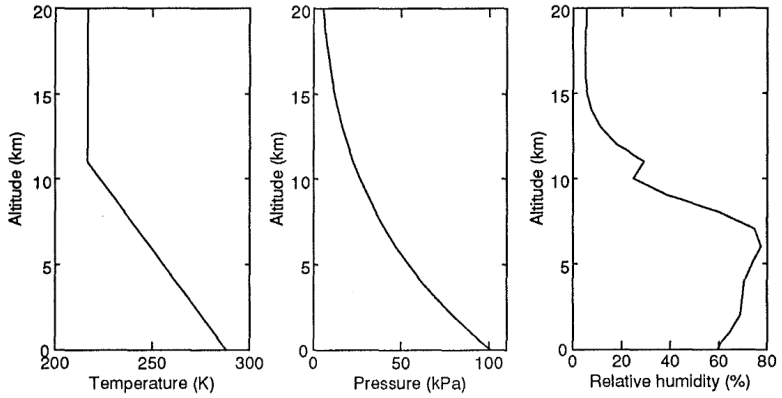

Figure 1.7: ISO standard atmosphere. Extracted from *Cleveland* [27].

Meteorological codes can give access to more accurate data by using a convective scale model to obtain the meteorological variables at different altitudes and positions. For this purpose, the model COSMO (Consortium for Small Scale Modeling) [148] was developed in Germany, the Unified Model in United Kingdom [38], and the model Arome (Applications of Research to Operations at Mesoscale) by Meteo France[149]. The model Arome has a horizontal resolution of 2.5 km and is initialized with mesoscale data assimilation in 3 h cycles. These models give a good approximation of macro effects, but do not have a high vertical resolution, which can be problematic for the estimation in the surface layer, close to the ground.

To have a better approximation close to the ground, models describing the meteorological profiles in the surface layer, close to the ground, are needed. The Monin-Obukhov Similarity Theory (MOST) [111, 73, 173] gives the temperature and wind profiles within the 50-100 m of the surface layer. With this model, the surface layer is characterized by two parameters measurable on the ground: the friction velocity u_* and the surface sensible heat flux Q_s. However, to have a complete description of the atmosphere, it is necessary to also take into account the micro effects.

Micro effects are mainly due to turbulence, which can be important in the Planetary Boundary Layer (roughly 1 km height). They have an important effect on the waveform, significantly altering the overpressure and the rise time. Their modeling is essential [137]. From an acoustical point of view, it is usual to consider frozen turbulence: because the time scale of turbulence is larger than the acoustic propagation one, the atmosphere

remains constant during the propagation. To obtain a frozen atmosphere representation, two main strategies exist: either by solving the Navier-Stokes equations numerically, or by using synthetic models. The Large Eddy Simulation (LES) model explicitly simulates the large eddies using the Navier-Stokes equations, and parameterizes the smaller ones. LES methods are used by Wilson *et al.* in [174]. They chose dimensions of $2.4 \times 2.4 \times 1\,\mathrm{km}$, with a resolution of $4 \times 4 \times 2.5\,\mathrm{m}$. Simulations were performed with 100 GPU, but the simulation duration is unspecified. In [90], Lihoreau *et al.* use the LES method, with three levels of grids. The one with the finest resolution was 2D, with 44×44 points and a resolution of 50 m, and the simulation duration is unspecified. In [179], Wilson *et al.* use $901 \times 901 \times 603$ grid nodes spaced every meter. The execution required 10 hours with 100 processors. This shows that, to have a good resolution, this method is numerically very expensive. That is why, despite its high fidelity, it is not frequently used.

Girimaji *et al.* [59] use Partially-averaged Navier Stokes (PANS) methods. PANS is a suite of turbulence closure models of various modeled-to-resolved scale ratios ranging from Reynolds Averaged Navier-Stokes (RANS) to Direct Numerical Simulations (DNS), which is the direct resolution of Navier-Stokes equations, and is even more expensive than LES. In [10], Bechmann *et al.* chose to use a hybrid RANS/LES method. Because the LES method has a high computational cost and the RANS method is less precise, they use the RANS method near the surface, where the LES costs the most, and the LES method above.

In [40], the RANS method, which is three orders of magnitude less demanding in computational resources than the LES method, is used. The RANS method consists of decomposing the flow variables into mean and fluctuating parts, so that the final equations appear under the form of Navier-Stokes equations for the mean part with an additional Reynolds-stress tensor. This one is unknown and has to be modeled to close the equations. However, according to Pinsky *et al.* [134], RANS is inappropriate for small turbulent scales analysis. LES is considered much more accurate, but only for scales above tens of meters.

As an alternative, synthetic turbulence can be used to calculate the temperature or the wind fluctuations turbulence. In [172], Wilson considers only the turbulent wind velocity spectrum, because the effect of wind fluctuations is usually more important than the one of temperature. In [14], both temperature and wind velocity are considered, and it is found that the effect of wind velocity turbulence is larger. Wilson *et al.* [179] consider that such methods do not realistically capture turbulent dynamics, but are still useful for testing theories for wave propagation. Moreover, they are numerically efficient, allowing a much higher resolution than the LES methods. To synthesize random fields, only the spectrum of the turbulence is prescribed. Several spectra are proposed: the Gaussian, the Kolmogorov and the von Kármán ones [170]. The turbulence spectrum can be separated in two subranges: the energy-containing subrange, at low wave-numbers, and the inertial subrange, at high wave-numbers. The Gaussian spectrum ([172]) shows limitations in the inertial subrange, where it decreases too fast. The Kolmogorov spectrum is realistic in the inertial subrange, with a $-5/3$ power decrease, as it can be seen on figure 1.8. However, this spectrum is not satisfying for describing the large eddies belonging to the energy-containing range. At last, the von Kármán spectrum agrees exactly with the Kolmogorov spectrum in the inertial subrange, while it appears realistic at low wave numbers [125]. In [169], the three spectral models are compared, and an anisotropic Gaussian model, the Wilson and Thomson model, is also considered. The von Kármán

model is viewed as the only one which can be applied to the full turbulence spectrum without obtaining unrealistic results. In [123], results of propagation with a von Kármán temperature spectrum agree well with measurements. In [175], Wilson *et al.* say that no model exists to accurately describe the entire turbulence spectrum for any flow. They agree that the von Kármán spectrum is the only one which can be used both in the energy-containing and in the inertial subranges. They outline that the Gaussian model can be accurate if it agrees well with the actual turbulence spectrum within the band of acoustically selected scales. Anisotropic models have been developed to have a more realistic description [171]. The Gaussian model [146, 14, 179, 37, 13, 108, 126, 177] and the von Kármán model [172, 176, 182, 13, 17, 25, 42] are widely used in the literature.

The choice of the turbulence model depends of the numerical resources, as well as on the required accuracy. For shock wave propagation, there is no need to have an overly realistic description of the turbulence field, because the study is focused on the wave. It is just needed to have a realistic interaction. For this reason,synthetic generation of kinetic turbulence is privileged, especially with a von Kármán spectrum. However, homogeneous and inhomogeneous models exist, and whether the latter one gives more accurate results still needs to be investigated.

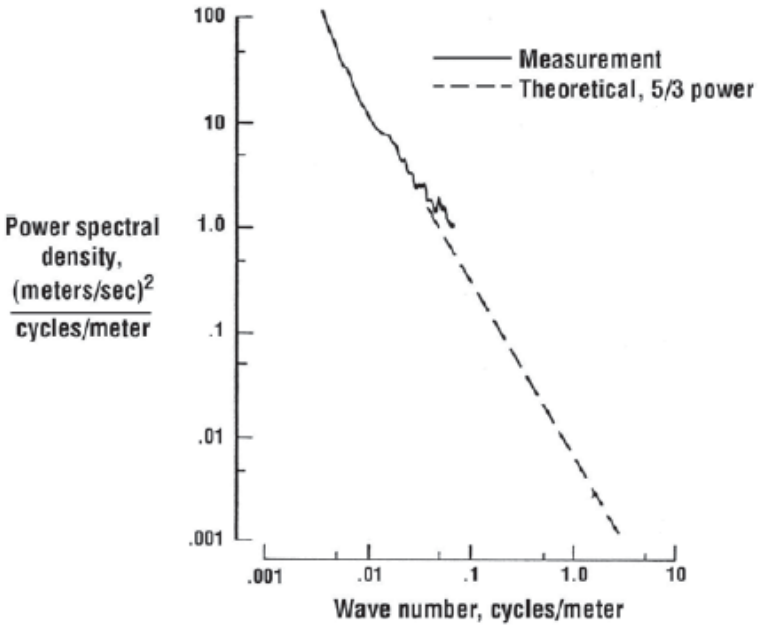

Figure 1.8: Measurement of a turbulence spectrum compared to an experimental one. Extracted from *Houbolt et al.* [69].

The stratified atmosphere (corresponding to the macro effects) or the turbulence model (micro effects) can then be used in numerical computations of propagation. These computations are extremely useful for shock waves study, because they easily enable to simulate multiple propagation cases with varying parameters, which is obviously much more difficult in experiments. Because the atmospheric conditions are often varying, a deterministic study with one set of parameters is often insufficient, and stochastic studies, which are facilitated by numerical models, are extremely useful.

1.2.6 Numerical simulations for the shock wave propagation

Many different numerical models are available to simulate the propagation of shock waves in the atmosphere, and can have high or low fidelity. Methods with the lowest computational cost to model the propagation of shock waves are numerical tools based on geometrical acoustics associated with nonlinear acoustics [136, 96, 50]. A few applications to propagation in a turbulent medium are found in the literature [14]. A shortcoming of this method is that there are areas where the geometrical approximation is invalid. More advanced techniques can be used to overcome this, mainly for the caustics [105, 145, 16] and the shadow zones [28]. A more global approach is the nonlinear parabolic approximation [58], either the "nonlinear progressive equation" (NPE) [109] or the Khokhlov-Zabolotskaya-Kuznetsov (KZK) equation [84]. This method is one way (the back-scattered field is neglected) and has an angular limitation which makes it valid only for small angles of propagation ($< 15°$) around the line-of-sight direction. Its application to sonic boom propagation [14] has been extended to take into account flows [6, 155, 18]. Another approach, called FLHOWARD3D method [54, 100] developed for both 2D and 3D simulations with a reasonable computational cost, does not suffer from this narrow angle limitation, and can take into account a random 3D turbulent velocity field superimposed to a mean atmospheric vertical stratification. Nevertheless, it remains a one way approximation. Finally, high fidelity models, directly solving the Euler equations [144], have been applied to 3D simulations [183]. However, their high computational cost makes them difficult to perform a high number of runs, and thus to be applied for a statistical approach.

For the propagation of shock waves, the most used method is the nonlinear parabolic approximation [184, 36, 72, 106, 130], with NPE, KZK or FLHOWARD3D, because they offer a good compromise between accuracy and computational cost. Even if some recent studies use 3D models [41, 18], a majority of the existing propagation codes relies on 2D configurations. The comparison in the accuracy of 2D versus 3D models still needs to be investigated. It is an important question to answer in order to tackle statistics, because a huge number of simulations is necessary to have a reliable statistics, and thus the computational cost of the simulation is an important parameter.

1.2.7 Uncertainty Quantification

Shock waves show high variations in pressure levels during their propagation in the atmosphere [161, 178]. This variance is mainly caused by the meteorological conditions (wind and temperature stratified profiles, and turbulence). However, it is difficult to quantify the exact values of these parameters. Thus, the quantification of the uncertainty is an important task, in order to understand and to describe shock wave propagation. The approach is to include an uncertainty in the input variables of the model, which induces uncertainties in the output (see figure 1.9). The typical approach is the Monte Carlo method [48], which consists in defining the uncertain parameters as random variables, and in computing a high number of propagation cases with different realizations of these variables. These computations provide the basic data for a stochastic analysis. This is a non-intrusive method, which means that the method does not modify the propagation model. This method is infrequent in acoustical waves propagation, because it needs a huge number of intensive computations. Because it is a reference method, it can however

be used to validate other methods. Its easier application is 1D cases, for example in [163] based on an augmented Burgers equation. In [64], a Latin Hypercube sampling (LHS) [110] is used with a Crank-Nicholson parabolic equation [162] to generate propagation data.The uncertainty is quantified by three different machine learning algorithms, and the results are compared to experimental data. The LHS method is also combined in [76] with a parabolic equation propagation method, and a model is built with the Kriging method to obtain the uncertainty of wind turbine noise. A method with a lower computational cost is the polynomial chaos method, which is based on polynomials to reproduce the response surface with a low number of runs, and create a metamodel. A metamodel is a simplified model of a higher fidelity one, thus allowing a quicker computation. In [47] [79], the polynomial chaos method is used to quantify the uncertainty of the acoustic wave propagation in ocean waveguides, with a parabolic equation code. In [32], accuracy of polynomial chaos methods is evaluated for a one-dimensional propagation model case. The influence of meteorological uncertainties on sonic boom is examined in [150] by means of polynomial chaos with an augmented Burgers equation. In [78] the polynomial chaos method, as well as Kriging [60] and Polynomial Chaos-based Kriging methods are applied with experimental measurements, for acoustic underwater waves in shallow water. An other solution is the FIR (Finite Impulse Response) filter method [95, 18]. This method consists in creating a filter which is convoluted to the initial signature to approximate the effect of turbulence. The filter is created by computing a propagation in an atmosphere with kinetic turbulence, doing the same with an unperturbed atmosphere, and performing a time domain matrix deconvolution using the two signatures. This method is linear: the nonlinearities have to be considered separately. In [18], a metamodel built with this method is used to study the effect of turbulence on low booms.

Uncertainty quantification for the propagation of shock waves in the atmosphere is still an open issue, especially with high fidelity models. The atmospheric profiles and the turbulence have to be parameterized to allow the uncertainty study, and how to parameterize them is still an open question.

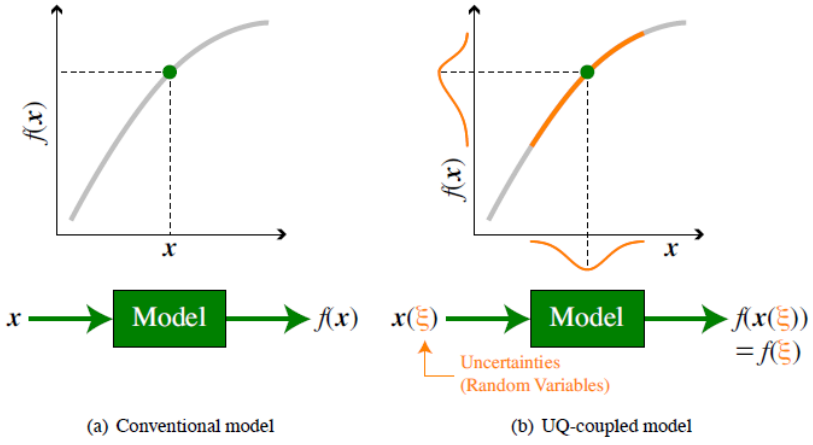

Figure 1.9: Comparison between a deterministic model and an uncertainty quantification model. Extracted from [150].

1.3 Objectives

There exist many numerical tools for shock waves propagation, with varying levels of fidelity. However, the use of a propagation code with a 3D model and wind fluctuations is quite recent. Uncertainty quantification with high fidelity models is also rarely done. Thus, one of the objectives of this thesis is to couple the high fidelity FLHOWARD3D model with an atmosphere whose physical parameters are not well known with the uncertainty polynomial chaos approach to quantify the effects of atmosphere variability on either sonic boom or blast wave propagation. In particular, the influence of kinetic turbulence on low-booms signatures in the last kilometer of propagation in the PBL is the objective of the first part of this work. Comparison with classical boom (N-waves) allows to evaluate the sensitivity of a low-boom to turbulence. In addition to the waveforms, the uncertainty of appropriate metrics for sonic boom also needs to be determined, because metrics represent the human response to sonic boom exposure. One way to answer these questions is to simulate the propagation of different types of sonic booms. As mentioned before, this is a numerical challenge. In particular, the dimensionality (2D/3D) to correctly describe the statistics, the choice of the model of turbulence, the way to make the statistics and to analyze them are still open issues that will be discussed in this manuscript.

Concerning the propagation of blast waves, an extensive database has been gathered by CEA (Commissariat à l'énergie atomique et aux énergies alternatives) over a four years period, for a total of more than 600 explosions recorded at five stations. This reference database will be examined in the second part of this dissertation with the viewpoint of uncertainty analysis regarding sensitivity to wind conditions.

1.4 Overview

The chapter 2 of this manuscript details the so-called FLHOWARD3D numerical model used in this work. Then, the configuration for sonic boom and blast waves are described, and finally, the improvements implemented in this code for this study are presented.

Chapter 3 introduces the study of sonic boom propagation through the PBL. Classical and low sonic-boom signals are presented, and the chosen turbulence models are outlined. Two- and three-dimensional statistics for classical and low sonic-booms are compared to one another and to flight test data to determine the reliability of both approaches.

Chapter 4 focuses on the stochastic study. An uncertainty quantification method using generalized polynomials chaos is used to quantify the influence of physical parameters of the kinetic turbulence on different boom signatures. The uncertainty of different metrics with respect to propagation distance is also analyzed. A database with more than one million of boom signatures is established, and the probability distributions for different metrics are compared for classical and low sonic booms.

Chapter 5 describes the blast waves database. The available characteristics of the source, the topography, the acoustical sensors and the meteorological medium are presented. A first analysis of the database is completed, and a clustering method is applied on the meteorological and source parameters. The influences of the source and of the atmosphere on the waveforms are analyzed using only raw data with no additional propagation model and with a simple wind and temperature categorization in three groups.

Chapter 6 applies the numerical propagation model to blast waves. Simulations are performed for different profiles selected among these groups. Characteristics of the resulting simulated waveforms are discussed and compared. An uncertainty quantification is then achieved with parameterized meteorological profiles. The numerical observations are compared to experimental ones, for each group.

Chapter 2

FLHOWARD3D model for simulating shock waves propagation

As mentioned in the introduction, the propagation of shock waves is computed with FLHOWARD3D software, developed by David Luquet during his PhD [99]. This software is based on a partially one-way equation [31] including diffraction without any angle restriction, non-linearity, wide-angle propagation through a scalar (temperature and density) and vectorial (wind) heterogeneous medium. Absorption and dispersion by thermoviscosity and molecular relaxation are also accounted for. It has been already validated using comparisons with analytic solutions [100]. There are two main objectives in this chapter. The first one is to recall the principle of the FLHOWARD3D method and to describe the initial and boundary conditions used for the simulations. This part is mainly a summary of the method used in [99]. The second objective is to show the different improvements made in the propagation code during my PhD. The first upgrade is to approximate a spherical wave amplitude decay with a two-dimensional cylindrical wave propagation. The proposed solution is an amplitude rescaling applied at each step of the propagation. The second upgrade allows the propagation code to use either the FLHOWARD3D or the KZK approaches by means of a simple switch. This simplifies a lot the comparison between these two resolution methods.

2.1 FLHOWARD3D

In this section, we recall the main features of the FLHOWARD3D model with first the equations, then the initial conditions and finally the boundary conditions.

2.1.1 Equations

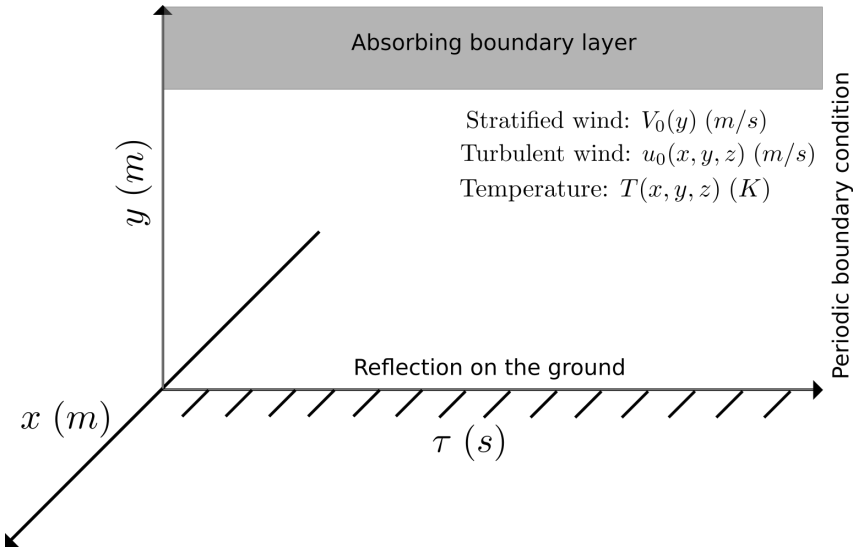

Figure 2.1: Illustration of the propagation medium. The main propagation direction is x, y is the vertical direction and τ is the delayed time. The transverse direction z is not represented on this figure.

For a 3D configuration, the main direction of propagation is the x-axis, the vertical coordinate is y and z designates the transverse one. At a position $\mathbf{x}$ and a time t, we note $\rho(\mathbf{x},t)$ the density, $c_0(\mathbf{x},t)$ the sound speed, $v(\mathbf{x},t)$ the flow velocity and $p(\mathbf{x},t)$ the pressure. The quantities associated with the medium are separated from the time varying acoustical fluctuations: $f(\mathbf{x},t) = f_0(\mathbf{x}) + f_a(\mathbf{x},t)$ with $f = (\rho, \mathbf{v}, p)$. The ambient flow is considered at first order as a mean stratified flow $\mathbf{V_0}(y)$ of order M (with M the Mach number: $M = ||\mathbf{V_0}||/c_0$). The maximum velocities in the next chapters never exceed 40 m/s, thus the maximum Mach number is $M \approx 0.11$. Turbulent fluctuations $\mathbf{u_0}(\mathbf{x})$ are of a smaller order: $\mathbf{v_0}(\mathbf{x}) = \mathbf{V_0}(y) + \mathbf{u_0}(\mathbf{x})$. The sound speed and the density fluctuations are separated between a mean component and a spatially varying one: $c_0(\mathbf{x}) = \bar{c_0} + c_0'(\mathbf{x})$ and $\rho_0(\mathbf{x}) = \bar{\rho_0} + \rho_0'(\mathbf{x})$. An illustration of the propagation medium is given by figure 2.1.

It is then possible to model the nonlinear propagation of acoustic waves in a moving inhomogeneous medium with a nonlinear scalar equation [31]:

$$\begin{aligned}&\frac{1}{c_0^2}\frac{D_s^2 p_a}{Dt^2} - \rho_0 \nabla.\left(\frac{\nabla p_a}{\rho_0}\right) = \\ &-2\frac{dV_{0j}}{dy}\int_{-\infty}^{t}\frac{\partial^2 p_a(\mathbf{x},t')}{\partial y \partial x_j}dt' - \frac{2}{c_0^2}\mathbf{u_0}.\frac{\partial \nabla p_a}{\partial t} + \frac{\beta}{\rho_0 c_0^4}\frac{D_s^2 p_a^2}{Dt^2} + \frac{\delta}{c_0^2}\frac{D_s \Delta p_a}{Dt} + \frac{1}{c_0^2}\sum_{i=1}^{N}\frac{D_s \zeta_i}{Dt},\end{aligned} \tag{2.1}$$

with

$$2\left(1 + t_i\frac{D_s}{Dt}\right)\zeta_i = c_0^2 c_i' t_i \Delta p. \tag{2.2}$$

The left-hand side term is the usual wave equation in a heterogeneous medium moving with speed V_0. The operator $D_s/Dt = \partial/\partial t + \mathbf{V_0}.\nabla$ is the convective derivative associated

to the ambient mean stratified flow. The first term on the r.h.s describes at first order the influence of the stratification of this mean flow. The second one is the wave convection by the turbulent fluctuations (at first order). The third one is the dominant nonlinear term, with $\beta = (\gamma+1)/2$ the fluid nonlinear parameter where $\gamma = c_p/c_v$ is the ratio of the specific heats. In [31], the last two terms of equation 2.1 are not given. The fourth r.h.s. term is the thermoviscous absorption with $\delta = \left[\frac{4}{3}\mu + \mu_B + \kappa(c_v^{-1} - c_p^{-1})\right]/\rho_0$ the sound diffusivity of the medium. Here, μ is the shear viscosity, μ_B the bulk one, κ the thermal conductivity, c_p and c_v the specific heats at constant pressure and constant volume. The last one describes the sound attenuation and dispersion due to relaxation of diatomic nitrogen ($i = 1$) and oxygen ($i = 2$) molecules. The internal variable ζ_i associated to each relaxation process satisfies the relaxation equation 2.2 with t_i the relaxation time and c_i' the increase of phase velocity undergone by the wave between the low (phase velocity c_0 when $\omega t_i << 1$) and the high (phase velocity $c_0 + c_i'$ when $\omega t_i >> 1$) frequency regimes.

As nonlinear, absorption and relaxation effects are all very small for considered applications (typically less than 10^{-3}), influence of convection on these terms is even lower and can be neglected. Therefore, a simplified version of equation 2.1 can be written:

$$\begin{aligned}&\frac{1}{c_0^2}\frac{D_s^2 p_a}{Dt^2} - \rho_0 \nabla.\left(\frac{\nabla p_a}{\rho_0}\right) = \\ &-2\frac{dV_{0j}}{dy}\int_{-\infty}^{t}\frac{\partial^2 p_a(\mathbf{x},t')}{\partial y \partial x_j}dt' - \frac{2}{c_0^2}\mathbf{u_0}.\frac{\partial \nabla p_a}{\partial t} + \frac{\beta}{\rho_0 c_0^4}\frac{\partial^2 p_a^2}{\partial t^2} + \frac{\delta}{c_0^4}\frac{\partial^3 p_a}{\partial t^3} + \frac{1}{c_0^2}\sum_{i=1}^{N}\frac{\partial \zeta_i}{\partial t},\end{aligned} \tag{2.3}$$

with

$$2\left(1 + t_i\frac{\partial}{\partial t}\right)\zeta_i = c_0^2 c_i' t_i \Delta p. \tag{2.4}$$

In equation 2.3, in the absorption term, the Laplacian has been replaced by $\frac{1}{c_0^2}\frac{\partial^2 p}{\partial t^2}$ using the wave equation at dominant order.

Now, the objective is to transform equation 2.3 into a form easier to handle numerically. The equation is first written in the form of a homogeneous wave equation with a perturbation term on the right hand side P, containing the terms linked to flow motion, medium heterogeneities, sound absorption and relaxation and nonlinearities:

$$\frac{1}{\bar{c_0}^2}\frac{\partial^2 p_a}{\partial t^2} - \frac{\partial^2 p_a}{\partial x^2} - \frac{\partial^2 p_a}{\partial y^2} - \frac{\partial^2 p_a}{\partial z^2} = P. \tag{2.5}$$

Then, a retarded time $\tau = t - x/\bar{c_0}$ is introduced, and the equation is rewritten in a time frame moving with the mean sound speed in the x-direction in order to follow the wave along its main direction of propagation:

$$\frac{2}{\bar{c_0}^2}\frac{\partial^2 p_a}{\partial x \partial \tau} - \frac{\partial^2 p_a}{\partial x^2} - \frac{\partial^2 p_a}{\partial y^2} - \frac{\partial^2 p_a}{\partial z^2} = P'. \tag{2.6}$$

A wide angle approximation is then applied, but only on the perturbation term P' rather than on the full wave equation. To do this, the second order derivative in x (P' depends on $\frac{\partial^2}{\partial x^2}$) is replaced in P' using the linear homogeneous equation written in retarded time:

$$\frac{\partial^2 p_a}{\partial x^2} = \frac{2}{\bar{c_0}^2}\frac{\partial^2 p_a}{\partial x \partial \tau} - \frac{\partial^2 p_a}{\partial y^2} - \frac{\partial^2 p_a}{\partial z^2} + O(M), \tag{2.7}$$

so that an error of order M^2 at most is achieved because P' is itself of order M. Finally, in order to handle shock waves numerically, the acoustic pressure p_a is replaced by a pseudo potential, which has the advantage to remain continuous through shocks [30]:

$$p_a(\mathbf{x}, \tau) = \frac{\partial \phi}{\partial \tau}(\mathbf{x}, \tau). \tag{2.8}$$

The so-called FLH model is then:

$$\frac{\partial^2 \phi}{\partial x \partial \tau}(\mathbf{x}, \tau) = D\phi(\mathbf{x}, \tau) + H\phi(\mathbf{x}, \tau) + N\phi(\mathbf{x}, \tau) + A\phi(\mathbf{x}, \tau), \tag{2.9}$$

where D is the operator representing diffraction effects, H the operator representing heterogeneities and wind effects, N the operator associated to the nonlinearities and A the operator representing the absorption and the relaxation effects:

$$D\phi(\mathbf{x}, \tau) = \frac{\bar{c_0}}{2}\left(\frac{\partial^2 \phi}{\partial x^2} + \frac{\partial^2 \phi}{\partial y^2} + \frac{\partial^2 \phi}{\partial z^2}\right), \tag{2.10}$$

$$H\phi(\mathbf{x}, \tau) = FLH(\mathbf{x}, \tau) + TH(\mathbf{x}, \tau), \tag{2.11}$$

with

$$FLH\phi(\mathbf{x}, \tau) = \frac{v_{0x}}{\bar{c_0}^2}\frac{\partial^2 \phi}{\partial \tau^2} - \frac{v_{0x}}{\bar{c_0}}\frac{\partial^2 \phi}{\partial x \partial \tau} - \frac{v_{0y}}{\bar{c_0}}\frac{\partial^2 \phi}{\partial y \partial \tau} - \frac{v_{0z}}{\bar{c_0}}\frac{\partial^2 \phi}{\partial z \partial \tau}, \tag{2.12}$$

and

$$\begin{aligned} TH\phi(\mathbf{x}, \tau) = {} & \frac{1}{2\rho_0}\left(\frac{\partial \rho_0}{\partial x}\frac{\partial \phi}{\partial \tau} - \bar{c_0}\frac{\partial \rho_0}{\partial x}\frac{\partial \phi}{\partial x}\right) - \frac{\bar{c_0}}{2\rho_0}\left(\frac{\partial}{\partial y}\left[\rho_0\frac{\partial \phi}{\partial y}\right] + \frac{\partial}{\partial z}\left[\rho_0\frac{\partial \phi}{\partial z}\right]\right) \\ & + \frac{\bar{c_0}}{2}\left(\frac{\partial^2 \phi}{\partial y^2} + \frac{\partial^2 \phi}{\partial z^2}\right) + \frac{2\bar{c_0}c_0' + c_0'^2}{2\bar{c_0}^3}\frac{\partial^2 \phi}{\partial \tau^2}, \end{aligned} \tag{2.13}$$

$$A\phi(\mathbf{x}, \tau) = \frac{\partial}{\partial \tau}\left(\frac{\delta}{2\bar{c_0}^3}\frac{\partial^2 \phi}{\partial \tau^2}\right) + \frac{\partial}{\partial \tau}\left(\sum_j \frac{c_j'}{\bar{c_0}^2}\int_{-\infty}^{\tau}\frac{\partial^2 \phi}{\partial \tau'^2}e^{-\frac{(\tau-\tau')}{t_j}}d\tau'\right), \tag{2.14}$$

and

$$N\phi(\mathbf{x}, \tau) = \frac{\beta}{2\bar{\rho_0}\bar{c_0}^3}\frac{\partial}{\partial \tau}\left[\left(\frac{\partial \phi}{\partial \tau}\right)^2\right]. \tag{2.15}$$

To solve the equation numerically, a split-step method is chosen [71]. It allows to solve each part of the equation separately and then to couple the solution by assembling the results:

$$\phi(x + \Delta x, y, z, \tau) = \phi^D_{\Delta x} \circ \phi^{H+A}_{\Delta x} \circ \phi^N_{\Delta x}(x, y, z, \tau) + O(\Delta x), \tag{2.16}$$

where $\phi^X_{\Delta x}$ is solution of the formal equation $\frac{\partial^2 \phi}{\partial x \partial \tau}(\mathbf{x}, \tau) = X\phi(\mathbf{x}, \tau)$ with operator $X = \{D, H + A \text{ or } N\}$ when advancing by a Δx step. Note that equation 2.16 is written as a first order split-step but a second order one is indeed implemented in FLHOWARD3D.

Each part of the equation is solved using an efficient numerical method adapted to each physical effect:

- The angular spectrum method for the diffraction in the 3D spectral space (ω, k_y, k_z),
- An analytic solution for absorption and relaxation effects and for phase shifts associated to medium heterogeneities and wind. This is performed in the frequency domain (ω, y, z),
- Finite differences for remaining wind and medium heterogeneities.This is performed in the same domain,
- The semi-analytic Burgers-Hayes method [30] for the nonlinear effects in the physical domain (τ, y, z).

Here, ω is the angular frequency and (k_y, k_z) is the wave vector in the plane orthogonal to the main direction of propagation. In the first step, evanescent waves are accounted for, but backward propagating ones are neglected. Hence, this allows to have a one-way approach satisfying as best as possible the exact dispersion relation for all forward propagating waves. Between these steps, Fast Fourier Transforms are used to change the space in which the resolution is done. All details are given in [99, 100]. To optimize the computational time, a parallelization of the code has been implemented with the Message Passing Interface (MPI) library.

In this thesis, we consider only propagation in air, with a density $\rho_0 = 1.2\,\mathrm{kg/m^3}$, a sound speed $c_0 = 340\,\mathrm{m/s}$, and a nonlinear parameter β =1.2. For the relaxation and absorption, the ISO 9613-1 norm (1993) [1] is chosen, with a relative humidity of $h_r = 43\,\%$ on the ground, an atmospheric pressure of $p_0 = 101\,325\,\mathrm{Pa}$ and a temperature of T_0 =14.5 °C.

2.1.2 Initial conditions

FLHOWARD3D enables the propagation of different geometries of acoustic waves, in 2D or 3D media. As seen in the previous section, FLHOWARD3D is a method with a marching scheme of step Δx in x-direction. Therefore, the initial condition $\phi(x = x_0, y, z, \tau)$ must be prescribed in the initial plan x_0 and is different for sonic booms (cylindrical waves) and blast waves (spherical waves). We assume that the sonic boom is a plane wave because it is considered far enough from the source, while we keep the spherical behavior for the blast waves. For 2D simulations, the initial sonic boom therefore appears as a plane wave and the initial blast wave as a cylindrical wave. A method to recover the correct amplitude decay of a blast wave is detailed in section 2.2.

We note $s(\tau)$ the initial waveform, and θ the angle of the plane wave with the vertical. The expression of the pressure field of the initial plane wave is :

$$p_a(x = x_0, y, z, \tau) = s\left(\tau + \frac{y \sin\theta}{c_0}\right). \tag{2.17}$$

In a configuration where there is a reflection on the ground, the initial condition is the superposition of 2 plane waves with opposite angles as illustrated by figure 2.2 (left) when $s(\tau)$ is an N-wave.

Blast waves are mainly studied in 2D where the are represented by cylindrical waves. They have to be initialized at a distance $x_0 > 0$ to avoid a singular behavior :

$$p_a(x = x_0, y, \tau) = \tilde{A}(x_0, y) s\left(\tau - \frac{x_0\left(\psi(x_0, y) - 1\right)}{c_0}\right).$$

with $\psi(x_0, y) = \sqrt{1 + \frac{y^2}{x_0^2}}$ the time shifting and $\tilde{A} = \frac{|H_0(f_0 x_0 \psi / c_0)|}{|H_0(f_0 x_0 / c_0)|}$ the amplitude correction with f_0 the characteristic frequency and H_0 the Hankel function of the first kind of order 0 [142]. Figure 2.2 (right) shows the initial condition for a cylindrical wave with $s(\tau)$ a sincos wave :

$$s\left(\tau\right) = \begin{cases} K \sin(2\pi f_0 \tau)\left(\frac{1-\cos 2\pi f_0 \tau}{2}\right) & \text{if } 0 < \tau < \frac{1}{f_0}, \\ 0 & \text{otherwise.} \end{cases} \tag{2.18}$$

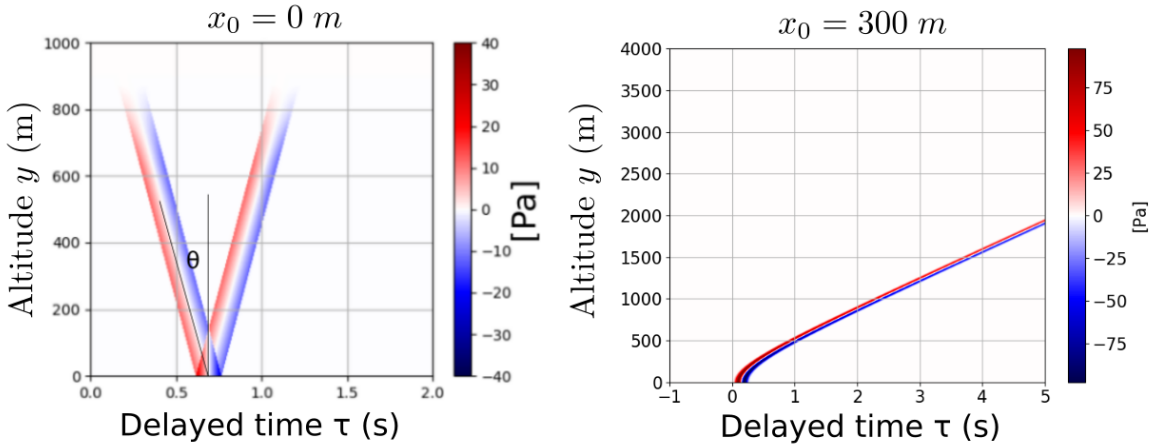

Figure 2.2: Initial pressure field $p(x = x_0, y, \tau)$ (in function of the altitude and the delayed time) for a planar N-wave (left) and a cylindrical sincos wave (right).

2.1.3 Boundary conditions

We can see on figure 2.1 that there are different kinds of boundary conditions. Rigid boundary conditions are chosen on the ground ($y = 0\,\text{m}$). Periodic boundary conditions are chosen in the time domain ($\tau-$axis). Absorbing Boundary Conditions (ABC) are chosen at the upper limit of the domain $L = y_{max}$, and for the lateral direction $L = z_{min}$ and $L = z_{max}$. A numerical absorption coefficient, independent of frequency, is added to the physical absorption in a layer of thickness a. This coefficient is

$$\zeta(h) = \frac{\alpha c_0}{a^3} h^2, \tag{2.19}$$

with h the penetration distance inside the absorbing layer $h = L - y$ or $h = L - z$. The values of a and α are empirically chosen to minimize the reflection of the wave on this boundary.

2.2 Spherical approximation in a 2D medium

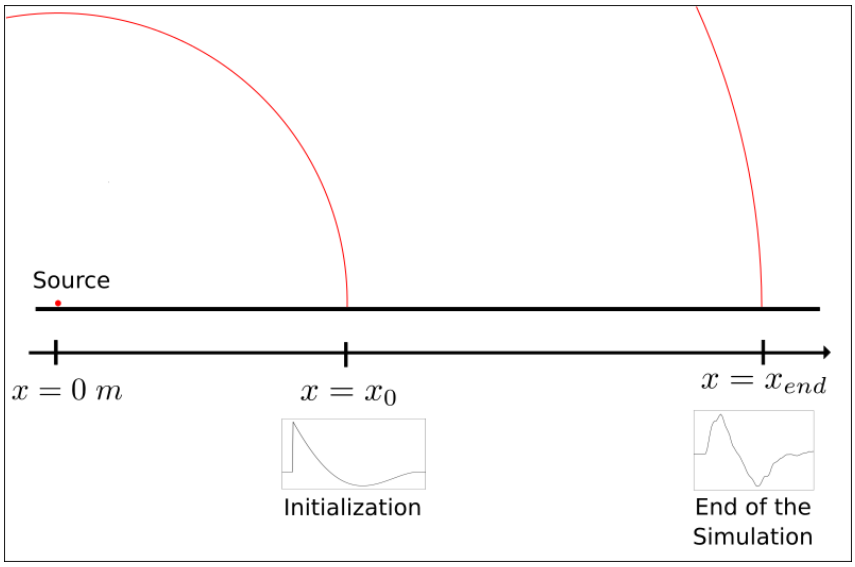

Figure 2.3: Illustration of the propagation of a spherical wave. x_0 correspond to the initialization distance and x_{end} to the distance corresponding to the end of the simulation.

The propagation of a spherical wave is sketched by figure 2.3. For computational reasons, in the propagation code, the pressure field is initialized at a distance $x = x_0 > 0$ from the source where x_{end} is the last point of computation. In linear regime, the decrease of the amplitude is different for cylindrical and spherical waves in far field: spherical waves decrease as $\frac{1}{r}$ while cylindrical waves decrease as $\frac{1}{\sqrt{r}}$ as illustrated on figure 2.4. So, there is an issue in simulating the amplitude of a spherical wave in a two-dimensional computational domain. This issue can be solved in linear regime by simply rescaling the amplitude by a factor $\frac{1}{\sqrt{r}}$ at the end or at the beginning of the simulation. But this is not possible in nonlinear regime for which cumulative effects are more important for a cylindrical wave than for a spherical one. The amplitude is not the single difference between cylindrical and planar waves, but correcting it would still make the spherical approximation far better.

2.2.1 Amplitude correction

To recover the correct amplitude in nonlinear regime with FLHOWARD3D, we propose to make an amplitude correction at each step Δx by multiplying the potential (direct output of the solver) by a correction coefficient $\alpha(x + \Delta x)$ whose values depends on the distance from the source:

$$\tilde{\phi}(x + \Delta x, y, \tau) = \alpha(x + \Delta x)\phi(x + \Delta x, y, \tau). \tag{2.20}$$

Here, $\alpha(x + \Delta x)$ is chosen for the new potential $\tilde{\phi}(x + \Delta x, y, \tau)$ to decrease as $1/x$.

Over a small space step Δx the amplitude for the cylindrical configuration decreases

with a factor $\frac{1}{\sqrt{\Delta x}}$, so:

$$\phi(x)\sqrt{x} \approx \phi(x+\Delta x)\sqrt{x+\Delta x} => \phi(x) \approx \frac{\sqrt{x+\Delta x}}{\sqrt{x}}\phi(x+\Delta x). \tag{2.21}$$

For the spherical waves this is:

$$\phi_{sph}(x)x \approx \phi_{sph}(x+\Delta x)(x+\Delta x) => \phi_{sph}(x) = \frac{x+\Delta x}{x}\phi_{sph}(x+\Delta x), \tag{2.22}$$

with $\phi_{sph}(x)$ the potential for the spherical waves.

Thus, assuming $\phi(x) = \phi_{sph}(x)$ at the beginning of the space step, we can apply the following correction at the end of the space step:

$$\frac{\sqrt{x+\Delta x}}{\sqrt{x}}\phi(x+\Delta x) = \frac{x+\Delta x}{x}\tilde{\phi}(x+\Delta x), \tag{2.23}$$

$$\tilde{\phi}(x+\Delta x) = \frac{\left(\frac{\sqrt{x+\Delta x}}{\sqrt{x}}\right)}{\left(\frac{x+\Delta x}{x}\right)}\phi(x+\Delta x), \tag{2.24}$$

therefore

$$\alpha(x+\Delta x) = \frac{\left(\frac{\sqrt{x+\Delta x}}{\sqrt{x}}\right)}{\left(\frac{x+\Delta x}{x}\right)} = \frac{\sqrt{x}}{\sqrt{x+\Delta x}}. \tag{2.25}$$

The corrected cylindrical amplitude after each step Δx, is superimposed on the cylindrical and spherical potentials on figure 2.4. We can see the aliasing effect on the zoom (right part of the figure) but the overall decrease is close to the spherical one.

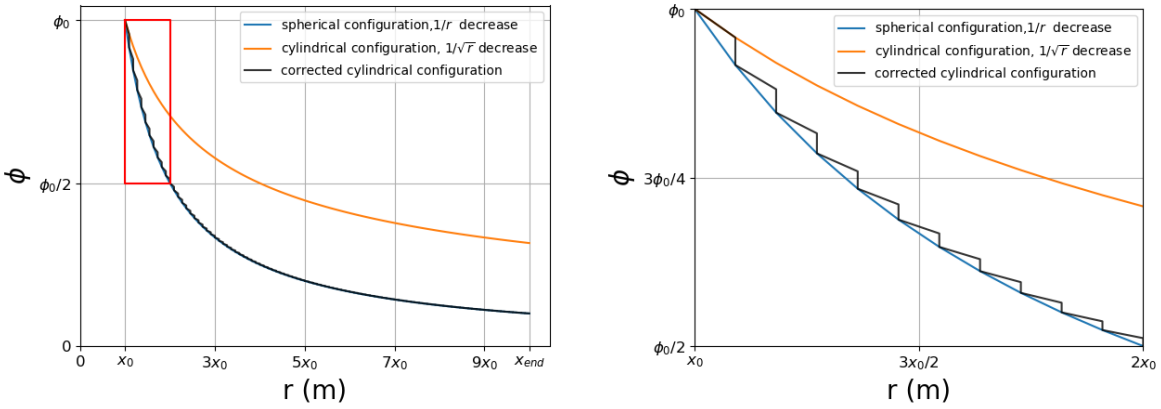

Figure 2.4: Amplitude decrease for the cylindrical configuration, the spherical configuration and the corrected cylindrical configuration. The figure on the right is the zoomed red rectangle on the left.

2.2.2 Validation

To validate this approach, evolution of amplitude is compared to semi-analytical solutions of different inviscid Burgers equations [30], which model the nonlinear propagation of plane, cylindrical and spherical waves in homogeneous medium.

For a plane wave, the inviscid Burgers equation for the pressure p_{pw} is:

$$\frac{\partial p_{pw}}{\partial x} - \frac{\beta}{\rho_0 c_0^3} p_{pw} \frac{\partial p_{pw}}{\partial \tau} = 0. \tag{2.26}$$

For a cylindrical wave, the inviscid Burgers equation for the pressure p_{cw} is:

$$\frac{\partial p_{cw}}{\partial r} + \frac{p_{cw}}{2r} - \frac{\beta}{\rho_0 c_0^3} p_{cw} \frac{\partial p_{cw}}{\partial \tau} = 0, \tag{2.27}$$

where r is the radial distance from the source center,$\tau = t - \frac{r - r_0}{c_0}$ and r_0 is the source radius.

For a spherical wave, the inviscid Burgers equation for the pressure p_{sw} is:

$$\frac{\partial p_{sw}}{\partial r} + \frac{p_{sw}}{r} - \frac{\beta}{\rho_0 c_0^3} p_{sw} \frac{\partial p_{sw}}{\partial \tau} = 0. \tag{2.28}$$

The change of variables described in [44] is used to obtain a dimensionless equation, recasted under the generic form:

$$\frac{\partial \bar{P}}{\partial \bar{d}} = 0.5\mu \frac{\partial \bar{P}^2}{\partial \bar{\tau}}, \tag{2.29}$$

with $\bar{P}$ a dimensionless pressure, $\bar{d}$ a dimensionless distance, $\bar{\tau} = \omega\tau$ the dimensionless retarded time, and μ is a coefficient. These changes of variables are:

- for plane waves, $\bar{P} = \frac{p_{pw}}{p_0}$ with p_0 the initial peak pressure, $\mu = 1$ and $\bar{d} = \bar{\sigma} = \frac{\beta\omega p_0 x}{\rho_0 c_0^3} = \frac{x}{Lc}$ with $Lc = \frac{1}{k\beta M}$, $k = \frac{\omega}{c_0}$ and $M = \frac{v_0}{c_0} = \frac{p_0}{\rho_0 c_0^2}$. For this case Lc is known as the shock formation distance,
- for cylindrical waves, $\bar{P} = \frac{p_{cw}}{p_0}\left(\frac{r}{r_0}\right)^{\frac{1}{2}}$, $\mu = \frac{2\omega r_0 \beta p_0}{\rho_0 c_0^3}$ and $\bar{d} = \left(\frac{r}{r_0}\right)^{\frac{1}{2}}$,
- for spherical waves, $\bar{P} = \frac{p_{sw}}{p_0}\frac{r}{r_0}$, $\mu = \frac{\omega r_0 \beta p_0}{\rho_0 c_0^3}$ and $\bar{d} = \ln\left(\frac{r}{r_0}\right)$.

In order to do the comparison, the propagation of a sine wave with a normalized amplitude 1 and a normalized frequency $\bar{f}_0 = 1$ (see figure 2.5) is chosen:

$$p_a\left(\bar{\sigma} = 0, \bar{\tau}\right) = \begin{cases} -\sin\left(\bar{\tau}\right) & \text{if } |\bar{\tau}| < \pi, \\ 0 & \text{otherwise.} \end{cases}$$

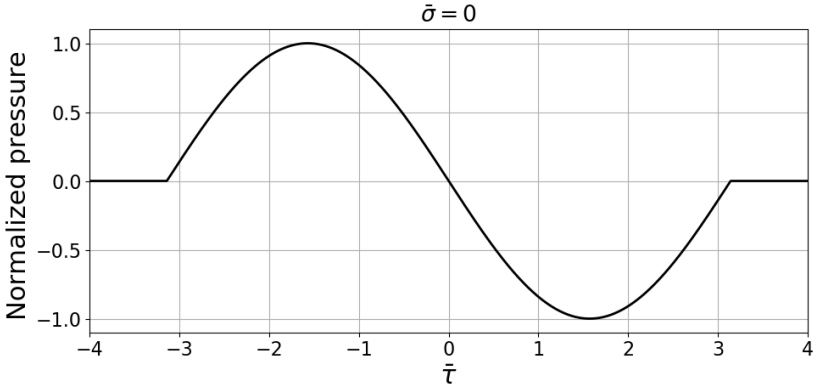

Figure 2.5: Initial sine wave with normalized pressure and frequency.

Figures 2.6 to 2.8 show the waveform at different distances from the source computed by different models of propagation:

- the nonlinear Burgers inviscid spherical wave (NLS) (dark blue),
- the FLHOWARD3D cylindrical wave rescaled after propagation (CA) (light blue),
- the FLHOWARD3D cylindrical wave rescaled before propagation (CB)(purple),
- the FLHOWARD3D cylindrical wave rescaled at each step of the propagation (CS) (black),

Let us comment figures 2.6 to 2.8 at distances respectively $\bar{\sigma} = 3.24$, $\bar{\sigma} = 10.66$ and $\bar{\sigma} = 31.88$. There are some perturbations in the simulated signals due to undesired reflections. However, clearly the CA case is always inadequate because computation is performed for a cylindrical wave for which nonlinear effects are much higher. The linear rescaling after the simulation is unable to compensate for them. The two other cases CB and CS show good agreement with the exact nonlinear case NLS. However, the case of rescaling before propagation (CB) tends to slightly underestimate nonlinear effects. As a conclusion, the CS method (rescaling at each step) is the recommended one.

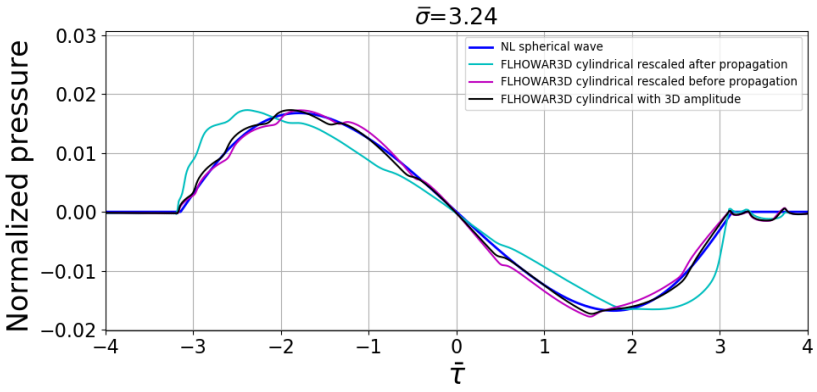

Figure 2.6: Evolution of an initial sine wave for different models of propagation for a normalized propagation distance $\bar{\sigma} = 3.24$.

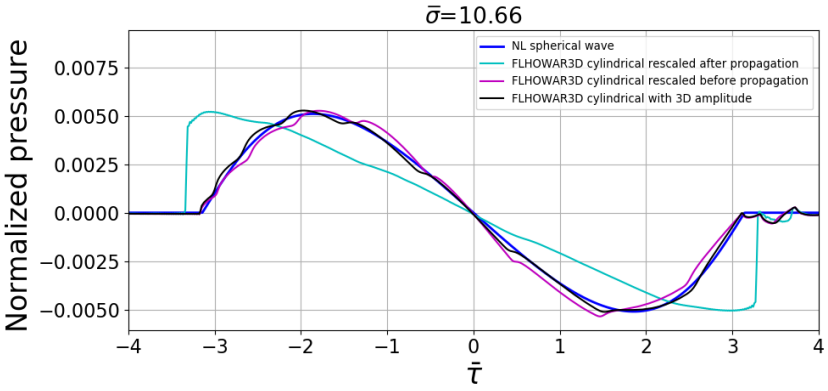

Figure 2.7: Evolution of an initial sine wave for different models of propagation for a normalized propagation distance $\bar{\sigma} = 10.66$.

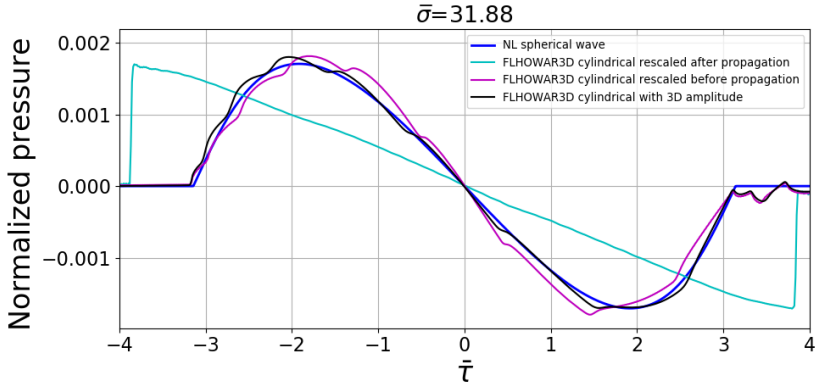

Figure 2.8: Evolution of an initial sine wave for different models of propagation for a normalized propagation distance $\bar{\sigma} = 31.88$.

2.3 KZK and FLHOWARD3D approximations

2.3.1 Dispersion curves associated to the diffraction operators

The usual KZK equation [62] is:

$$\frac{\partial^2 p_a}{\partial x \partial \tau} - \frac{c_0}{2}\nabla_\perp^2 p_a - \frac{\delta}{2c_0^3}\frac{\partial^3 p_a}{\partial^3 \tau} = \frac{\beta}{2\rho_0 c_0^3}\frac{\partial^2 p_a^2}{\partial \tau^2}, \tag{2.30}$$

with $\nabla_\perp^2$ the Laplacian in the transverse direction. Note that this is the classical equation which includes neither heterogeneities nor flow effects. We rewrite this equation with the potential (equation 2.8) as it was done for the FLHOWARD3D model:

$$\frac{\partial^2 \phi}{\partial x \partial \tau} = \frac{c_0}{2}\nabla_\perp^2 \phi + \frac{\delta}{2c_0^3}\frac{\partial^3 \phi}{\partial^3 \tau} + \frac{\beta}{2\rho_0 c_0^3}\frac{\partial}{\partial \tau}\left[\left(\frac{\partial \phi}{\partial \tau}\right)^2\right]. \tag{2.31}$$

Or under the form:

$$\frac{\partial^2\phi}{\partial x\partial\tau} = D_{(KZK)}\phi + A\phi + N\phi, \tag{2.32}$$

with N and A the operators described in section 2.1.1, and

$$D_{(KZK)}\phi = \frac{c_0}{2}\nabla_\perp^2\phi = \frac{c_0}{2}\left(\frac{\partial^2\phi}{\partial y^2} + \frac{\partial^2\phi}{\partial z^2}\right). \tag{2.33}$$

Note that operator A can be modified to include molecular relaxation effects; in this case it would have the same expression as in section 2.1.1.

The main difference between the FLHOWARD3D and KZK models comes from the diffraction operator D, which is for FLHOWARD3D model:

$$D\phi = \frac{c_0}{2}\nabla^2\phi = \frac{c_0}{2}\left(\frac{\partial^2\phi}{\partial x^2} + \frac{\partial^2\phi}{\partial y^2} + \frac{\partial^2\phi}{\partial z^2}\right). \tag{2.34}$$

In order to quantify it, the dispersion relation of each wave equation considering only diffraction effect and therefore only operator D or $D_{(KZK)}$ is calculated:

$$\frac{\partial^2\phi}{\partial x\partial\tau} = D\phi \text{ or } \frac{\partial^2\phi}{\partial x\partial\tau} = D_{(KZK)}\phi. \tag{2.35}$$

The plane wave has the expression:

$$\phi(\mathbf{x},t) = Ae^{i(\mathbf{x}.\mathbf{k}-\omega_0 t)} = Ae^{i(k_x x+k_y y+k_z z-\omega_0(t-x/c_0)-\omega_0(x/c_0))} = Ae^{i((k_x-k_0)x+k_y y+k_z z-\omega_0\tau)}, \tag{2.36}$$

with $k_0 = \frac{\omega_0}{c_0}$ the wave number. We obtain

$$\phi(\mathbf{x},t) = Ae^{ik_0\left(\left(\bar{k}_x-1\right)x+\bar{k}_y y+\bar{k}_z z-c_0\tau\right)}, \tag{2.37}$$

with $\bar{k}_x = \frac{k_x}{k_0}$, $\bar{k}_y = \frac{k_y}{k_0}$, $\bar{k}_z = \frac{k_z}{k_0}$.

For the FLHOWARD3D model, the dispersion equation becomes:

$$(\bar{k}_x-1)c_0 = -\frac{c_0}{2}\left((\bar{k}_x-1)^2+\bar{k}_y^2+\bar{k}_z^2\right) => \bar{k}_x = +\sqrt{1-\bar{k}_\perp^2}, \tag{2.38}$$

with $\bar{k}_\perp = \sqrt{\bar{k}_y^2+\bar{k}_z^2}$. Therefore, the dispersion curve is the positive ($\bar{k}_x > 0$) half-circle of the full wave equation. Note that the one-way character of FLHOWARD3D model arises from the choice of the the positive signal in equation 2.38 in the numerical solver of the diffraction operaton D.

For the KZK model, replacing ϕ by its expression, we get:

$$(\bar{k}_x-1)c_0 = \frac{c_0}{2}\left(\bar{k}_y^2+\bar{k}_z^2\right) => \bar{k}_x = 1-\frac{1}{2}\bar{k}_\perp^2. \tag{2.39}$$

The dispersion curve is the parabola osculating the circle at $\bar{k}_\perp = 0$. This dispersion relation is equal to the second order Taylor expansion of the previous one.

Both dispersion curves $\bar{k}_x = f(\bar{k}_\perp)$ are plotted on figure 2.9. The exact circle is also plotted. The angle with the x-direction is called θ. The half circle and parabola are superposed to the unit circle for small values of θ. It means that waves with a propagation

direction close to the main one ($\theta = 0$) are well described by both models. However, when θ increases, then only FLWOWARD3D remains valid while KZK equation is less and less accurate. For $\theta > 90°$, neither the FLHOWARD3D nor the KZK model gives a solution, because those are one-way methods: the backscattered field is neglected in both cases. For a more complete analysis of dispersion relations in case of a uniform flow, the reader is referred to [99, 100].

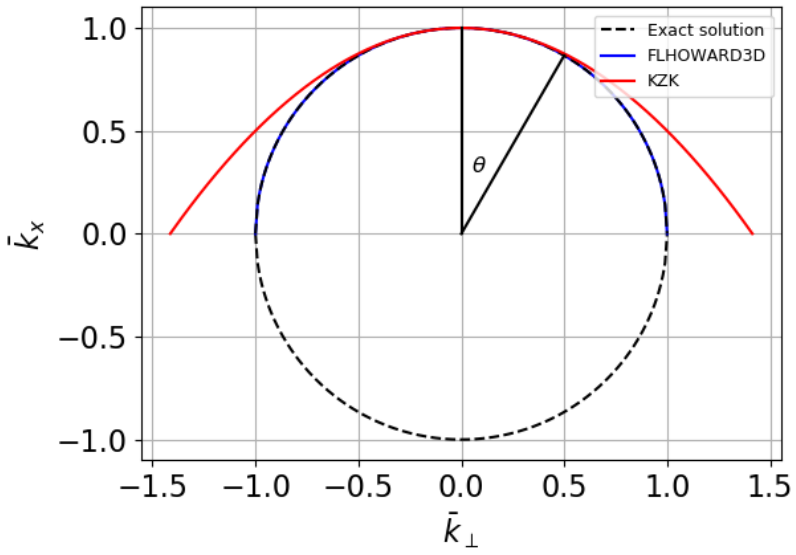

Figure 2.9: Dispersion relations for the wave equation, and for the FLHOWARD3D and KZK models.

2.3.2 Numerical resolution of the diffraction operators

The time Fourier transform along the τ axis is defined as:

$$\hat{\phi}\,(x, y, z, \omega) = \int_{-\infty}^{+\infty} \phi(x, y, z, \tau) e^{-i\omega t} d\tau, \tag{2.40}$$

and the 2D spatial Fourier transform in the plane orthogonal to the main propagation x-direction as:

$$\bar{\bar{\phi}}(x, k_y, k_z, \tau) = \int_{-\infty}^{+\infty} \int_{-\infty}^{+\infty} \phi(x, y, z, \tau) e^{-ik_y y} e^{-ik_z z} dy dz. \tag{2.41}$$

Using these transforms, the equation 2.35 becomes for the FLHOWARD3D model:

$$\frac{d^2 \bar{\bar{\hat{\phi}}}}{dx^2} - 2ik \frac{d\bar{\bar{\hat{\phi}}}}{dx} - (k_y^2 + k_z^2)\bar{\bar{\hat{\phi}}} = 0, \tag{2.42}$$

with $k = \omega / c_0$.

The equation is solved analytically. Its discriminant is $\Delta = 4\left[-k^2 + (k_y^2 + k_z^2)\right]$. There are 2 solutions but the FLHOWARD3D method selects only the one for propagation in the positive x-direction:

if $-k^2 + (k_y^2 + k_z^2) < 0$:

$$\overline{\overline{\hat{\phi}}}(x + \Delta x, k_y, k_z) = \overline{\overline{\hat{\phi}}}(x, k_y, k_z) \exp\left(\Delta x \left[ik - i\sqrt{k^2 - (k_y^2 + k_z^2)}\right]\right). \tag{2.43}$$

If $-k^2 + (k_y^2 + k_z^2) > 0$, only the wave evanescent in the positive x-direction is selected:

$$\overline{\overline{\hat{\phi}}}(x + \Delta x, k_y, k_z) = \overline{\overline{\hat{\phi}}}(x, k_y, k_z) \exp\left(\Delta x \left[ik - \sqrt{-k^2 + (k_y^2 + k_z^2)}\right]\right). \tag{2.44}$$

For the KZK approximation, the equation 2.33 gives:

$$\frac{d\overline{\overline{\hat{\phi}}}}{dx} - i\frac{(k_y^2 + k_z^2)}{2k}\overline{\overline{\hat{\phi}}} = 0 \tag{2.45}$$

This equation is solved analytically, and the solution is:

$$\overline{\overline{\hat{\phi}}}(x + \Delta x, k_y, k_z) = \overline{\overline{\hat{\phi}}}(x, k_y, k_z) \exp\left(i\Delta x \frac{k_y^2 + k_z^2}{2k}\right) \tag{2.46}$$

The solution is then retrieved in the physical space using the inverse Fourier transforms. We can see that the solutions of FLHOWARD3D (equations 2.44 and 2.43) and KZK (equation 2.46) are different: once again they match near the propagation axis and deviate far from it. Moreover, whatever the transverse wave number, the KZK equation does not lead to any evanescent wave. From a numerical perspective, it is easy to compute one or the other with the same framework (simply by switching between the formulas). This option to have the KZK resolution is thus added to the FLHOWARD3D code, in order to easily enable the comparison between both models. Such comparison is performed in the next chapter.

2.4 Conclusion

In this chapter, the numerical code used to simulate the propagation of shock waves, FLHOWARD3D, is recalled. Starting from a nonlinear wave equation for pressure in a moving heterogeneous and absorbing medium, a delayed time τ and a potential ϕ are introduced, and an equation separating the different physical effects is obtained. These effects are solved separately with adapted methods, relying on a second order split-step and massive use of FFTs. The initial and the boundary conditions of the problem are also described. The two geometries studied in this work, the plane wave and the cylindrical one, are examined. The two main modifications provided to the propagation code are described. First, an option to rescale a cylindrical wave, in order to recover a spherical wave decay, is introduced. This allows 2D simulations of a spherical point source, especially in the nonlinear case. A switch to solve the KZK equation instead of the FLHOWARD3D one is also introduced. This makes the comparison between the two models easier. These two additional features are used in the following chapters.

Chapter 3

Sonic boom propagation: deterministic study

In this chapter, the propagation of sonic booms generated by supersonic aircraft and the influence of turbulent wind fluctuations in the planetary boundary layer (PBL) on these sonic boom is studied. The PBL roughly corresponds to the last kilometer before the ground, and is where kinetic turbulence is the most important. First, the waveforms studied in this chapter are presented. Two different types of signature are available: the classical booms and the less disturbing low booms. One of the main objectives of the two following chapters is to compare the effect of kinetic turbulence on these two types of signal. For this purpose, the turbulence model used in this study is then described. An more complex model with inhomogeneities is also considered, to enable a comparison between the two. Then, initial conditions specific to this study are described. Instead of a vertical propagation towards the ground, the propagation here is done parallel to the ground. A convergence study is then performed, in order to optimize the computational time while preserving a good accuracy. The propagation of the sonic boom signals is then computed for a single realization of the turbulence, and their behavior in 2D and 3D media is observed. Other propagations with different parameters are computed, and a novel comparison between 2D, 3D and experimental observations is performed, to evaluate the accuracy of the simulations. Comparisons between KZK and FLHOWARD3D models, as well as between the two turbulence model described previously are also performed, to see if the variation in the models have an important effect on the results. The studies in this chapter pave the way for the stochastic study in the next chapter.

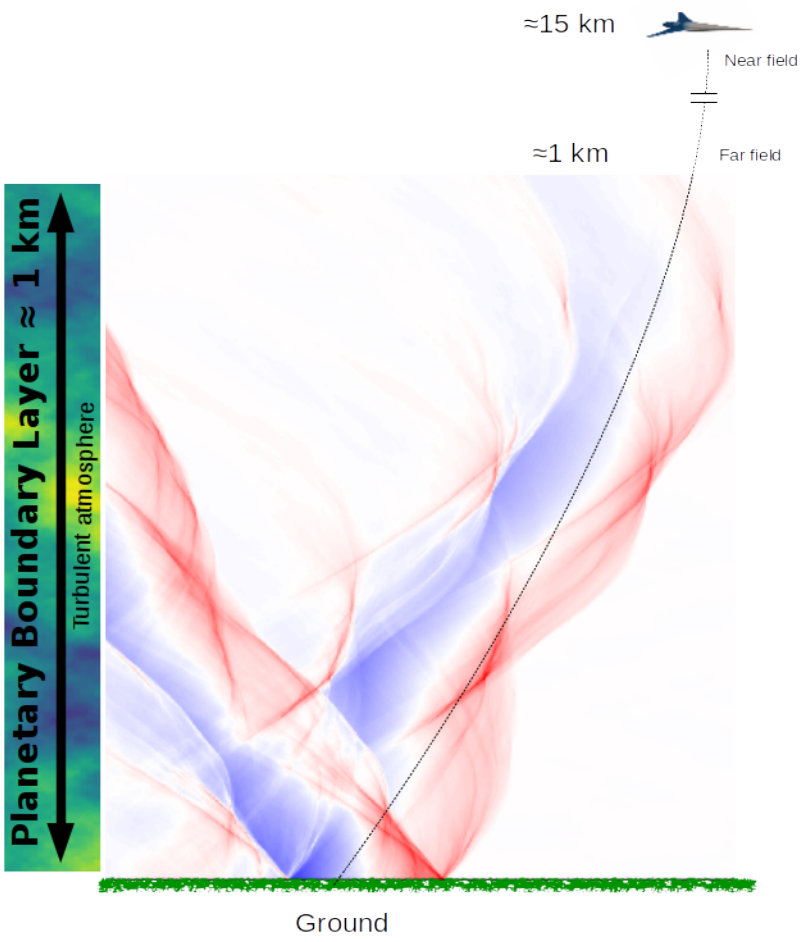

Figure 3.1: Propagation of a sonic boom signature produced by a supersonic aircraft flying parallel to the ground.

3.1 Sonic boom signatures

Supersonic aircraft fly at an altitude close to 15 km above the ground. As said before, acoustical signatures are generated in the near field of the aircraft, and are then propagated to the far field and until the ground. Because we are interested in the effect of the kinetic turbulence in the PBL, we are not considering sonic boom signatures in the near field of the aircraft but directly above the PBL, at around 1 km above the ground (see figure 3.1), in order to have signatures not yet affected by turbulence, but with a shape close to the final one.

Three signatures have been selected for this study. The first signature is an typical N-wave with a rise time of around 1.5 ms. This can be considered our reference signal.

Indeed, for existing aircraft (Concorde, fighters, ...) in a calm atmosphere, the typical waveform observed at the ground is the classical N-wave, which means that this is the shape that future supersonic aircraft have to compare to. However, its amplitude is around 25 Pa, far lower than the ones emitted by the Concorde, which were around 100-200 Pa. This signature is considered a "classical boom".

The next two signatures, instead, are called "low-booms". This is because their shape should make their noise less disturbing for the population, hence the name "low-boom". The first one is a boom measured from an F-18 aircraft doing a dive. This maneuver make this signal less disturbing, and thus make it a low-boom signature. Its rise time is around 9.2 ms, higher that the N-wave one. Its amplitude is also around 25 Pa, very close to the N-wave ones. These first two signatures have been used in the AIAA sonic boom prediction Workshop in 2014.

Then, the last sonic boom signature is the result of a simulation. It comes from the propagation of the low-boom configuration "NASA C25D". The near field has been provided by the NASA [127]. It was calculated as a preliminary design for a NASA low-boom demonstrator aimed at reproducing low-booms for community surveys. The C25D near-field pressure has then been propagated through a standard atmosphere with humidity by means of a non-linear ray tracing boom propagation code [96]. Its rise time is around 13.7 ms, which is comparable but higher than the F-18 one. Its initial peak pressure is around 19 Pa. However for the purpose of comparison, this signature has been rescaled to 25 Pa to have a peak overpressure comparable to the other two. The 3 input signatures have a duration of 2 s.

The final objective is to study the annoyance of sonic boom, and many parameters contribute to this annoyance, such as the amplitude, the duration or the rise time of the signal. Several metrics have thus been selected for quantifying the sonic boom disturbance. Among them, six have been preselected by ICAO (International Civil Aviation Organisation) as the most promising ones: Sound Exposure Level (SEL) with A, B, D and E weighting (noted A-SEL, B-SEL, D-SEL and E-SEL), Stevens Mark VII Perceived Level (PL) and ISBAP which is a combination of PL, A-SEL and C-SEL [153, 97].

Signatures before propagation are shown on figure 3.2. The spectrum of the N-wave peaks at 4.4 Hz, the F-18 signature at 3.8 Hz and the C25D signature at 7.6 Hz, according to their duration. The levels expressed in different metrics are given Table 3.1 (distance $x = 0$ m). Metrics are computed with the package developed during the Rumble project and provided to us by Dassault-Aviation (see deliverable 3.1. of the RUMBLE project ([143])

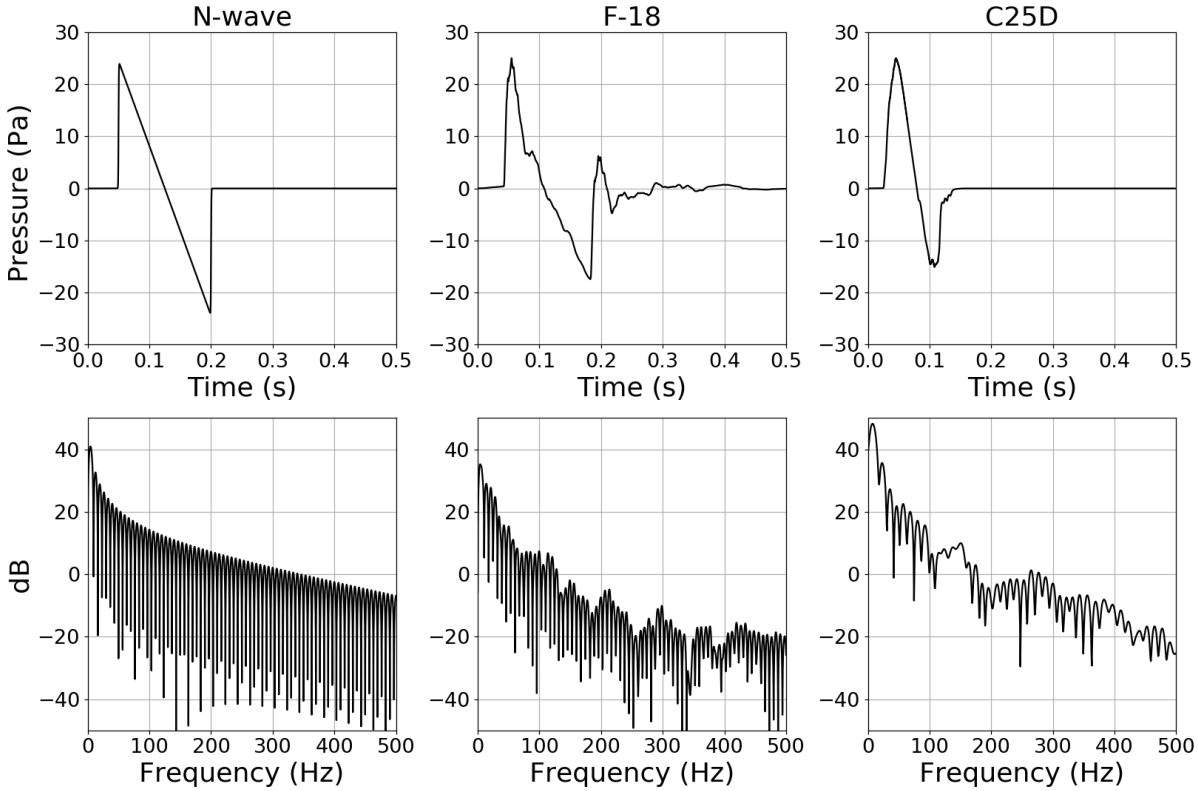

Figure 3.2: Boom signatures and their spectra: N-wave (left), signature measured from a F-18 aircraft (middle) and NASA C25D low boom simulation (right).

3.2 Generation of the turbulent wind fluctuations

The time scales of propagation (around a fraction of second over the integral scale of turbulence at around 340 m/s) is much shorter than the one of turbulence [172]. For this reason, wind fluctuations are considered frozen. Regarding the influence of the ground (the propagation in the last meters of the PBL called the surface layer), Maglieri [101] observed that signatures on the ground are close to those at 75 m, which means the distortions in the surface layer are weak. So it is a reasonable assumption to consider first a homogeneous and isotropic turbulence to describe the wind fluctuations in the PBL.

In this work, the kinetic turbulence generation methods (or spectral methods) are chosen to synthesizing the random turbulent fields. Turbulent fluctuations can be computed either for the temperature or the wind fluctuations. However, in [172], Wilson considers only the turbulent wind velocity spectrum, because its effect is usually more important than the one of temperature fluctuations. Moreover, in [14], both temperature and wind velocity are considered, and it is found that the effect of wind velocity turbulence is larger. Therefore, only the wind velocity turbulent field is considered in this study. Several spectra are available, the main ones being the Gaussian spectrum, the Kolmogorov spectrum and the von Kármán spectrum. Because this last one is considered the only one which can be applied to the full turbulence spectrum without obtaining unrealistic results [175], it is the one chosen in this study. These 3 main spectra can be observed on figure 3.3.

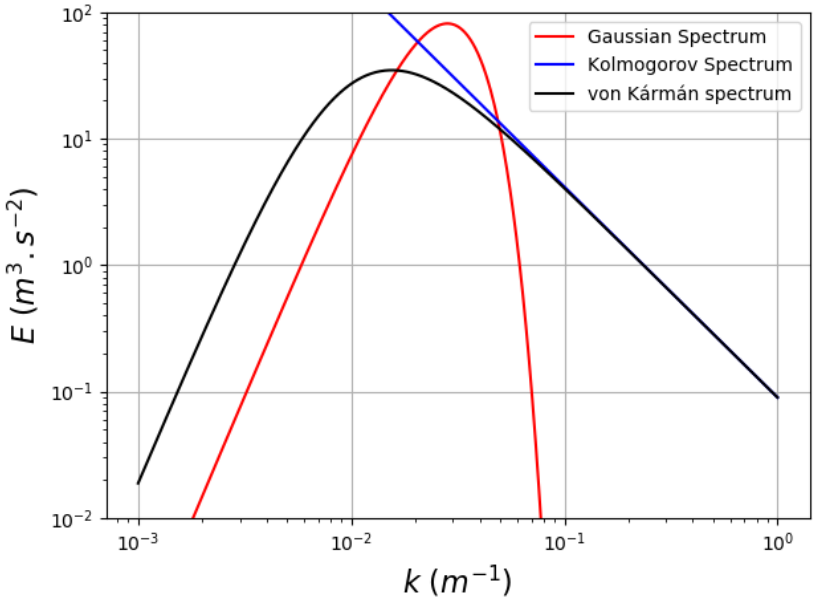

Figure 3.3: Gaussian spectrum, Kolmogorov spectrum and von Kármán spectrum.

Three dimensional turbulent wind fluctuations are computed by the random field generation method [49] as described below, and 2D ones are obtained by taking a slice of a 3D map. This method creates an isotropic and homogeneous map of wind fluctuations.

The von Kármán energy spectrum E is:

$$E(k) = \frac{4\Gamma\left(17/6\right)}{\sqrt{\pi}\Gamma\left(1/3\right)} \frac{\sigma^2 k^4 L_0^5}{\left(1+k^2L_0^2\right)^{17/6}}. \tag{3.1}$$

This spectrum depends solely on two parameters : the amplitude of the turbulence σ and the characteristic size of the turbulence L_0. Γ is the Gamma function and k is the norm of the wave-vector $\underline{k}$.

A discretized velocity field is reconstructed from the energy spectrum by:

$$u_{0j}\left(x,y,z\right) = \sum_{m_x=0}^{N_x-1}\sum_{m_y=0}^{N_y-1}\sum_{m_z=0}^{N_z-1} w_j\left(k_{m_x},k_{m_y},k_{m_z}\right)\exp\left[i\left(xk_{m_x}+yk_{m_y}+zk_{m_z}\right)\right]. \tag{3.2}$$

with $j \in \{x,y,z\}$, $k_{m_p} = m_p\Delta k_p$, with $p \in \{x,y,z\}$ the discrete wave-vector components and $\Delta k_p = \frac{2\pi}{N_p\Delta_p}$. N_p is the number of sampling points in the p direction and Δ_p is the step in the p direction. x, y and z are also discretized such as $x = l_x\Delta x$, $y = l_y\Delta y$ and $z = l_z\Delta z$, with $0 \leq l_x \leq N_x - 1$, $0 \leq l_y \leq N_y - 1$ and $0 \leq l_z \leq N_z - 1$. Vector $\underline{w}$ is defined as follows:

$$\begin{pmatrix} w_x \\ w_y \\ w_z \end{pmatrix} = \begin{pmatrix} H_{11} & 0 & 0 \\ H_{12} & H_{22} & 0 \\ H_{13} & H_{23} & H_{33} \end{pmatrix} \times \begin{pmatrix} R_1 \\ R_2 \\ R_3 \end{pmatrix}, \tag{3.3}$$

with R_1, R_2 and R_3 the components of the random vector $\underline{R}$:

$$R_j\left(m_x,m_y,m_z\right) = a_j\left(m_x,m_y,m_z\right) + ib_j\left(m_x,m_y,m_z\right). \tag{3.4}$$

Here the real $a_j\left(m_x, m_y, m_z\right)$ and imaginary $b_j\left(m_x, m_y, m_z\right)$ parts of the complex random vector $\underline{R}(m_x, m_y, m_z)$ are realizations of two uncorrelated random Gaussian variables satisfying the properties:

$$\left\langle a_j^2\left(m_x, m_y, m_z\right)\right\rangle = \left\langle b_j^2\left(m_x, m_y, m_z\right)\right\rangle = 1$$
$$\left\langle a_j\left(m_x, m_y, m_z\right) b_j\left(m_x, m_y, m_z\right)\right\rangle = 0,$$

where $< >$ is the mean of the variable inside.

The lower triangular matrix $\underline{\underline{H}}(m_x, m_y, m_z)$ is given by:

$$H_{11}(m_x, m_y, m_z) = \sqrt{\phi_{11}(k_{m_x}, k_{m_y}, k_{m_z})\Delta k_x \Delta k_y \Delta k_z} \tag{3.5}$$

$$H_{12}(m_x, m_y, m_z) = \frac{\phi_{12}(k_{m_x}, k_{m_y}, k_{m_z})\sqrt{\Delta k_x \Delta k_y \Delta k_z}}{\sqrt{\phi_{11}(k_{m_x}, k_{m_y}, k_{m_z})}} \tag{3.6}$$

$$H_{13}(m_x, m_y, m_z) = \frac{\phi_{13}(k_{m_x}, k_{m_y}, k_{m_z})\sqrt{\Delta k_x \Delta k_y \Delta k_z}}{\sqrt{\phi_{11}(k_{m_x}, k_{m_y}, k_{m_z})}} \tag{3.7}$$

$$H_{22}(m_x, m_y, m_z) = \sqrt{\phi_{22}(k_{m_x}, k_{m_y}, k_{m_z})\Delta k_x \Delta k_y \Delta k_z - H_{12}^2(m_x, m_y, m_z)} \tag{3.8}$$

$$H_{23}(m_x, m_y, m_z) = \frac{\phi_{23}(k_{m_x}, k_{m_y}, k_{m_z})\Delta k_x \Delta k_y \Delta k_z - H_{12}(m_x, m_y, m_z)H_{13}(m_x, m_y, m_z)}{\sqrt{\phi_{22}(k_{m_x}, k_{m_y}, k_{m_z})\Delta k_x \Delta k_y \Delta k_z}} \tag{3.9}$$

$$H_{33} = 0 \tag{3.10}$$

and

$$\phi_{ij}\left(\underline{k}\right) = \frac{E(k)}{4\pi k^4}\left(\delta_{ij}k^2 - k_i k_j\right). \tag{3.11}$$

Examples of velocity fields with different parameters are shown on figure 3.4. The first two (left and middle) are 2D maps for a computation with the same random vector $\underline{R}$, with two different values of L_0. The turbulent field shows the same pattern, the field structures are located in the same places, but they are more detailed when L_0 is small. The third one has been generated with a different random vector $\underline{R}$, and obviously shows a different geometrical pattern. In conclusion, according to the model we chose, the turbulent velocity field is fully determined by three parameters: the 2 physical parameters σ and L_0, and the random draw $\underline{R}$.

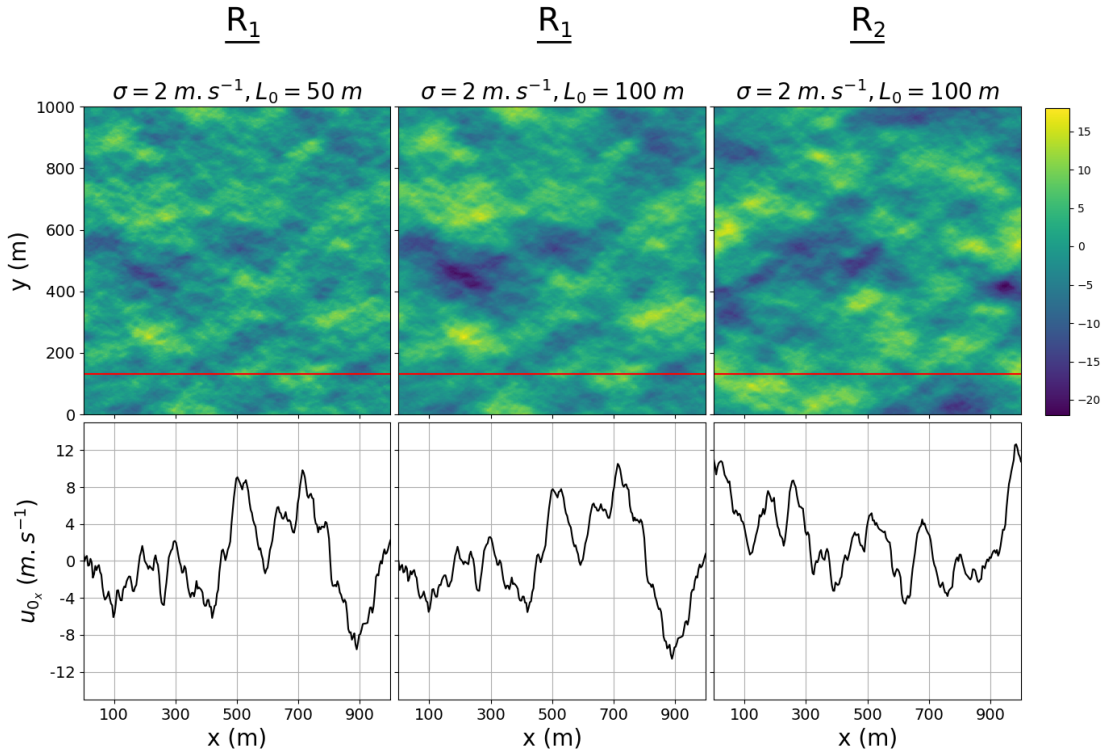

Figure 3.4: Velocity fields in m.s^{-1} (in color level) in the x-direction u_{0x} in 2D (top) and along the horizontal red line $y = 132\,\mathrm{m}$ (bottom) for $\sigma = 2\,\mathrm{m\,s^{-1}}$ and: $L_0 = 50\,\mathrm{m}$ and $\underline{R} = \underline{R}_1$ (left), $L_0 = 100\,\mathrm{m}$ and $\underline{R} = \underline{R}_1$ (middle), $L_0 = 100\,\mathrm{m}$ and $\underline{R} = \underline{R}_2$ (right).

In addition to the random field generation method, the Random Fourier Modes (RFM) method of Blanc-Benon *et al.* [75, 26, 14] is also used to generate more complex atmospheres, whose fields depend on the altitude, with both wind and temperature turbulence. This is done to compare our results with those obtained by Stout in his PhD [154].

The fields are computed by sampling the energy spectra and adding wavenumber components together with amplitudes prescribed by the spectra and with uniformly randomized direction and phase: the temperature and wind fluctuations at position $\underline{x}$ are computed via the following equations:

$$T'(\underline{x}) = \sum_{i=1}^{N} T(\underline{K}_i) \cos(\underline{K}_i.\underline{x} + \phi_i) \tag{3.12}$$

$$u(\underline{x}) = 2 \sum_{i=1}^{N} \underline{U}(\underline{K}_i) \cos(\underline{K}_i.\underline{x} + \phi_i), \quad \underline{U}.\underline{K}_i = 0 \tag{3.13}$$

where $\underline{K}_i$ and ϕ_i are the wavenumber vector and random phase associated with the ith mode, and $T(\underline{K}_i)$ and $|\underline{U}(\underline{K}_i)|$ are the mode amplitudes. The requirement for the modal velocity vector to be orthogonal to the wavenumber ensures incompressibility of the field. The amplitudes are calculated as:

$$T(\underline{K}_i) = \sqrt{G(K_i, h)\Delta K_i}, \quad K_i = |\underline{K}_i| \tag{3.14}$$

$$|\underline{U}(\underline{K}_i)| = \sqrt{E(K_i, h)\Delta K_i} \tag{3.15}$$

where ΔK_i represents the spacing between modal wavenumbers, h the altitude, E is the energy spectrum for the velocity fluctuations (see equation 3.1) and G is the energy spectrum of the temperature fluctuations:

$$G(K, h) = \frac{8\Gamma(\frac{11}{6})}{\sqrt{\pi}\Gamma(\frac{1}{3})} \frac{\sigma_T^2 K^2 L_T^3}{(1 + K^2 L_T^2)^{\frac{11}{6}}} \tag{3.16}$$

Then, for the scalar turbulence σ_T and L_T are calculated with the following equations [124]:

$$\frac{\sigma_T^2(h)}{T_*^2} = \frac{4}{[1 + 10(-h/L_{MO})]^{2/3}} \tag{3.17}$$

$$\frac{L_T(h)}{h} = 2\frac{1 + 7(-h/L_{MO})}{1 + 10(-h/L_{MO})} \tag{3.18}$$

where h is the altitude, T_* the surface-layer temperature scale and L_{MO} the Monin-Obukhov length scale defined as:

$$L_{MO} = -\frac{z_i u_*^3}{\kappa w_*^3} \tag{3.19}$$

where z_i is the boundary layer height, $\kappa = 0.4$ the von Kármán constant, u_* is the friction velocity and w_* the mixed-layer velocity scale.

For the vectorial turbulence, wind shear and buoyancy are both taken into account:

$$\sigma_s^2 = 3u_*^2, \quad L_s(h) = 1.8h, \tag{3.20}$$

$$\sigma_b^2 = 0.35w_*^2, \quad L_b(h) = 0.23z_i \tag{3.21}$$

Where s corresponds to shear production and b to wind production. The equation 3.20 is valid close to the surface and 3.21 is valid until around $0.9z_i$. The combined variance is thus given by this equation [68]:

$$\sigma_{vector}^2 = 3u_*^2 + 0.35w_*^2 \tag{3.22}$$

The values of z_i, T_*, u_* and w_* are chosen to be the same as those used by Stout in [154].

At the end of this chapter, the propagation is computed for the 2 models of atmosphere, to see if the choice of an simpler atmosphere and the absence of temperature turbulence significantly affect the signal.

3.3 FLHOWARD3D parameters for sonic boom propagation

The propagation is computed using the code FLHOWARD3D. For the absorbing boundary conditions, The absorption coefficient is

$$\zeta(h) = \frac{\alpha c_0}{a^3} h^2, \tag{3.23}$$

with $h = 100\,\text{m}$ and $\alpha = 20$.

For the heterogeneities, the stratified temperature and wind profiles are considered to be constant, and only turbulent wind fluctuations are taken into account. The propagation is considered in a 2D and a 3D medium. The initial signature is a plane wave with an angle of 10° with the vertical, and the initialization is done with both the incident and reflected waves, as shown on the left of figure 3.5 for a N-wave. Between 800 and 900 m, a Tukey filter is applied to the initial signature, in order to have a smooth transition until the absorbing layer. The right of figure 3.5 shows the signature after propagation, disturbed by the kinetic turbulence.

In 3D, the propagation takes place in a medium of $1\,\text{km} \times 1\,\text{km} \times 600\,\text{m}$ side. In addition to the variables and conditions described previously, $z \in [-300, 300]$ m correspond to the lateral direction, and absorbing boundary conditions with the same coefficient for $|z| > 200\,\text{m}$ are applied.

To compare results with those of Stout [154], a 3D vertical propagation is also performed. In this case, x is the vertical direction, with $x = 0\,\text{m}$ corresponding to an altitude of 1 km, and the last position $x = 1000\,\text{m}$ corresponding to the ground (see figure 3.6). y and z are the lateral directions and vary between -300 and 300 m. Absorbing boundary conditions are present for $y > 900\,\text{m}$ and $|z| > 200\,\text{m}$.

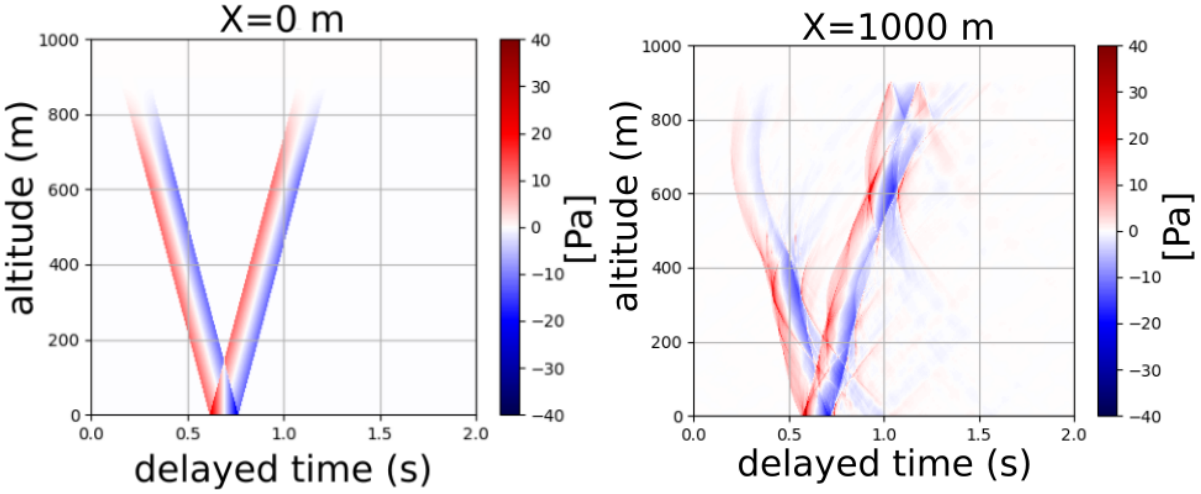

Figure 3.5: Pressure field (in function of the altitude and the delayed time) of a planar N-wave before (left) and after (right) a propagation of 1 km with the FLHOWARD3D code, in a medium with 2D turbulent wind fluctuations.

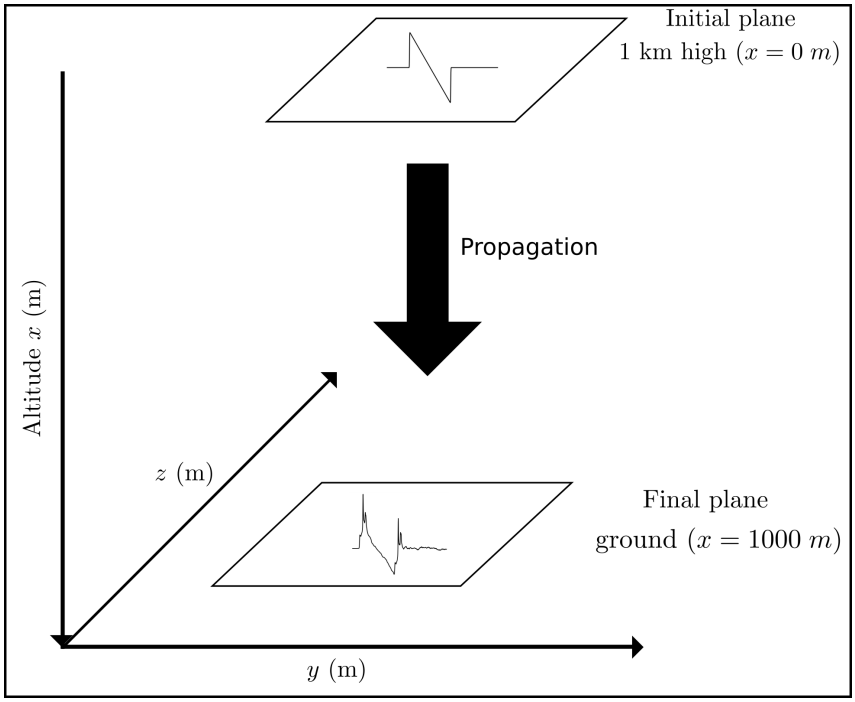

Figure 3.6: Illustration of the vertical propagation (for the comparison with the results of Stout).

3.4 Convergence studies

The convergence of the numerical model is assessed regarding the temporal and spatial sampling, in order to optimize the computation cost for a sufficient accuracy. Indeed, a very fine sampling will make the computation cost too high, while an insufficient sampling will cause the results to be false.

3.4.1 Temporal sampling

The temporal sampling must provide a fine discretization of the signatures and, in particular, a sufficient resolution of the shocks. The convergence of various metrics is used as a quantitative criterion. Figure 3.7 displays the values of the peak overpressure (denoted p_{max}) and of the sound exposure level with A-weighting ($A - SEL$) in function of the sampling frequency of the N-wave, chosen as the waveform with sharpest shocks and therefore the most demanding one in terms of convergence. One can see that a sampling frequency f_s of at least 1600 Hz is required to have variations less than 0.1 Pa for p_{max} and less than 1 dBA for A-SEL metric. A similar or a lower sampling frequency would be obtained using PL or other metrics. Note this result does not depend on the numerical solver itself.

To assess the sampling effect of the numerical solver, an N-wave is propagated in a square of 1 km side, within a quiescent two-dimensional homogeneous medium. The spatial sampling is high enough to discard any influence. Results are shown on the right of Figure 3.7 for p_{max} and $A - SEL$, which are the slowest metrics to converge. While a sampling frequency $f_s = 512$ Hz is clearly insufficient, differences between the

reference case (here f_s =4096 Hz) are below 2 dBA for f_s = 1024 Hz and below 0.5 dBA for f_s = 2048 Hz. This last value will therefore be chosen in what follows.

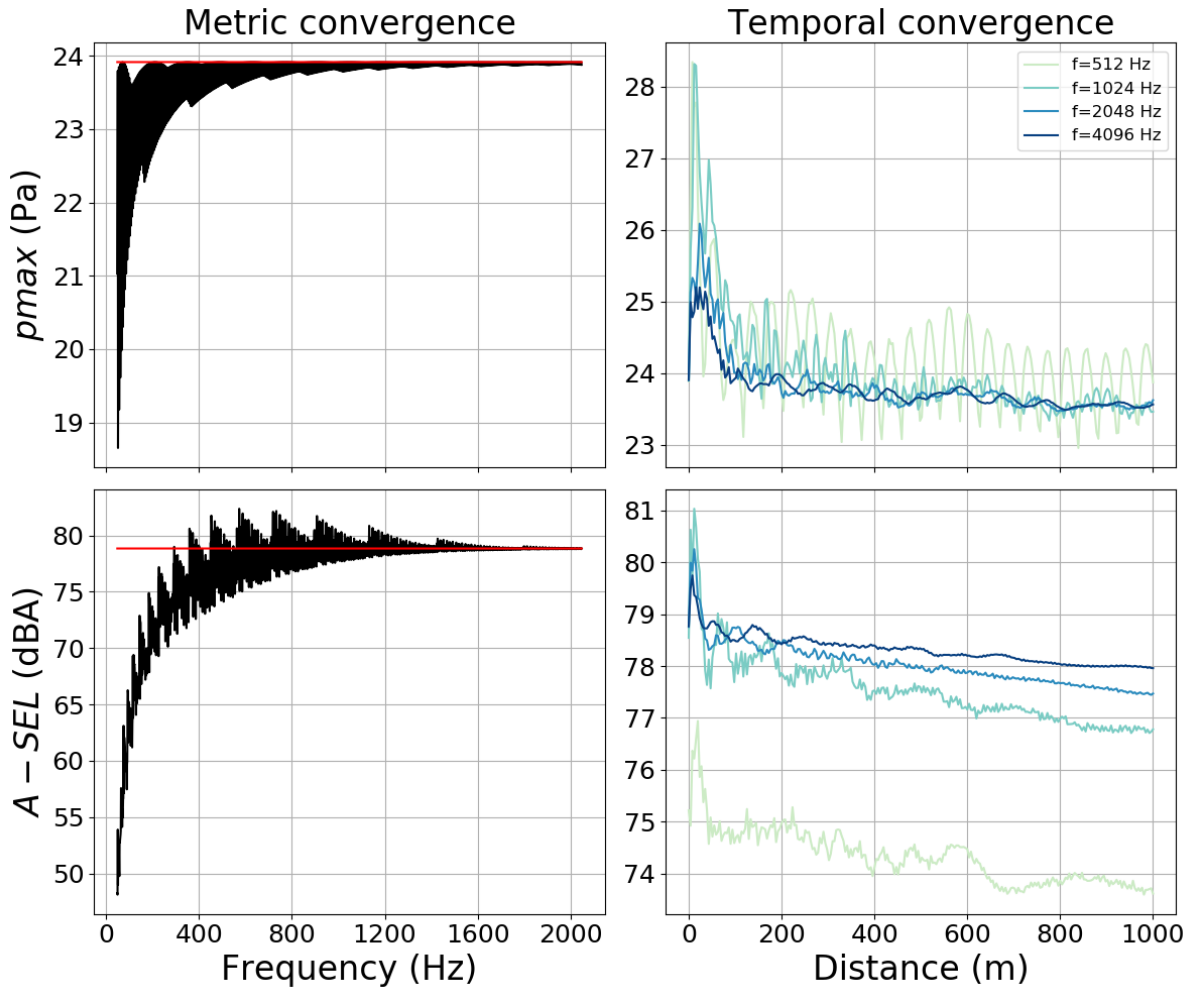

Figure 3.7: Temporal convergence of metrics p_{max} (top line) and $A - SEL$ (bottom line) with sampling frequency for the N-wave before propagation (left), and after 2D propagation inside a square of 1 km side, with an angle of 10° with the ground, with a homogeneous, quiescent medium for four values of f_s, from 512 to 4096 Hz. Horizontal line on left side is theoretical value.

3.4.2 Spatial sampling

The assessment of the spatial sampling is achieved in two steps. The first one consists in determining the values of spatial steps Δx and Δy best suited for the propagation of an N-wave in a two-dimensional quiescent and homogeneous medium (without turbulence), with an angle of 10° with the ground. The second step consists in examining the spatial sampling of the turbulent field.

For the first step, one-way methods are known to be efficient concerning the advancement in the x-direction and the convergence is already reached for $N_x = 128$ (again for a 1 km propagation). In the vertical direction, convergence results of the ground pressure

for the same two metrics are shown on the left of figure 3.9. The two lower values $N_y = 512$ and $N_y = 1024$ induce too large oscillations and deviations, while the two higher ones $N_y = 1510$ and $N_y = 2048$ show a much smoother evolution and differences always less than 1 dBA. Therefore the value $N_y = 1510$ is chosen in what follows, and for 3D simulations, the value $N_z = 1510$ is also selected.

3.4.3 Turbulence size

It is also necessary to determine the required minimal size of the turbulence discretization. Indeed, depending on the smallest wavelength of the propagating signatures (here 16 cm), there should be a size of the turbulent field below which its smaller structures will hardly affect the propagation. This will determine the minimal sampling of the turbulence. To determine this second spatial sampling, the von Kármán spectrum (with physical parameters $\sigma = 3\,\mathrm{m/s}$ and $L_0 = 100\,\mathrm{m}$) is filtered with a low-pass Tukey filter (see figure 3.8). Its cut-off wave-number is denoted k_c so that only scales above $\lambda_c = \frac{2\pi}{k_c}$ are present in the turbulence. The propagation with different values of k_c is then compared with the propagation in the unfiltered medium. Simulations are performed again at 2D in a square of 1 km side. Comparisons of p_{max} and $A-SEL$ at the ground level for an N-wave propagating with two values of k_c are shown on the right side of figure 3.9. The smallest wave number $k_c = 0.5\,\mathrm{m}^{-1}$ shows deviations of the peak pressure higher than 1 Pa, and of the sound level higher than 1 dBA. On the contrary for $k_c = 1\,\mathrm{m\,s}^{-1}$, these variations are lower than respectively 0.5 Pa and 0.5 dBA, which is consistent with our other convergence criteria. This last value is therefore chosen, corresponding to a wavelength of 6 m. Note this result is consistent with laboratory-scale experiments, showing that heterogeneities below about $c_0T/5$ with T the typical signature duration (here about 100 ms), only weakly affect the signature [55]. For a size of 1 km, this means there should be at least 167 points in all directions. This is satisfied with $N_y = 1510$, but the horizontal discretization has to be increased, and a value $N_x = 256$ is finally chosen.

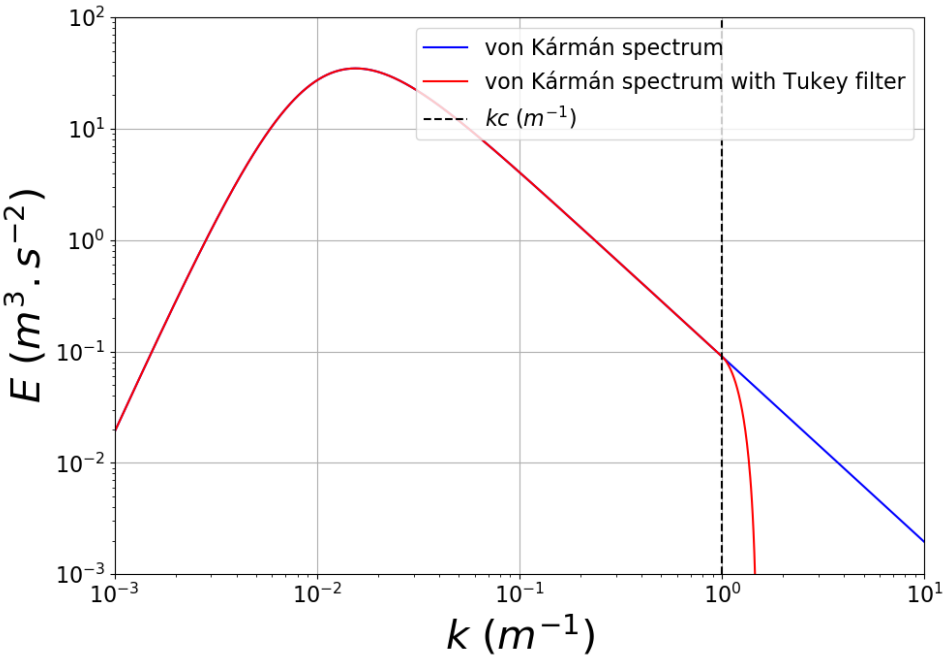

Figure 3.8: Von Kármán with and without a low-pass Tukey filter.

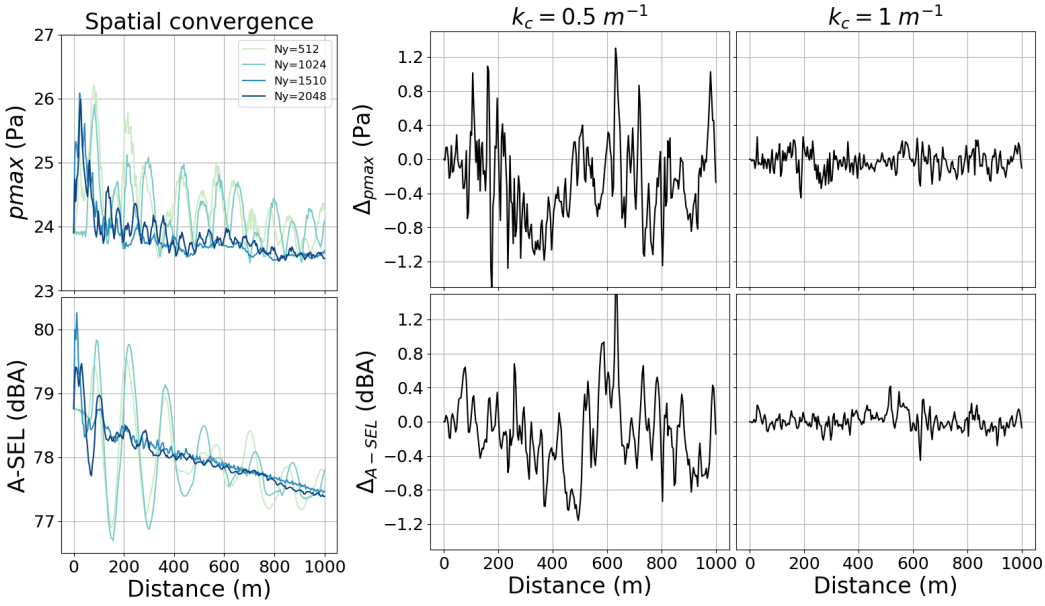

Figure 3.9: Spatial convergence of metrics p_{max} (top line) and A-SEL (bottom line) at the ground level for the N-wave after 2D propagation inside a square of 1 km side. Left : convergence with spatial vertical discretization (4 values, color lines online) in case of a homogeneous and quiescent atmosphere. Middle and right : differences between propagation in a filtered and an unfiltered turbulence spectrum for $k_c = 0.5\,\mathrm{m\,s^{-1}}$ (middle) and for $k_c = 1\,\mathrm{m\,s^{-1}}$ (right).

3.5 Deterministic propagation in a turbulent wind field

3.5.1 Three-dimensional propagation with ground through homogeneous kinetic turbulence

The three selected sonic boom signatures are propagated in a three-dimensional medium of 1 km × 1 km × 600 m with the turbulence characterized by its intensity $\sigma = 2\,\mathrm{m/s}$ and its scale $L_0 = 100\,\mathrm{m}$. The direction of propagation x is parallel to the ground. The initial wavefront makes a 10° angle with the vertical y-axis. Geometrical configuration and pressure field are illustrated on figure 3.10 for one particular realization (one particular $\underline{R} = \underline{R}_1$). The figure represents the time pressure waveform after 1 km in the horizontal direction of the initial N-wave at the ground, distorted by kinetic turbulence and oscillating in the transverse horizontal z direction , and the incident and reflected wavefronts in the central plane $z = 0\,\mathrm{m}$.

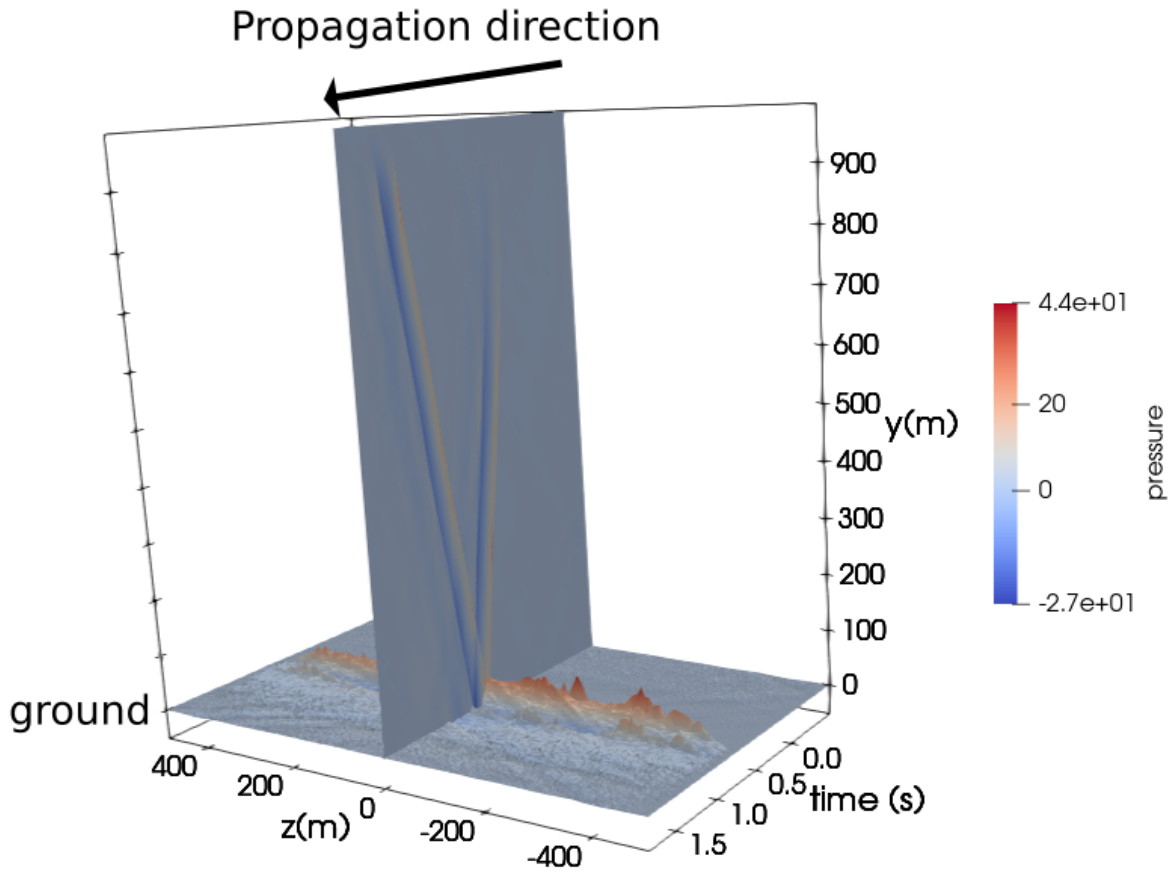

Figure 3.10: Illustration of 3D numerical simulation of a sonic boom (initial wavefront of an N-wave with a 10° angle with vertical plane) in a synthetic turbulent atmosphere (here with a von Kármán energy spectrum with $\sigma = 2\,\mathrm{m/s}$ and $L_0 = 100\,\mathrm{m}$ and one particular realization $\underline{R}_1$). Pressure (in Pa, color online) at the ground after 1 km of propagation as function of z (lateral direction) and t (retarded time). Incident and reflected wavefronts in the central plane $z = 0\,\mathrm{m}$.

In addition, figure 3.11 shows signatures on the ground at different lateral positions. The left one corresponds to the propagation of the N-wave, as shown on figure 3.10, while the other 2 correspond to propagations in the same atmosphere of the F-18 boom and the C25D configuration. These figures show that there are variations in the waveform, depending on the positions. For example, the N-wave at 124 m is close to a U-wave, when it has a more classical form at 43 m. These variation are caused by turbulence. Furthermore, there is more variations in the N-wave waveforms than for the F-18 and C25D booms.

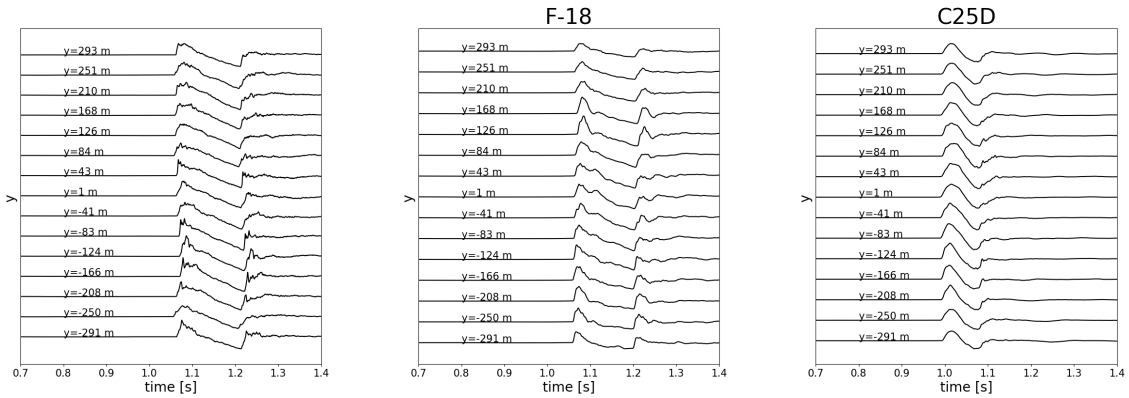

Figure 3.11: Signatures on the ground at different lateral positions, after 1 km of 3D propagation in a synthetic turbulent atmosphere, for the N-wave (left), F-18 boom (middle) and C25D configuration (right).

3.5.2 Two-dimensional propagation with ground through homogeneous kinetic turbulence

Propagation in a two-dimensional medium is also computed, and ground signatures at four different distances ($x = 0$ m, $x = 196$ m, $x = 392$ m and $x = 1000$ m) are extracted and plotted in figure 3.12, for the three different input signatures but the same choice of $\underline{R}$. As expected, kinetic turbulence has a strong effect on the signatures. At 196 m, changes are moderate and affect mostly the N-wave with tiny spikes altering the two shocks. At 392 m , the shock amplitudes are reduced and post-shock oscillations appear. At 1000 m, a large amplification of the N-wave waveform is visible, peak overpressure has doubled, with an N+U shape characteristic for the vicinity of a random caustic [75], and the peak of the U-wave having split in two. This transformation also affects the two other waveforms, but it is less pronounced because of a lesser content of their spectrum in the high frequencies more sensitive to turbulence. The U-shape of the N-wave at 1000 m can be observed in flight tests (for example in [103]) and this range of overpressure amplification is reported in several flight data: for instance, variations from 0.6 to 2.6 psf in [168], from 0.8 to 2 psf in [103], from 1.36 to 2.57 psf in [67]. Many numerical simulations also reproduce this kind of waveforms [14, 6, 4, 155, 100, 18].

Corresponding values of p_{max}, of SEL values (with various weightings) and of rise time on the ground for the same cases (same turbulent realization, same propagation distances) are shown in Table 3.1. For all metrics, the N-wave turns out more sensitive to turbulence

than the C25D reduced boom. This will be quantified more systematically in the next chapter.

	Distance	p_{max} (Pa)	A-SEL (dBA)	B-SEL (dBB)	D-SEL (dBD)	Rise time (ms)
N-wave	0 m	23.9	77.6	88.3	88.0	1.5
	196 m	31.8	81.9	91.1	90.7	1.5
	392 m	21.8	77.3	87.3	87.0	0.98
	1000 m	43.3	82.8	92.0	91.5	14.7
F-18	0 m	24.7	68.1	82.8	83.7	9.2
	196 m	25.7	71.0	84.4	84.8	9.3
	392 m	22.4	67.2	81.1	82.2	10.7
	1000 m	28.3	72.0	84.8	85.3	15.1
C25D	0 m	24.7	63.2	78.1	81.1	13.7
	196 m	25.3	66.2	79.7	81.9	14.2
	392 m	23.4	62.3	76.5	80.3	15.1
	1000 m	28.5	66.5	80.0	83.0	21.0

Table 3.1: Values of the peak pressure, sound level in dBX for X-weighted Sound Exposure Level (X=A, B, D), and rise time for the waveforms of Fig.3.12.

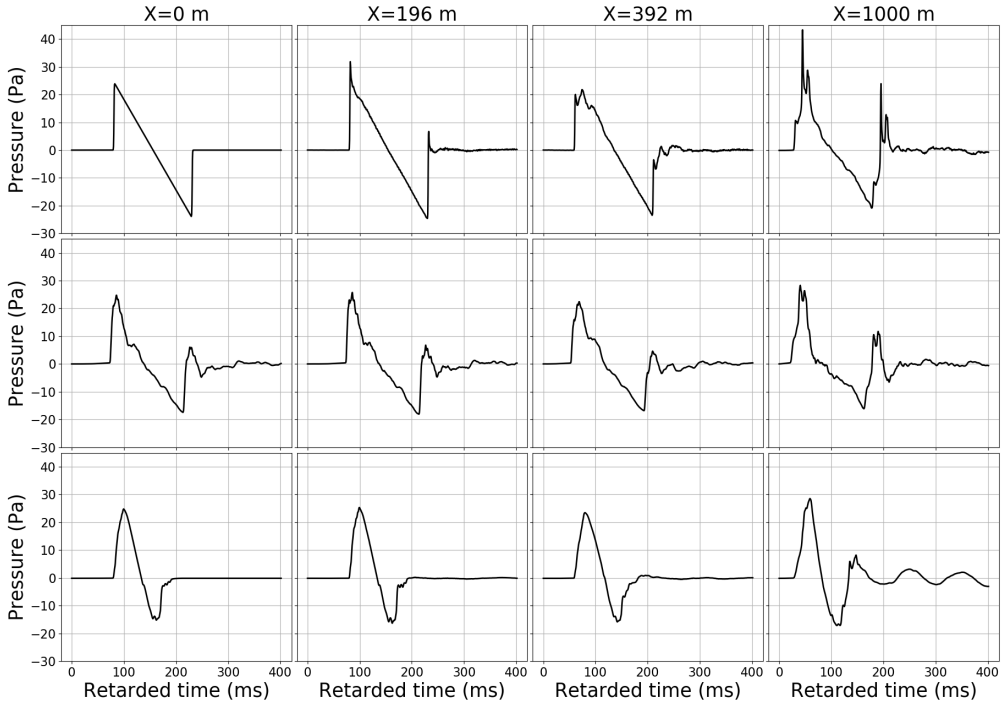

Figure 3.12: Ground signatures simulated in the conditions of Fig.3.10. Initial (left column) theoretical N-wave (up), measured boom from an F-18 operating a dive maneuver (middle), and simulated boom from the C25D configuration (bottom), and after propagation over 192 m, 396 m and 1000 m (from left to right).

3.5.3 Three-dimensional propagation without ground trough inhomogeneous and homogeneous turbulence

In his thesis, Stout [154] (figures 6-6 and 6-7 page 189-190) observes numerically possible strong amplifications in 3D of the initial signature up to a factor 8 compared to 2D simulations for which the maximum amplification factor is about 4. Even though such high levels are very unlikely (probability less than 0.0001), they are said to exist. Our observations are a bit different, since we find a maximal amplification under 4 P_0 for 2D and 3D. Nevertheless, several differences exist with this study. Indeed, results have been obtained for numerical simulations based on a Khokhlov-Zobolotskaya-Kuznetzov model (KZK model [84], see chapter 2) and an inhomogeneous synthetic turbulence also using a von Kármán energy spectrum (see section 3.2). The KZK model is based on a parabolic approximation which implies an angular restriction on the direction of propagation of the wave ($\pm 15°$). This is a difference with the solver used in this study. Indeed, FLHOWARD3D has no angular restriction and is valid for waves with angles up to 90°. The inhomogeneous model of turbulence uses the same von Kármán spectrum than the homogeneous model, but parameters can now depend on the altitude. Temperature fluctuations are also computed, and also depend on the altitude. This atmospheric model should be more realistic than the homogeneous one. Furthermore, he considers vertical propagation, while our simulations use horizontal propagation.

Vertical propagations (see figure 3.6) are computed with the FLHOWARD3D code with and without the KZK approximation in the 2 models of atmosphere described in section 3.2. To do that, the FLHOWARD3D model has been adapted to the KZK model for this test, by modifying the part of the code solving the diffraction effects to solve the KZK equation (see chapter 2). The ground peak pressure on the ground after propagation is shown on the left and the middle of figure 3.13. The figure on the right represents the differences between the FLHOWARD3D model and the KZK one. They are seen to be be negligible: even when the differences between the models are the highest, they only amount to about 0.5 Pa.

The difference between the 2 atmospheres comes not only from the models, but also from the random seeds. This means that the positions of the focusing are different. However, their range of values seems to be similar. On figure 3.14 is plotted the probability distributions of the ground pressures for the 2 atmospheric models, for the propagation with the FLHOWARD3D model (the configurations of the middle of figure 3.13), with data from 4 simulations for the homogeneous model, and 6 simulations for the inhomogeneous model. The 2 distributions are relatively similar with about 74 % of similitude in their pdf. The shapes of the distributions are both slightly skewed toward the lower values. The means are nearly the same, with 25.0 Pa for the homogeneous case and 24.7 Pa for the inhomogeneous one. The variation range is also the same, with values between 7 and 70 Pa in both cases. The main difference comes from the standard deviation: it is equal to 7.6 Pa for the homogeneous case, and 6.1 Pa for the inhomogeneous one. This means that pressures are more likely to be distant from the mean in the homogeneous case: pressure variations could be overestimated.

In both cases amplifications by a factor 8 are not observed: The amplifications shown in [154] are not reproduced. However, we had a different propagation code (even if we use it to solve KZK equation), a different sampling of the signature, and probably a N-

wave with a slightly different rise-time (and this parameter is critical). These differences could explain our results. Furthermore, our results are in agreement with the literature [18, 156].

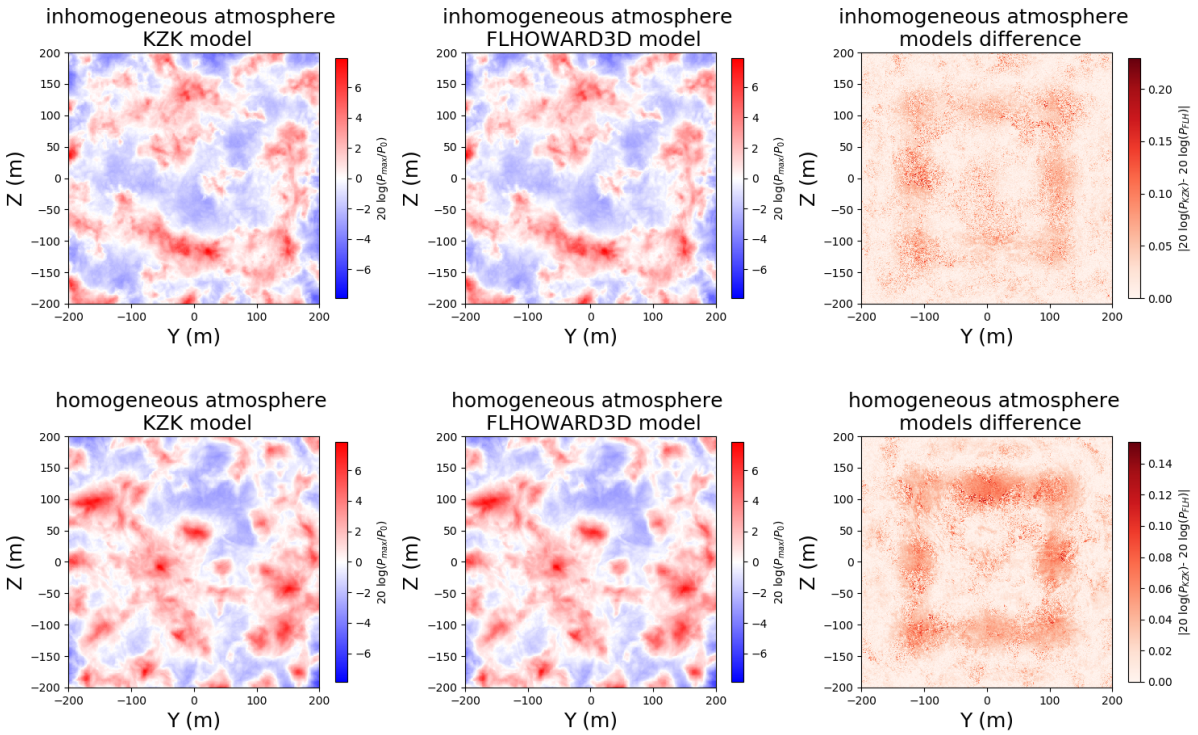

Figure 3.13: Peak pressure on the ground (supposed to be reached at the last distance) for the vertical propagation of a N-wave with different models and atmospheres (left and middle) and absolute value of the difference between the propagation with the KZK model and the FLWOWARD3D model (right). P_0 correspond to the peak pressure on the ground for a propagation in a homogeneous atmosphere.

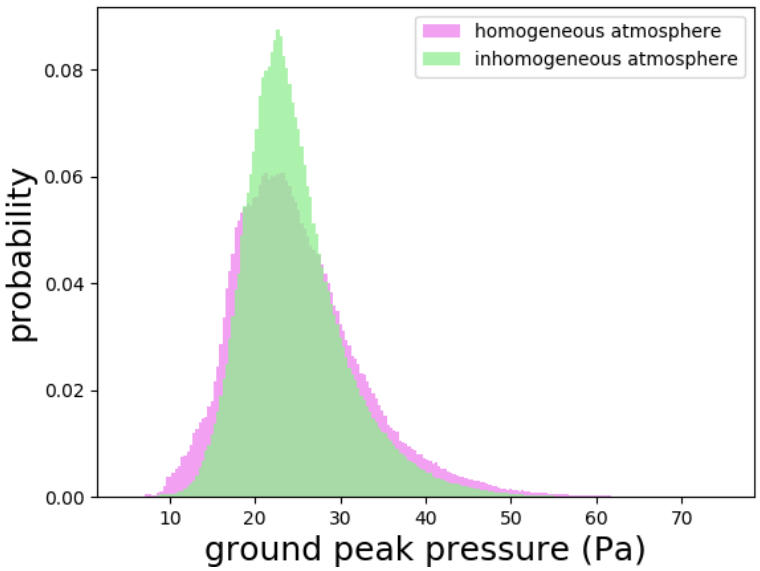

Figure 3.14: Distribution of the peak pressure on the ground (supposed to be reached at the last distance) for the 3D vertical propagation of a N-wave with homogeneous (4 simulations) and inhomogeneous (6 simulations) models of atmosphere, with the FL-HOWARD3D code.

3.5.4 Comparison of the two- and three-dimensional propagations with experimental measurements

Multiple three- and two-dimensional simulations of the propagation of an N-wave and a C25D boom are now compared in order to quantify the effect of the dimensionality of the wind fluctuations and to assess if sonic boom signatures are more realistic in 3D compared to 2D for this particular configuration.

For the 2D simulations, 1800 turbulent atmospheres have been synthesized, with 36 different couples (σ, L_0) (with $\sigma \in [1,3]$ m/s and $L_0 \in$ [50,150] m), and 50 different random vectors $\underline{R}$. The choice of the 36 couples (σ, L_0) is detailed in the next chapter. Note that the selected range for σ is comparable to the one observed during SonicBAT flight campaign [18] ([0.5,2] m/s). For the 3D simulations, only 36 atmospheres are considered, for a single random vector $\underline{R}$ but for the same 36 couples of (σ, L_0) as 2D simulations. Then, for each realization of the atmosphere, the ground pressure signatures during the propagation (for each of the 256 points between 0 and 1000 m) are extracted, and the metrics are calculated. A large amount of data are thus obtained (460800 signatures in 2D, 5160960 in 3D). Figure 3.16 presents the normalized cumulative probability $\mathcal{P}$ of the simulated signature $p(t)$, for metrics, either $m(p) = p_{max}$ or $m(p) =$ PL, normalized by its value for the input boom $m(p_{input})$ to equal or exceed a given level L: $\mathcal{P}(m(p)/m(p_{input}) > L)$ for p_{max}, $\mathcal{P}(m(p) - m(p_{input}) > L)$ for PL.

For the N-wave, the curves can be compared with experimental data from the SonicBAT flight campaign, the most extensive and recent flight campaign dedicated to sonic boom propagation through turbulence [18]. This campaign measured the distortion by atmospheric turbulence of the standard N-shaped boom produced by an F-18 USAF jet,

first at NASA's Armstrong Flight Research Centrer AFRC (Edwards Air Force base, California) in July 2016, then at NASA's Kennedy Space Center (Florida) in August 2017. The two sites were chosen because of different humidities, with expected rise times smaller in humid air (KSC) than in dry one (AFRC). Multiple booms were measured (around 2000 in each site) at different distances from the flight path. When aggregating all data and normalizing the peak amplitude by the median one for a given distance from flight path [18](see figure 3.15), cumulative probabilities turn out insensitive to measurement distance from flight track. A dry atmosphere induces a higher variability, but the effect is not dramatic: in both cases, about 99 % of booms keep a peak overpressure below twice the median value, and the probability to have a peak overpressure less than half the median value is between 0.1 % (AFRC) and 1 % (KSC). This last difference may be due to erratic clouds appearing in KSC, that are known to further reduce boom amplitude [8]. Only very rare events (probability around 0.1 %) reach three times the median value. Such typical values are clearly reproduced by our simulations for the N-wave, either at 2D or 3D. For cumulative probabilities between 1 % and 99 %, the 2D and 3D curves can hardly been told from one another. Differences appear only for the rarest events, either at very low or very high amplitudes. Two-dimensional simulations tends to underestimate the probability of very low amplitude booms, maybe because it cannot handle scattering of energy amplitude in the lateral direction. Note also our simulated behavior of these rare, low amplitude events, is closer to what was observed in AFRC than in KSC, maybe again because the present simulations do not include random occurrence of clouds. High amplitude events are also underpredicted at 2D. One possible reason is that random 2D caustics that are associated to pressure amplification, do not show the the richness of 3D ones, as shown by catastrophe theory [11]. However, for 98 % of boom events, 2D and 3D simulations are statistically coherent, and also reproduce the SonicBAT experimental data. In terms of loudness, the same conclusions can be drawn. Only booms with a rare (less than 1 % probability) increase of PL level more than 5 PLdB are underestimated by 2D simulations. Booms with a PL level increasing more than 8 dB have a probability less than 0.1 % at 3D. Again, these results are similar to those observed for SonicBAT and for recent numerical simulations (see figure 10 of Ref.[156]).

For the C25D boom, the cumulative probability shows a behavior quite similar to the N-wave for boom levels lower than the reference value, at either 2D or 3D. Differences however appear for cases of pressure amplification, with factors larger than 1.5 having a probability less than 1 % and factors above 2 extremely rare (at 3D). This is explained by the smoother shocks of the input boom waveform, that contain much less high frequencies, those which are indeed most amplified near caustics. In terms of boom metrics, this difference with N-wave is also observed, but to a lesser extent, only for boom amplifications larger than +10 PLdB which are anyway very rare events. The comparison between 2D and 3D again shows that the 98 % most frequent events can be reasonably predicted at 2D. The main difference is observed for cases of "large" peak pressure amplification, which are found to be rarer at 3D than at 2D. Very spiky U waves are extremely unlikely in case of low booms. Nevertheless, in terms of PL, the trend is very similar to N-waves, with 2D simulations underestimating amplifications more than +5 PLdB.

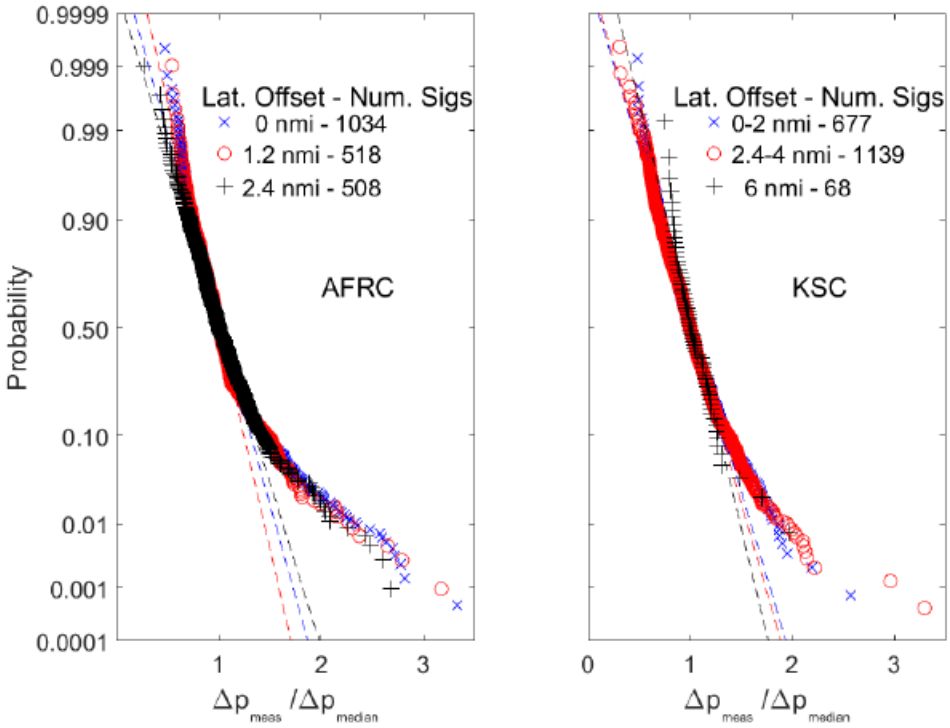

Figure 3.15: Cumulative probability of the ratio of measured to median overpressure, with the measures done at various lateral locations during the SonicBAT flight test programs at the Armstrong Flight Research Center (AFRC) (left), and at the Kennedy Space Center (KSC) (right) (extracted from [18], pp. 106, fig 81b).

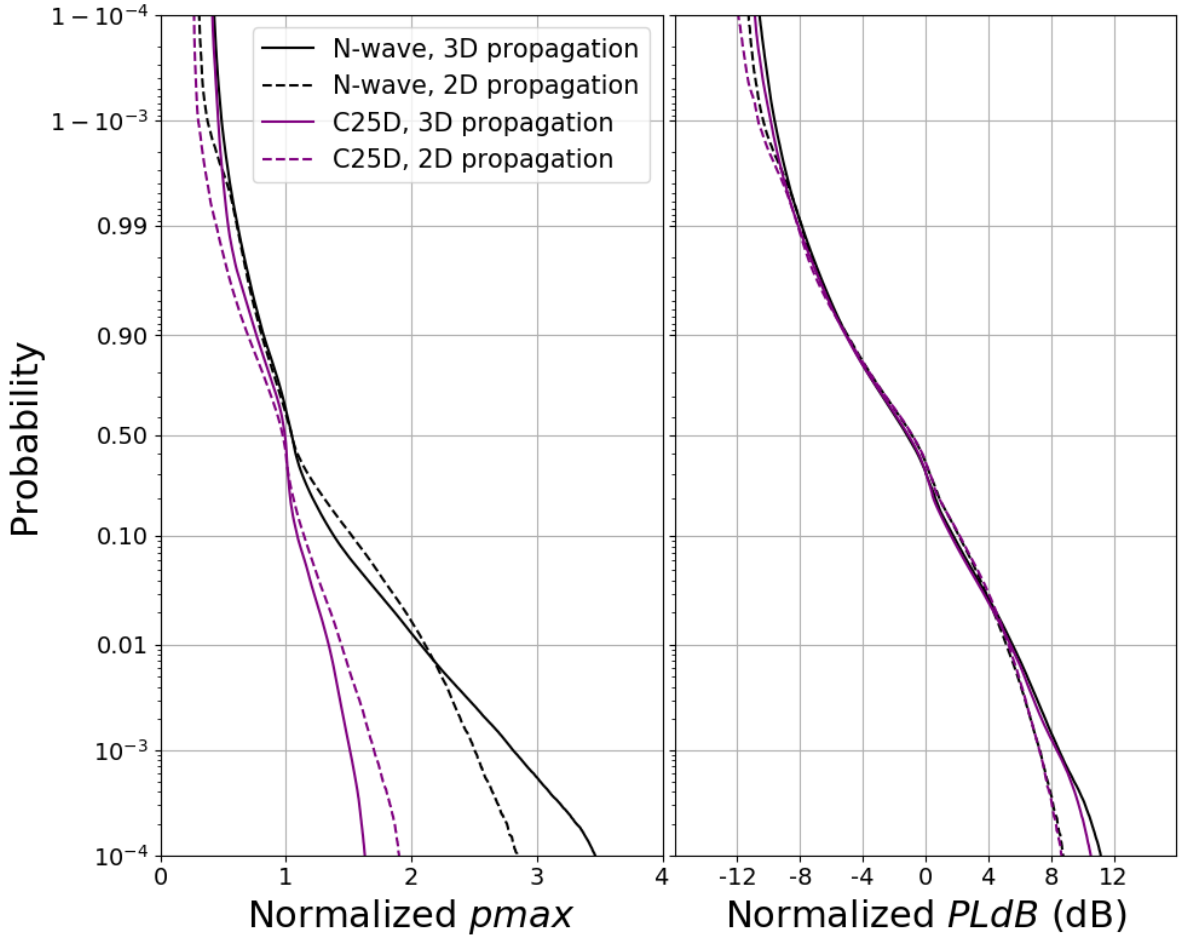

Figure 3.16: Cumulative probability for the normalized peak pressure (left) and the normalized $PLdB$ (right), for the 2D and 3D propagations of the N-wave and the C25D boom.

3.6 Conclusions

In conclusion, 2D and 3D simulations of classical and low sonic booms propagation in an atmosphere with wind velocity fluctuation have been performed. A convergence study was beforehand realized to have an optimal sampling, and to determine the minimal size of turbulent fluctuations. 2D simulations provide satisfactory results compared to 3D ones, with mostly rare most amplified events (one in a hundred) underestimated. Given the huge differences in computational cost (about 8 hr for 32 processors at 3D, versus 40 min for 1 processor at 2D), only 2D simulations will be performed in the next chapter. Homogeneous and inhomogenous turbulence also give similar results, with the main difference being that a homogeneous medium induces a higher variance and thus less predictable results. Homogeneous turbulence is chosen in the next part, which means that the variations could be slightly smaller than what will be observed.

Chapter 4

Sonic boom propagation: stochastic study

In the previous chapter, the possibility to compute the propagation of different sonic boom signatures through a medium with turbulent wind fluctuations using a high-fidelity solver which accounts for diffraction, nonlinear effects, absorption, relaxation and heterogeneous effects has been demonstrated. Nevertheless, the results strongly depend on the medium itself and lead to the question: How to quantify the effect of the turbulence on the sonic boom propagation ? In this chapter, this issue is investigated by coupling an uncertainty quantification method of the physical parameters governing the turbulence with a statistical approach for the intrinsic randomness of turbulence. The study has been conducted with two-dimensional simulations.

4.1 Uncertainty quantification using polynomial chaos method

The model of wind fluctuations uncertainties depends on three parameters: the magnitude of the turbulence σ, the characteristic length scale L_0 and the random vector $\underline{R}$, with σ and L_0 containing physical parameters of the turbulence and $\underline{R}$ being related to the randomness. The value range of the physical parameters is determined by a literature review (table 4.1), and $\sigma \in [1, 3]$ m s^{-1} and $L_0 \in [50, 150]$ m are chosen.

σ	L_0	Condition	Reference
$0.6\,\mathrm{m\,s^{-1}}$	30 m	Kolmogorov spectrum	[135]
$1.87\,\mathrm{m\,s^{-1}}$	160 m		[182]
$3\,\mathrm{m\,s^{-1}}$	4λ = 150-200 m		[3]
0-$2.5\,\mathrm{m\,s^{-1}}$	100-200 m	experimental values	[94]
$0.48\,\mathrm{m\,s^{-1}}$	$1.5z$	near the ground	[172]
$2\,\mathrm{m\,s^{-1}}$	0.1 m => 50-100 m after re-scaling	laboratory scale	[75]
0.5 and $2\,\mathrm{m\,s^{-1}}$	100 m		[99]
0.3-$3.3\,\mathrm{m\,s^{-1}}$	5λ =200-250 m		[169]
$0.07\,\mathrm{m\,s^{-1}}$	1 m	near the ground	[123]
0.6-$1.6\,\mathrm{m\,s^{-1}}$	100-200 m		[176]

Table 4.1: Values of σ and L_0 in different articles.

To quantify how the propagation of sonic booms is affected when these parameters are modified, a study of uncertainty quantification is conducted, and a statistical method is needed.

A well known statistical method is the Monte Carlo method [48]. It relies on repeated random sampling to obtain numerical results. It consists in defining the model of the possibles inputs, generating the inputs randomly from a probability distribution over the domain, performing a deterministic computation on the inputs and finally aggregating the outputs. This method is used in a wide range of applications. Despite the convergence of this method being independent of the number of random variables, it is is very slow ($O\left(1/\sqrt{N_{simulations}}\right)$), which means that around one million computations of the direct solver are needed to have a converged result. Thus, the computational cost becomes unaffordable in the current framework. One alternative to increase the efficiency of the statistical method is to employ variance reduction techniques, like for example Quasi Monte Carlo (QMC) [112] based on pseudo random generators or the Latin Hypercube Sampling (LHS) based on stratified sampling [110]. With this sampling method, each sample is the only one in each axis-aligned hyperplane containing it. An example for 40 samples, 2 variables and uniform distributions is shown on figure 4.1. The probability domain is divided in 40×40 squares. For the LHS sampling, it is seen that each row and each column only have one sample. In contrast, with the random sampling, some columns and rows have no sample, and some have more than one sample. This means that the samples are better distributed for the LHS sampling. For this reason, the convergence is faster (nearly $O\left(1/N_{simulations}\right)$), and only between 1000 and 10000 computations are needed. However, because around 40 min are needed for a 2D simulation in this work, this method is still difficult to use.

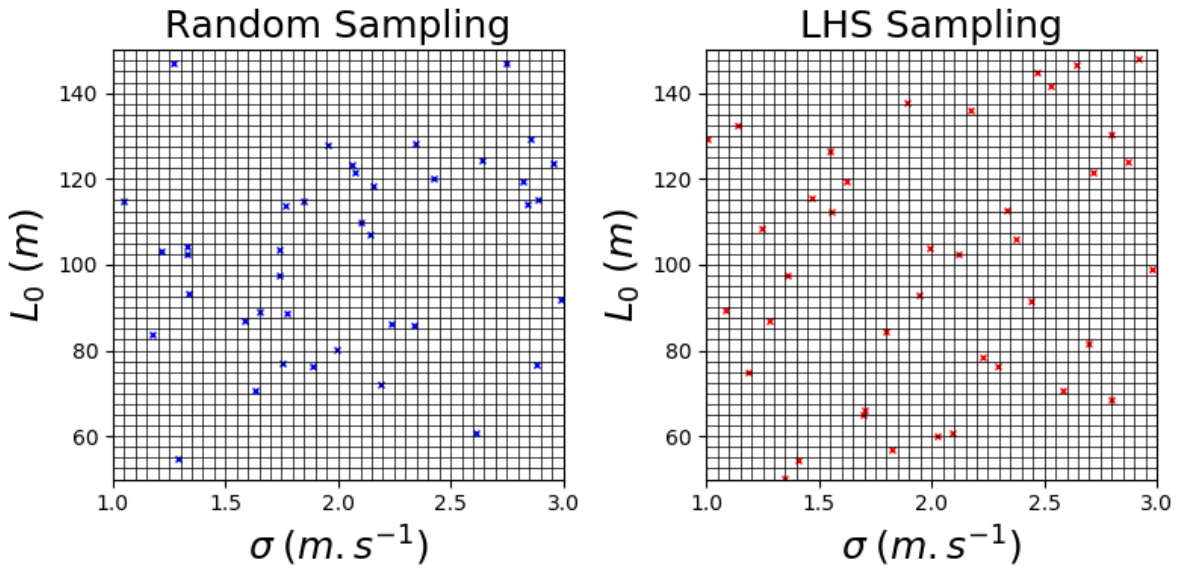

Figure 4.1: Comparison between random sampling (left) and LHS sampling (right).

Therefore, other methods has been developed to further reduce the computational cost of the stochastic study. One of them is the generalized polynomial chaos method (gPC method) [181], which is used in this study. This method is very efficient to deal with multidimensional distributions compared to Monte-Carlo or Latin Hypercube Sampling methods. From the methodological point of view adopted in the present work, two random variables, σ and L_0 are chosen while the random vector $\underline{R}$ is fixed for a given study. This method allows access to the level of pressure on the ground (and so all the metrics) and its moments (average, standard deviation and probability density) for a predetermined continuous range of values of σ and L_0 by calculating a meta-model $p(x, t, \sigma, L_0)$ with the help of discrete values for which simulations have been run. In a second stage, different realizations of the random vector $\underline{R}$ are computed and a gPC study is made for each one of them. This approach makes it possible to establish a large database for different sonic boom signatures on the ground with good statistics.

In the gPC method, the output random variable $p(x, t, \sigma, L_0)$ is represented with a polynomials series expansion:

$$p(x, t, \sigma, L_0) = \sum_{n=0}^{\infty} \hat{p}_n(x, t)\Phi_n(\sigma, L_0), \tag{4.1}$$

with (σ, L_0) the random variables, $\hat{p}_n$ the coefficients of the expansion and $\Phi_n(\sigma, L_0)$ polynomials of degree n. The random variables σ and L_0 are assumed to have a uniform distribution, with $\sigma \in [1, 3]$ m s^{-1} and $L_0 \in [50, 150]$ m. This assumption fixes the kind of polynomials: $\Phi_n(\sigma, L_0)$ are Legendre polynomials. In practice, the polynomial order is truncated at an order N:

$$p(x, t, \sigma, L_0) = \sum_{n=0}^{N-1} \hat{p}_n(x, t)\Phi_n(\sigma, L_0). \tag{4.2}$$

The polynomials $\Phi_n(\sigma, L_0)$ are normalized such as $< \Phi_i(\sigma, L_0), \Phi_j(\sigma, L_0) >= \delta_{ij}$. The coefficients $\hat{p}_n(x,t)$ are then calculated thanks to the orthogonality property:

$$\hat{p}_n(x,t) =< p(x,t,\sigma,L_0), \Phi_n(\sigma,L_0) >_{P(\sigma,L_0)}= \int_\sigma \int_{L_0} p(x,t,\sigma,L_0)\Phi_n(\sigma,L_0)P(\sigma,L_0)d\sigma dL_0, \tag{4.3}$$

where $P(\sigma, L_0)$ is the probability distribution. The integral is then calculated with quadrature rules:

$$\hat{p}_n(x,t) = \sum_{k=0}^{K-1} p(x,t,\sigma_k,L_{0k})\Phi_n(\sigma_k,L_{0k})w_k, \tag{4.4}$$

with K the number of quadrature points, and (σ_k, L_{0k}) the random variables and w_k the weights at each of those points. Quadrature points and weights are chosen accordingly to the probability distribution of the input random variables. The number of quadrature points K can be determined by performing a convergence study. Here, a quadrature order of 5 has been chosen (see section 4.2), which means that the number of required FLHOWARD3D simulations is equal to $K = (5+1) \times (5+1) = 36$. This is much less than for the LHS or the Monte Carlo method. The values of σ_k and L_{0k} weighted by w_k for this configuration are shown figure 4.2.

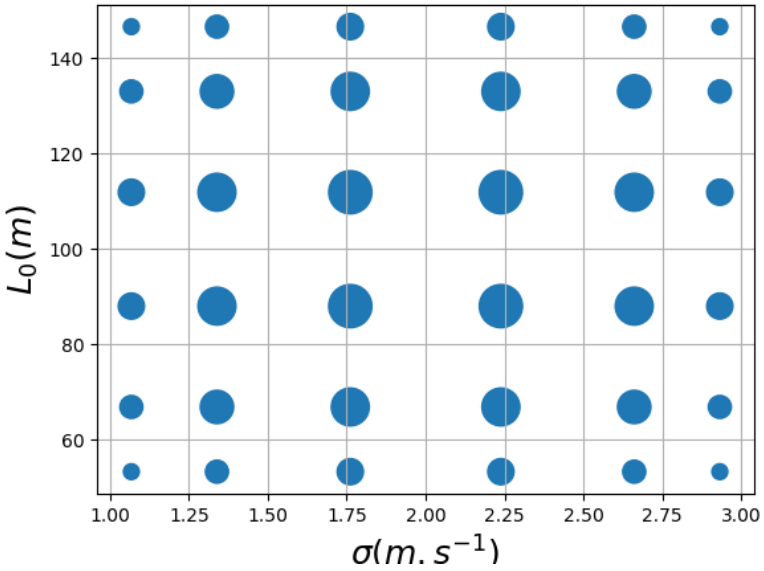

Figure 4.2: Nodes for the gPC study, for a quadrature order of 5. The surface of the points is proportional to their weight.

To summarize, gPC method consists in the following steps:

- set the sonic boom signal (N, F18 or C25D),
- choose the number of quadrature points K,
- for each quadrature point :

  - set the values of the random variables σ_k and L_{0k},
  - compute the turbulent wind fluctuations (code synthetic turbulence): u_k,
  - compute the pressure (code FLHOWARD3D): $p_k(x, y, t)$,
  - extract the ground pressure $p(x, t, \sigma_k, L_{0k})$,
- compute the coefficients $\hat{p}_n(x, t)$ (equation 4.4) by using quadrature rules at points k (gPC method),
- compute the meta-model $p(x, t, \sigma, L_0)$ (equation 4.2) with the series expansion,
- apply the Monte Carlo method to the metamodel by running it a huge number of time (1 million) with random parameters, and use the results to obtain the mean, the standard deviation and the probability distribution of the propagation. Because the metamodel requires only purely algebraic operations, this step is not time-consuming.

With this method, the quadrature points are tensorized. This means that the number of quadrature points correspond to $(N + 1)^d$, with N the order of the method and d the dimension (the number of variables). Thus, the computational time is also proportional to $(N + 1)^d$. In this study, $d = 2$, and the method is thus very effective. However, in cases were d is high, this method may become very expensive thanks to the corresponding curse of dimensionality. To overcome this problem, sparse grid-based polynomial chaos methods can be employed [180]. These methods select sample points based on Smolyak algorithm [21] and thus can significantly reduce the number of quadrature points for high polynomial order. By construction, gPC methods will be very efficient when the response surface is smooth, but they are less accurate if there are sudden changes in the surface, like discontinuities with the random space. For this case, adaptive methods [87] where the random space is partitioned can be employed in order to circumvent the lack of accuracy.

4.2 Order of the gPC model

The accuracy tests concerning the gPC method are presented in this section. As presented previously, polynomials series expansion has to be truncated at an order N which determines the number of quadrature nodes and so the number of simulations to run. Because each run is time consuming, the order of the quadrature should be as low as possible, but high enough to ensure converged results. An optimal order N has to be found. Because there are 2 input variables, the number of quadrature points is equal to $(N+1)^2$, with N the order of the quadrature. To find an optimal order, the gPC method with the order 3, 5 and 7 has been applied on the propagation of the N-wave. As a reference, a Latin Hypercube Sampling (LHS) method has been used to generate a near random sample of 1000 couples of parameters, which were used for a quasi Monte-Carlo simulation. Because there were only 1000 samples, this method is not completely converged, but it still makes a good reference. The mean and the standard deviation for p_{max}, $A-SEL$ and $D-SEL$ for the different methods are shown figure 4.3. For the mean, for all the studied variables, the curves for the orders 3, 5, 7 and for the LHS sampling are nearly the same. This means that the mean is already converged with the order 3. For the standard deviation,

order 3 seems insufficient, but order 5 is similar to order 7, and both of them are very close to the curve obtained with LHS. In conclusion, a quadrature order $N = 5$ is chosen for the gPC method. It means that 36 quadrature points are required to estimate the meta-model. Even though 36 FLHOWARD3D runs are requested by the gPC method, it is much less than the 1000 ones requested by LHS method.

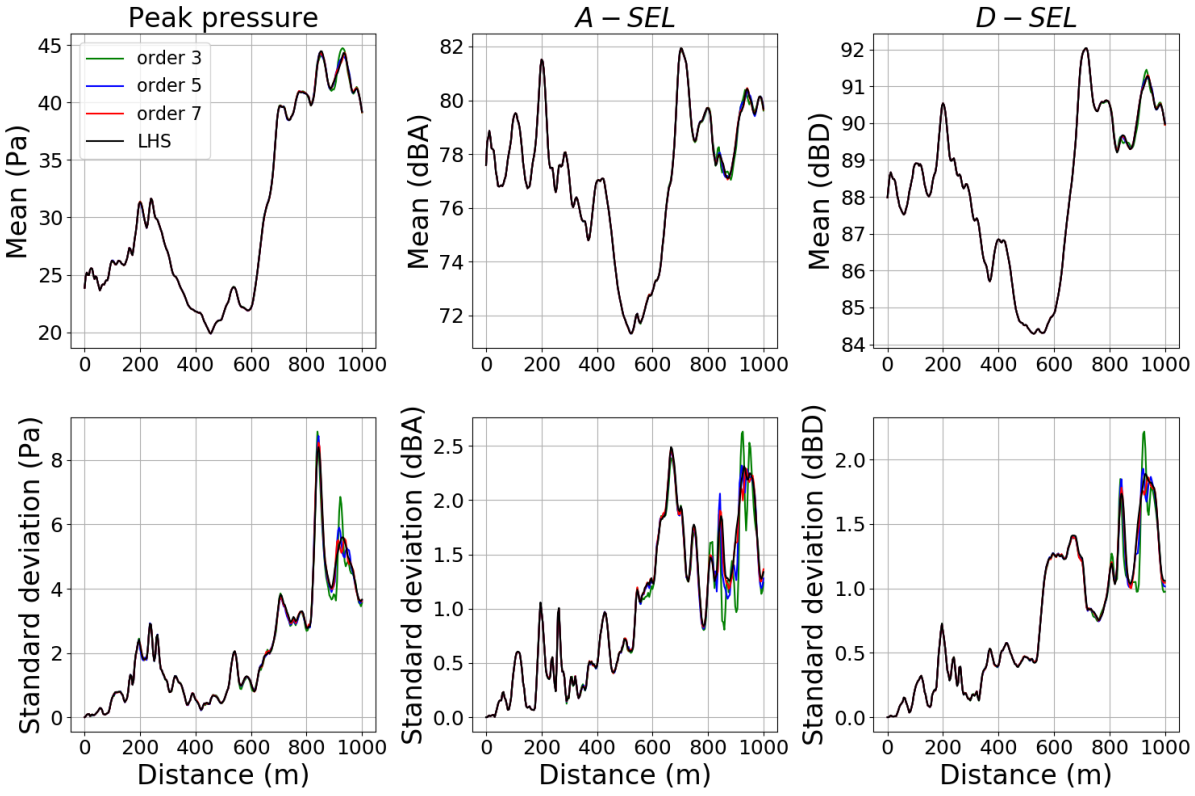

Figure 4.3: Comparison of the mean (up) and the standard deviation (bottom) of the peak pressure (left),$A-SEL$ (middle), and $D-SE$L (right) in function of the propagation distance, for the gPC method with order 3, 5 and 7 and for the LHS method, for the N-wave boom.

4.3 Impacts of the magnitude and the characteristic length scale of the turbulence for a fixed random vector

The meta-model of the propagation in a 2D atmosphere with σ and L_0 variable and a fixed random vector $\underline{R}$ for the three different input signals described previously (N-wave, the F-18 boom and the C25D boom) has been obtained. In Figure 4.4, different metrics according to the distance of propagation are presented. For each one, the green curve corresponds to nominal parameters ($\sigma = 2\,\mathrm{m\,s^{-1}}$ and $L_0 = 100\,\mathrm{m}$) the black curve corresponds to the mean, the red shades is the probability density function. This is the result for 1 random atmosphere (1 random vector $\underline{R_1}$).

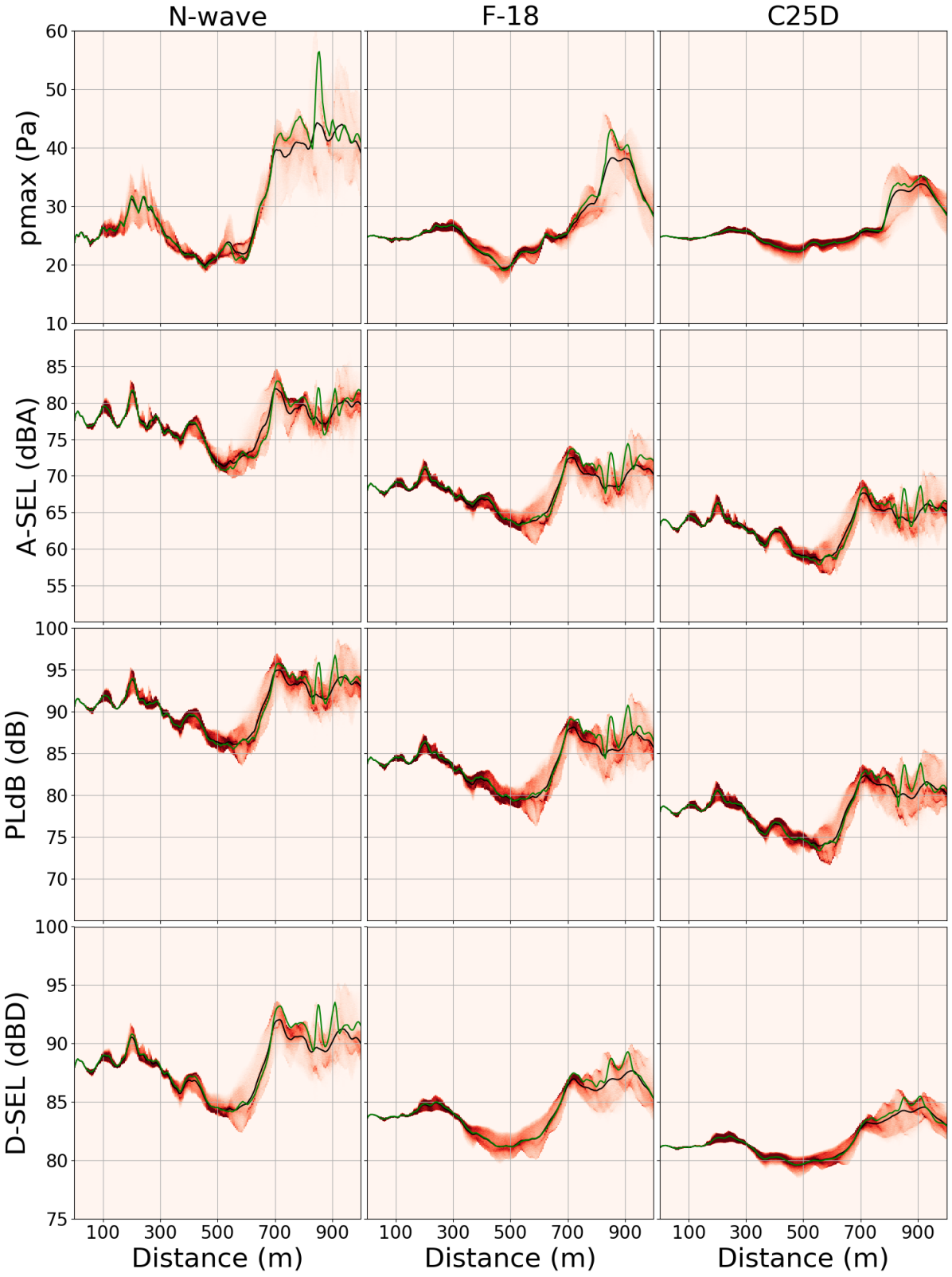

Figure 4.4: Mean (in black), nominal propagation ($\sigma = 2\,\mathrm{m\,s^{-1}}$ and $L_0 = 100\,\mathrm{m}$, in green) and probability density function (in red) of the peak pressure p_{max}, $A-SEL$, $PLdB$ and $D-SEL$ for the N-wave (left), the F-18 boom (middle) and the C25D boom (right).

Depending on the propagation distance, the mean propagation and the nominal propagation can be different, showing that the effects of the atmosphere on the propagation are not linear. Moreover, the probability density function is not symmetric and sometimes the most probable values (dark shade) are different from the nominal and mean ones (for example around 600 m).

Concerning the propagation, for the peak pressure p_{max}, a focusing can be seen around 200 m, followed by a defocusing around 500 m and finally another focusing after 700 m. These effect are particularly present for the N-wave, where the mean of p_{max} attain 44 Pa around 900 m. The focusing are less visible for the F-18 boom, whose mean only attain 39 Pa at 900 m. Finally, the C25D boom seems to be the less affected by the propagation, its value of the mean of p_{max} is the lowest of the 3 booms, with a value of 35 Pa at 900 m. The first focusing is also nearly unnoticeable, with a increase of only a few Pa. The probability density function shows that there is also differences in the uncertainty of the variables. For the N-wave, for the last focusing, the values of p_{max} vary between 30 and 60 Pa. This variability is large, and show that huge values of pressure (which are not welcome) can be attained. For the F-18 boom, at the same distance, the values are between 30 and 45 Pa. This boom is more predictable. Finally, for the C25D boom, the variability is the lowest between around 28 and 37 Pa. This boom is the more predictable of the 3, and don't attain values of pressure too high.

For the metrics $A-SEL$ and $PLdB$, The propagation seems to have more focusing than the previous one, with supplementary focusing at 100 m and 400 m. Except for the lift caused by the initial value, the 3 booms have evolution of $A-SEL$ and $PLdB$ comparable between them, with similar values range and probability density.

For $D-SEL$, more differences can be seen between the 3 booms than for $A-SEL$ and $PLdB$: The extra focusing observed on $A-SEL$ and $PLdB$ are only visible for the N-wave, and there is more variability for the N-wave than for the low-booms. Furthermore, between the low-booms, there is more variability for the F-18 boom. The probability density function follow the same trend, it is the largest for the N-wave, and the lowest for the C25D boom.

Therefore, For this random realization of the wind velocity fluctuation, low booms, though still affected by turbulence, tend to show a smaller variability when propagating in a turbulent atmosphere, compared to classical N-wave. The quantification of this variability for low booms is however strongly dependent on the choice of the boom metric, some metrics being less sensitive than other ones.

It is interesting to come back to the waveform of the signals on the ground in order to see the effects of wind fluctuations. Analysis of the meta-model shows that there exist regions where the mean, the nominal and the most probable values for a given metric are very close (for instance at $x = 400\,\mathrm{m}$) or with large variations (for instance at $x = 843\,\mathrm{m}$). Figure 4.5 show the wave-forms on the ground after propagation at $x = 400\,\mathrm{m}$ and $x = 843\,\mathrm{m}$ for 3 couples of values (σ,L_0) corresponding to the values given the extremal values of the pressure for the N-wave at these distances. As predicted by the meta-model, wave-forms are very close at $x = 400\,\mathrm{m}$ and have significant differences at $x = 843\,\mathrm{m}$. The differences are mainly concentrated around the shocks. Indeed, the overall waveform is quite similar but we can observe that the level of the shocks can be significantly different: at 843 m, for ($\sigma = 1.06\,\mathrm{m\,s^{-1}}, L_0 = 53\,\mathrm{m}$) the waveform looks like the classic N-wave while for ($\sigma = 2\,\mathrm{m\,s^{-1}}, L_0 = 100\,\mathrm{m}$) and ($\sigma = 2.23\,\mathrm{m\,s^{-1}}, L_0 = 146\,\mathrm{m}$)

the shape is more a U-wave with an amplification close to 1.6. Of course it is important to note that only increasing values of (σ, L_0) is not sufficient to explain the amplification.

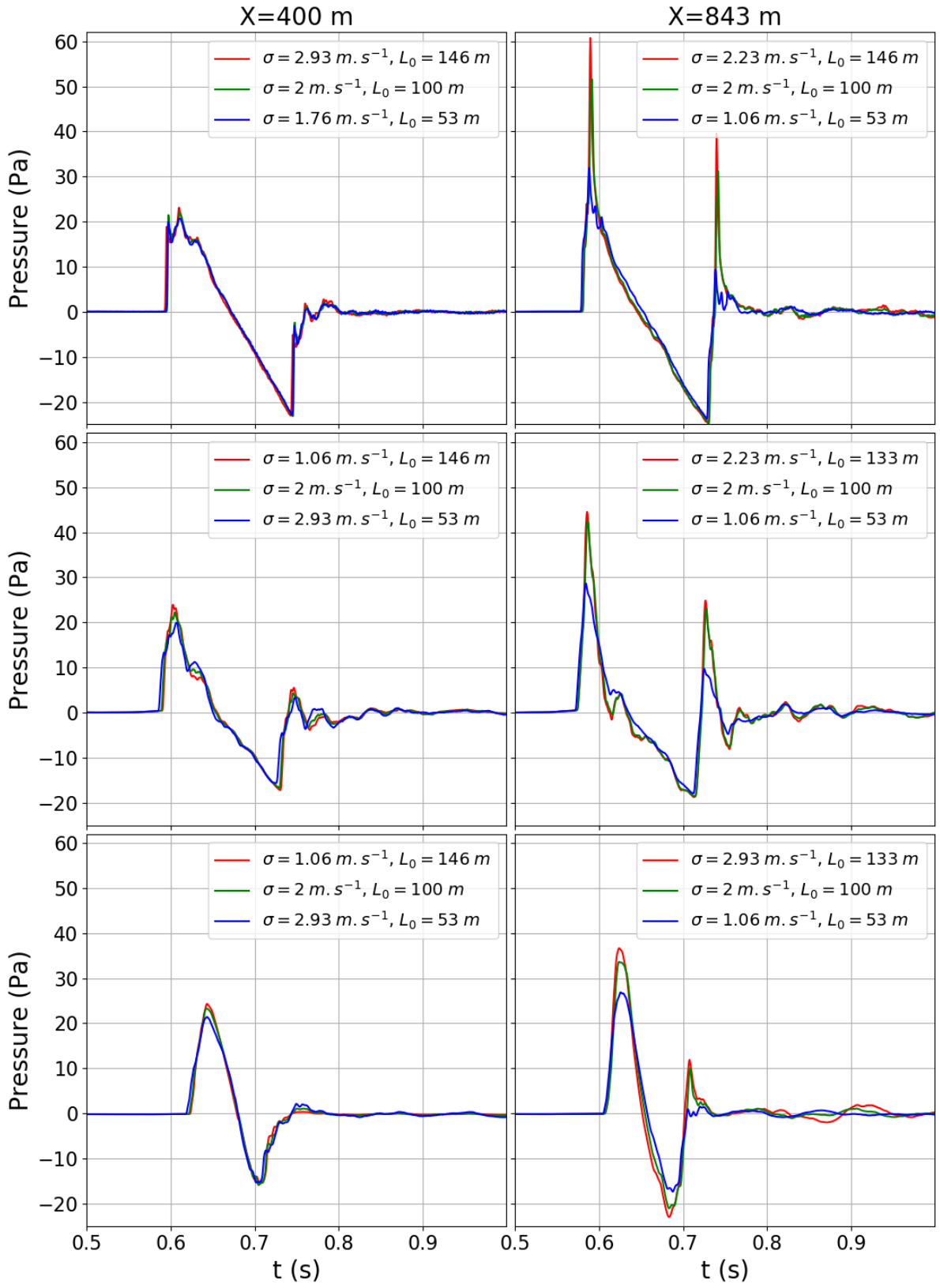

Figure 4.5: Wave-forms for the N-wave (up), the F-18 boom (middle) and the C25D boom (down) at the ground for different values of the uncertain parameters at $x = 400\,\mathrm{m}$ (left) and $x = 843\,\mathrm{m}$ (right).

In conclusion, for each variable, the classical boom presents higher variability and uncertainty than the low-booms, and can attain higher values. The low-booms have similar propagation for the $A-SEL$ and $PLdB$ metrics (with the exception of the initial shift), and for p_{max} and the metric $D-SEL$, the classical boom has more variability and uncertainty than the low-booms.

4.4 Influence of the random vector

The previous observations are based on a study with a single realization of the random vector $\underline{R}$, with σ and L_0 variables. This means that to confirm the results, there is a need to study the propagation with other random vectors $\underline{R}$. The previous gPC analysis has been done for 50 different atmospheres (50 random vectors $\underline{R}$) and for the three input signals described previously. For each study, the signals on the ground have been computed, extracted and collected.

Figure 4.6 shows the evolution of the mean, the nominal and the probability density function values of different metrics depending on the distance of propagation. This figure is similar to Figure 4.4 but it is plotted for a different random vector (referenced as $\underline{R_2}$). As previously, depending on the distance of propagation, the mean propagation and the nominal propagation can be different, showing the importance of the parameters σ and L_0 and the interest to consider them as uncertain. Nevertheless, we can also see that the regions of amplification and the regions where the amplitude drops are different from Figure 4.4. Here the focusing is important at $x = 400\,\text{m}$ and the main defocusing zone is located at $x = 600\,\text{m}$. Therefore, the role of the random vector is major and it is responsible for the global shape and in particular for the position of focus areas. Common tendencies are also visible between Figure 4.4 and Figure 4.6 : (i) at the beginning all curves are close together showing that there is no effect of the variations of σ and L_0, (ii) the width of the possible events increase with the distance of propagation showing that the effect of the turbulent fluctuations on the propagation is cumulative.

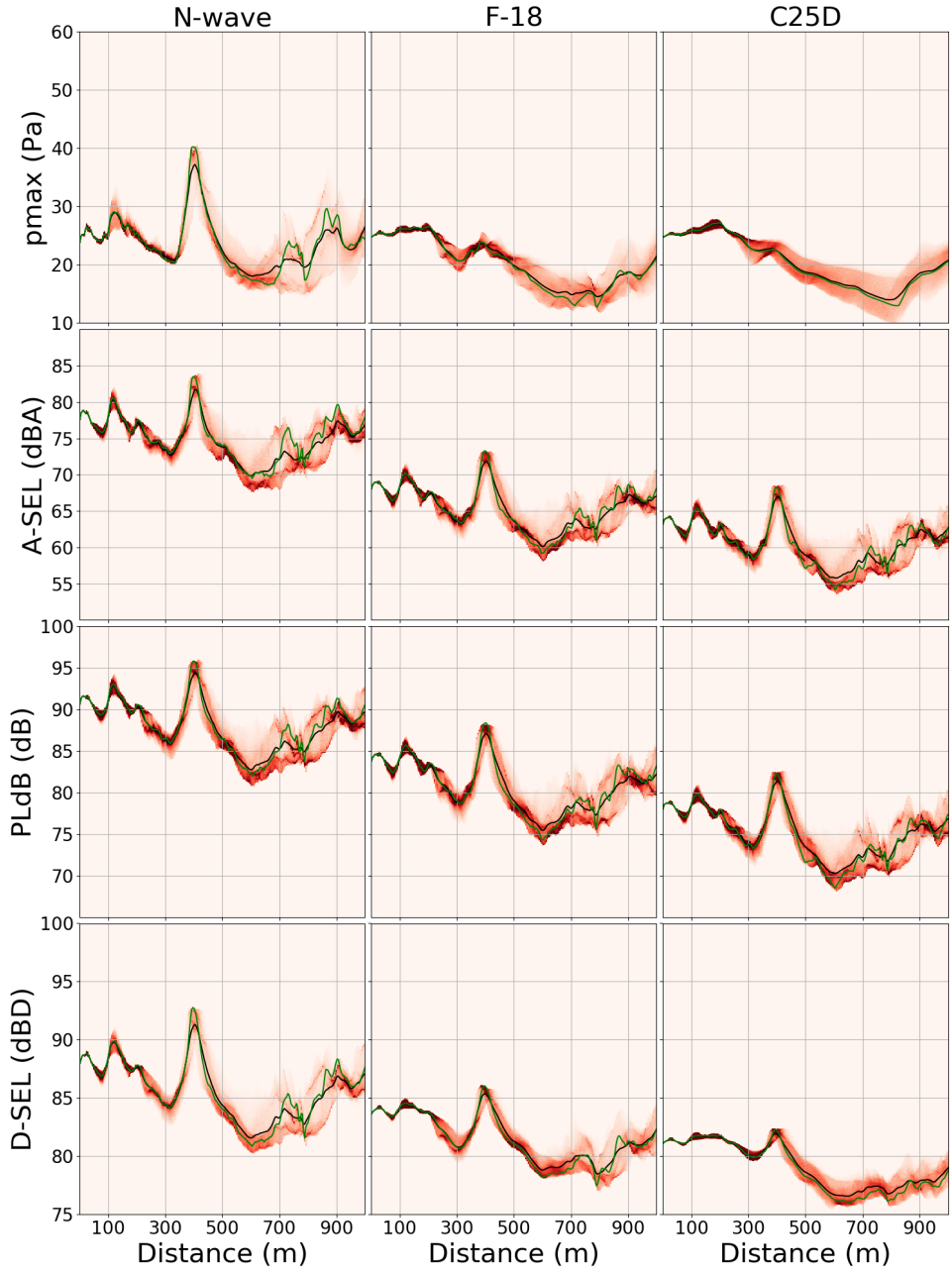

Figure 4.6: Mean (in black), nominal propagation ($\sigma = 2\,\mathrm{m\,s^{-1}}$ and $L_0 = 100\,\mathrm{m}$, in green) and probability density function (in red) of peak pressure p_{max}, $A-SEL$, $PLdB$ and $D-SEL$ for the N-wave (left), the F-18 boom (middle) and the C25D boom (right) for a new random vector $\underline{R_2}$.

On Figure 4.7, the wave-forms of the three booms with different couples of parameters (σ, L_0) at 400 m and 843 m are traced. As seen before, the wave-forms show that there are more variations for the N-wave than the low-booms.

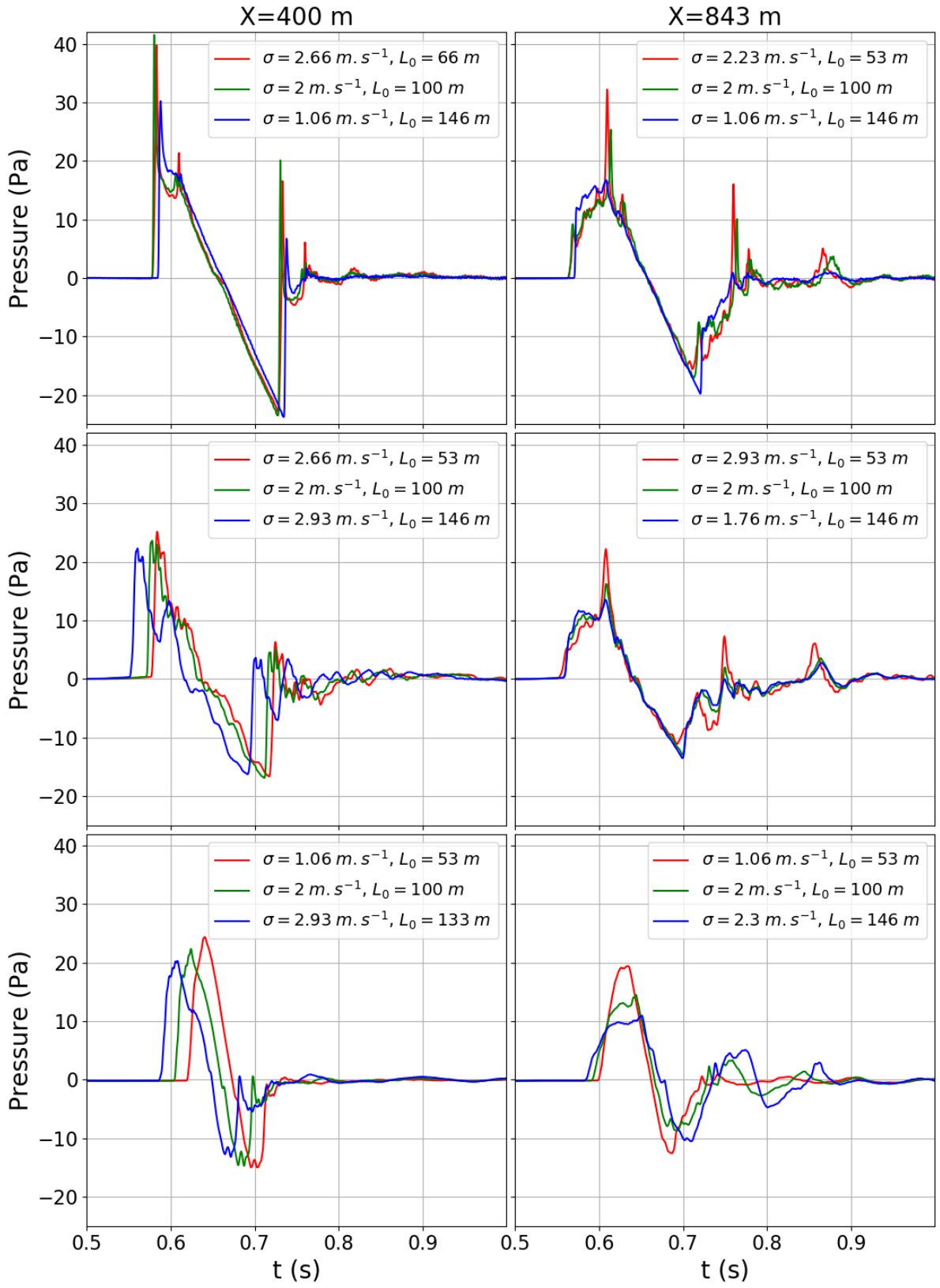

Figure 4.7: Wave-forms for the N-wave (up), the F-18 boom (middle) and the C25D boom (down) at the ground for different values of the uncertain parameters at $x = 400\,\mathrm{m}$ (left) and $x = 843\,\mathrm{m}$ (right), for the propagation in the atmosphere computed with $\underline{R_2}$.

Figure 4.8 presents maps of $p_{max}(\sigma, L_0)$ for the 3 sonic booms at 843 m, for the 2 different random vectors $\underline{R}$. The variations of p_{max} are coherent with the curves of figure 4.5 and figure 4.7: there are strong variations for $\underline{R_1}$ especially for the N-wave, and less variations for $\underline{R_2}$. For a given signal, the maps are different with an different $\underline{R}$: a couple of parameters (σ, L_0) which gives the higher pressure for $\underline{R_1}$ will not do the same for $\underline{R_2}$. Nevertheless, all these maps have a general tendency of increasing the pressure with the level of turbulence σ. There are exceptions, but globally, the low pressures correspond to small σ and the high pressure to high σ. With the same $\underline{R}$, the maps are close to each other, except that the N-wave shows higher values and variations, as seen before.

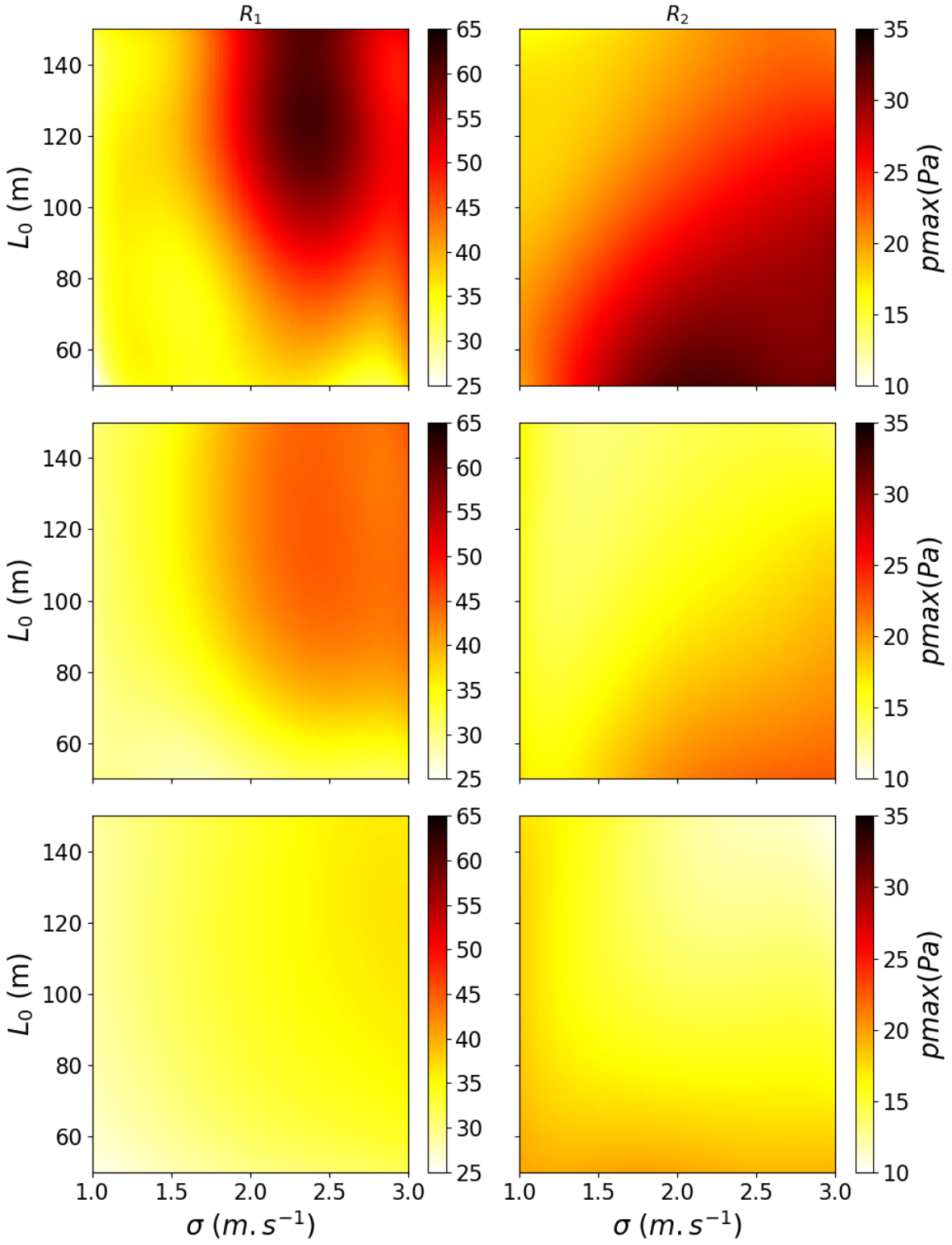

Figure 4.8: Response surfaces of p_{max} in function of σ and L_0 calculated using the gPC model, at 843 m, for the N-wave (up), the F-18 boom (middle) and the C25D boom (down), for the random vectors $\underline{R_1}$ (left) and $\underline{R_2}$ (right).

In conclusion, the parameter with the most influence on the variations of the propaga-

tion is the random vector $\underline{R}$, which determines the position of the focusing and defocusing. However σ and L_0 still have an important impact on the propagation, and should not be neglected.

4.5 Influence of 50 random vectors: presentation of the results

A database of $3 \times 50 \times 36 \times 256 = 1382400$ signatures has been collected for this study. Many signals are available, with various behaviors. In order to observe these different behaviors, an agglomerative clustering method is applied on the peak pressures during the propagations. The samples are the $50 \times 36 = 1800$ propagations, and the variables are the peak pressures for the 256 positions, for each of the 3 boom signals: there are 256×3 variables for this clustering study. More details on the clustering method are given in the next chapter. 9 groups are chosen, and the peak pressure for these groups are shown figure 4.9 for the N-wave and figure 4.10 for the C25D boom.

A lot of different propagations are observed. For the N-wave propagation, there is a lot of variability within each cluster, and even more between the clusters. The first cluster contain propagations whose the main property is a focusing at 700 m. The second cluster has a focusing at the end of the propagation, around 1000 m. The third cluster has a strong focusing between 300 and 700 m, as well as a defocusing after 900 m. The fourth cluster has a small focusing between 400 and 400 m. The fifth cluster has a small focusing around 250 m, and a strong focusing after 800 m. The sixth cluster has a small focusing around 400 m. The seventh cluster has a focusing between 200 and 500 m and a defocusing after 800 m. The eight cluster has small clustering around 300 m and 800 m. Finally, the last cluster has no notable significant focusing. The peak pressure ranges from -8 Pa to 75 Pa.

For the C25D boom, the characteristic of the cluster are globally the same as for the N-wave. However the focusing are smaller and the defocusing are lower than for the N-wave. There is less variability in the peak pressures: the propagations within the clusters are closer.

Finally, on figure 4.11 are traced temporal signals with different waveforms, for the N-wave and the C25D boom, at 1 km of propagation. The signals are chosen in order to show the various types of waveforms present in the database.For the N-wave propagation, the brown signal has a shape close to a classical N-wave. The violet signal has a form close to a U-wave, with a high second peak at the end of the signal. The grey signal is the same, but with a lower rise time. The other signals are more complex: the blue one and the orange one have 3 peaks: in these cases, the turbulence cause a second arrival. The second peak is even higher than the first. Then, the red signal is quite low and also presents many small peaks. The pink signal shows only one arrival, but it is very disturbed, and not peaked. Finally, the green signal is also not peaked at the start, but shows a high peak at the end of the signals. For the C25D boom, some of these observations are still valid, but the pressures are lower and the waveforms smoother. These signals are only a small part of the database, but they shows that the available waveforms are diverse.

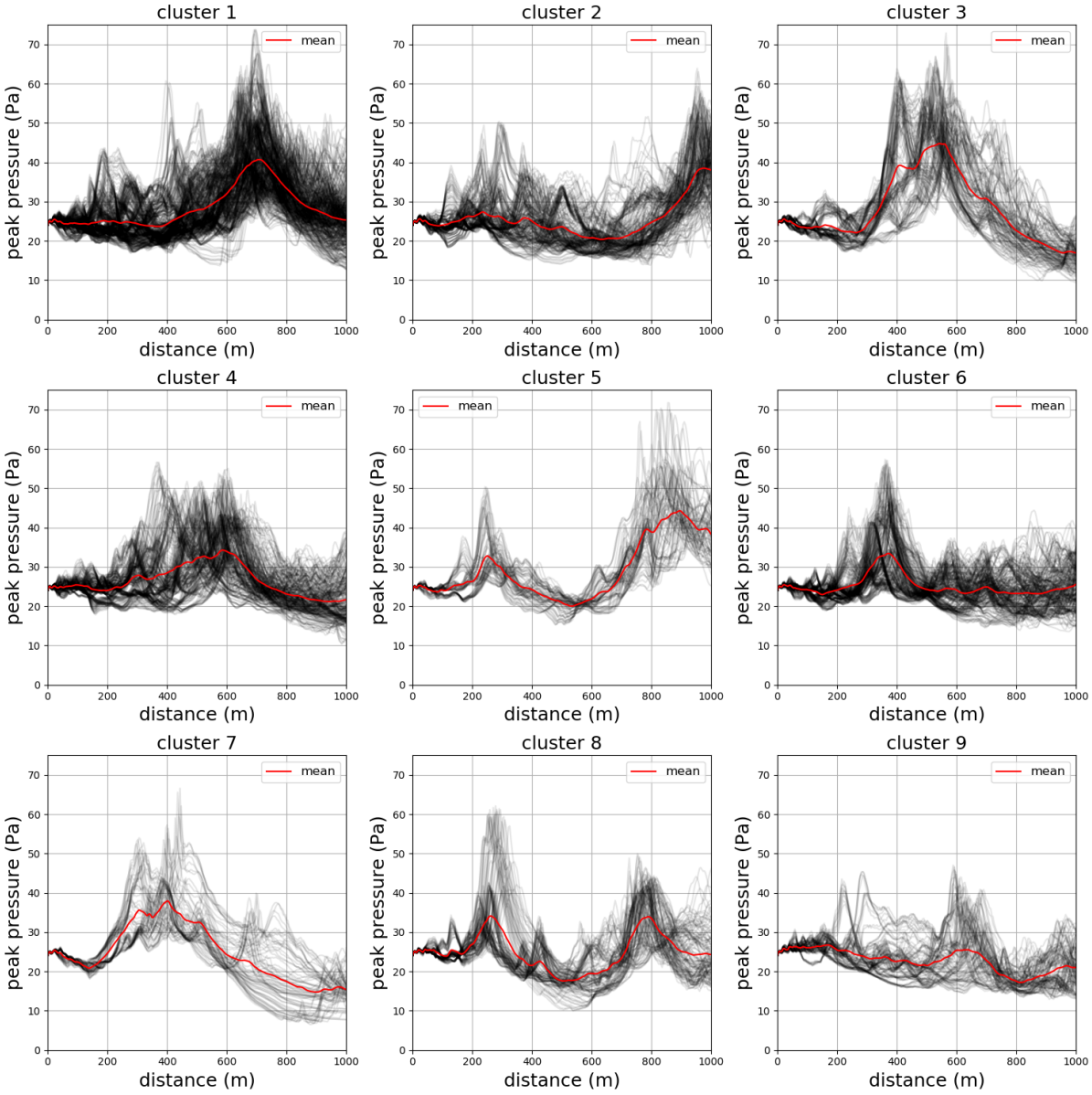

Figure 4.9: Peak pressure in function of the propagation distance, for all the simulation in the database, for the N-wave. The signals were divided in 9 groups with an agglomerative clustering method. The mean for each group is plotted in red.

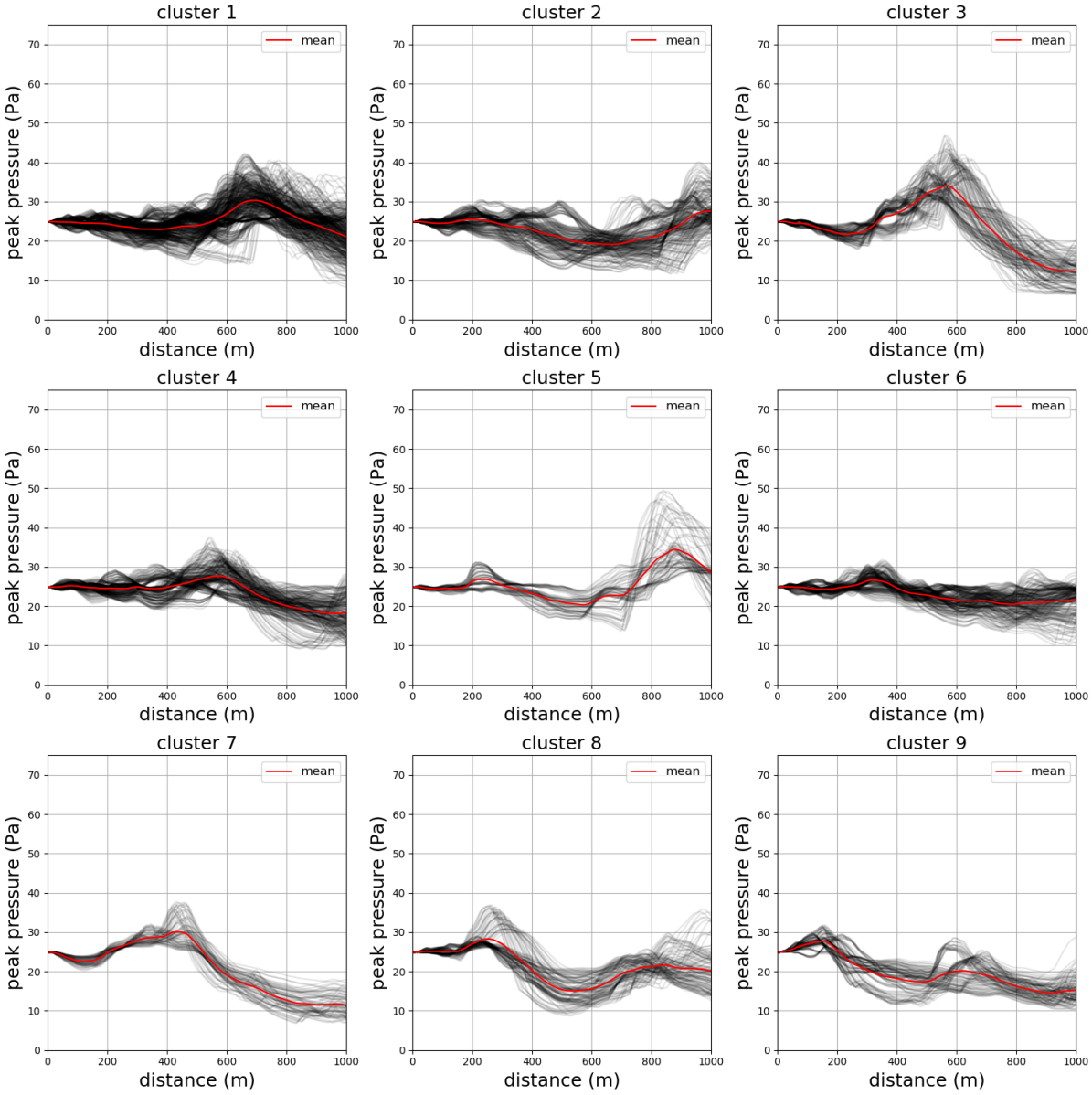

Figure 4.10: Peak pressure in function of the propagation distance, for all the simulation in the database, for the C25D signal. The signals were divided in 9 groups with an agglomerative clustering method. The mean for each group is plotted in red.

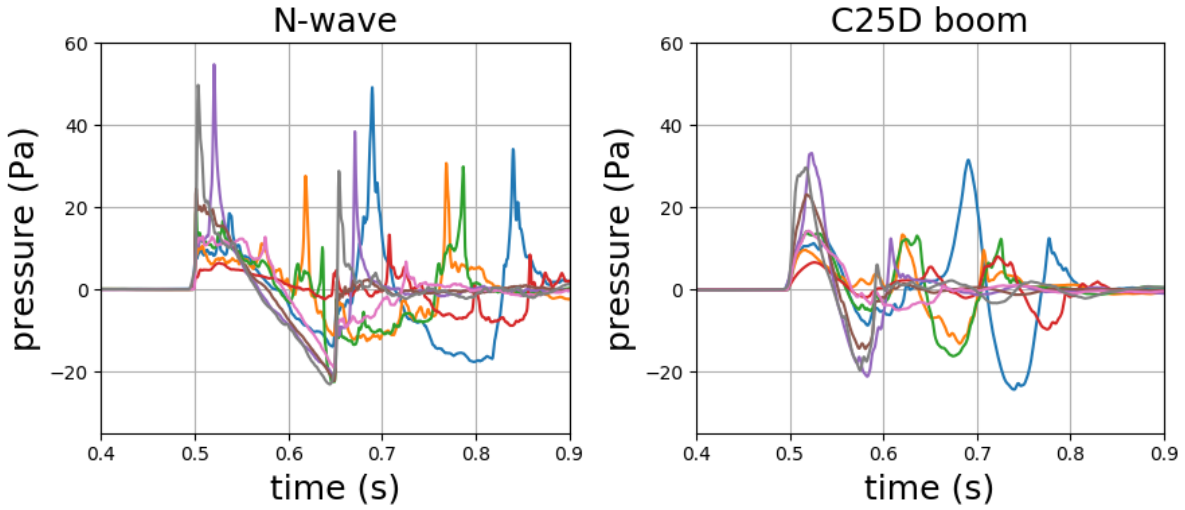

Figure 4.11: Temporal signals at 1 km, with different meteorological conditions, for the N-wave and the C25D boom.

4.6 Sensitivity of the propagation to the turbulence magnitude and to the characteristic length for the 50 random vectors

The stochastic study is done with the parameters σ and L_0 as variables. How each of these parameters contribute to the propagation can be determined by a sensitivity analysis. It consists in studying how the uncertainty in the output of a mathematical model or system can be divided or allocated to different sources of uncertainty in its inputs. The method used is the variance-based sensitivity analysis (Sobol method) [152]. It decomposes the variance of the output of the model in fraction which can be attributed to inputs or sets of inputs. In this case, the variance of the output (p_{max} or $PLdB$) is decomposed and attributed to σ, L_0 or to the interaction of the 2.

The sensitivity of the propagation of the C25D boom in one atmosphere (one $\underline{R}$) to the two input parameters σ and L_0, for p_{max} and $PLdB$ is shown at the top of figure 4.12. The blue curve is the fraction of the variance caused by σ, the red curve is the fraction caused by L_0 and the violet curve is the fraction caused by the interaction of the 2. For p_{max}, σ is nearly always predominant, except around 180 m, 500 m and 600 m. For $PLdB$, σ is predominant nearly everywhere. The interaction between σ and L_0 is always low, but globally not negligible. L_0 is predominant when σ is not.

The variations of the maximum of pressure and of the metrics are mostly due to the amplitude σ. However, at some distances (here for 180 m, 500 m and 600 m) the propagation become more sensitive to L_0. Thus, Even if σ has more influence on the variations, the two parameters have to be taken into account to reflect the complexity of the propagation. This study has been done on the N-wave and the F-18 boom with similar results.

To further this study, the average of the sensitivity has been calculated for the 50

random vectors in order to evaluate the influence of physical parameters independently of the vector $\underline{R}$. The result is shown at the bottom of figure 4.12. It is shown that the variance is still mainly caused by σ along the propagation, but there is still 30 % that is caused by L_0, and the coupling increases with the propagation distance, especially for the $PLdB$. this confirm that the amplitude of turbulence σ is the most sensitive parameter but that the influence of the characteristic length of turbulence L_0 cannot be ignored. Both parameters, though of unequal importance, have to be considered.

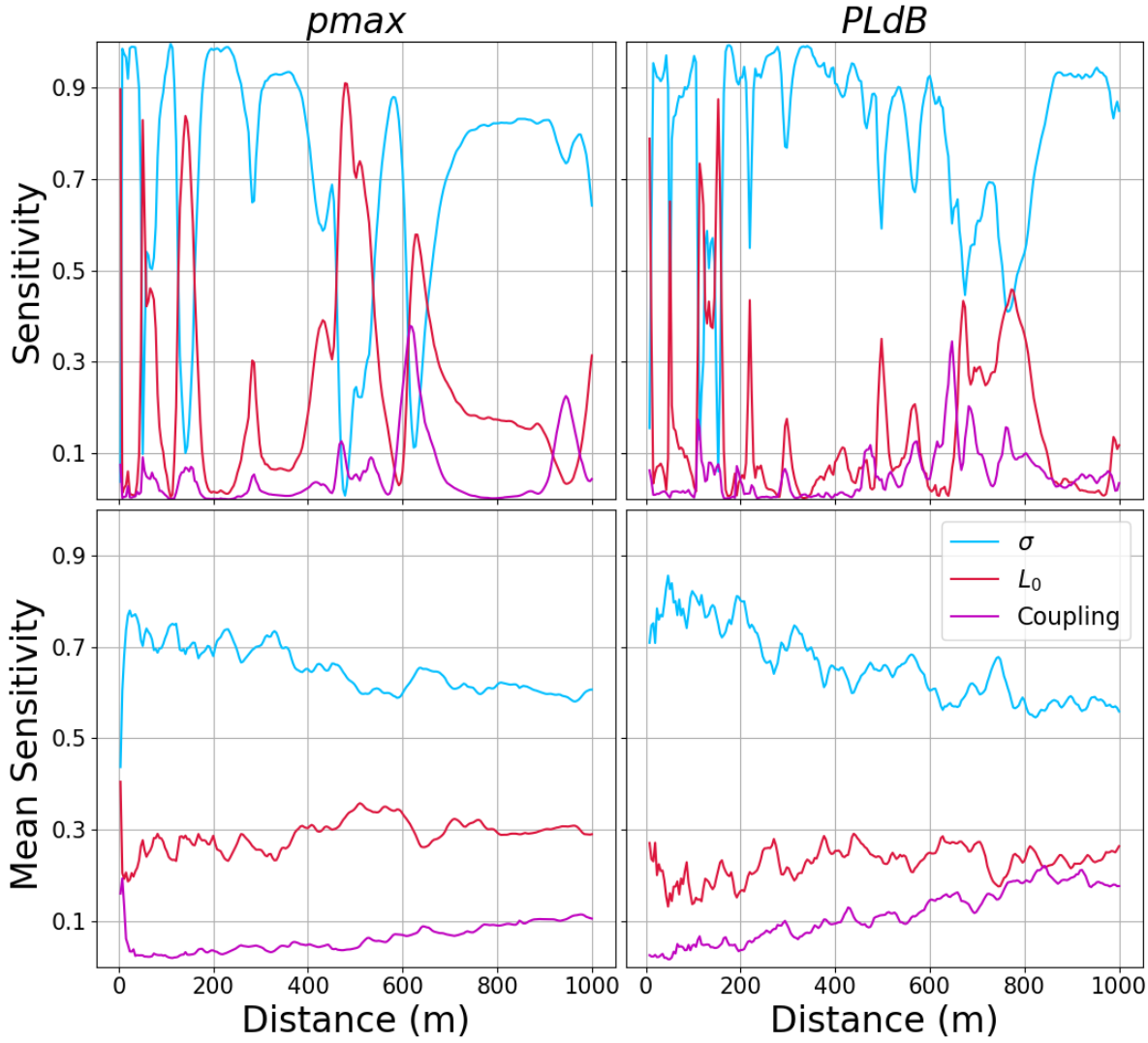

Figure 4.12: Sensitivity for 1 $\underline{R}$ (up) and mean sensitivity (for 50 realization of $\underline{R}$) (down), in terms of partial variances, of p_{max} (left) and $PLdB$ (right), for the C25D boom, in function of the propagation distance.

4.7 Influence of the propagation distance

As already mentioned, results are sensitive to the propagation distance. This effect has been attributed to the randomness of the turbulent fluctuations and not to the uncertainties of the physical parameters of the turbulence. Therefore, the evolution of the

standard deviation of the different metrics in function of the distance of propagation is studied. Mean standard deviations for the 3 booms for p_{max}, $D - SEL$ and $PLdB$ are plotted on Figure 4.13.

Figure 4.13 shows that for each of the 3 studied booms, the standard deviation of p_{max} increases with the propagation distance. This means that, as seen previously, the importance of the turbulent fluctuations on the propagation is cumulative. Furthermore, the increase is more important for the N-wave, which is in agreement with previous results: The N-wave is more affected by the propagation than the low-booms. The increase is globally linear, especially for the two low-booms. The same tendencies are found for $D - SEL$, where the increase of the standard deviation is faster for the N-wave (1.6 dB/km) than the F-18 boom (1.2 dB/km) and the C25D boom (1 dB/km). However, for the $PldB$, the increase of the standard deviation is the same for the 3 booms. Overall, the variance of boom level tends to increase more or less linearly with propagation distance in a turbulent atmosphere. Depending on the choice of the metric, this increase rate may or may not differ between an N-wave or a low boom signal.

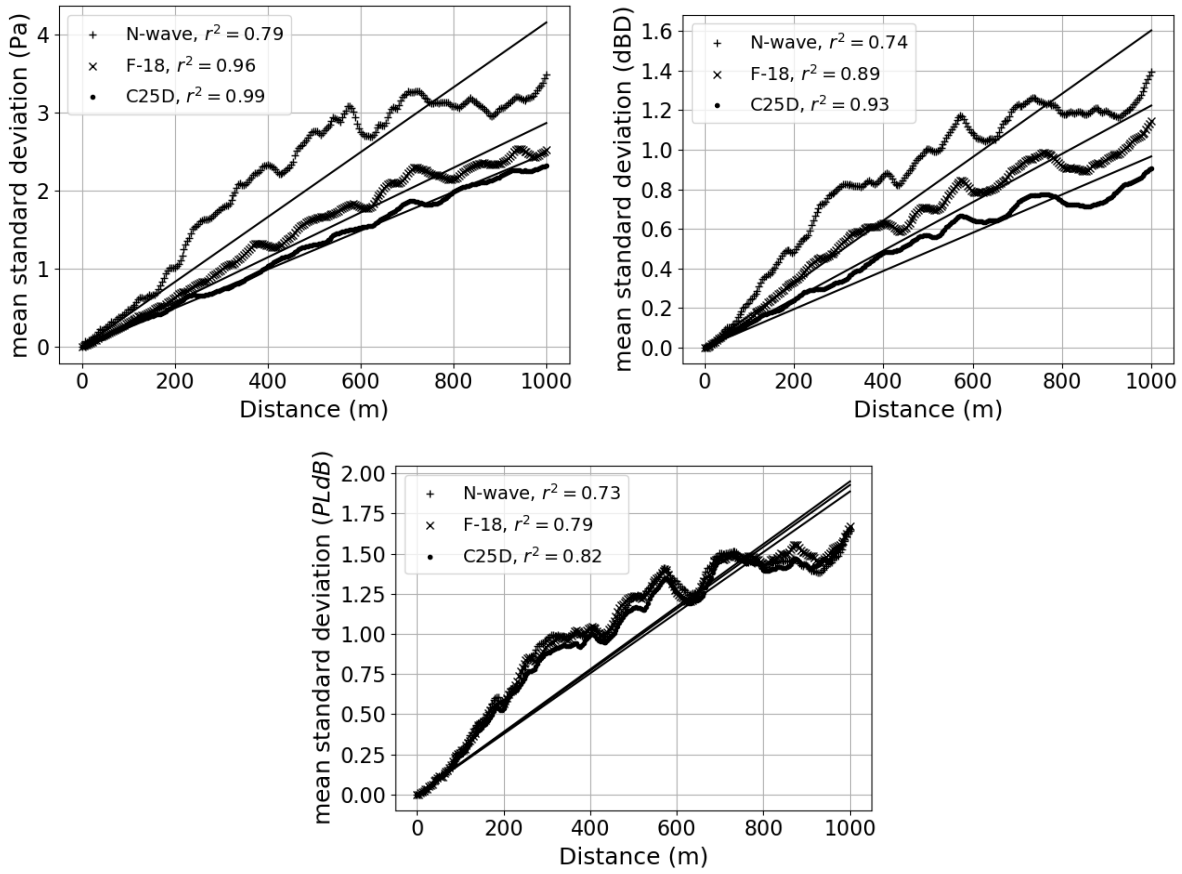

Figure 4.13: Mean of the 50 standard deviations of the peak pressure p_{max} (left), of $D - SEL$ (right) and of $PLdB$ (down) in function of the propagation distance for the N-wave, the F-18 boom and the C25D boom, and linear regressions of these standard deviations.

4.8 Influence of the wind fluctuations on low and classical booms

On figure 4.14 are traced the probabilities of the maximum of the peak pressure, $PLdB$ and $D-SEL$ for the 3 booms during the propagation. The C25D boom has a maximum of 50 Pa, twice its initial value, while the F-18 boom has a maximum of 60 Pa and the N-wave a maximum of 75 Pa, thrice its initial value. Thus, the extreme values of pressure are higher for the classical boom than for the low-boom. Furthermore, the C25D boom have a probability of less than 50 % to exceed 30 Pa and of around 5 % to exceed 40 Pa during the propagation, while the peak pressure of the N-wave will exceed 30 Pa more than 95 % of the time, an 40 Pa more than 70 % of the time. The F-18 has results higher, but close to the C25D boom. This shows the the classical boom is more likely to attain high values of peak pressure, and is therefore more perturbed by the wind velocity fluctuations. For the other metrics, $D-SEL$ has a tendencies close to the peak pressure, while the results for $PLDB$ are the same between the 3 booms. This shows once more that the metrics are not affected the same way by the propagation.

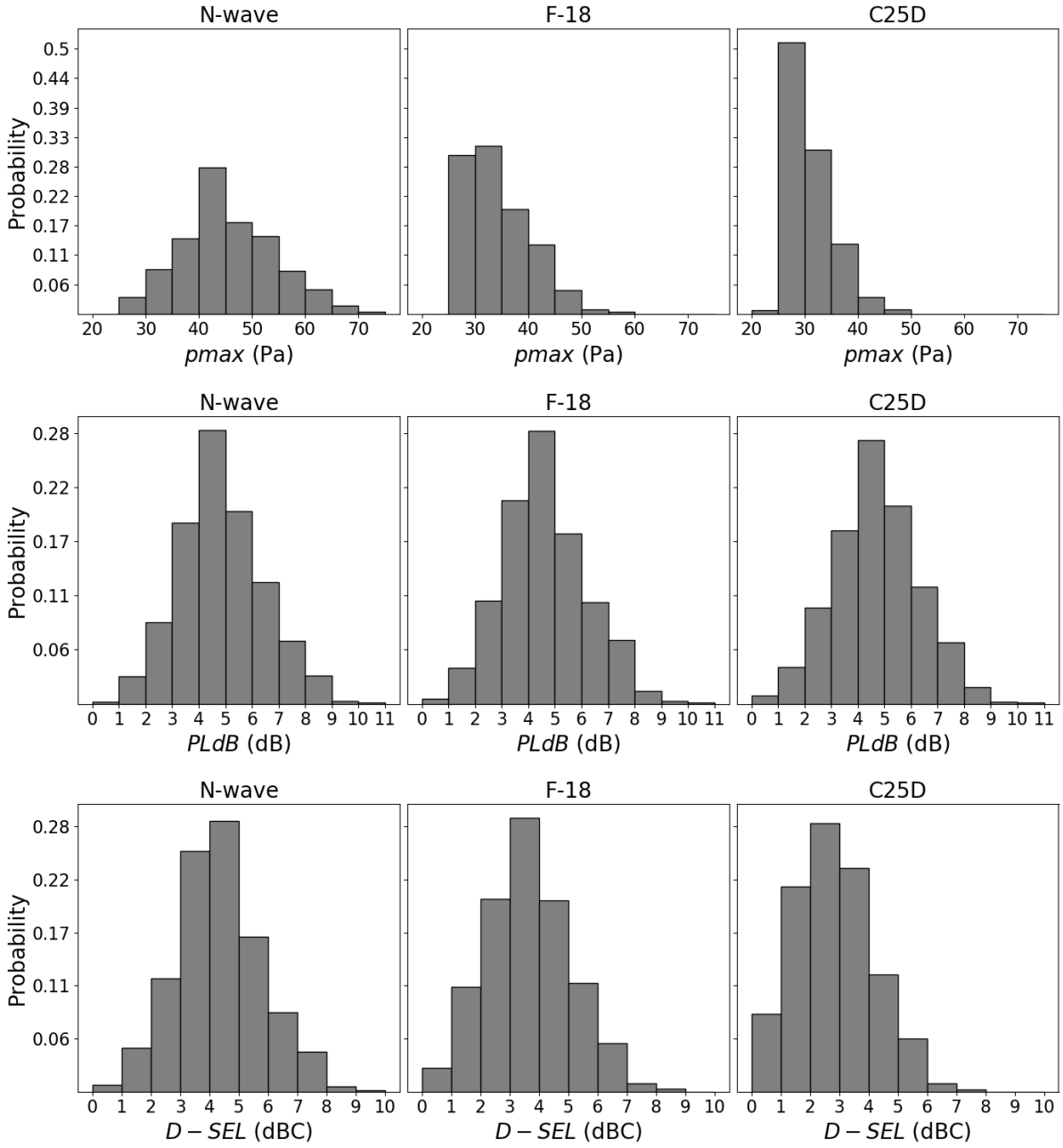

Figure 4.14: Probability distribution of the maximum of the peak pressure (up), normalized $PldB$ (middle) and normalized $D - SEL$ (down), attained during the propagation, for the three signals, calculated with the data from the database.

4.9 Conclusion

A stochastic study has been realized with 2D simulation. For a fixed random vector, a generalized polynomials chaos method is used to obtain a meta-model of the pressure field at the ground. This meta-model allows access to the pressure at the ground for all values of σ and L_0 but also to its statistical moments (mean, standard deviation) and to its probability density function. The assumption that parameters σ and L_0 are uncertain

is valid since the relationship between these parameters and the propagation is not linear: we observe distances where results are not sensitive to the values σ and L_0 but also regions where the sensitivity is important. Both σ and L_0 have influence on the propagation. The effects of σ and L_0 are located near the shocks while the global randomness (vector $\underline{R}$) changes the global waveform. We observe that the standard deviation increases with the distance (cumulative effects) and this result depends on the wave-forms (the N-wave is more sensitive than the low-booms) and also on the metrics. This means that low-booms should be less disturbing for the population, and that future civil supersonic aviation could be possible. This study paves the way to a full 3D study. Other effects such as thermal turbulence and large-scale gradient could also be added to the propagation model to have more realistic propagation.

Chapter 5

Experimental blast waves database

The pyrotechnic site located near Rivesaltes (Pyrénées Orientales, South of France at the Mediterranean foothill of Pyrénées) was an industrial site for the production of metal plates melted by explosions. When the site was open, one to four explosions were operating every day. These explosions generate blast waves, due to the sudden and local release of a finite amount of energy from an impulsive source. Then, a spherical pressure shock wave expands in air, with a fast decay in amplitude with the distance. The resulting propagation is strongly nonlinear in the near field, and weakly nonlinear in the far field. This regular source of blast waves therefore appears as a valuable site to investigate shock wave propagation in a given site under varying sources and atmospheric conditions. The CEA (Commissariat à l'Energie Atomique et aux Energies Alternatives) has installed a set of microphone stations at different locations around this site between 300 m and 20 km from the source to record the overpressures generated by these explosions between 2015 and 2018. During this period, more than 600 explosions were recorded [51]. This database provides a unique opportunity to investigate the propagation of blast waves in a real atmosphere. In particular, it paves the way to a systematic and statistical comparison between numerical simulations and measurements, an approach that will be the objective of our study.

Some data have already been used in previous studies. In [115], propagation is modeled by an Euler HPC method in the near field and a one-way acoustic propagation model in the far field, with the topography of the site. Simulated peak overpressures are compared with measured ones. In [117], direct fully nonlinear two-dimensional simulations are computed, taking into account the topography, the ground roughness and the meteorological conditions, with a detonation model for the explosive phase. Numerical results were then compared to pressure measurements. In [116], a one way coupling procedure between the high order Euler HPC code in the near field and a parabolic linear model in the far field is proposed. An empirical source model is also proposed. Results are once again compared to measurements. Finally, in [51], a wide angle parabolic equation code is used with Arome meteorological data and IGN topography. Comparisons between simulated and measured overpressures are also performed.

This chapter provides a description of the database. The objectives are two fold: give a comprehensive overview of the content of this database in order to be able to extract the most relevant information, and provide a first analysis of this database. Characteristics of the source, the acoustical sensors, the waveforms, and the meteorological data are

first discussed. Then, a classification study is performed on both the wind and source conditions, in order to explain the variability of the waveforms.

Figure 5.1: Satellite view of the pyrotechnic site located near Rivesaltes.

5.1 Presentation of the database

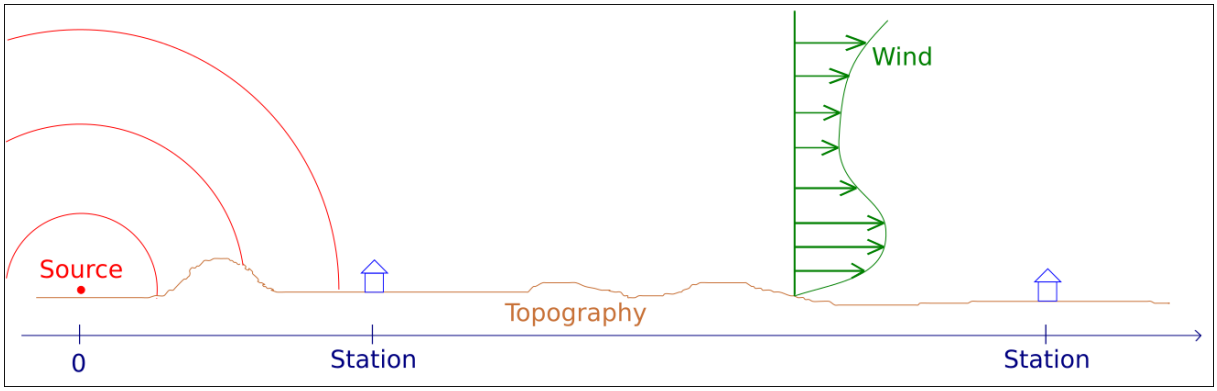

Figure 5.2: Sketch of the experiment

This database contains overpressure measurements of each explosion and various metadata, such as the source charge, the topography, and wind speeds and directions. Those metadata are presented in this section. A sketch of the experiment is shown on figure 5.2.

5.1.1 Characteristics of the source

Explosions are carried out in an industrial context to fuse metal plates, which cannot be welded otherwise using standard technics. The process is called explosion welding [83]. It starts with two metal plates: the base plate called the welder, and a thinner plate called the alloy cladder. The alloy cladder is placed on the welder, with a gap between the two. Explosive powder is placed on the cladder, as shown on the left of the figure 5.3. Then,

when the explosion takes place, the air between the plates is ejected and the cladder is welded on the welder, as seen on the right of the figure.

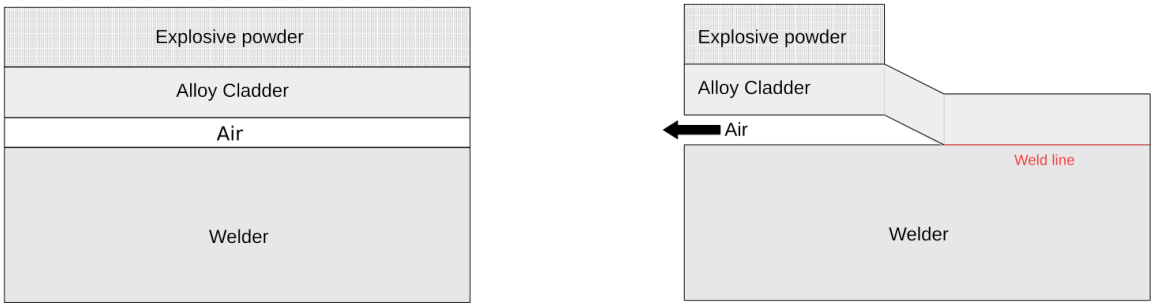

Figure 5.3: Schematic view of the plates before (left) and during (right) the explosion welding.

The plates are located in the pyrotechnic site in figure 5.1. Their exact position may vary slightly (about 20 m) in the source area from one explosion to another. However, the propagation being studied over several kilometers, the source is considered to be at the same position for each explosion, except for the nearest measurement site called K2 station.

In addition to its position, the source is characterized by four other parameters:

- the **number of metal slabs** (one slab corresponds to a set of a welder, a cladder and the explosive powder) is variable between 1 and 8 slabs (see lower part of figure 5.4). When there is only one slab, the source can be assumed to be a point. When there is more than one slab, they are spatially separated by a few meters, usually in two columns. This makes the source more complex. However, most of the time, after a few hundred meters, the shock waves generated by the different slabs recombine due to non-linearities, which makes it acceptable to consider a single source, but with a spatial expansion.

- the **type of explosive** varies for each event. Indeed, explosives are mixtures of ANFO (ammonium nitrate fuel oil). There are 3 different blends denoted A, B or C, with different shock velocities. Each slab has one type of explosive. However, an explosion can have more than one slab, which means that it can have more that one type of explosive. The available data is the ANFO weight for each of the 3 types, which can be used to determine the percentages of types for each event. The breakdown of the explosive type is displayed at the upper-left of figure 5.4. Types A and B have a similar number of occurrences, while type C is by far the rarest.

- the **explosive charge** ranges between 300 and 500 kg TNT equivalent (one kg TNT equivalent is the energy related by the explosion of 1 kg of trinitrotoluene and is equal to 4.184 MJ). The charge is calculated knowing the yield and the weight of each of the slab types. When there are multiple slabs exploded simultaneously, the charge corresponds to the sum of the charges for each slab.

- the slabs can be **confined**. A confined slab is surrounded by water during the explosion, which reduces the effective charge of the explosion. This means that for

the same initial charge, the blast wave generated by explosion is less powerful if the slabs are confined. Most of the explosions are not confined (see figure 5.4, upper-right). Just under half of the explosions have all the slabs confined and 7 % have both confined and not confined slabs.

Thus, the blast waves are all different from one another due to the variability of the position of the source, the number of slabs, the type and the charge of the explosives and the confinement. All of these characteristics are known for each explosion.

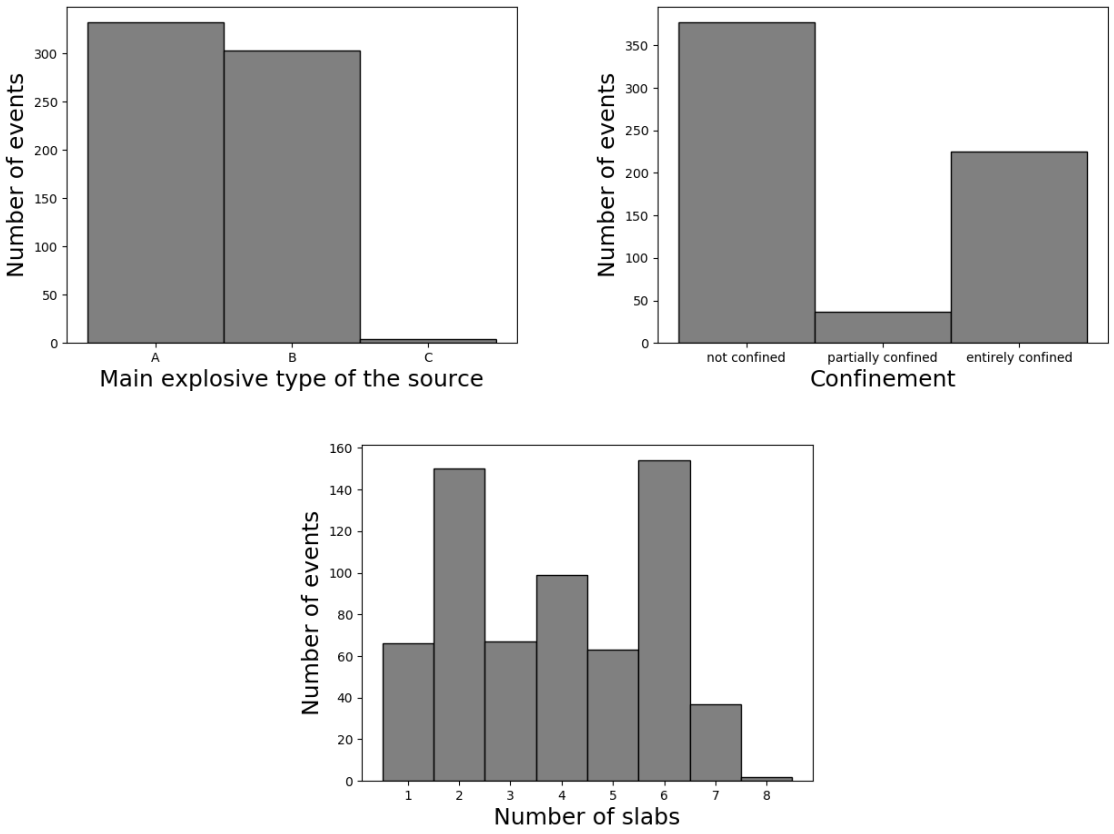

Figure 5.4: Classification of the events depending on the type of explosive (upper left), the confinement (upper right) and the number of slabs (down).

5.1.2 Topography

A map with elevation of the surrounding area is visible on figure 5.5. The surface altitude is given for x-values (Eastern direction) between −4 km and 21.5 km, and y-values (Northern direction) between −10 km and 5 km, with the source at the origin (figure 5.5). The data are available on a grid with a resolution of 25 m. Altitudes range between 0 and 556 m, and the source is at 276 m, in a local canyon. However, the measuring stations are located towards the south-east direction relative to the source, where altitudes range between 0 and 400 m. Note that after a short distance from the source, about 2 km, the altitude does not exceed 100 m.

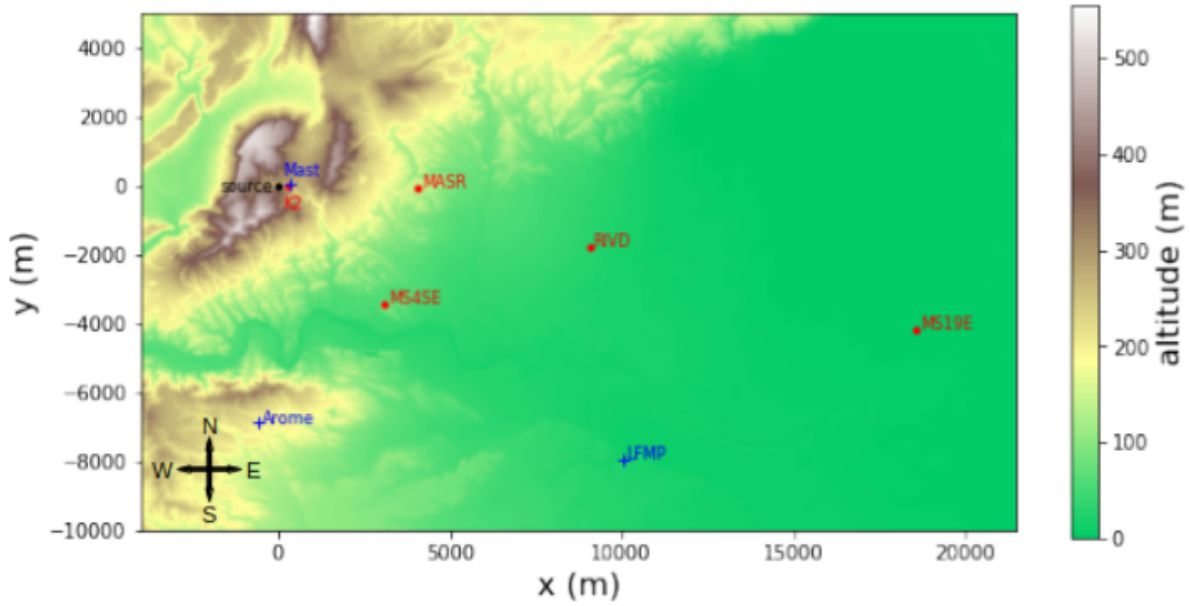

Figure 5.5: Altitude map of the site, with the source (black point), the meteorological mast near the source (blue cross), the measuring stations (red dots), the meteorological station LFMP (blue cross), and the position of the reference Arome meteorological profile (blue crosses).

5.1.3 Characteristics of the acoustical sensors

Blast waves are measured by microphones located at five different stations between 300 m and 20 km away from the source. The positions of these stations are indicated in figure 5.5 as red points. The positions of the source, the meteorological mast near the source, the meteorological station LFMP and the position of the reference meteorological profile Arome (see section 5.1.5) are also displayed. Stations are called K2 at 300 m away from the source, MASR at 4.3 km, MS4SE at 4.6 km, RIVD at 9.2 km and MS19E at 19 km. The K2, MASR, RIVD and MS19E stations are almost aligned in the ESE direction, which makes it easier to compare the signals, because a wave at one of these stations can be considered as having passed over the other stations closer to the source. This figure also shows the topography around the stations: there are hills and canyons around the source and station K2, then the terrain is much flatter.

At K2, the sensor is a Kistler 4043A, with a digitizer sampled at 2000 Hz. This sensor's response is almost linear between 0 and 2 Bar, allowing the measurement of the blast pressure at short range. For stations at larger distances, microphones developed by the CEA DAM are used.

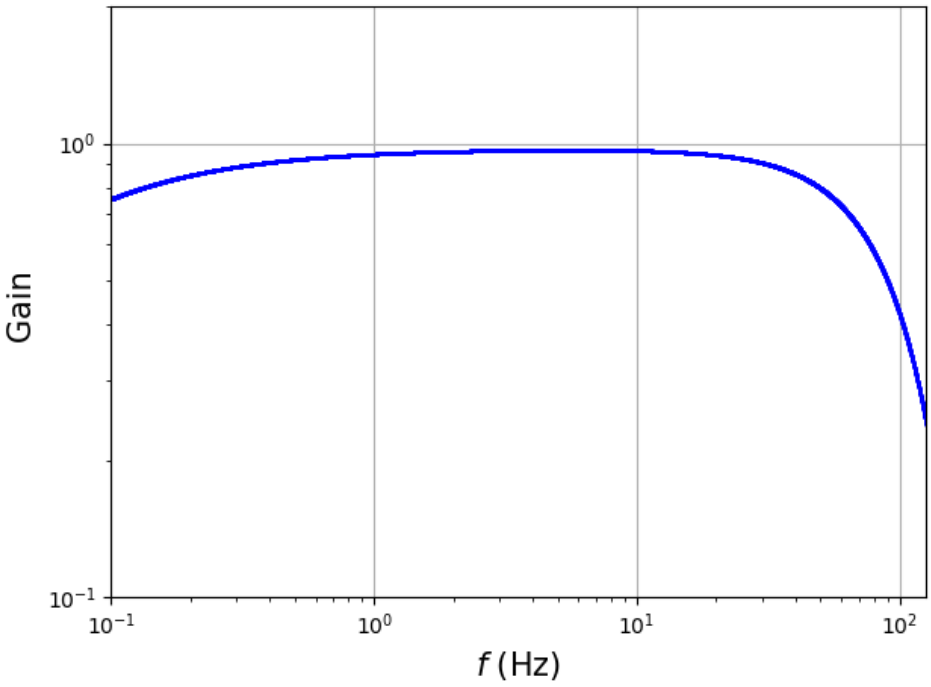

Figure 5.6: Frequential response of the sensors with the digitizer.

The frequency response of these sensors is given by the product of a cardinal sinus of order 3, due to the digitizer, and a second term, coming from the physical behavior of the microphone [53]:

$$H(\omega) = \frac{\sin\left(\frac{N\omega}{2f_{\text{mod}}}\right)^3}{N^3 \sin\left(\frac{\omega}{2f_{\text{mod}}}\right)^3} \times \frac{-3.54.10^{13}\ \omega}{\omega^4 - 4.72.10^5\ \omega^3 - 1.67.10^5\ \omega^2 - 3.63.10^{13}\ \omega - 6.66.10^{12}} \tag{5.1}$$

with $N = 1024$ and $f_{\text{mod}} = 256 \times 10^3\,\text{Hz}$ The frequency response (with digitizer) is plotted on figure 5.6 and turns out very flat. The cutoff frequency at $-3\,\text{dB}$ is 65.6 Hz. The sampling frequency is 250 Hz. Despite the calibration of sensors, the uncertainty of the amplitude is of $\pm 5\,\%$ between the sensors, and the absolute uncertainty is $\pm 10\,\%$.

The stations were not active during the whole duration of the experiment and therefore missed some explosions. Among a total of 639 events, 554 events were recorded by station K2, 584 by station MASR, 605 by station RIVD, 461 by station MS19E and 317 by station MS4SE. On figure 5.7 can be seen the recorded events for each station. In particular, MS4SE was not active after April 2017.

In this work, each event is labeled according to the time of the explosion: for example, the event corresponding to an explosion on October 5, 2016 at 8 am is named "2016-10-05 08h".

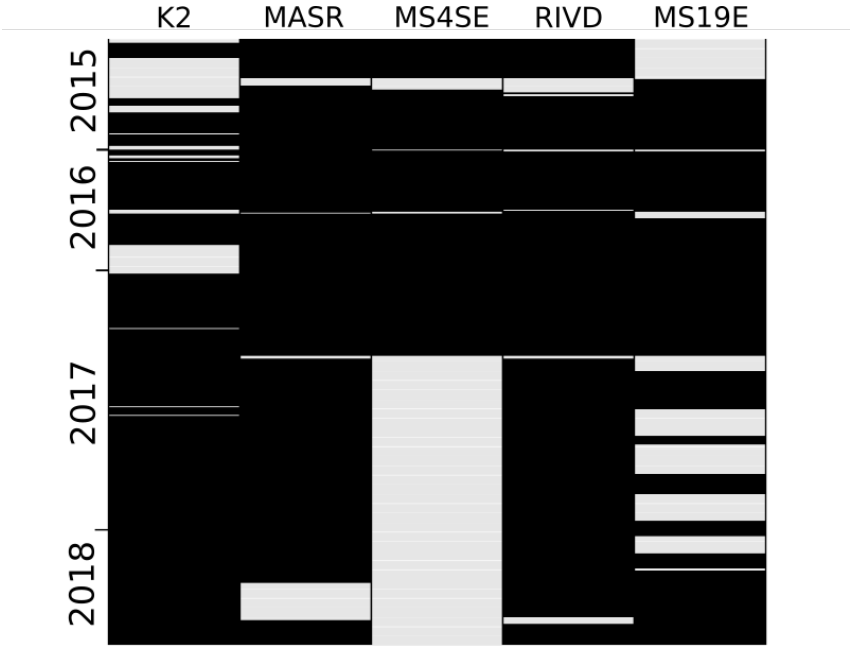

Figure 5.7: Recorded events for each station, Each line is associated with an event. The event is recorded if the box is dark.

5.1.4 Signatures at different stations

Eight different pressure waveforms measured at the four almost aligned stations are shown in figure 5.8. For each subfigure, the same color corresponds to the same explosion. Schematically, the amplitude of the signals decreases with distance: for the first peak, the maximum is around 4000 Pa for station K2. For other stations, the pressure is normalized by P_{ref}, with P_{ref} the maximal pressure measured at MASR station. In a first approximation, the shock wave can be considered to be spherical, with an amplitude decaying as the inverse of the distance. Despite the initial charge being the same, there is a lot of variability in the waveforms, and this variability increases with the distance. The waveforms at station K2 keep relatively close to one another and vary mostly in amplitude by a factor 2. On the opposite, many more differences than only amplitudes can be observed at the stations, for instance at the most distant one station MS19E. In addition, a single event can have a relatively high pressure at one station and a relatively low pressure at another one. For example, the orange signal "2018-03-09 09h" is one of the lowest at station K2, and the second highest at station MASR. On the contrary, the purple signal "2017-10-24 12h" is the second highest at station K2 and comparatively lower at station MASR. Other parameters being fixed, this variability is most likely attributed to the influence of the weather conditions.

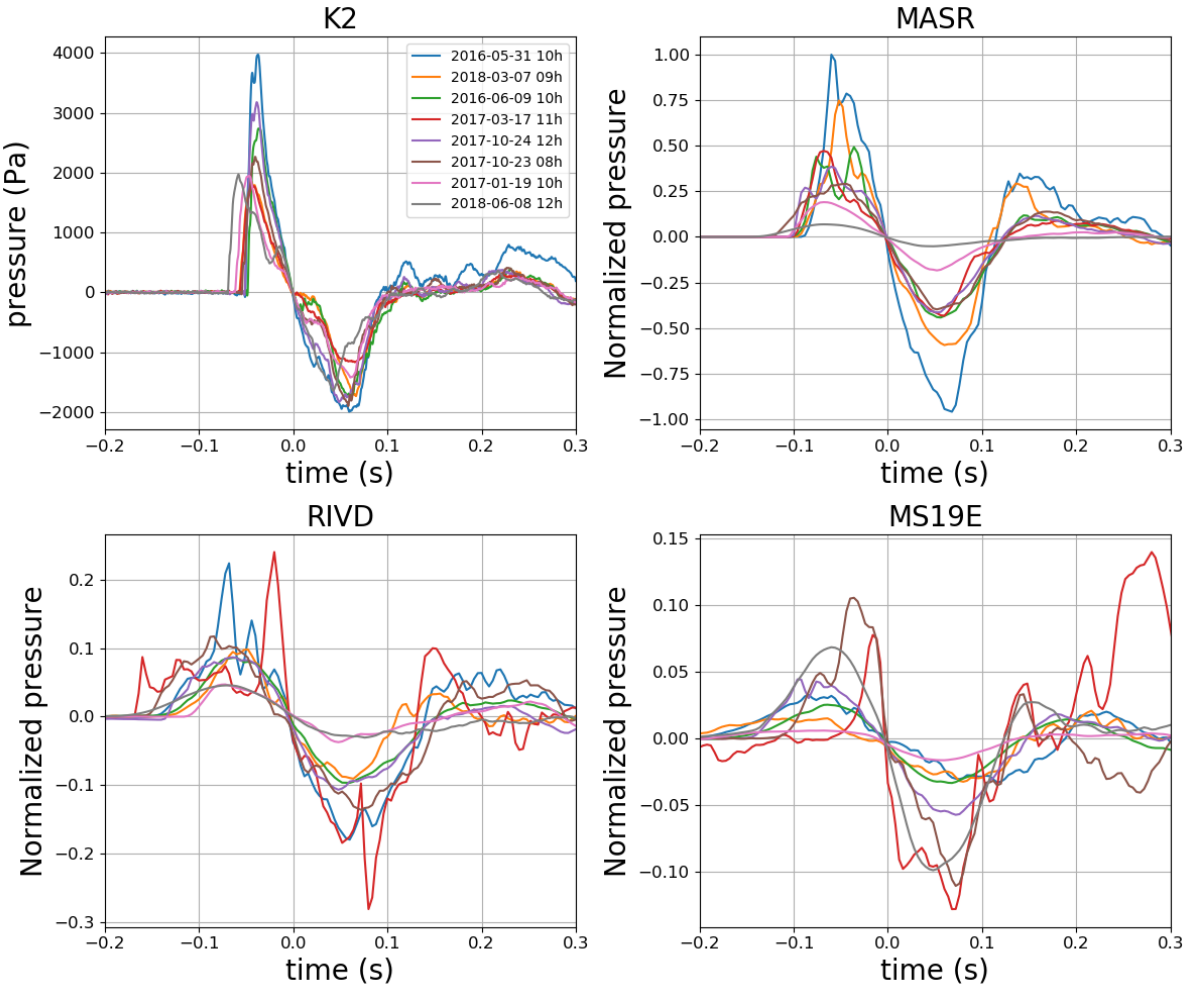

Figure 5.8: Various waveforms at stations K2 (absolute values), MASR, RIVD and MS19E (values relative to maximum at MASR). Each event is characterized by a single color indicated on the K2 subfigure.

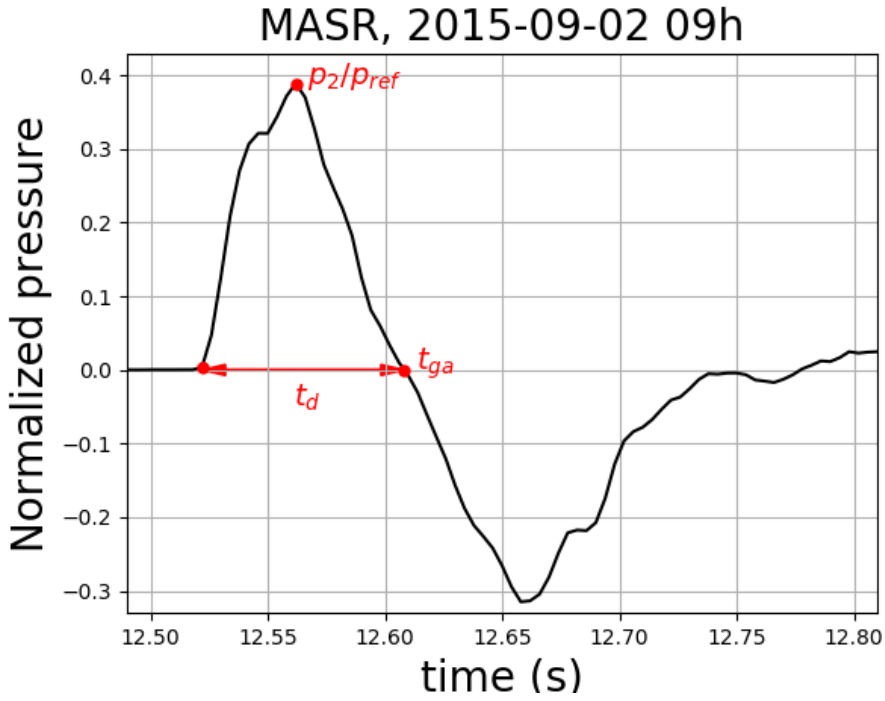

Figure 5.9: Main parameters of the measured signal

Nevertheless, some features are common to all of the waveforms and can be used to describe them. Figure 5.9 shows one measured waveform at the station MASR with the following main parameters:

- p_2 corresponds to the peak pressure,
- t_{ga} is the arrival time of the signal at the station. It is defined as the time when the signal crosses 0 after the first pressure peak. For the signal in figure 5.9, t_{ga} 12.6 s, which is consistent with the distance from the source (indeed, $12.6\,\text{s} \times 340\,\text{m}\,\text{s}^{-1} \approx 4.3\,\text{km}$, which corresponds to the position of station MASR). In what follows, in order to better compare the signals with one another, t_{ga} is set to 0,
- t_d is the duration of the positive phase. It is calculated by measuring the time between the first instant before the peak pressure p_2 for which the signal reaches 1 % of the peak ($0.01p_2$), and the arrival time t_{ga}.

5.1.5 Meteorological data

Measured data

During the experimental measurements, temperature, relative humidity, wind direction and wind speed near the ground were measured by two meteorological stations. The first one was close to the source. The measurements were carried out by a meteorological mast 2 m high. The data are averaged over a period of 6 min. The second is the meteorological station of the Perpignan-Rivesaltes airport and is referenced as "LFMP". This station records additionally the atmospheric pressure on the ground. Data are averaged over a

period of 30 min. Both stations are located in figure 5.5 (blue crosses with labels "source" and "LFMP").

Numerical data

In addition to the data from the meteorological stations, data from Météo France's local, high resolution atmospheric forecast model "Arome" are used [149]. The data were extracted at the point marked "Arome" in the figure 5.5. The variables are the same as for the meteorological stations, but are also computed at the altitude were the effective wind speed is maximal, between the ground and 3000 m.

Meteorological data are available for all events between 2015 and 2018 at the source. Only 526 events are available for LFMP and 481 for "Arome". There are 394 events for which the three meteorological data are available.

The wind speed and direction for each of these three "stations" are displayed in figure 5.10. The angle 0° measures the direction from which the wind is blowing, relative to the northern direction and clockwise. Therefore a 45° value corresponds to a wind blowing from North-East to South-West (see figure 5.12 for a schema). It can be seen that the angle values are rounded to the nearest multiple of 22.5° at the site, and to the nearest multiple of 10° at LFMP. It should be noted that higher wind speeds are measured at LFMP and Arome than at the source. The majority of the angles are either:

- between 90° and 180°, which corresponds to a humid north-westward wind coming from the Mediterranean sea (on the East of the site) locally known as "vent d'autan" or sea wind,
- or between 270° and 350°, which corresponds to a dry south-eastward offshore wind, locally known as "Tramontane".

Tramontane wind can be relatively strong and narrowly orientated because it is guided and accelerated in a zone of low altitude orientated in the SE/NW direction between two mountain ranges, Pyrénées in the South and Massif Central in the North.

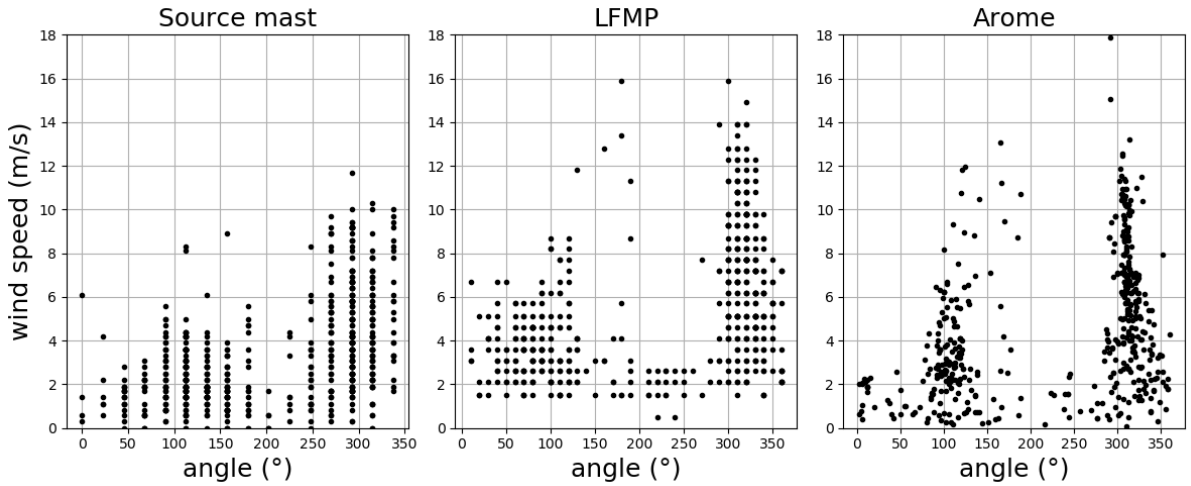

Figure 5.10: Wind speed as function of its direction, for the 3 different sources of meteorological data.

To deepen the meteorological study, and to be able to simulate the propagation in the atmosphere, more exhaustive "Arome" data are used. The meteorological data for 2774 dates and times calculated between 2015 and 2018 are available (hours can be from 7 a.m to 4 p.m, with a step of 1 h), at all the positions corresponding to the crosses in the figure 5.11. The days and times for these files are not necessarily the same as those for the shock events. The data are available at 15 altitudes between 0 and 17 km, including 9 between 0 and 4000 m and 5 between 0 and 1000 m. Available data include: density, eastward and northward wind, pressure, relative humidity, surface altitude and temperature.

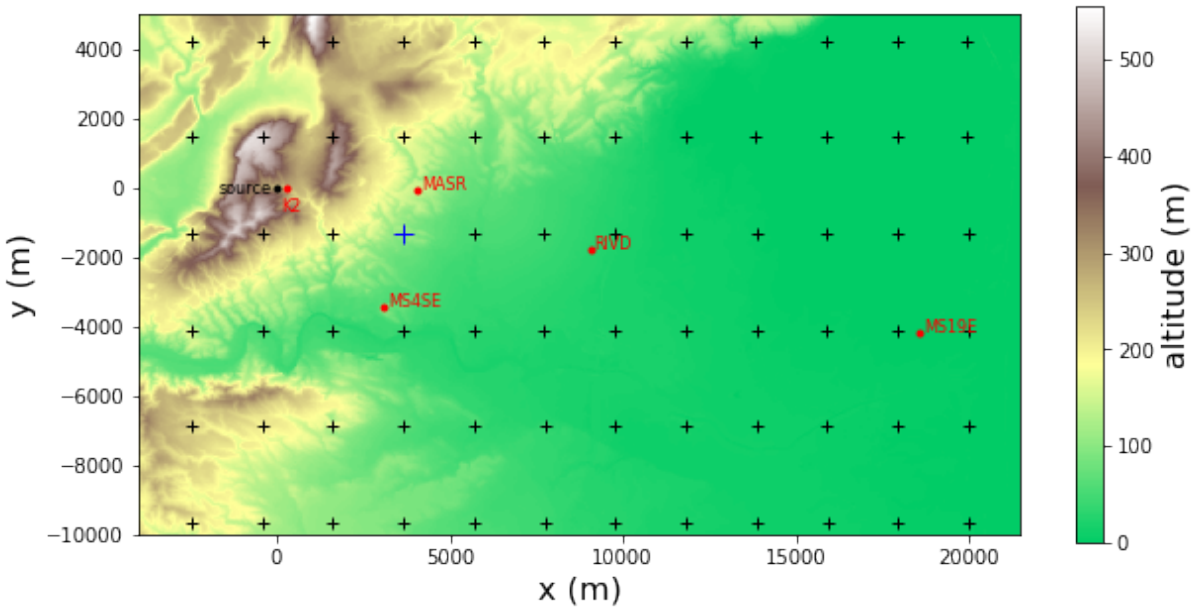

Figure 5.11: Locations where the Arome data are available.

At first order, propagation is mostly affected by the wind in the direction of sound propagation (source to station direction). This projected wind is extracted for each station from the eastward and northward components.

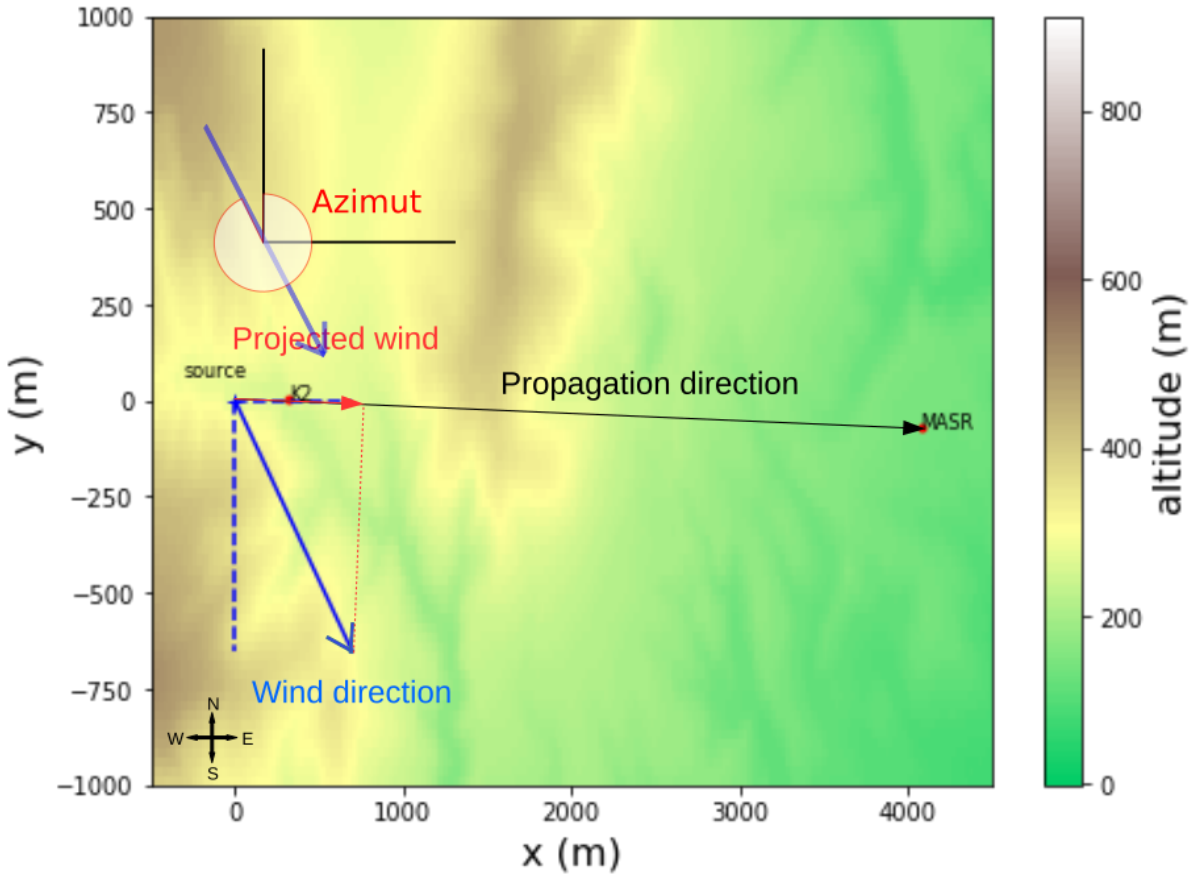

Figure 5.12: Schematic view of the positions of the source and MASR station, and the components of the wind.

Examples of temperature and projected wind speed profiles between the ground and 4 km of altitude obtained at the Arome point closest to the MASR station are displayed in figure 5.13. These profiles were extracted at different times and on different days, and are therefore very diverse. However, we can see that the projected wind speed is generally between -20 and $30\,\mathrm{m\,s^{-1}}$, while the temperature shows a relatively constant decay, in agreement with theoretical value of about $6.5\,\mathrm{K/km}$ for adiabatic atmosphere.

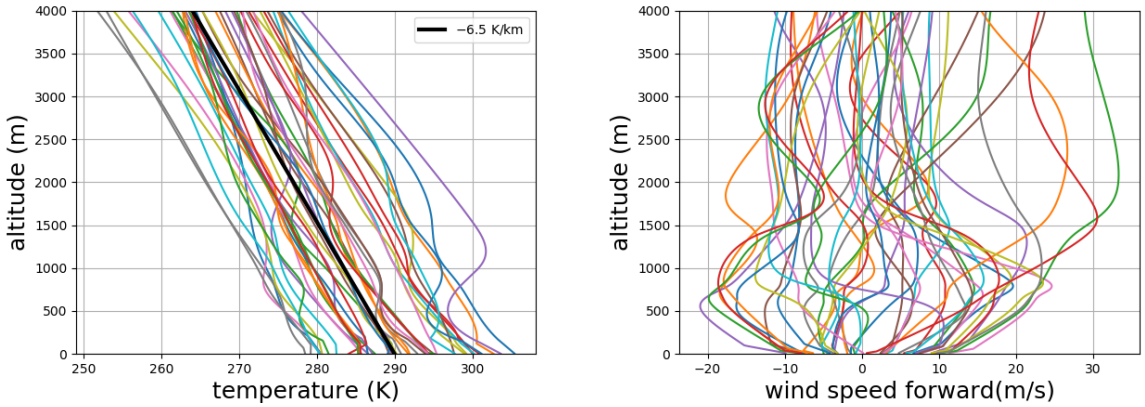

Figure 5.13: Temperature (left) and projected wind speed (right) vertical profiles at the station MASR for a selection of various dates.

These profiles come from 9 points calculated by Arome between 0 and 4000 m. Linear interpolation is performed between the first 2 points, and cubic Bézier curves are then used to interpolate the variables at other elevations. Other interpolation methods have been tried on this set of data, such as linear or polynomial interpolations, but Bézier curves give the smoothest profiles. Theoretically, the wind speed on the ground must be equal to 0, to respect the properties of the boundary layer. However, in our case, the wind speed between 0 and 10 m is chosen constant (equal to its value at 10 m) in order to avoid the problems caused by wind variations between 2 sampling points.

5.1.6 Conclusions

In conclusion, a database of more than 600 explosions events has been recorded. This database contains the properties of the source for all the explosions, as well as the meteorological data the days of the explosions. The acoustical signals at 5 measurement stations at different distances from the source are recorded. Available data are summarised in table 5.1.

data	source	639 explosions			
		explosive type: A, B or C	number of slabs: 0 to 8	charge: 300 to 500 kg eq. TNT	confinement
	topography	Surface altitude of the site near Rivesaltes with a precision of 25 m			
	station K2	554 waveforms			
	station MASR	584 waveforms			
	station MS4SE	317 waveforms			
	station RIVD	605 waveforms			
	station MS19E	461 waveforms			
	Mast	ground: wind speed, direction and temperature for 639 explosions			
	LFMP	ground: wind speed, direction and temperature for 526 explosions			
	Arome	ground: wind speed, direction and temperature for 481 explosions			
		Wind speed and temperature vertical profiles for 2774 dates and hours			

Table 5.1: Overview of the available data.

5.2 Analysis of the database

The previous section shows that several variables are required to describe the source, the meteorological data and the measured waveforms. These variables can vary significantly depending on the explosion. In this section, we propose to explore how these variables are distributed for the 639 explosions and to determine whether some patterns exist or not. With this in view, a clustering algorithm is used to perform unsupervised classification, first on the meteorological data, then on the source parameters and finally on the waveforms characteristics.

5.2.1 Unsupervised classification: clustering

Cluster analysis does not refer to a single algorithm, but to the general task of grouping data in groups, or clusters, in which data are more similar [129]. There are a multitude of clustering algorithms [104]. In this study, the agglomerative hierarchical clustering is chosen [118].

The dataset is a matrix of size $N_{\text{events}} \times N_{\text{variables}}$, and the variables are relative to the medium state or the source parameters. The agglomerative hierarchical clustering starts with each data corresponding to an event in a cluster. Then, at each step the two "closest" clusters are merged, until the chosen number of clusters is reached. To determine which clusters are the closest, a distance function is first needed. In this case, we choose the Euclidian distance d between two points a and b of the dataset: $dist(a,b) = \sqrt{\sum_{i=1}^{N_{var}} (a_i - b_i)^2}$. Then, a "linkage" criterion is chosen, to determine how close the clusters are. Here, the "ward" "linkage" is chosen, which means that the closest clusters are the ones with the smallest combined variance, with the variance of a cluster defined by $\sum_{a \in Cluster} dist(a, \bar{a})^2$, with $\bar{a}$ the mean of the cluster.

With this method, a number of clusters has to be chosen before the computation. Different methods exist for choosing an optimal number of clusters, but there is no consensus on which is the best. Two of the main ones are the ward method and the average silhouette method.

The ward method tries to minimize the variance within the cluster. This method uses the hierarchical clustering dendrogram (see figure 5.19). It consists in finding the greatest vertical distance which is not crossed by a horizontal line. Then a horizontal line is drawn at the bottom of the vertical line, and we count the number of clusters crossed by this line. This is the optimal number given by the ward method.

The average silhouette method measures the quality of the clustering. For a given number of clusters K, the silhouette coefficient is calculated with the equation $\frac{ba}{max(b,a)}$ with a the average distance between an event and all the other points in the same cluster, and b the average distance between an event and all other points in the next nearest cluster. The average of the silhouette coefficient for all the events is then calculated and the average silhouette coefficient is thus obtained for K clusters. This average coefficient is then calculated for different K and the average score of the silhouette as a function of the number of clusters is plotted (see on the right of the figure 5.14). The highest value of the score corresponds to the optimal number of clusters given by the method of the average silhouette.

Classification of the wind conditions on the ground

In this section, we are looking for patterns in the wind conditions obtained at the ground.

The dataset is made of 394 events (the events when all meteorological data are available) with 6 variables :

- The eastward wind speed at the Mast meteorological station,
- The northward wind speed at the Mast meteorological station,
- The eastward wind speed at the LFMP meteorological station,
- The northward wind speed at the LFMP meteorological station,
- The eastward wind speed at the Arome meteorological position,
- The northward wind speed at the Arome meteorological position.

The ward method gives an optimal number of 3 clusters, and the silhouette method gives low scores, and an optimal number of 2 clusters, the minimum allowed value of this method, as seen in the figure 5.14 .

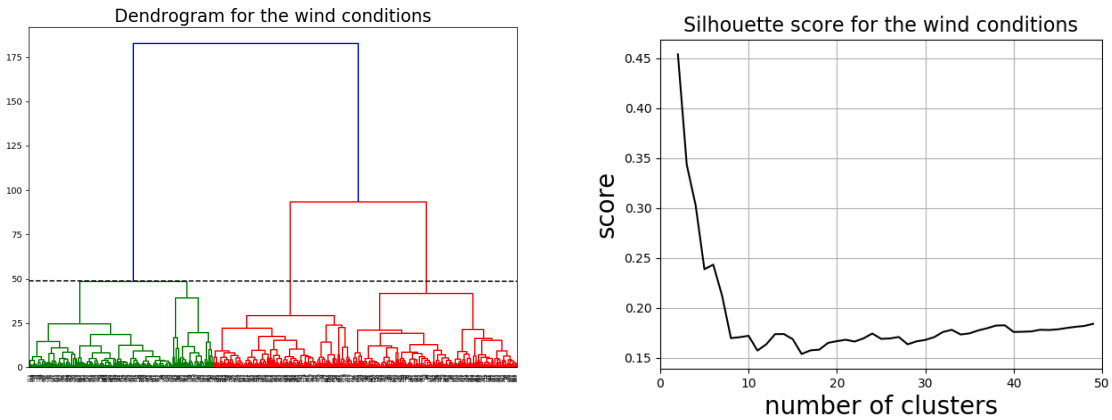

Figure 5.14: Dendrogram (left) and silhouette score (right) for the clustering with the wind conditions.

Thus, a number of 3 clusters is chosen. They can be seen in the figure 5.15. The blue cluster (149 events) clearly corresponds to the sea wind conditions, the green cluster (132 events) to the Tramontane weak wind conditions (typically less than 6 m/s) and the red cluster (113 events) to the Tramontane strong wind conditions (typically more than 6 m/s). As these three categories are clearly related to well identified meteorological conditions regarding ground wind speeds, they are retained in what follows.

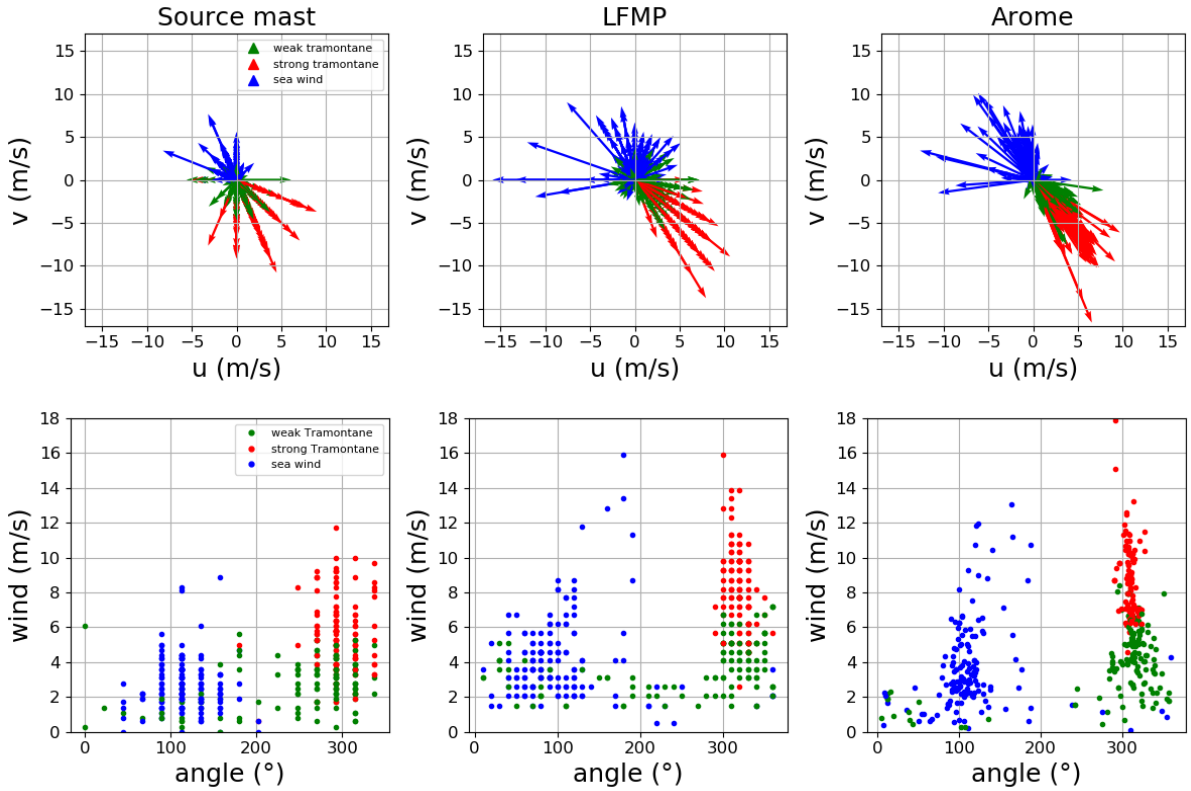

Figure 5.15: Clustering for the wind: Eastward wind in function of Northward wind for the 3 stations (top) and wind speed in function of its backward direction for the 3 sources of meteorological data (down).

Clustering of the meteorological profiles

In this section, the objective is to determine how the temperature and wind profiles are distributed.

The meteorological properties are taken from the Arome dataset. As a reminder, 2774 Arome profiles are available, corresponding to different dates and times between 2015 and 2018. However, all these profiles do not necessarily correspond to an explosion event, and conversely, all explosions do not have a corresponding "Arome" profile. However, these profiles provide a good overview of the weather conditions at the Rivesaltes site over the four years.

In the previous section, a clustering study on the wind condition at the ground was realized, and 3 groups were identified. Our first objective is to see if these 3 groups are still observed if the clustering is performed on the wind stratification. The chosen dataset corresponds to the profiles of the forward wind speed, *e.g.* the wind speed projected in the axis between the source and the station MASR, at the measurement point closest to the station, for the 2774 "Arome" profiles. Only the wind speeds between 0 and 1000 m are used for the clustering study, because a propagation over a distance of 4 km (from the source to MASR station) is mainly affected by the first km above the ground. Because only a few points are available for each stratification (4 or 5 between 0 and 1000 m), and because the altitudes of the points are not necessarily the same between the different "Arome" profiles, a linear interpolation is done between 0 and 1000 m, and 250 points

equally distributed between 0 and 1000 m are thus obtained for each stratification. The dataset is therefore constituted of these 250×2 points, for each of the 2774 "Arome" profiles.

The agglomerative hierarchical clustering method is then applied on the data, and the ward method gives an optimal number of 3 clusters, while the silhouette method gives low scores with a maximum for the lowest number of clusters (see figure 5.16). Thus, an optimal number of 3 clusters is chosen.

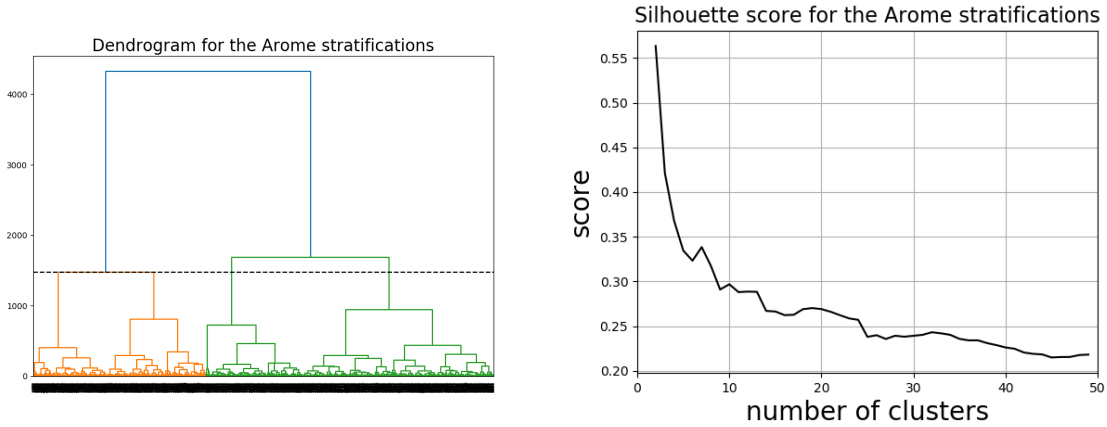

Figure 5.16: Dendrogram (left) and silhouette score (right) for the clustering with the Arome stratification data.

The 2774 profiles of the forward wind speed are shown on figure 5.17, with the color depending of the group. The groups are named according to the strength and direction of the wind. Here, the forward wind speed of the "upwind" group (in blue) corresponds well with the previous "sea wind" group: for this group the propagation will be almost entirely with a negative projected wind speed. Both temperature and wind profiles are expected to create upward refracting propagation conditions. The "strong downwind" group (in red) corresponds well with the "strong Tramontane" group: in this case we can expect propagation conditions favorable to downward refraction with a relatively strong forward wind values (mostly in the range 5 to 20 m/s) increasing with altitude. Finally the "weak wind" group (in green) has some similarities with the "weak Tramontane" group, with small projected wind values and a global trend towards positive values. However, it also includes part of the weak sea wind group. In this group, no clear trend between upward or downward refraction conditions can be *a priori* expected. Overall, the previous 3 groups are recognized.

The vertical profiles of the forward wind speed are shown separately for these 3 groups on the first line of figure 5.18. There are 581 profiles in the "upwind" group, 1035 in the "strong downwind" group and 1144 in the "weak wind" group. The temperature profiles are shown on the second row of figure 5.18. There is much less variability, as all profiles tend to show a linear decrease close to the adiabatic value. Only ground temperature varies between 275 K and 310 K. However, no temperature below 280 K is present for the "upwind" case because of warming effect provided by sea wind coming from Mediterranean sea, even in winter. Note however some cases of temperature inversion above the ground can be observed, especially in the weak ad upwind clusters.

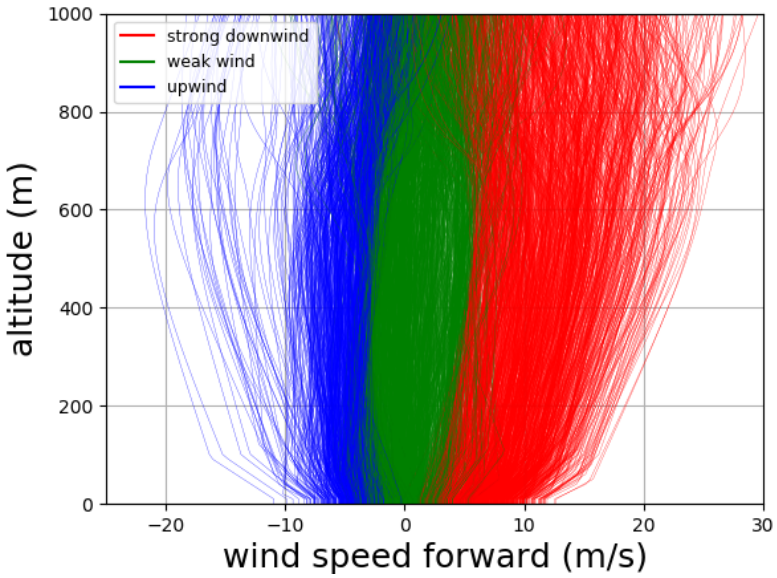

Figure 5.17: Altitude as function of the forward wind speed at Arome point closest to MASR station, with the three clusters identified by their color.

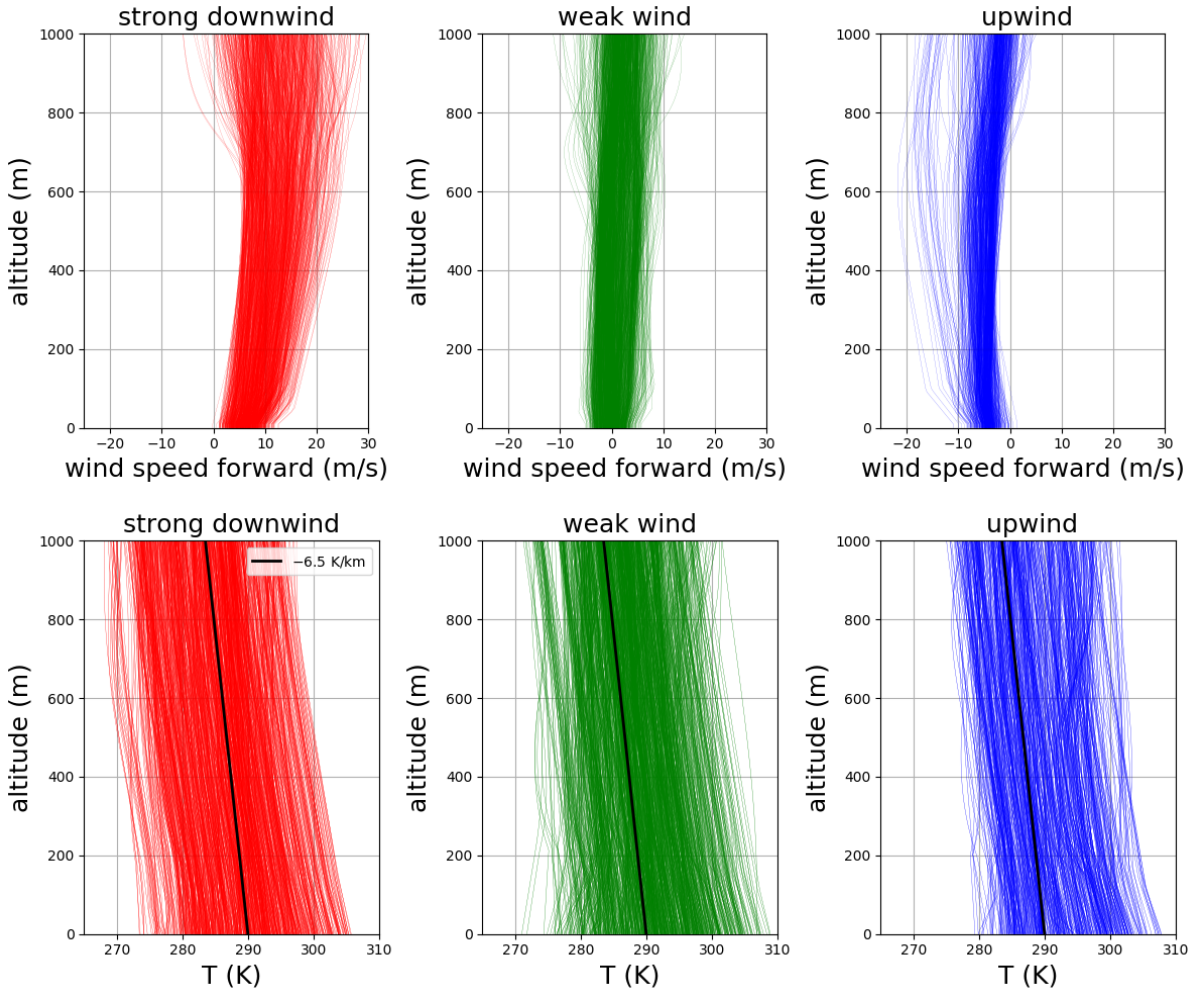

Figure 5.18: Altitude as function of forward wind speed (first line) and temperature (second line) at Arome point closest to MASR station, for the "strong downwind" (left column), "weak wind" (middle column), and "upwind" (right column) groups.

Classification of the source

As stated previously, there are four main parameters describing the source:

- the number of slabs,
- the type of explosives,
- the explosive charge,
- the confinement of the source.

For a given explosion, all these parameters can be different from one another. The question here is to explore how these parameters are distributed and whether we can define some "standard" explosion.

The dataset is made of 639 events with 5 variables:

- the percentage of type A explosive,

- the percentage of type B explosive,
- the percentage of slabs with confinement,
- the charge of the explosive W in kg equivalent TNT,
- the number of slabs.

These variables are normalized and reduced so as to have the same variance in the clustering method. The ward method and the average silhouette method both give an optimal number of 4 clusters (5.19). The four clusters have different numbers of events: the first one has 311 events and the fourth one 217 events. In comparison, the third one has only 76 events and the second one merely 35 events.

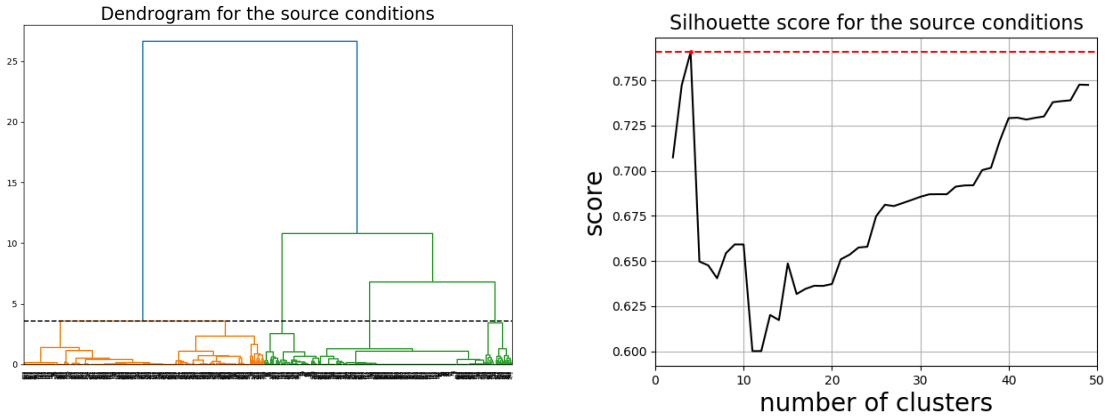

Figure 5.19: Dendrogram (left) and silhouette score (right) for the clustering with the source conditions.

The T-distributed Stochastic Neighbor Embedding (T-SNE) method is used to display the results [129]. This is a statistical method for visualizing high-dimensional data by giving each datapoint a location in a two- or three-dimensional map. Specifically, it models each high dimensional datapoint by a two or three dimensional point in a way such that similar datapoints are represented with high probability by nearby points, while dissimilar ones are represented by distant points. Here, the data are plotted using T-SNE in two dimensions (figures 5.20 and 5.21). Clusters are identified in the figure 5.20 in the T-SNE projection. Each of the five variables are plotted in color in the same projection in figure 5.21: the correspondence between figures allows to identify the main characteristics of each cluster. The first cluster greatly corresponds to a percentage of type A above 90 %. Similarly, the third and the fourth cluster corresponds to a percentage of B above 90 %. Finally, the second cluster corresponds to percentages of A and B between 10 % and 90 %. The distribution of the confinement shows that the first and third clusters are not confined, the fourth cluster is confined and the third cluster is partially confined. The first cluster has between 1 and 6 slabs, the fourth between 4 and 8, the third between 1 and 5 and the second between 3 and 7. Finally, the charge does not seem to have an influence on the clusters.

Number	Events	A percentage	B percentage	Confinement	Slabs	Charge	Name
1	311	$A > 90\,\%$	$B < 10\,\%$	no	1 to 6	no particular group	"A"
2	35	$10\,\% < A < 90\,\%$	$10\,\% < B < 90\,\%$	partial	3 to 7	no particular group	"Partial conf"
3	76	$A < 10\,\%$	$B > 90\,\%$	no	1 to 5	no particular group	"B"
4	217	$A < 10\,\%$	$B > 90\,\%$	yes	4 to 8	above 490 kg eq TNT	"Bconf"

Table 5.2: Characteristics of the different clusters.

This analysis shows that there exists mainly 4 patterns (see Table 5.2). Among them, two patterns are dominant:

- explosions of type A without confinement ($\approx 50\,\%$ of the explosions)
- explosions of type B with confinement and a charge above 490 kg ($\approx 33\,\%$ of the explosions)

The cluster of explosions of type A with no confinement is referenced as "A", the one of explosions of type B with confinement as "Bconf", the one of explosions of type B without confinement as "B", and the last one as "Partially conf".

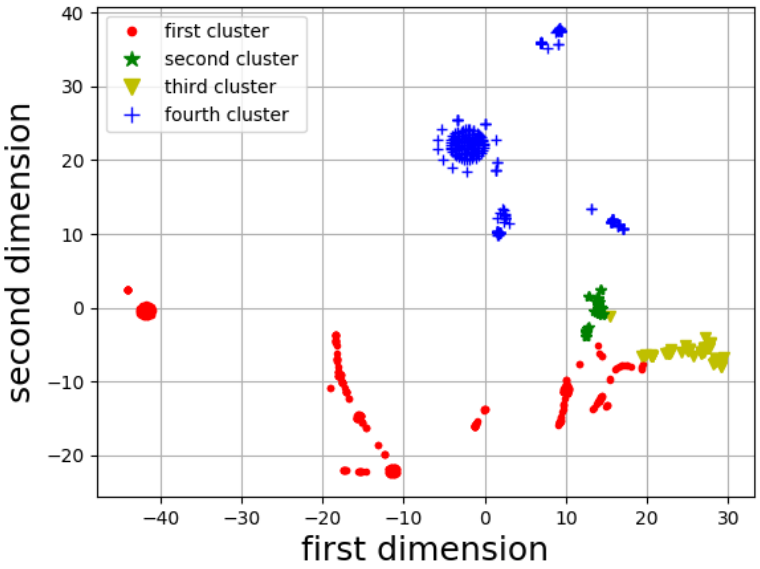

Figure 5.20: Clustering at the source. The second variable obtained by the T-SNE method is plotted as function of the first variable. The colors and markers corresponds to the cluster number.

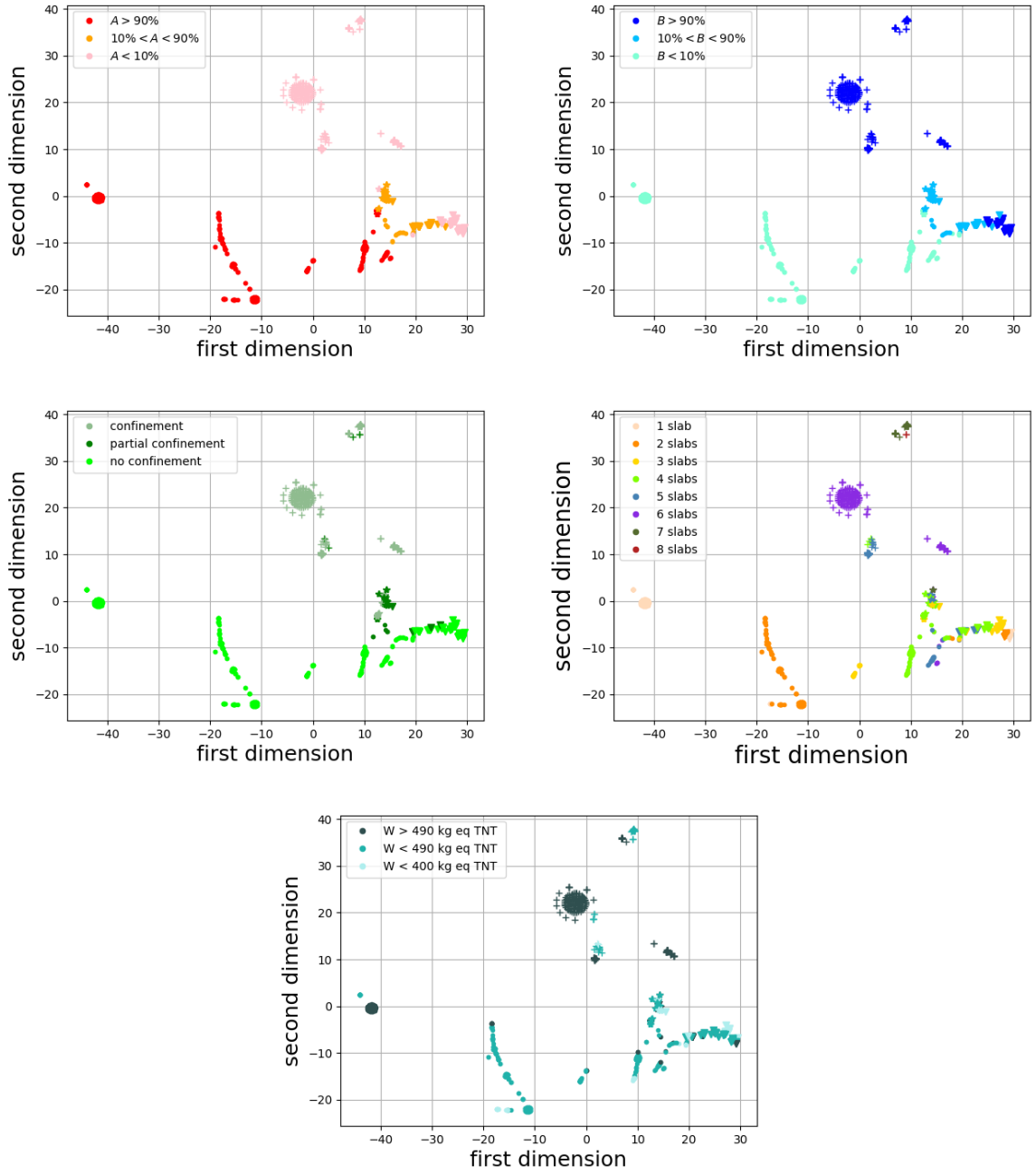

Figure 5.21: Source parameters in the T-NSE projection with the clusters as markers (see figure 5.20). The percentage of type A explosive is shown in the upper left, the percentage of type B explosive in the upper right, the confinement in the middle left, the number of slabs in the middle right, and the charge is shown in the lower figure.

Previous paragraphs thus showed that the wind conditions can be classified into 3 categories and the source parameters into 4 categories.

5.2.2 Influence of meteorology and source parameters on the waveforms at the closest station.

The objective here is to see the effects of the meteorological conditions and of the source parameters on the waveforms at station K2 close to the explosion, using the clusters found in the previous sections.

On the left of figure 5.22 are plotted waveforms for different wind speed forward measured at K2 for different events, with only 1 slab at the source and an initial effective charge of 500 kg equivalent TNT, the explosive type A and without confinement (cluster "A", Table 5.2). It is observed that the measured waveforms are close to one another, even though their peak overpressures p_2 vary of about 25 %. This variations can be explained by the effect of the wind: the left of figure 5.22 shows that there is a correlation between the increase of the peak pressure and the amplitude of the wind speed forward, with large positive wind speeds favorable to downward refracting conditions and therefore to higher amplitudes. Let us recall however that station K2 is only 300 m from the site, and propagation is expected to be highly nonlinear over this short distance.

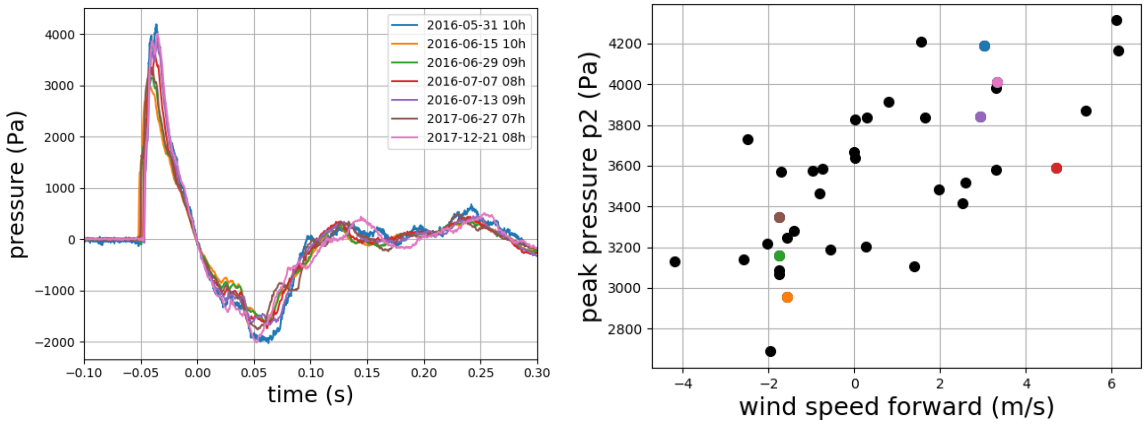

Figure 5.22: Waveforms at station K2 for different events with a charge of 500 kg equivalent TNT, without confinement, 1 slab at the source and the explosive type A (left). Peak overpressure p_2 in function of the wind speed forward measured at the source mast for all waveforms with the same source parameters (right). Colored points correspond to left waveforms of the same color, black ones to other waveforms not shown on the left subfigure.

Figure 5.23 shows the effects of the different source parameters. At the top left of the figure, the effect of the number of slabs is studied: all the waveforms correspond to the same type of explosive, to the no confinement case, and to a charge between 490 and 500 kg equivalent TNT. Only the number of slabs varies. The differences between the waveforms are greater compared to the one slab case: the number of slabs strongly influences the shape of the waveform because of the spatial distribution induced at the source. The source cannot be seen as punctual anymore and the signal results from different contributions. The nonlinear effects tend to merge the various shocks (except for the 2 slabs case). Moreover, there is no clear direct relationship between the maximum pressure and the number of slabs. At the top right of figure 5.23, the effect of confinement

is illustrated. All waveforms have a charge between 490 and 500 kg equivalent TNT and type B explosive. Note that the number of slabs is not constant because the database does not contain comparable configurations with and without confinement. As expected, waveforms with a confined source have a lower peak pressure. Finally, the lower part of figure 5.23 shows the effect of the charge. All waveforms are of type A, without confinement and with only 1 slab. For 3 different charges, the waveforms with the maximum and minimum peak pressure are plotted. We see that the pressure peak increases with the initial charge.

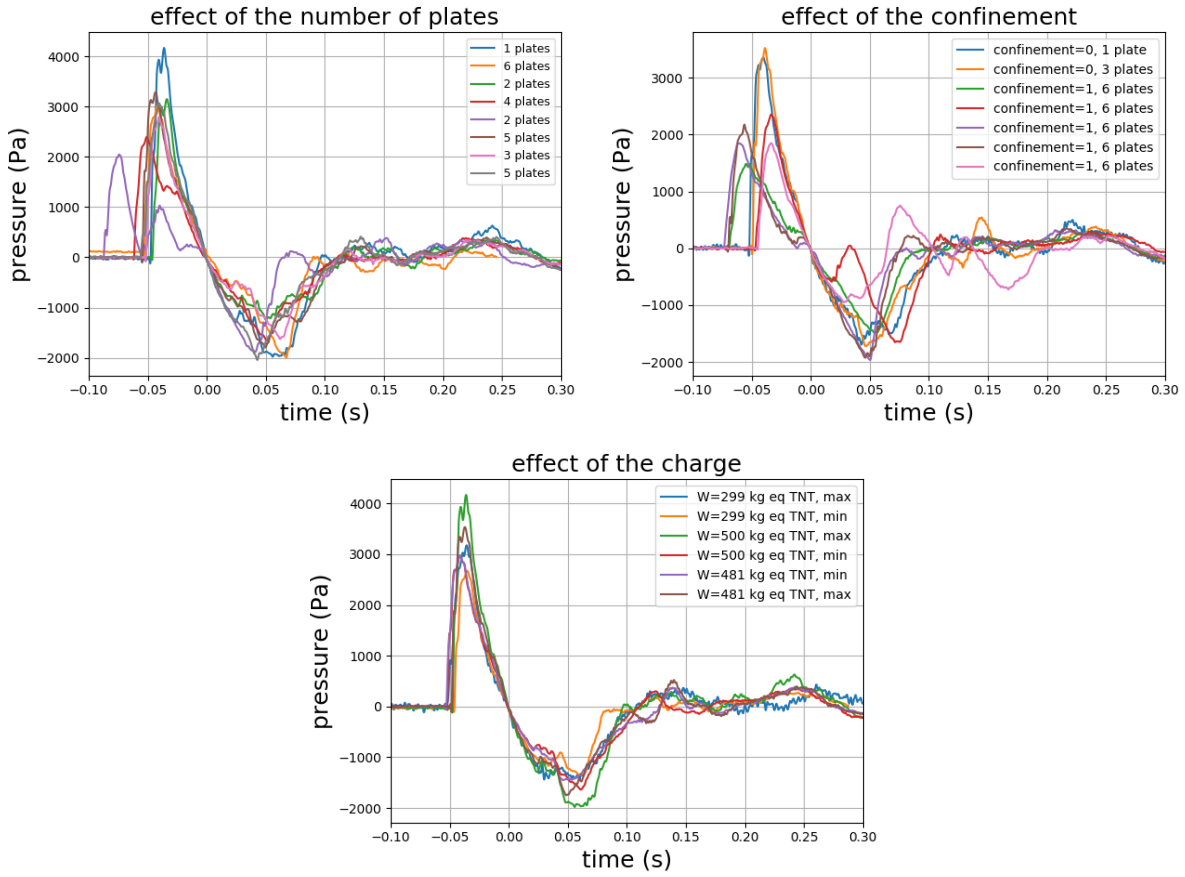

Figure 5.23: Waveforms at K2 for different events with a charge between 490 and 500 kg equivalent TNT, the explosive type A and a variable number of slabs at the source (upper left). Waveforms with the explosive type B, a charge between 490 and 500 kg equivalent TNT with and without confinement (upper right). Waveforms with one slab, without confinement, with the explosive type A and varying charges (down).

The waveforms for the different clusters formed with the source parameters are then plotted on figure 5.24, each figure corresponding to one cluster. For the "A" and "B" clusters, the peak pressure varies between around 2000 and 4000 Pa, and the shape of the waveforms are relatively close between these two clusters. The clusters "partially conf" and "Bconf" have lower peak pressures, between 1500 Pa and 3000 Pa, as already seen on figure 5.23. However, there are still large variations within each cluster.

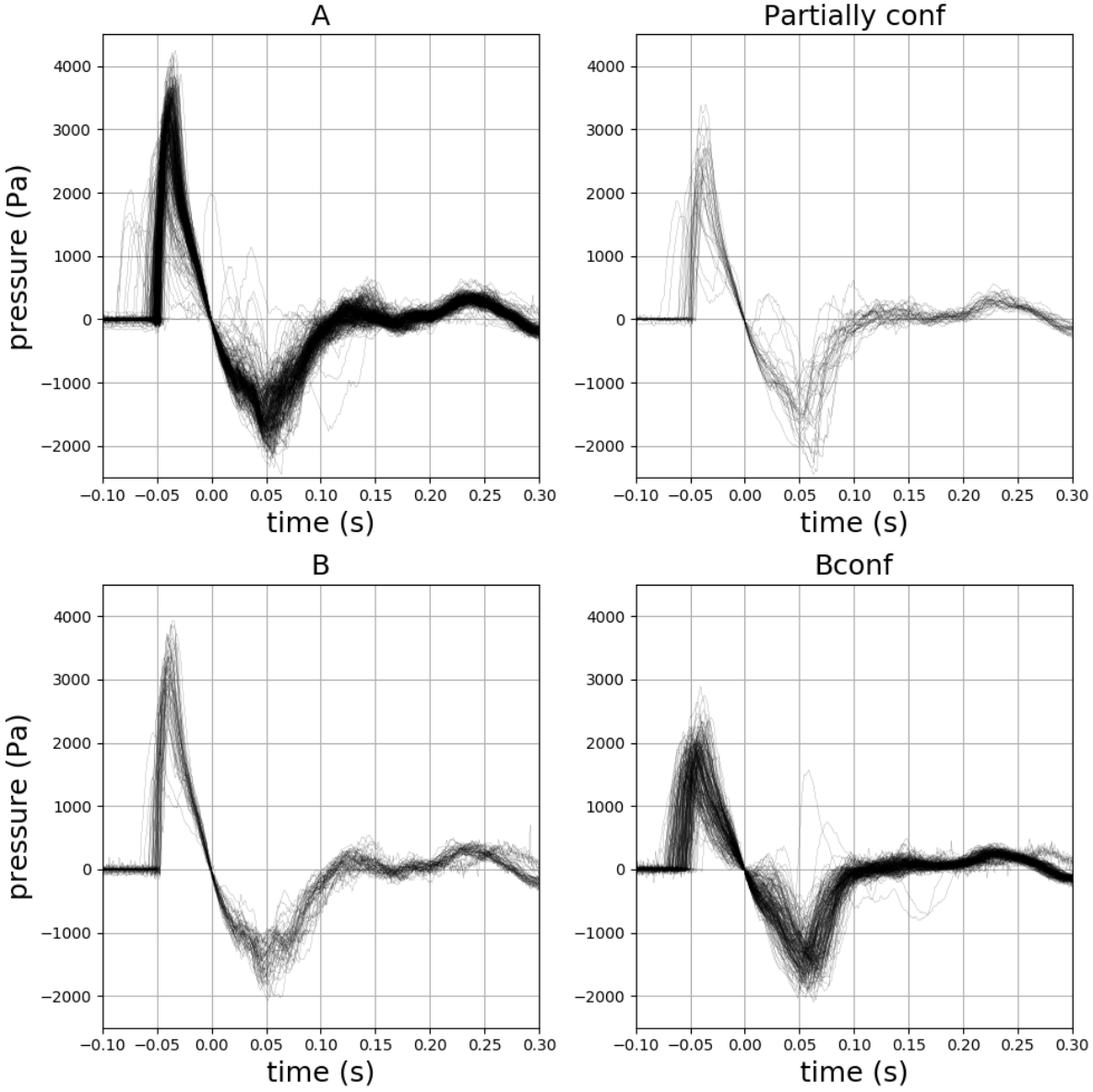

Figure 5.24: Waveforms at station K2 for the different clusters.

Finally, the influence of the source parameters on the peak pressure p_2 and the waveform positive phase duration t_d is examined.

First, on the left of the figure 5.25, the peak pressure p_2 is plotted as function of the positive phase duration t_d, the coloring depending on the source cluster. We observe that groups "A" and "B" are mixed, but are separated from group "Bconf" on the y-axis. "Partial conf" is between groups "A" and "Bconf". This also is due to the fact that the equivalent charge W_{eq} is lower when the source is confined, which is the case for "Bconf", and therefore the peak pressure is lower (see on the right of the figure 5.25).

Indeed, the equivalent charge takes into account the initial charge W, the presence of the ground (factor 2 for reflection on a rigid ground) and the possible confinement of the slab [52]:

$$W_{eq} = 2 \times W \times (1 - 0.4 \times (\mathrm{nb}_{\text{confined slabs}}/\mathrm{nb}_{\text{slabs}})) \tag{5.2}$$

It is also observed on the right of figure 5.25 that for a fixed equivalent charge W_{eq}, the peak pressure can be quite variable: the pressures vary between 1200 and 3000 Pa for 300 kg equivalent TNT, and between 1600 and 4300 Pa for 500 kg equivalent TNT. The pressure can therefore be more than doubled, almost tripled for the same equivalent charge. This is mainly caused by the type of explosive and the number of slabs (the confinement is already taken into account empirically in W_{eq}). In conclusion, there is still a lot of variations inside each cluster: the clustering is not sufficient to efficiently characterize the signals.

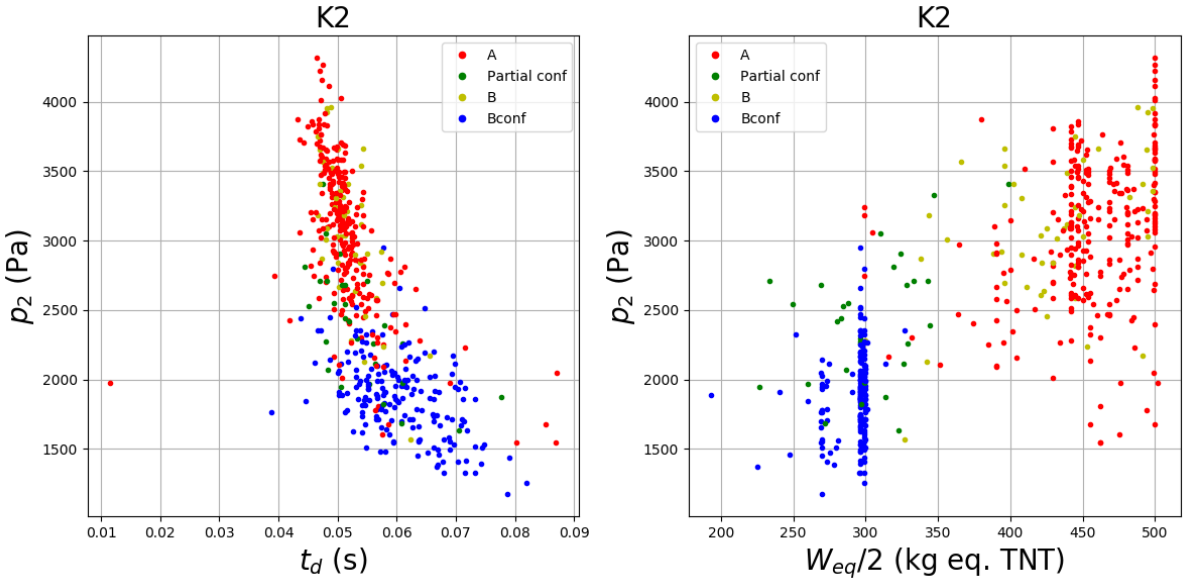

Figure 5.25: Peak overpressure p_2 at station K2 as function of the positive phase duration t_d (left) and of the equivalent charge W_{eq} (right).

5.2.3 Effects on the peak overpressure and positive phase duration

Now we will examine the effect of the characteristics of the wind on the peak pressure p_2 and on the positive phase duration t_d of the waveforms at different stations. Wind is expected to significantly affect the signal along the propagation, increasingly with distance. For comparison with the case of a point explosion in a homogeneous, quiescent atmosphere, we introduce the dimensionless pressure $p_{\text{scaled}} = \frac{p_2 R}{P_0 R_0}$, where R is the propagation distance, P_0 is the atmospheric pressure and $R_0 = (E_{eq}/P_0)^{1/3}$ is the charge equivalent radius (where $E_{\text{eq}} = 4.184 \times 10^6\, W_{\text{eq}}$ the equivalent energy of the explosion in Joule). In a similar way, the positive phase duration t_d is scaled by $t_{\text{scaled}} = \frac{t_d c_{\text{eff}}}{R_0}$ with c_{eff} the effective sound speed.

These two quantities are plotted versus the wind speed forward at the mast, at each of the five stations (figure 5.26). Table contains the mean, the standard deviation and the skewness for the 5 stations, for the three meteorological groups. At K2 station, we

observe that the effect of the wind is weak on p_2 and t_d, because the mean and the standard deviation of the normalized pressure and the positive phase duration stays very close when the wind speed forward increases. This makes sense, because station K2 is very close to the source and wind is expected to have little influence compared to source variability. There is only a light increase with the wind speed.

For the other stations, the peak overpressure can also be normalized by the peak overpressure at station K2, as shown on figure 5.27. This allows us to check whether the pressure variations at these different stations are mainly due the source or to the wind. However, the variability in figure 5.27 is very comparable to the one of p_{scaled} figure 5.26, which shows that the main cause of variability is not due to the source but to propagation.

The wind effect is greater at MASR and MS4SE stations. For wind speed forward between $-7.5\,\mathrm{m\,s^{-1}}$ and $0\,\mathrm{m\,s^{-1}}$ (blue points), the pressure tends to increase with the speed of wind. However, when the wind speed is positive, there is no longer any clear effect. For the positive phase duration t_d, the wind has no great effect on the average value, but it affects the range of variation: the standard deviation is significantly lower for the weak tramontane group. This shows that when the absolute value of the wind speed is small, the variations of t_d are small too.

At RIVD and MS19E stations, the relation between the wind parameters and the signal properties seems more complex. One explanation is that this effect is range dependent, and until now we have considered that the wind speed is the same along the propagation with its value measured at one station, which may be far from the other stations. This means that there is greater uncertainty about the wind conditions than for closer stations. Another possibility is that a single measurement of ground wind speed and direction cannot effectively describe the complexity of weather effects. When the station is further away, the upper wind can be very different from the wind on the ground, and its cumulative effect can be stronger than for the closer stations.

		sea wind			weak tramontane			strong tramontane		
		mean	std	skew	mean	std	skew	mean	std	skew
K2	p_2	0.235	0.051	-0.136	0.253	0.053	0.118	0.270	0.057	-0.149
	t_d	0.604	0.114	0.982	0.594	0.113	0.732	0.582	0.113	0.315
MASR	p_2	0.052	0.026	2.30	0.081	0.028	1.43	0.086	0.029	0.980
	t_d	1.28	0.238	1.67	1.12	0.146	0.397	1.22	0.193	0.261
MS4SE	p_2	0.042	0.030	5.04	0.061	0.016	1.288	0.057	0.021	1.79
	t_d	1.44	0.56	5.05	1.24	0.128	0.710	1.44	0.258	0.723
RIVD	p_2	0.050	0.065	3.19	0.056	0.032	2.44	0.054	0.024	1.16
	t_d	1.31	0.269	0.253	1.28	0.170	0.383	1.42	0.283	0.566
MS19E	p_2	0.090	0.084	1.49	0.060	0.068	2.72	0.051	0.057	4.95
	t_d	1.29	0.405	0.973	1.33	0.306	0.617	1.48	0.320	0.394

Table 5.3: Mean, standard deviation and skewness for the normalized peak pressures and positive phase durations for the sea wind, weak tramontane and strong tramontane groups, at the 5 stations.

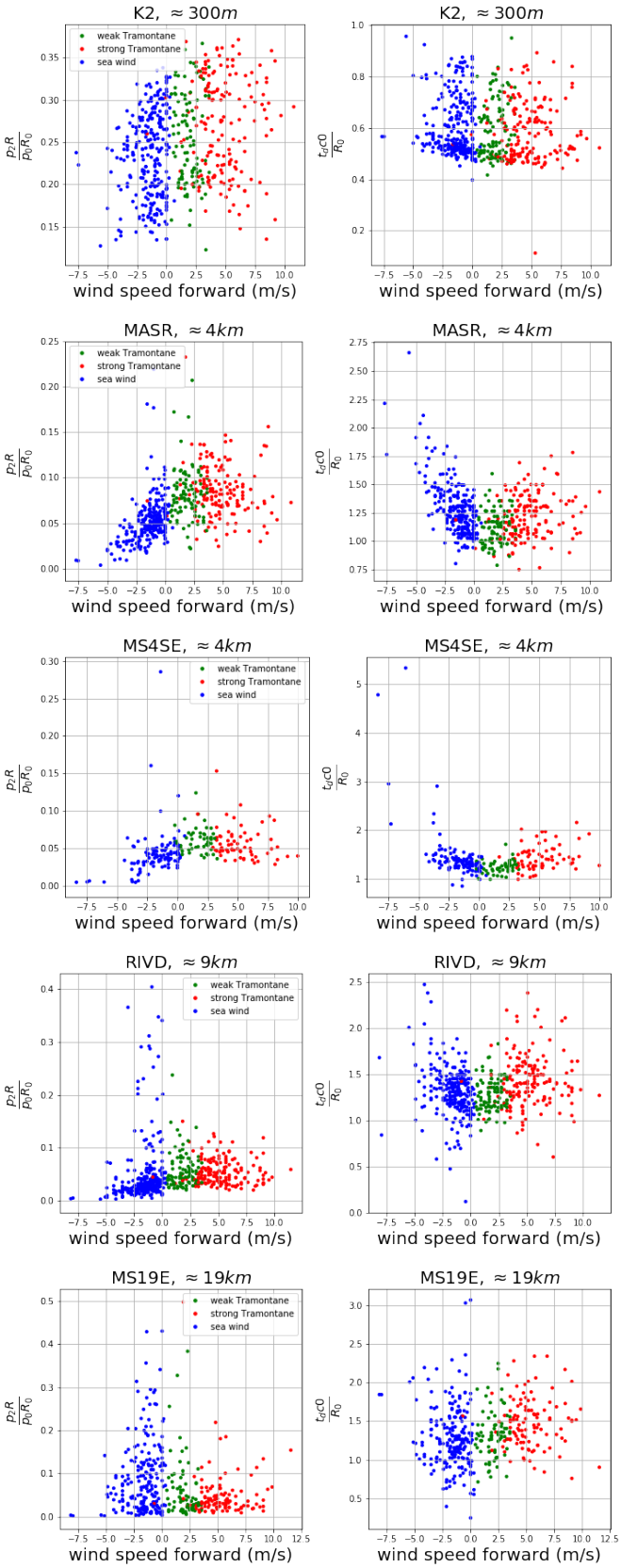

Figure 5.26: Normalized peak overpressure $\frac{p_2 R}{P_0 R_0}$ and normalized positive phase duration $\frac{t_d c_0}{R_0}$ in function of the projected wind, at each of the five stations.

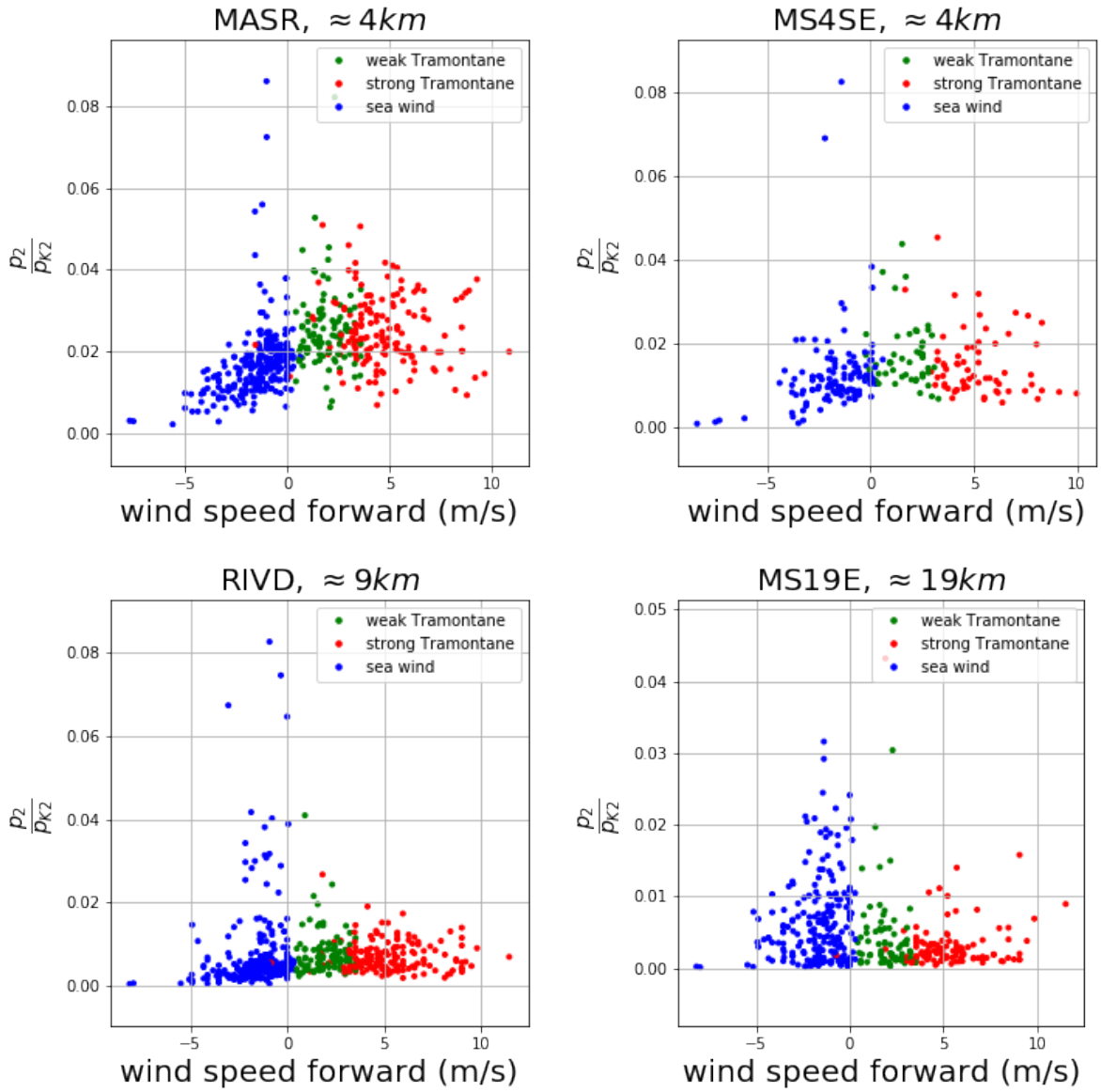

Figure 5.27: Normalized peak overpressure $\frac{p_2}{p_{K2}}$ in function of the projected wind, at each of the four stations.

Figure 5.28 shows two examples (for the MASR station) of the evolution of the wind speed forward with altitude. The profile is not constant, so that the apparent directions on the ground and in altitude can be different. For the left one, the wind speed forward is positive on the ground (downwind conditions) and negative above around 700 m. For the right one, the wind speed forward is negative on the ground (headwind conditions) and positive above around 700 m. In both cases, there is what we call an inversion in the wind direction, which can all the more influence the propagation as observation is more remote.

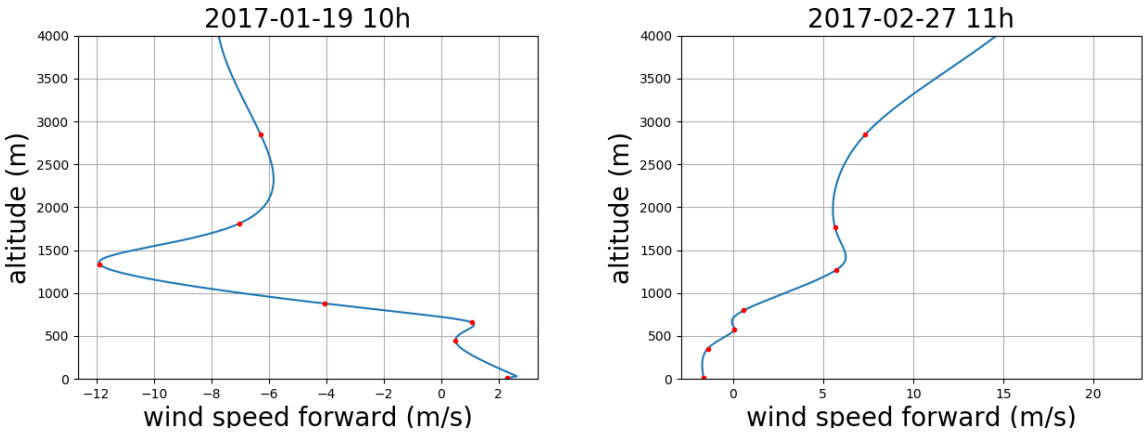

Figure 5.28: Examples of inversion, for downwind (left) and headwind (right) ground conditions, for the MASR station, obtained with the AROME profiles.

To confirm this assumption, Figure 5.29 shows the difference between the angle of the wind on the ground and at the altitude where the effective sound speed is maximal between 0 and 3000 m according to Arome at its various simulation points (see figure 5.5). The points above the red line have a difference in direction greater than 90°, and are therefore considered to show an inversion of the wind direction. They correspond to about 15 % of the events.

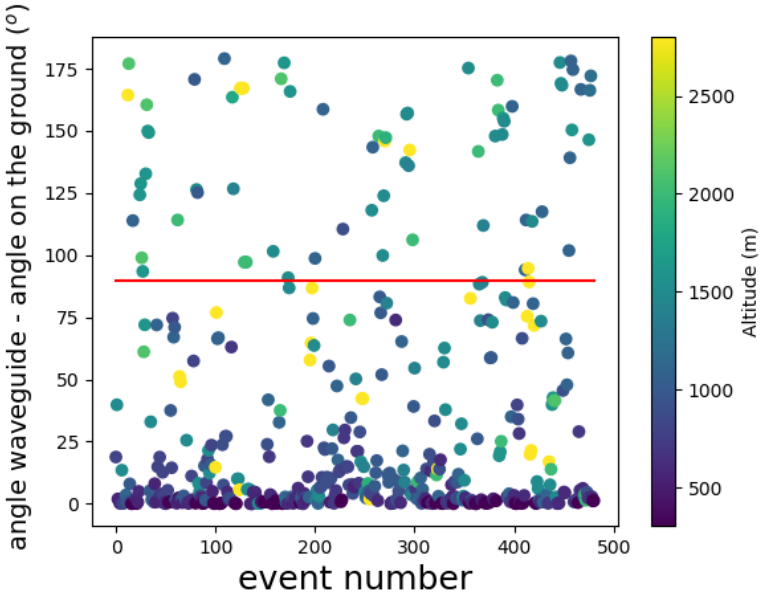

Figure 5.29: Difference between the wind direction on the ground and at the altitude (between 0 and 3000 m) where the effective sound speed is maximal for all Arome simulation points.

In figure 5.30, the scaled peak pressure p_2 is plotted against the scaled positive phase duration t_d, for each of the stations other than K2. Colors are used to differentiate between upwind and downwind on the ground, and to see if there is an inversion.

For MASR and MS4SE stations, 4 km from the source, inversions with headwind on the ground have a low peak pressure p_2, which is in agreement with the previous figure. Because the distance between the source and the station is relatively small, the wind on the ground has a much greater effect effect than the wind aloft, and therefore the peak pressure p_2 is higher when the wind is downwind than when the wind is opposite.

However, for more distant stations (RIVD and MS19E), ground upwind cases with inversions also lead to comparatively higher peak pressures p_2. In fact, they correspond to events with upper downwind, and since there is sufficient propagation distance, this upper wind increases the peak pressure p_2 at the station. This shows that the wind in altitude has an effect for more distant stations, and that the wind at a fixed position on the ground is insufficient to understand the propagation.

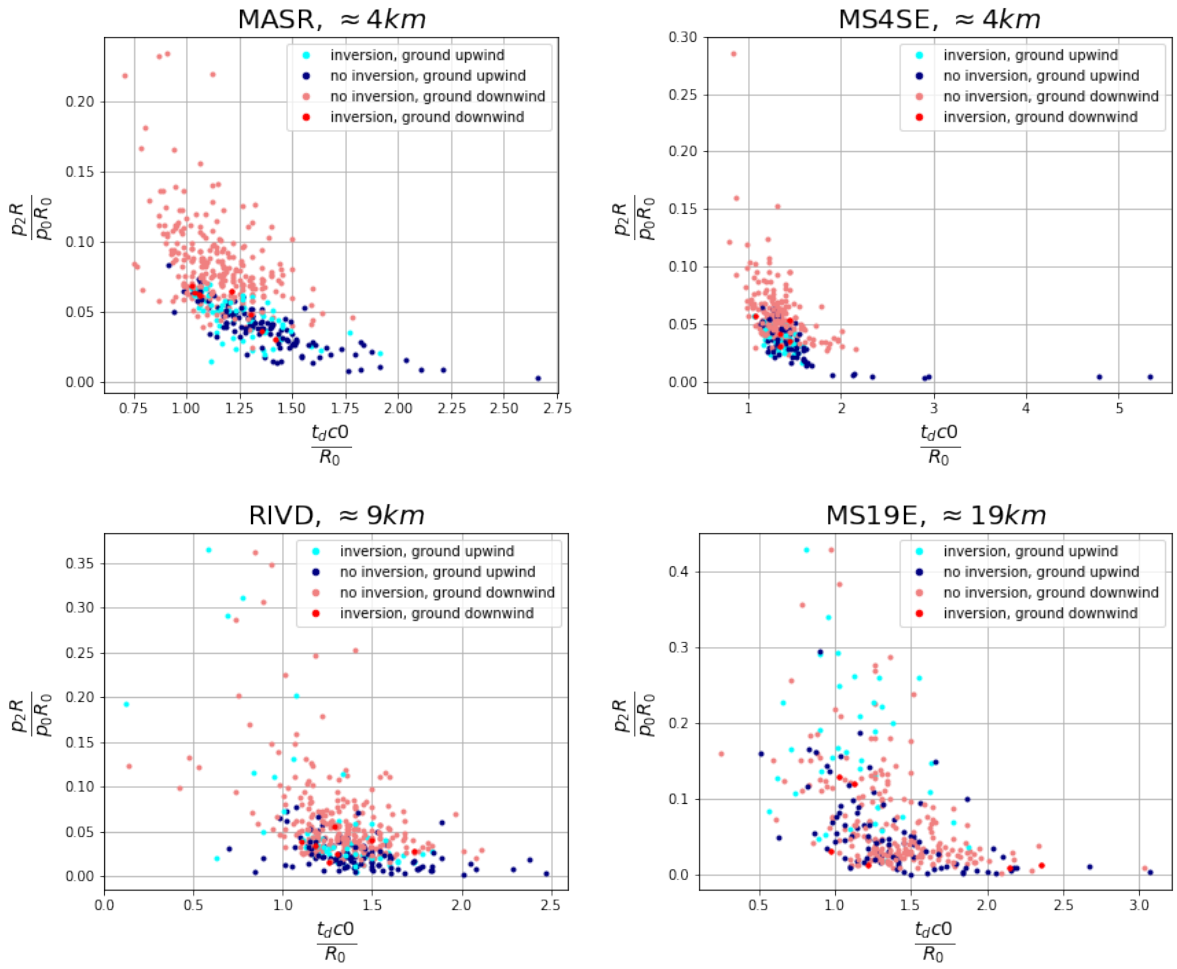

Figure 5.30: Normalized peak pressure p_2 plotted against the positive phase duration t_d, for 4 stations, with 4 groups corresponding to uwind/downwind on the ground and inversion/no inversion in altitude.

5.3 Conclusion

A large database of 639 explosions, with their acoustic waveforms measured at 5 stations at different distances from the source is described. The weather conditions on the days of the explosions, as well as parameters of the source, are also available.

In order to better understand the variability of the measured waveforms, a clustering method was applied to the data, and groups based on the properties of the source or the weather conditions were built. The characteristics of the waveforms (the peak pressure and the positive phase duration) in these clusters were compared. For the clusters based on the source conditions, a significant variability of the waveforms at the station closest to the source (K2) was observed even within each cluster, with a factor of 2 in the pressure variations. The main difference between the clusters was caused by the confinement of the source. Changes in the duration of the positive phase were also independent of the cluster group. Likewise, the clusters based on meteorological data were insufficient to explain the variability of the peak pressures and of the positive phase durations. A tiny trend of an increase of the peak pressure with the wind speed for the stations distant about 4 km is observed. However, for more distant stations, the effect of the wind is too complex to be clearly seen on the peak pressure and on the positive phase duration of the various clusters. This complexity was partly explained by the use of wind information at altitude in addition to those on the ground: downwind conditions either at the ground or in altitude also make high amplitude observations more likely.

Therefore, the main conclusion of this chapter is it is not possible to reasonably predict the waveforms from the only knowledge of the source parameters and of the wind characteristics on the ground. Indeed, the influence of the overall medium of propagation, and especially of the entire wind vertical profile, seems crucial. To take this into account, we propose to use advanced digital tools to quantify more accurately the propagation of this kind of shock wave signals. Thus, in the next chapter, the FLHOWARD3D propagation code already described above in this manuscript, will be used with the corresponding vertical wind profiles to simulate the propagation and attempt to characterize the influence of meteorological effects on the acoustical waveforms.

Chapter 6

Blast waves propagation: deterministic and stochastic studies

In this chapter, the propagation of shock waves from the source to the station MASR (over a distance of around 4 km) is investigated. The first objective is to understand the influence of the meteorological conditions on the propagation of weak shock waves, in order to predict the acoustic waveforms after a few kilometers of propagation. The second one is to determine the uncertainty of the waveform main parameters, namely the peak overpressure and the positive phase duration, depending again on the meteorological conditions. These ones were separated in three clusters in the previous chapter. In this chapter, the study on sensitivity to meteorological conditions is done separately for each cluster and in two steps. First, a deterministic study is performed: for each cluster, the wind and temperature profiles corresponding to the measured waveforms are extracted, and a simulation with the FLHOWARD3D code is performed for each case. This one-to-one comparison between simulated and measured signals provides a first overview of the effects of meteorological conditions. The variability within each cluster is also examined. This first approach is complemented by a stochastic study. A dimension reduction method is applied on the vertical profiles in order to parameterize them with a small number of variables. A gPC study is then performed with these variables as input, and gives us a meta-model of the propagation, depending on the meteorological cluster. This meta-model can instantly compute the simulated waveform, knowing the atmospheric profiles. Using this model, the uncertainties of the peak pressure and of the positive phase duration are obtained, depending on the meteorological cluster.

6.1 Numerical simulation parameters

6.1.1 Parameters of the propagation

The propagation is computed with the propagation code FLHOWARD3D, previously presented in this manuscript. Simulations are performed in a 2D medium, between the source considered as a point one and the MASR station at 4300 m, over a ground flat. In practice, the input signal is initialized at a 300 m distance from the source, which means that the propagation distance is 4 km. The 2D geometry corresponds to a cylindrical configuration, but the wave amplitude is scaled during the propagation to recover the

decay of a spherical wave (see chapter 2).

The propagation of the shock wave is realized in a square domain of dimensions 4 km × 4 km, with x-axis the main direction of propagation (parallel to the ground) and $y-$axis the altitude measured above the ground.

For the absorbing boundary conditions, The absorption coefficient is

$$\zeta(h) = \frac{\alpha c_0}{a^3} h^2, \tag{6.1}$$

with $h = 2500$ m and $\alpha = 1.5$.

An example of the 2D pressure field in a near homogeneous atmosphere (with wind speed profile under 1 m/s) at the emission and after 4 km of propagation is shown on figure 6.1.

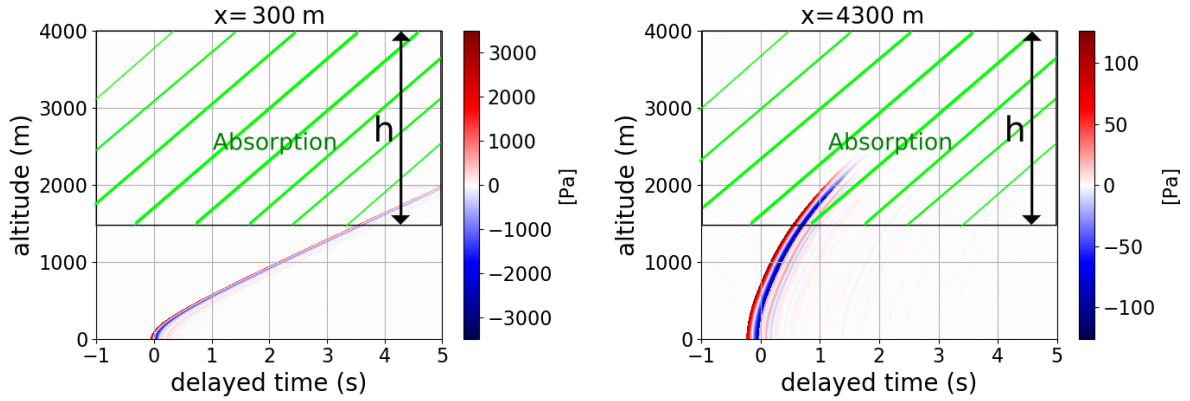

Figure 6.1: Pressure field (in color) as function of the altitude and the delayed time) of a signal. Left: input signal at K2 station. Right: signal computed with the FLHOWARD3D code after 4 km of propagation, with weak wind conditions (wind speed under 1 m/s and a temperature profile close to the theoretical −6.5 K/km decrease.

6.1.2 Source signature

The choice of the source signature used in the simulations is discussed in this section. This signal should be characteristic for a blast wave emitted by an explosion. Measured and empirical waveforms are considered. A model of signature is first discussed, and then compared to the measurements at K2 station (the closest to the source) to decide which signature should be used as input.

Close to the source, the signature can be predicted theoretically by the empirical Reed's model [139] which faithfully represents mostly the positive pressure phase (for $t < t_a$), while the negative phase is known to be poorly represented.

The overpressure is given by:

$$p\left(t_{\text{norm}} = \frac{t - t_a}{t_d}\right) = -p_{\max} t_{\text{norm}} \times \left(1 - \frac{1 + t_{\text{norm}}}{1 + \sigma}\right) \times \left(1 - \left(\frac{1 + t_{\text{norm}}}{1 + \sigma}\right)^2\right), \tag{6.2}$$

with $\sigma = \frac{12}{5}$ and $t_a = 0$ s (t_a is the arrival time of the signal).

There are 2 parameters in this model: the peak overpressure $p_{\max}$ and the positive phase duration t_d. Their values are determined according to the literature. In [117], a two-dimensional axisymmetric and nonlinear direct simulation resolving the Euler equations, taking into account the detonation phase into the explosive, is performed. The resulting free field propagation at different distances is shown on figure 13 of [117]. In particular, the result at station MASR is shown in the lower right of the figure. These simulations are used in reference [116] to develop an empirical source for linear propagation, such that after a linear simulation, $p_{\max}$ and t_d at station MASR are the same as for a nonlinear simulation in a homogeneous medium. The initial values of $p_{\max}$ and t_d (at 300 m from the source) in this work also come from these simulations. However, only their values for the linear model of [116] are available. Thus, these values at station MASR are used to deduce the nonlinear parameters at 300 m from the source, with the expressions of $p_{\max}$ and t_d from Korobeinikov [82].

Figure 6.2 shows the evolution of $p_{\max}$ and t_d with the propagation distance for different models, for a source with $W = 300$ kg equivalent TNT. The blue curve corresponds to the linear propagation model used in [116], the violet curve is the simulation with FLHOWARD3D in a homogeneous medium, and the other colors are nonlinear and weakly nonlinear models described in [116] and [82].

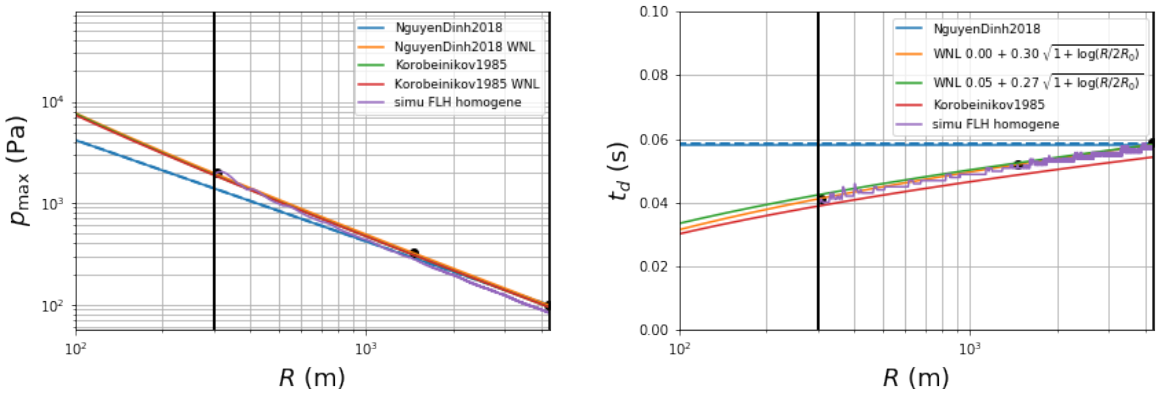

Figure 6.2: Peak pressure $p_{\max}$ (left) and positive phase duration t_d (right) for different models and simulations during the propagation.

Our initial model follows the work of [82]. The positive phase duration t_d is given by:

$$\frac{t_d\, c_0}{R_0} = (Z - 0.24) - \left(Z - 0.22\sqrt{\gamma} - \frac{0.4}{\sqrt{2\alpha\gamma}} \sqrt{1 + \log(Z/2)} \right), \tag{6.3}$$

while the peak overpressure is:

$$p_{\max} = \frac{0.326 P_0}{Z\sqrt{1 + \log(Z/2)}}. \tag{6.4}$$

In above equations, P_0 is the atmospheric pressure ($P_0 = 101\,325$ Pa), while $R_0 = \left(\frac{E_{\text{eq}}}{P_0}\right)^{1/3}$ is the characteristic radius associated to the energy of a point explosion of energy $E_{\text{eq}} = 4.184 \times 10^6 W_{\text{eq}}$ in Joule. The quantity $Z = \frac{R}{R_0}$ is the normalized distance, $\gamma = 1.4$ the ratio of specific heats and $\alpha = 0.805406$.

The overpressure predicted by the Reed model depends on the distance R from the source, we choose here $R = 300\,\mathrm{m}$ for station K2. We also set the arrival time t_a there equal to 0. We recall that the equivalent charge W_{eq} (measured in kg equivalent TNT) takes into account the charge (denoted W, generally $W = 500\,\mathrm{kg}$ eq TNT), the presence of the ground (by a factor 2 for the reflection) and the possible confinement of the plates [52]:

$$W_{eq} = 2 \times W \times (1 - 0.4 \times (nb_{\text{confined plates}}/nb_{\text{plates}})). \tag{6.5}$$

Without confinement, the equivalent charge is equal to two times the effective charge. For a fully confined explosion, a correction factor of $0.6 \times 2 = 1.2$ is applied to the charge.

Among the measuring stations, K2 is the closest to the source, therefore it is the best approximation of the source signals available among all measured signals. On figure 6.3 are plotted the temporal signals measured at station K2 for seven different events with different peak pressures, with only 1 plate at the source and an initial effective charge of 500 kg equivalent TNT, the explosive type A and no confinement, as defined in the previous chapter (see Table 5.2. The theoretical Reed's signature with the same initial charge is superimposed in black. The positive phase durations are similar, but the peak signal overpressure is slightly lower than the experimental ones. We assume that this is due to the topography. Indeed, the ground elevation is not flat between the source and the K2 station, as shown on figure 6.4 (left). On figure 6.4 (right) one can see that there is also a canyon which can cause 3D effects. Since K2 station is close to the source, the effects of the meteorological conditions are expected to be relatively small, which means that the main difference between measurements and theory arises from the topography, which induces an amplification of the pressure. This effect of the topography is also observed in [117]: the pressure at station K2 was calculated without and with topography (figure 13), this last case having a peak pressure around 25 %. This pressure increase shows the signal at station K2 is not a suitable choice for an input source to simulate long range propagation, because it is not representative of the overpressure field in altitude. However, the signals at station K2 are still useful in understanding source variability because relative differences between emitted blast waves of similar characteristics can be observed at this station.

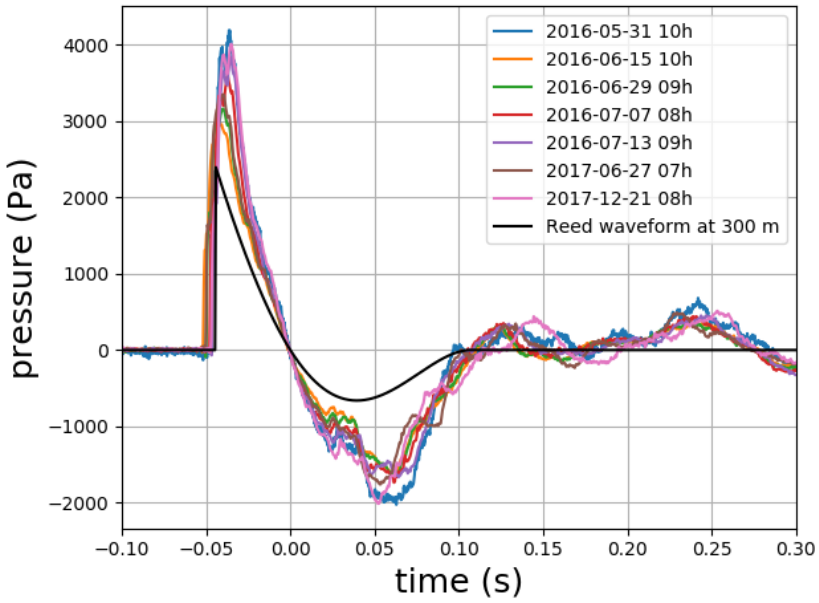

Figure 6.3: Signals (in colour) at K2 station for seven different events, with a charge of 500 kg TNT equivalent, without confinement, for 1 plate at the source and the explosive type A. In black, theoretical Reed's waveform without topography for a charge of 500 kg equivalent TNT .

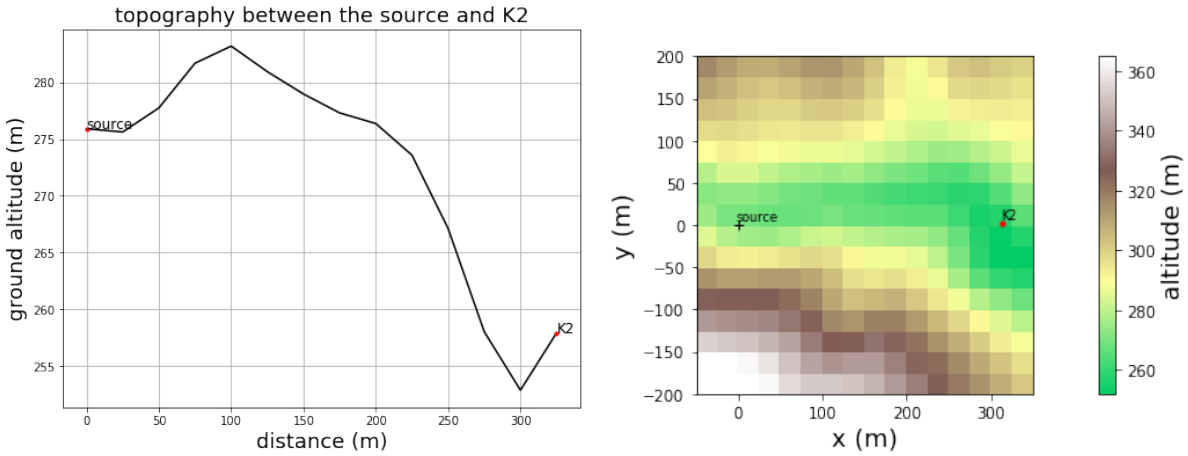

Figure 6.4: Local topography around the source and K2 (right), and altitude versus distance along the segment between the source and K2 (right).

For these reasons, the signal used as a source in the following parts of this chapter is the Reed's waveform with an initial charge of 500 kg equivalent TNT.

6.1.3 Meteorological profiles

The three wind groups obtained in the previous chapter contain a lot of profiles and therefore provide a good overview of the meteorological conditions on the pyrotechnic site during the four years of the database. However, these profiles are not necessarily

available at the dates of the explosions. For example, for most of the days, Arome profiles are available from 7 h to 16 h, with one profile every hour, thus a total of 10 profiles per day. For most of the database, there are only 2 or 3 explosions per day. Furthermore, Arome profiles are available from January 2015 to October 2017, while the explosions were recorded from June 2015 to July 2018. Hence, there are Arome data with no explosion the same day, and explosions with no profile for the same day.

The objective of this part is to select measured signals with relatively uniform source conditions, and, if possible, find the Arome profile at the same day which is the closest in time to the explosion. This gives us couples of profile/measured signals to be used for comparison between simulation and measurements. To determine the relevant couples, we apply the following procedure:

1. Start with all the signals measured at station MASR (584 dates),
2. Among those measured signals, select those with an initial charge above 480 kg equivalent TNT, without confinement (102 dates),
3. For each of the remaining signals, find the Arome profile of the same day and closest in time (if it exists) (85 dates),
4. Allocate the remaining profiles to the corresponding group (20 for "upwind", 20 for "strong downwind" and 45 for "weak wind").

The selected profiles are displayed on figure 6.5.

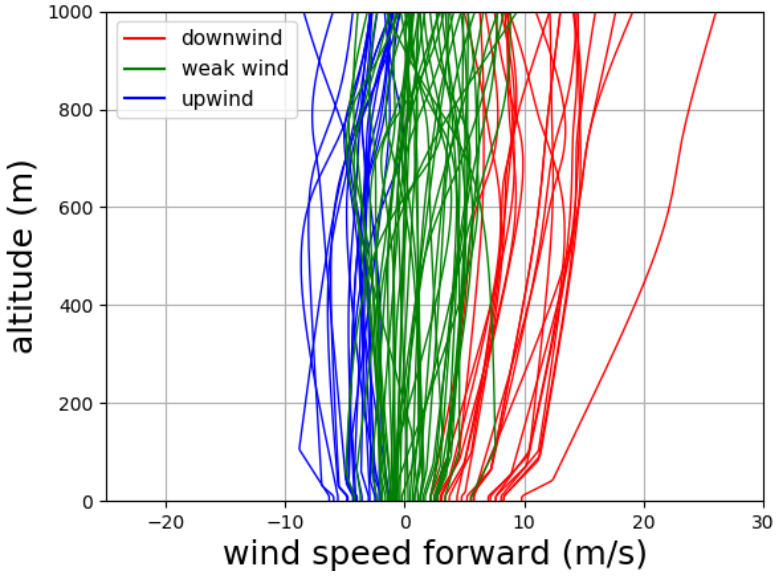

Figure 6.5: Selected Arome profiles (closest to MASR station) of the wind speed projected in the source-MASR station direction. The colors correspond to the three groups detailed in previous chapter.

6.2 Deterministic simulations of the propagation of blast waves in MASR station

In this section, FLHOWARD3D code is used to compute the propagation in the atmosphere with the stratified profiles selected in section 6.1.3. Because we are interested in the results at MASR station, the propagation distance is chosen equal to 4 km. For each of the three atmospheric groups, computed and measured waveforms are compared. In all cases, the peak pressures are normalized by P_{ref}, with P_{ref} the maximal overpressure measured at MASR station for the four years. The sampling values of $N_x = 1024$, $N_y = 4096$ and $f_t = 1024Hz$ showed converged results. The initial waveform is the Reed signature presented previously with $W = 500$ kg eq TNT, without confinement.

6.2.1 Upwind meteorological conditions

First, the waveforms simulated for the atmospheric profiles of the "upwind" group are shown on the left of figure 6.6, and the corresponding measured signals at station MASR are shown on the right. The same color is used on both figures for one case (one case at one date).

First we observe that the amplitude range for both simulations and measurements are close to one another: highest normalized pressures are around 0.25, and lowest ones around 0.15 (except for 2 measured signals). The positive phase duration seems slightly higher for the measured signals and more dispersed. To be more quantitative, the measured and simulated normalized peak pressures (resp. phase durations) are plotted one versus the other on the left (resp. on the right) of figure 6.7. Solid lines indicate linear regressions. For the normalized peak pressure, the simulated overpressure tend to be slightly above the measured ones, but values are reasonably close. Furthermore, highest measured values correspond to highest simulated ones, which is the expected behavior. On the contrary, for the positive phase duration t_d, the measured values (between 0.11 and 0.19 s) are always higher than the simulated ones (between 0.08 and 0.11 s except one case) and cover a larger range though highest measured values of t_d correspond to higher simulated t_d (positive slope of the linear regression). To summarize, measured signals are not perfectly reproduced, because simulated signals have significantly lower positive phase durations, though the global behavior is reasonably good regarding peak overpressures.

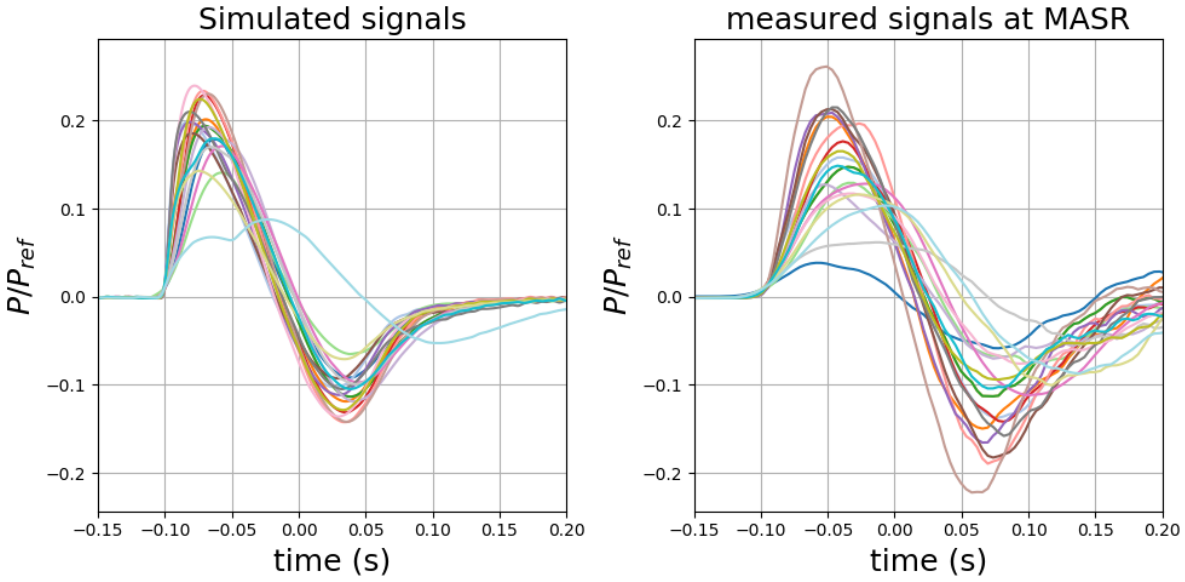

Figure 6.6: Twenty superimposed simulated (left) and corresponding (same color) measured (MASR station, right) waveforms for upwind cluster.

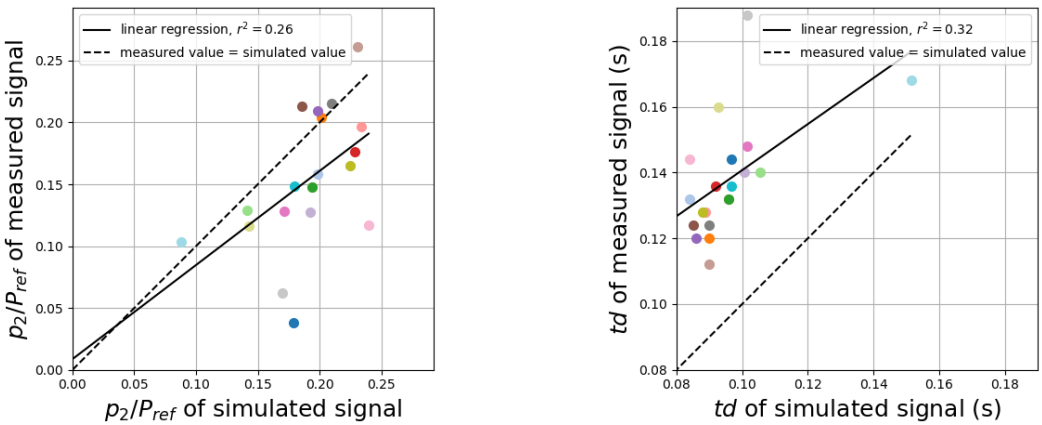

Figure 6.7: Measured versus simulated normalized peak overpressure (left) and positive phase duration (right) for upwind cluster. Solid lines indicate linear regressions between measurements and simulations. same color code as in figure 6.6

6.2.2 Weak wind meteorological conditions

The simulated and measured waveforms (45 cases) for the "weak wind" cluster are visible on figure 6.8. Except for one waveform, all the normalized measured peak overpressures are below 0.5, while 14 of the simulated waveforms (31 % of the cases) are above. Clearly the simulation predicts a significant number of cases with higher peak pressures than measured. However, a significant group of signals with overpressures lower than 0.3 is observed both for simulations and at the station (42 % of the waveforms). Also values of negative overpressures seem to be more comparable (in the range -0.1 to -0.3). As for the

previous cluster, the measured positive phase durations are larger than simulated ones, though this last ones now show a larger dispersion than in the upwind case.

Figure 6.9 shows the measured normalized values of p_2 and t_d plotted versus simulated ones. For simulated normalized p_2 under 0.4, the correspondence between simulated and measured values is quite good, showing a reasonable clustering around the ideal diagonal. Above 0.4 however, measured peak pressures do not match at all the high simulated values. To understand this behavior, this figure is reproduced in figure 6.10, but now with the color depending on the ground wind direction (blue: upwind, red: downwind). A high correlation is found between the simulated waveforms below 0.4 and a negative ground wind speed forward (upwind case), and between the simulated waveforms above 0.4 and a positive ground wind speed forward (downwind). Values for upwind are much better simulated that downwind ones, as shown by the linear regression.

For the positive phase duration t_d, as before, all the measured values are larger than the simulated ones. There is a similar variability of a factor about 2 (roughly between 0.05 and 0.1 s for simulations, between 0.07 and 0.14 s for recordings), and high simulated values are associated with high measured values. Linear regression shows an expected increase of the measured positive phase duration with the simulated one for the upwind conditions, but an unexpected decrease for the downwind conditions. Again, it confirms that downwind conditions are more difficult to reproduce than upwind ones. Possible explanations are micro-meteorological effects, as well as effects of the topography.

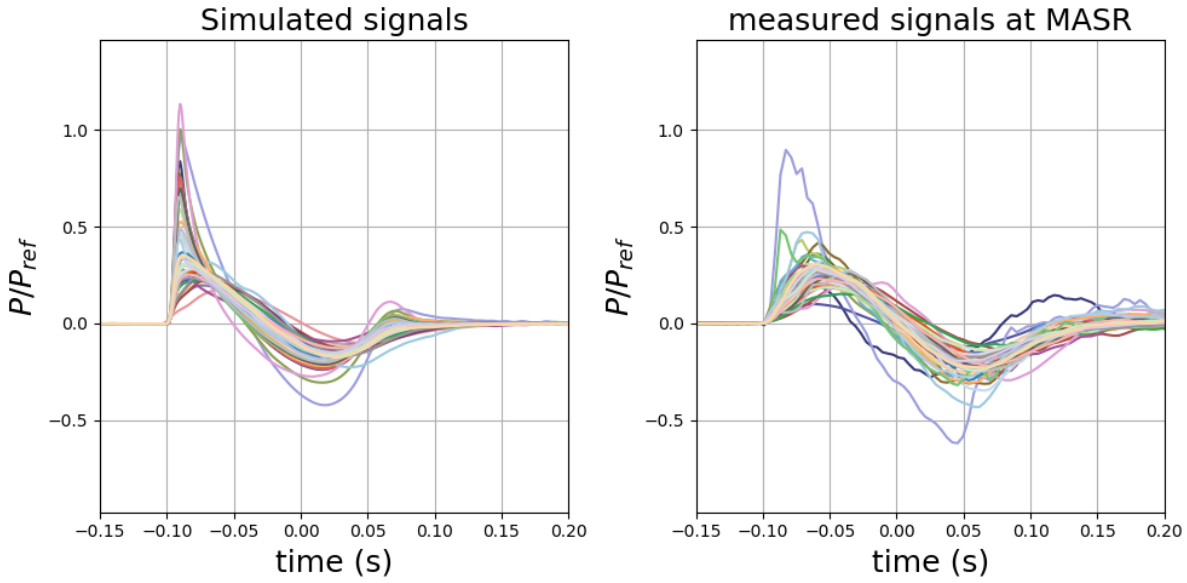

Figure 6.8: Forty-five superimposed simulated (left) and corresponding (same color) measured (MASR station, right) waveforms for weak wind cluster.

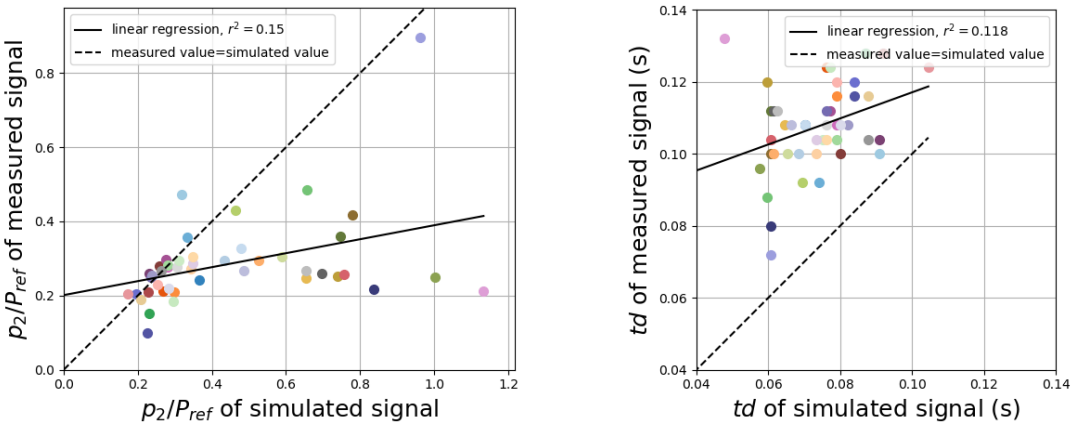

Figure 6.9: Measured versus simulated normalized peak overpressure (left) and positive phase duration (right) for upwind cluster. Solid lines indicate linear regressions between measurements and simulations. same color code as in figure 6.8.

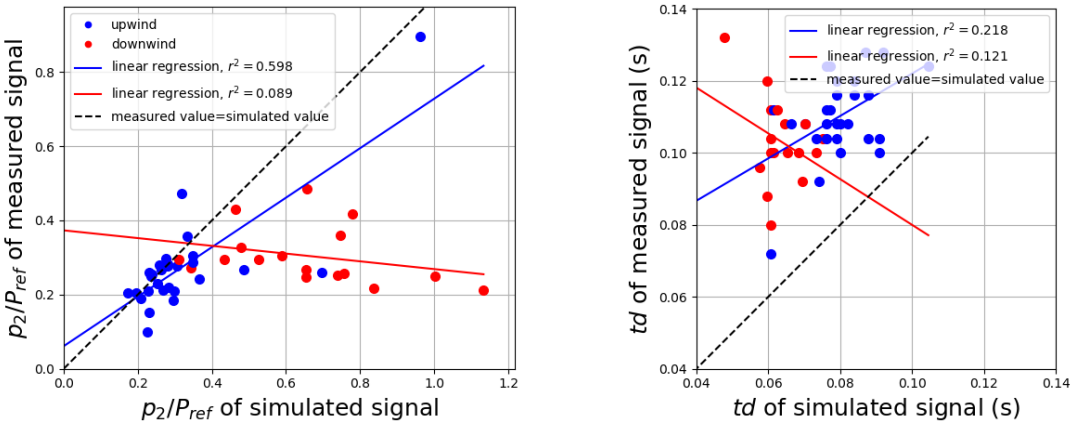

Figure 6.10: Measured versus simulated normalized peak overpressure (left) and positive phase duration (right) for upwind cluster. Solid lines indicate linear regressions between measurements and simulations. Blue (red) points: weak upwind (downwind) conditions.

6.2.3 Downwind meteorological conditions

The 20 simulated and measured waveforms for the "downwind" cluster are collected on figure 6.11, and the corresponding values of peak ovepressure and positive phase duration are displayed on Figure 6.12. Fifteen (75 %) of the simulated waveforms have a normalized peak pressure larger than one (maximum measured value in all cases), up to 1.4, while all measured signals but two are below 0.6. Obviously, the simulated overpressures are far higher than the measured ones. Simulated values of t_d also show much lower values and dispersion (mostly in the range 0.05-0.07 s) than measured ones (in the range 0.08-0.14 s). Linear regressions show a very low correlation (coefficient r^2), with even a negative correlation for phase duration. This confirms, in an amplified case, the observations of the weak wind cluster, that downwind simulations poorly reproduce the observations.

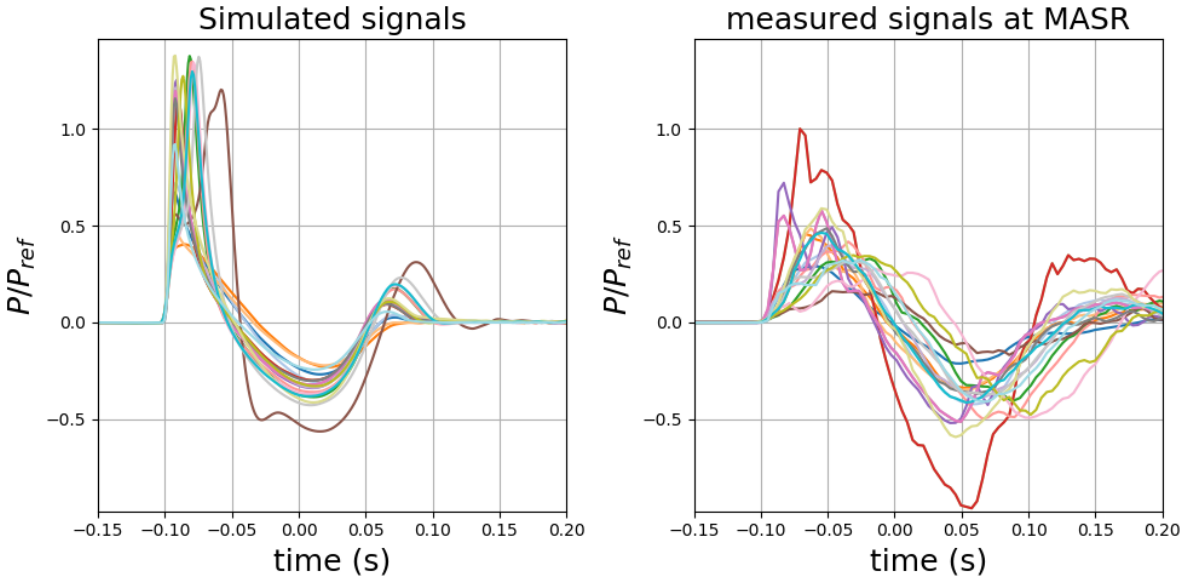

Figure 6.11: Twenty superimposed simulated (left) and corresponding (same color) measured (MASR station, right) waveforms for downwind wind cluster.

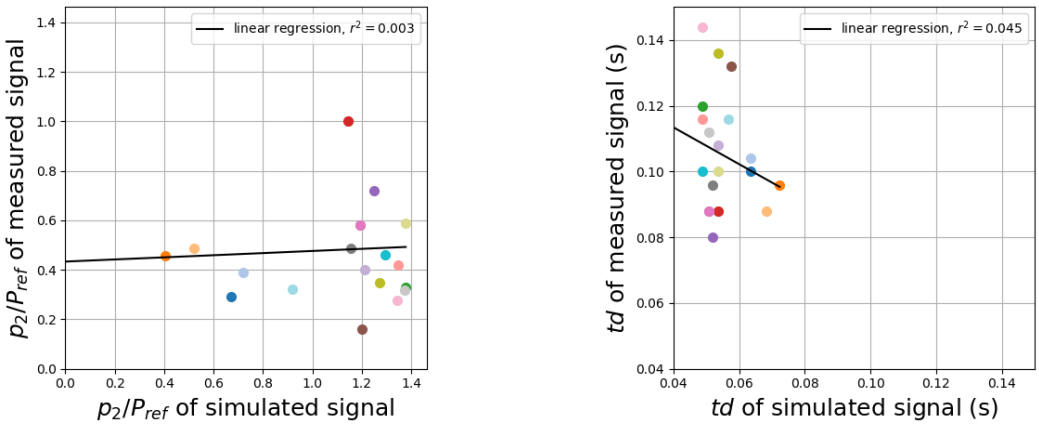

Figure 6.12: Measured versus simulated normalized peak overpressure (left) and positive phase duration (right) for downwind cluster. Solid lines indicate linear regressions between measurements and simulations. same color code as in figure 6.11.

6.2.4 Influence of the wind conditions on the propagation over a flat ground

In this section, the simulated waveforms obtained for the three groups are all gathered for their comparison on the left of figure 6.13. For the upwind conditions (blue curves), the waveforms are simple and rounded. For the downwind conditions, all the waveforms are peaked, and six of them show a second arrival (likely due to a tropospheric waveguide), which makes the waveform more complex. Finally, the weak wind conditions include both kinds (rounded and peaked waveforms), but without second arrival. The peak pressures and the positive phase durations are compared on the right of figure 6.13.

The upwind conditions show the highest positive phase durations and the lowest peak pressures, while the downwind conditions induce the opposite behaviour (lowest positive phase durations and highest peak pressures). The weak wind conditions have the largest range of variations, comparable to either the upwind observations or the downwind ones. Thus the upwind conditions tend to smooth the signal, leading to low amplitudes and large positive phase durations, while the downwind conditions tend to produce peaked signals with larger amplitudes and shorter positive phases duration, and sometimes show a second arrival.

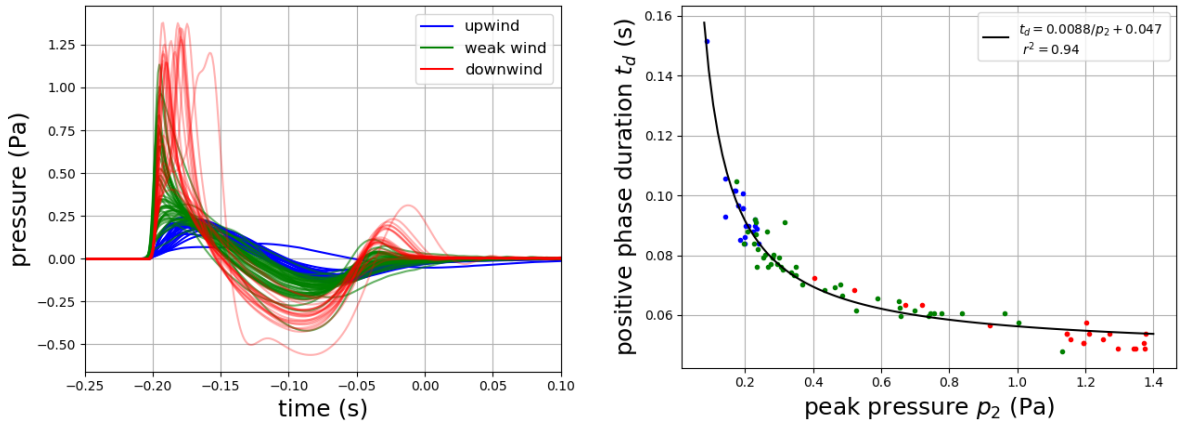

Figure 6.13: Left: all simulated waveforms with color depending of the wind cluster. Right: Simulated positive phase durations versus peak pressures with the same color code.

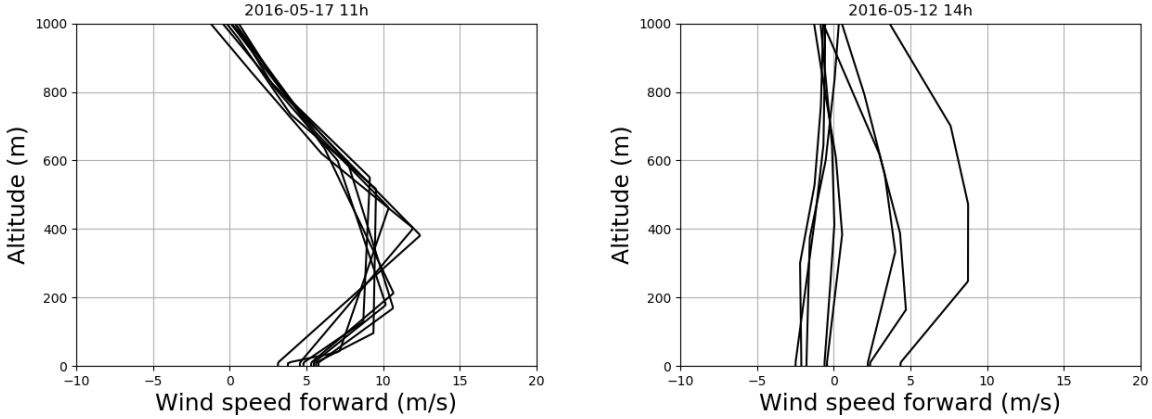

Figure 6.14: Wind profiles for the 8 Arome points closest to the propagation, at a date with a good accord between the profiles (left), and a bad accord between the profiles (right).

In conclusion, the comparison between measurements and simulations shows the propagation with the FLHOWARD3D code gives reasonably good results for upwind conditions, and much less satisfying ones for downwind conditions. The main reason for this is probably due to the coupling between the downwind conditions and the topography,

which is expected to have a strong effect on the pressure. For example, the high relief west of the source could impede the tramontane wind, and thus explan measurements lower than the simulation. Moreover, downwind conditions tend to create tropospheric waveguides refracting the sound towards the ground, and therefore increasing the coupling with the ground. In both cases, the positive phase duration is also underestimated by the simulation. This can be explained by various sound attenuation mechanisms not taken into account in our simulations, such as finite ground impedance or scattering by atmospheric turbulence. The comparison between the various simulations shows that, for propagation over a flat ground, upwind conditions lead to lower pressures and longer positive phases, and downwind conditions to higher pressures and shorter positive phases.

However, accurate atmospheric profiles are not always available, and these profiles do not necessary correspond faithfully to the actual meteorological conditions during the propagation, for example because they are taken at a fixed point while the propagation extends over some distance (here 4 km), or because they are not provided at the exact time of the explosion. For example, figure 6.14 shows such profiles (wind speed forward) at the 8 available points closest to the propagation. On the left, the differences between the profiles are small, while the differences are large on the right. This indicates that taking the profile at a single point can be insufficient. Moreover, this study was carried out for only a few dozens of profiles per meteorological conditions, which may be insufficient to be representative of the considered cluster. Because this study is deterministic, it also cannot provide an evaluation of the uncertainty of the results.

For these reasons, to better take into account the uncertainty of the atmospheric profiles, and to have a more exhaustive characterization of the groups, a stochastic study of the propagation is performed in the next section in order to determine the uncertainty of the propagation for each of the 3 meteorological groups. Because the number of measured signals is insufficient for a reliable statistic study, a meta-model is generated with the the help of simulations, and examined in a stochastic way.

6.3 Stochastic simulations of the propagation of shock waves in MASR station

In this section, a stochastic study of the propagation is performed. First, for each meteorological group, a more extensive dataset is completed. The combined dataset is made of 2774 atmospherics profiles (both temperature and wind) with a regular sampling. Then, a dimension reduction method is applied on the profiles, in order to characterize them with a small number of variables. Finally, a gPC method is applied by using these inputs as random variables. This allows us to observe the influence of the meteorological profiles on the propagation, and to quantify the variations caused by the stratification. A meta-model of the pressure signal at 4 km is thus obtained, and is used to instantly compute waveforms for any initial meteorological conditions.

6.3.1 Parameterization and dimension reduction of the profiles

An important number of atmospheric profiles is required, to have an accurate probability distribution. For this purpose, besides the data on the point closest to the MASR station,

the wind and temperature are extracted at the 8 Arome points closest to the source/MASR path (see figure 6.15)

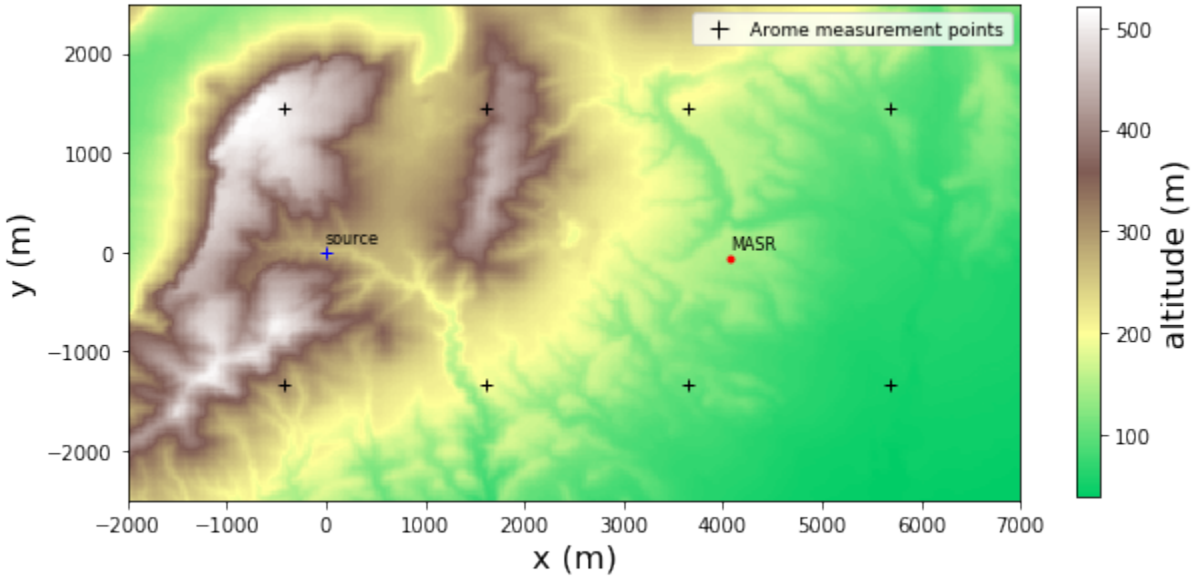

Figure 6.15: Map of the site of Rivesaltes, with the source in blue, the MASR station in red and the positions of the Arome points in black.

In order to parameterize the profiles, the principal components analysis (PCA) is chosen. The PCA is an orthogonal linear transformation that transforms the data to a new coordinate system such that the greatest variance by some scalar projection of the data comes to lie on the first coordinate (called the first principal component), the second greatest variance on the second coordinate, and so on [129]. This means that the variations in the profiles are mainly described by the few first components given by the PCA. These components are then chosen as the input random variables for a gPC analysis, which is used to generate a meta-model of the propagation for the chosen meteorological group. This meta-model enables the study of the influence of the wind conditions on the blast waves propagation. An advantage of this method is that the variables given by the PCA are independent to each other, which makes i easier to conduct a gPC study. Other methods like polynomial approximations can parameterize the profiles with a low number of variables, but there is no reason to think that these variables would be independent.

In practice, for the "upwind" group, the profiles of the wind speed forward and of the temperature are extracted for the Arome points, and a linear interpolation is done on theses data, in order to have 250 values of the wind and temperature equally distributed between 0 and 1000 m. This makes more than 3000 couples of profiles, which are here the datapoints constituting the dataset. Each datapoint has thus 500 variables (250 per profile). Then the dataset is centered, and its variance is normalized to one. Next, the PCA is applied on the dataset. On the left of figure 6.16 is shown the explained variance in function of the number of variables (or components). It is observed that with 2 variables, more than 90% of the variance is explained. Thus, a number of 2 variables is chosen. Their distribution is displayed on the right of figure 6.16. Even if their distribution is not exactly Gaussian, it is relatively close to it. Therefore, in first approximation, they are

considered as normal distributions.

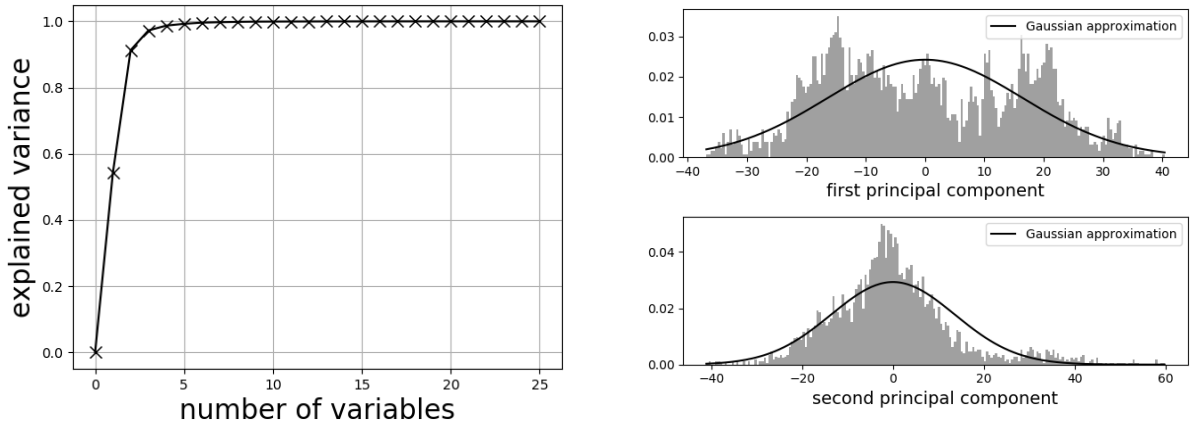

Figure 6.16: Explained variance given by the PCA in function of the number of components (left), and probability distribution of the first two components with their modeling by a normal distribution (right), for the upwind cluster.

On figure 6.17 are shown different steps of the PCA analysis. On the left are plotted the original profiles. On the middle are the profiles reconstructed with the first two components. Indeed, for each datapoint, the PCA gives the values of the 2 components which explain the most the variance. A reverse PCA is performed with only these 2 parameters as input, and the projection of the original profiles on the two components are obtained. Finally, on the right, reverse PCA are realized, with random values of the 2 parameters following the normal distribution shown on the right of figure 6.16.

The profiles on the left and the middle are very similar. The middle one are less complex than the left ones, because they are calculated with only 2 parameters, but their behaviors are comparable. The right one is more different. The temperature decrease with the altitude is similar to the original one, but the value of the ground temperature has a wider range of variation, probably because the normal distribution can give values outside the variation range of the original distributions. For the wind speed forward, some profiles with strong negative wind speed on the reconstructed figure don't appear on the random one. However, this concern only a small part of the profiles.

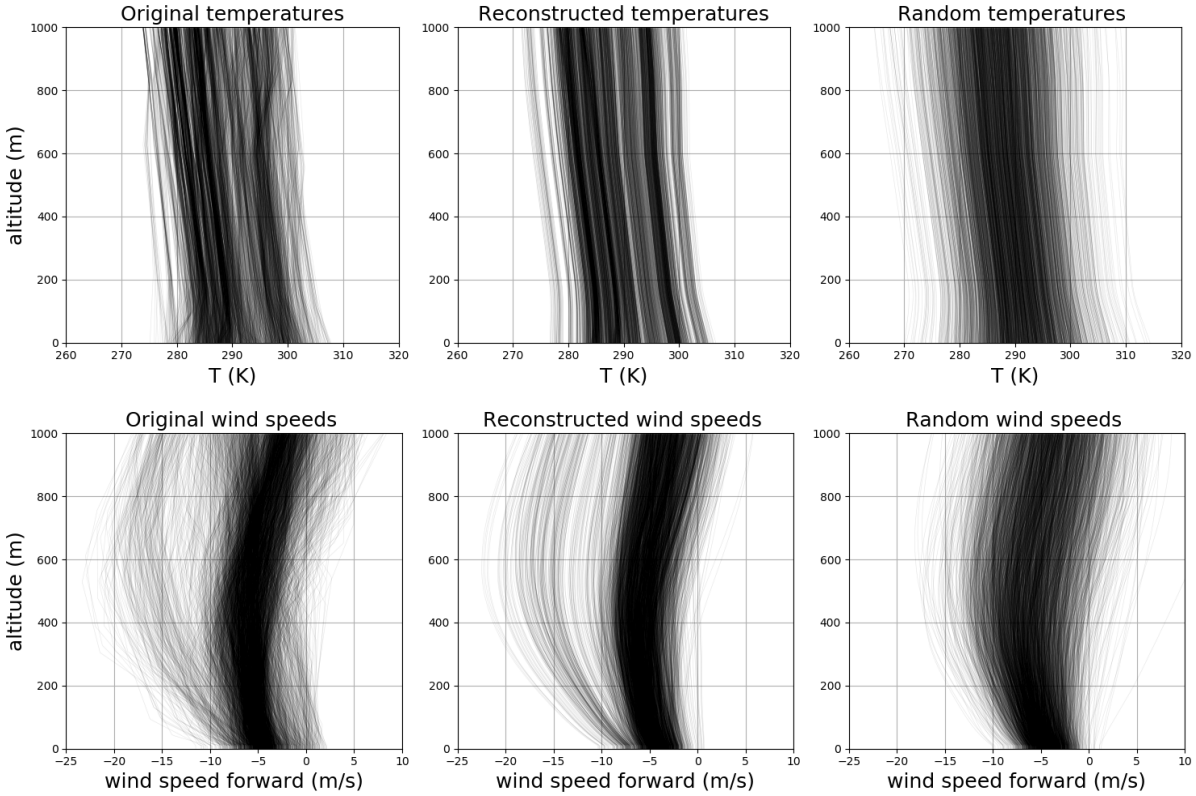

Figure 6.17: For the upwind cluster, original temperature profiles (upper left), temperature profiles projected on the two components obtained with the PCA (upper middle), and temperature profiles calculated with 2 random components obeying the Gaussian distributions shown figure 6.16 (upper right). Original wind profiles (lower left), wind profiles projected on the two components obtained with the PCA (lower middle), and wind profiles calculated with 2 random components obeying the Gaussian distributions shown figure 6.16 (lower right).

The same procedure is applied to the "weak wind" group and the "downwind" group. Figures 6.18 and 6.19 show the steps and the results of the PCA for the "weak wind" group. 87% of the variance is explained by 2 components. The distributions of the components are closer to Gaussian than for the upwind, and the initial and computed profiles are close to each other. Finally, for the downwind, the steps and the results of the PCA are shown figure 6.20 and figure 6.21. 93% of the variance is explained by 2 components. The Gaussian approximation of the distributions is relatively good, and the profiles are close to each other. Thus, for each of the 3 groups, the first 2 components of their PCA are chosen as the input random variables of a gPC analysis, with the probability distributions shown before.

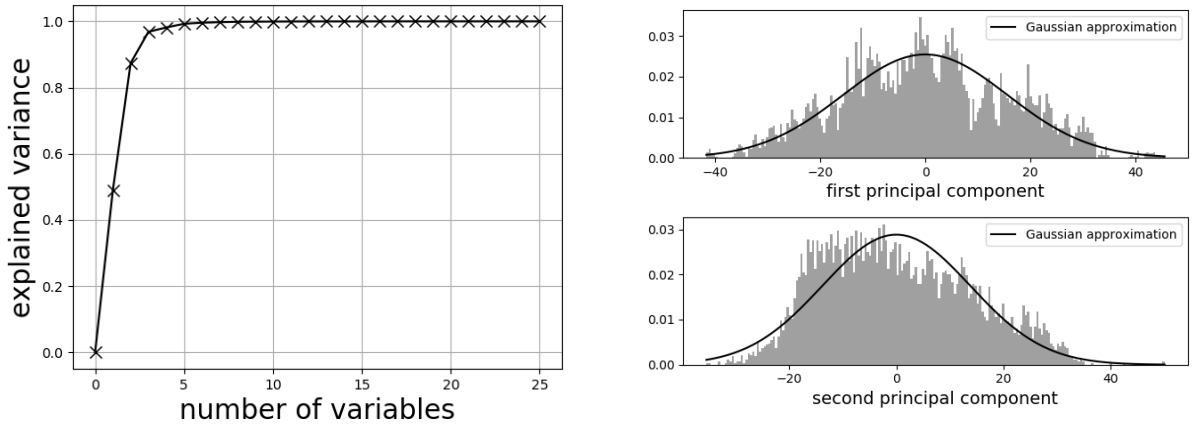

Figure 6.18: Explained variance given by the PCA in function of the number of components (left), and probability distribution of the first two components with their modeling by a normal distribution (right), for the weak wind cluster.

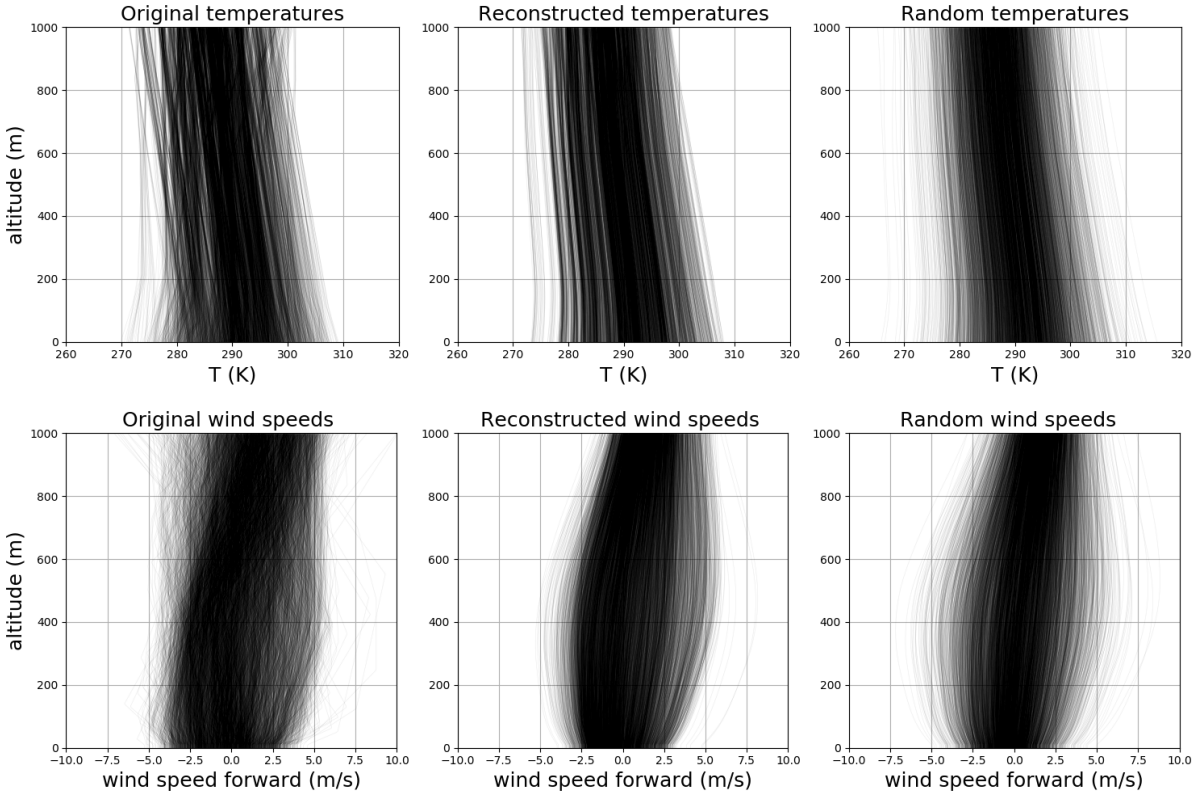

Figure 6.19: For the weak wind cluster, original temperature profiles (upper left), temperature profiles projected on the two components obtained with the PCA (upper middle), and temperature profiles calculated with 2 random components obeying the Gaussian distributions shown figure 6.16 (upper right). Original wind profiles (lower left), wind profiles projected on the two components obtained with the PCA (lower middle), and wind profiles calculated with 2 random components obeying the Gaussian distributions shown figure 6.16 (lower right).

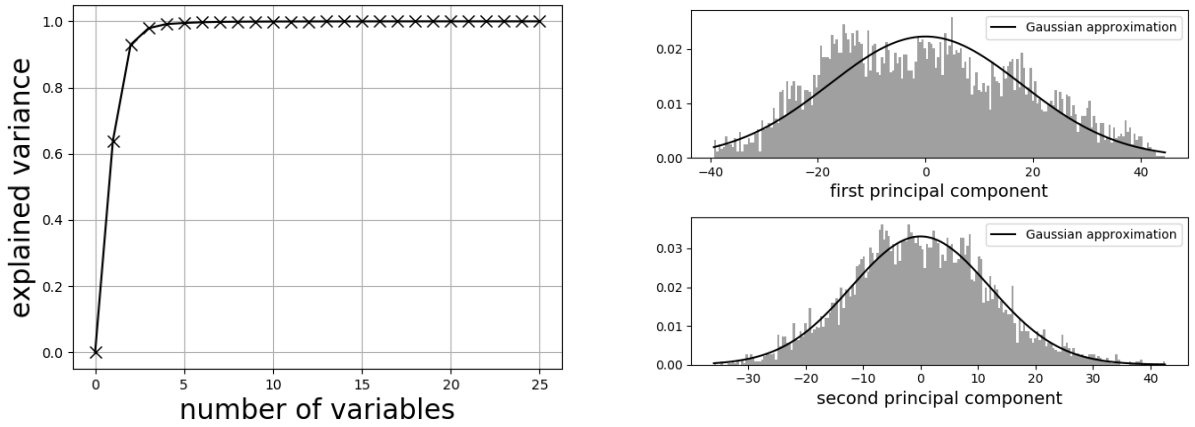

Figure 6.20: Explained variance given by the PCA in function of the number of components (left), and probability distribution of the first two components with their modeling by a normal distribution (right), for the strong downwind cluster.

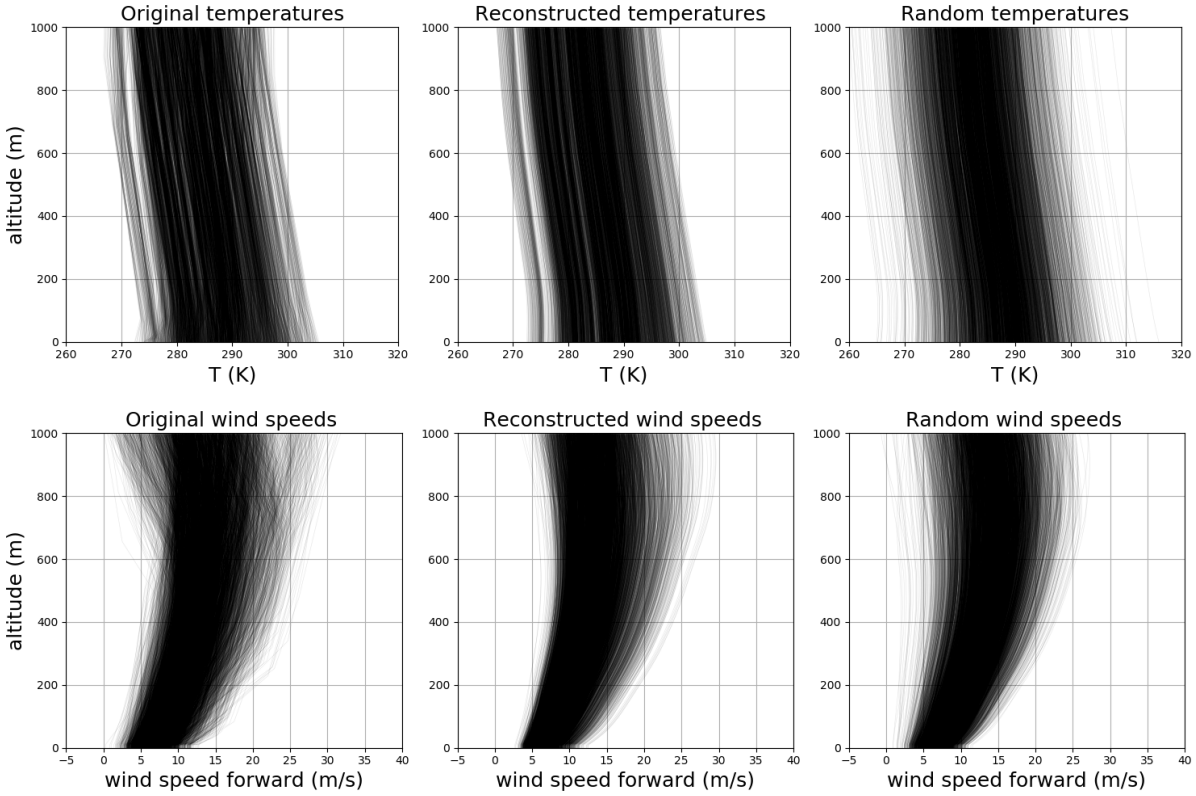

Figure 6.21: For the strong upwind cluster, original temperature profiles (upper left), temperature profiles projected on the two components obtained with the PCA (upper middle), and temperature profiles calculated with 2 random components obeying the Gaussian distributions shown figure 6.16 (upper right). Original wind profiles (lower left), wind profiles projected on the two components obtained with the PCA (lower middle), and wind profiles calculated with 2 random components obeying the Gaussian distributions shown figure 6.16 (lower right).

6.3.2 Results of the stochastic study

Upwind meteorological conditions

The gPC method is applied on the propagation, with the 2 principal components of the PCA as variables. These components are here called cp_0 and cp_1. An order 5 is chosen for the method, which means that 36 couples (cp_0,cp_1) are used, in accord with their probability distributions. This results in 36 different temperature and wind speed profiles. These profiles are plotted on figure 6.22. The transparency of the profiles is related to the weight of the nodes: less likely profiles are less visible. The first component cp_0 has an influence mainly on the temperature, while the second component cp_1 has an influence on the wind speed forward. Wind speed on the ground have values between -10 and 2 m/s, and can vary between -20 and 10 m/s in altitude. It is interesting to note that at some altitudes, mainly 100 m and 900 m, several profiles intersect at a single node. It is not caused by specificities in the probability density, but by the way the couples cp_0 and cp_1 are chosen.

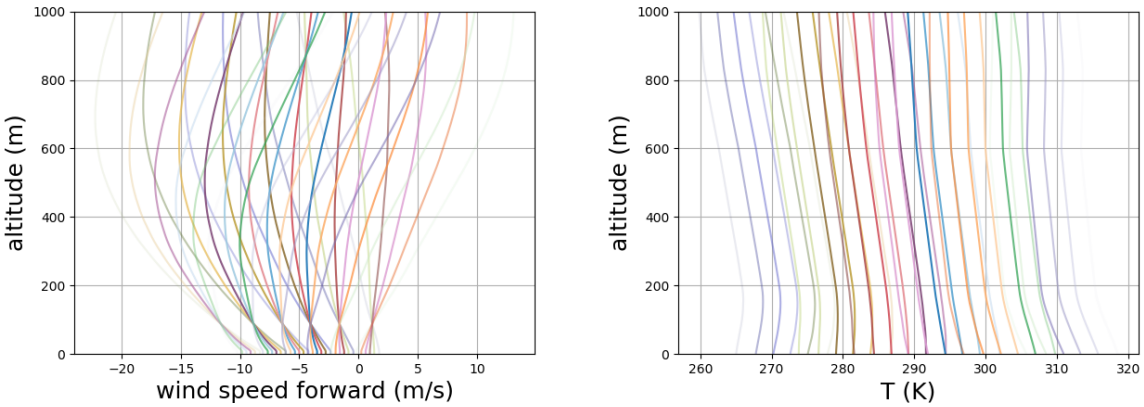

Figure 6.22: Wind and temperature profiles at the nodes of the gPC study, with the transparency depending of the weight of the node.

On figure 6.23 are plotted the simulated waveforms after 4 km of propagation, with the meteorological profiles shown figure 6.22. The colors of the waveforms are the same as their corresponding wind profile. The arrival time is determined by the temperature profile: higher temperatures induce smaller arrival times. Indeed, higher temperature mean higher effective wind speed, which cause the arrival time to be sooner. The normalized peak pressures p_2/P_{ref} are more related to the wind speed profile: higher pressures come from higher wind speeds.

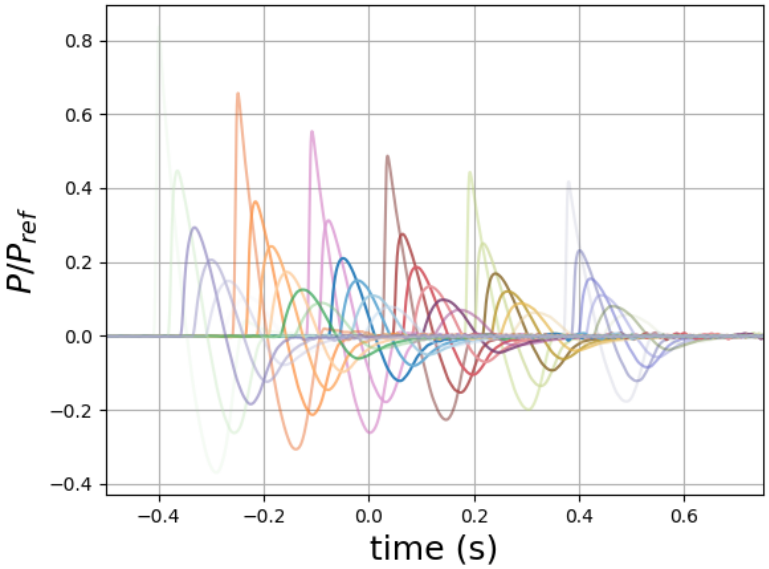

Figure 6.23: Simulated waveforms for the meteorological conditions corresponding to the nodes of the gPC study, at 4 km with the transparency depending of the weight of the node.

These simulations are used to establish a meta-model of the propagation knowing the input variables cp_0 and cp_1. This meta-model gives the ground pressure $p(t, cp_0, cp_1)$ after the propagation. The 2 main properties of these signals are their normalized peak pressure p_2/P_{ref} and their positive phase duration t_d. We can easily deduce from the meta-model the response surfaces of these 2 properties $p_2(cp_0, cp_1)/P_{ref}$ and $t_d(cp_0, cp_1)$. Theses surfaces are plotted on figure 6.24. The peak pressure is influenced by both cp_0 and cp_1, but the influence of cp_1 is higher. For the positive phase duration, only cp_1 has an influence on it. It was previously seen on the profiles that cp_0 is mainly correlated to the temperature profile, while cp_1 is mainly correlated to the wind profiles. Thus, the influence of the wind profiles on the variations is higher. The computation time is around 8 hours for 1 simulation with 2 processors.

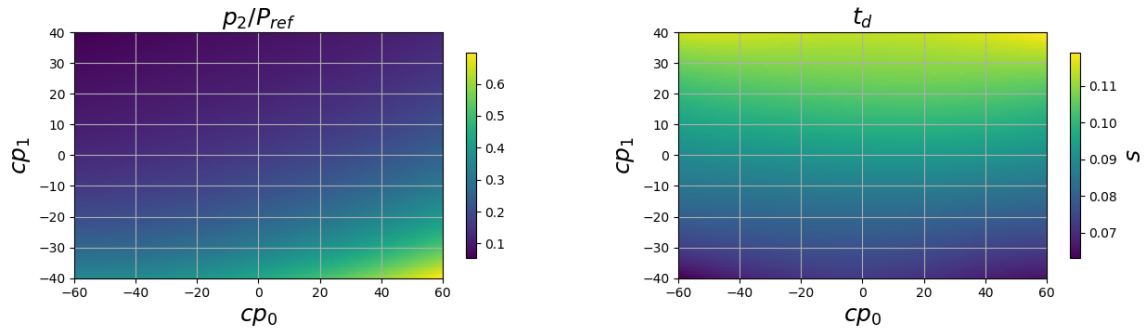

Figure 6.24: Response surface of the normalized pressure (left) and the positive phase duration (right) in function of the gPC parameters: the 2 main components of the PCA.

Knowing the probability distributions of cp_0 and cp_1, a Monte-Carlo analysis is performed, using the meta-model solver to compute 1000000 random realizations of the propagation. This analysis gives us the probability distributions of the normalized peak pressure p_2/P_{ref} and the positive phase duration t_d. These distributions are plotted on figure 6.25 for the upwind meteorological group. The distribution of t_d is really close to a normal distribution, while the distribution of p_2 is a bit skewed toward the lower pressures. 90 % of the normalized peak pressures are contained between 0.11 and 0.28, which is in agreement with the values of the measured waveforms. For t_d, 90 % of the values are between 0.08 and 0.11 s. This is below the measured values, which are mainly between 0.12 and 0.15 s. However, the width of the variation range is similar between the simulations and measures, showing that the variations are well reproduced.

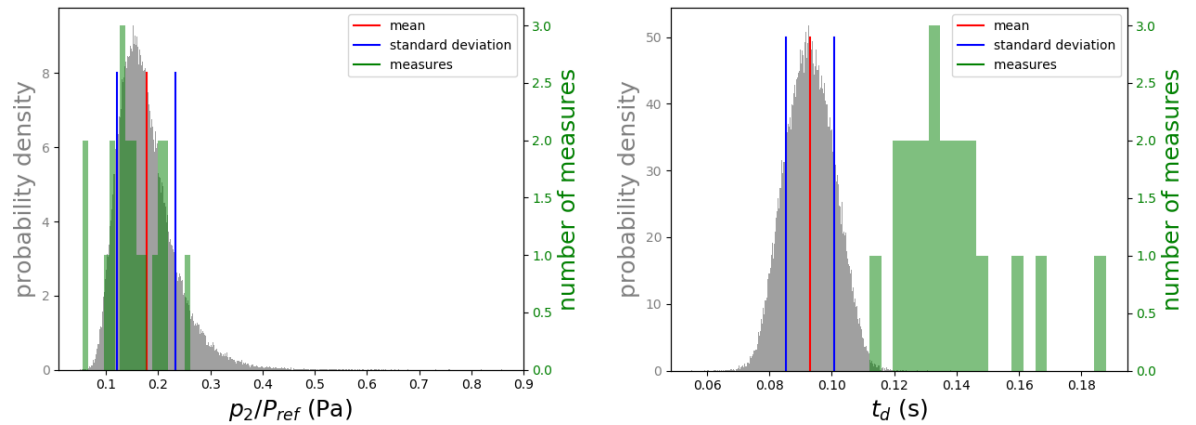

Figure 6.25: Probability density functions for the normalized peak pressure p_2 and the positive phase duration t_d, for the upwind group.

Finally, on figure 6.26 are plotted in red the experimental signals measured at the station MASR with initial charges $W > 480$ kg equivalent TNT and no confinement, and in blue the signals produced by the meta-model, for the couples (cp_0, cp_1) corresponding to the meteorological profiles closest in time to the measures for each of the 8 Arome

positions. This means that there are 8 times more generated signals than measured ones. On figure 6.27 are shown the 8 generated temporal signals which present the largest variations for the same date. This shows that the geographical position of the profile can induce a variability in the propagated waveform. The variation range of the normalized peak pressure is comparable between simulation and measurements, with a maximum under 0.3 and a minimum around 0.1 (except two very low amplitude signals). The difference is more important for the positive phase duration: all the simulated signals have t_d less than the measured one. This difference is supposed to be caused by the relief between the source and MASR station which masks the propagation of high frequencies. The waveforms also have similar shapes.

In conclusion, despite having a higher positive phase duration, the simulations give nonetheless a good approximation of the propagated waveforms, for the upwind meteorological conditions: the measured peak pressures are contained within the uncertainty of the simulations, and the width of the simulated positive phase duration is similar with its experimental range.

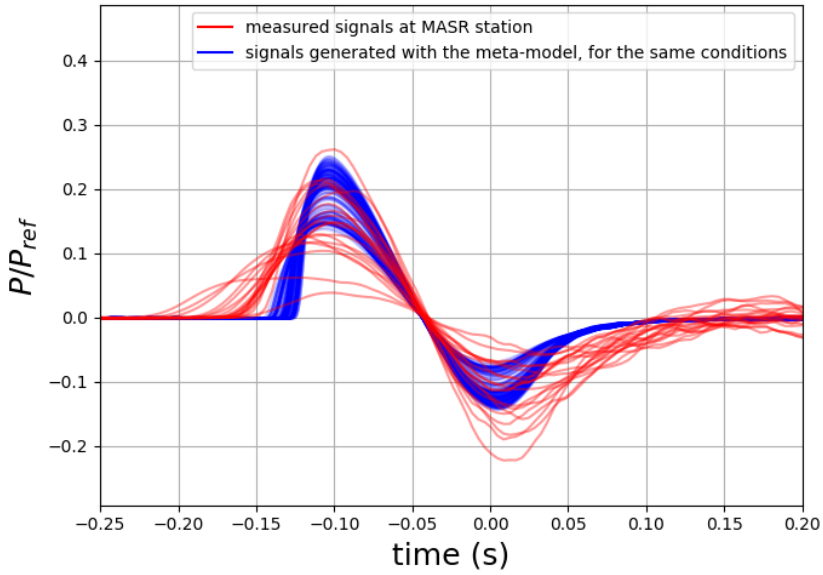

Figure 6.26: Signals measured at the MASR station for the upwind meteorological conditions, with an initial charge $W > 480\,\text{kg}$ equivalent TNT and no confinement (red) and signals generated with the meta-model, for the variables (cp_0, cp_1) corresponding to the profiles closest to the times of the measured waveforms, for each of the 8 Arome positions (blue).

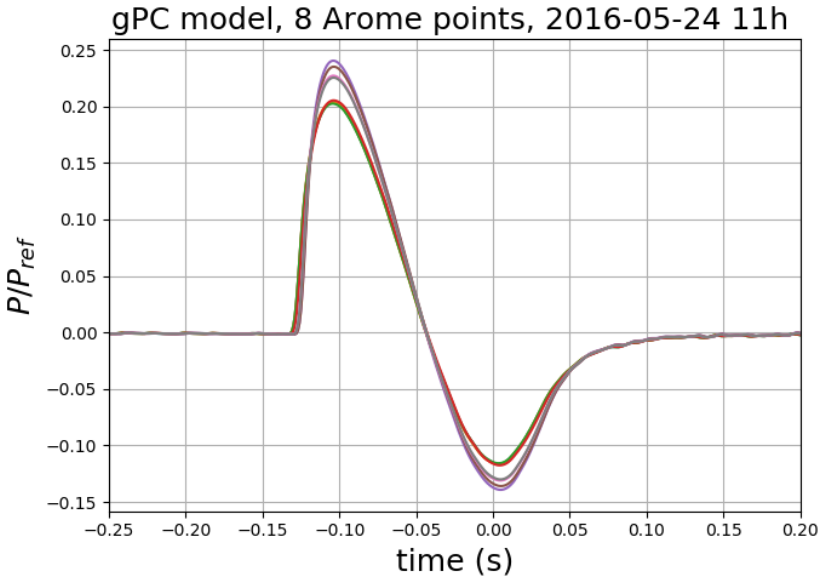

Figure 6.27: Signals generated with the meta-model, for the variables (cp_0, cp_1) corresponding to the profiles of the 8 Arome positions, for the indicated date.

Weak wind meteorological conditions

As previously, the gPC method is applied on the propagation, with the 2 principal components of the PCA as variables. Because the PCA is done with different data, cp_0 and cp_1 are not the same variables as for the upwind conditions. The order of the gPC method is 5, the same value as previously. The profiles are plotted on figure 6.28. The first component cp_0 still has an influence mainly on the temperature, while the second component cp_1 has an influence on the wind speed forward. Wind speed on the ground have values between -5 and 5 m/s, and can vary between -8 and 8 m/s in altitude. Nodes were several profiles intersect are still present, bu here around 200 m.

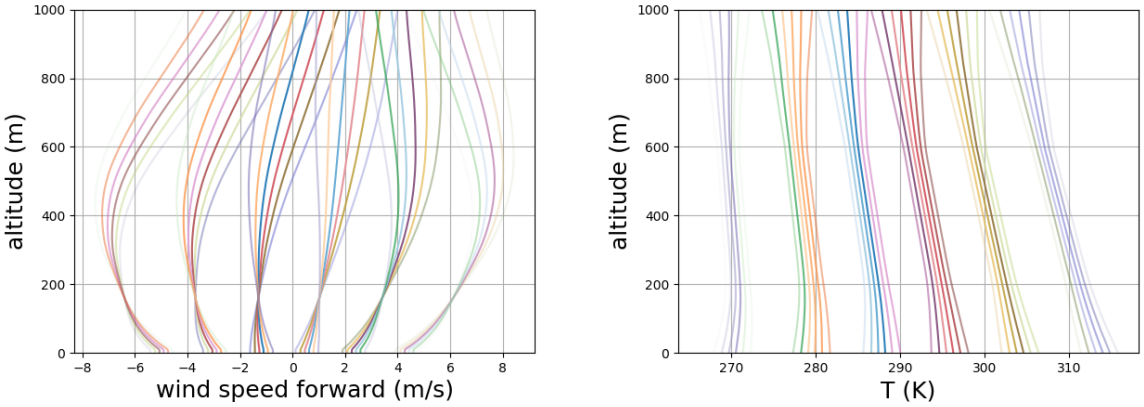

Figure 6.28: Wind and temperature profiles at the nodes of the gPC study, with the transparency depending of the weight of the node for the weak wind meteorological group.

On figure 6.29 are traced the simulated waveforms after 4 km of propagation, with

the previous meteorological profiles. The colors of the waveforms are the same as their corresponding wind profile. The normalized peak pressures varies between 0.15 and 1.35. Note that the maximal normalized measured peak pressure is by definition equal to 1: having simulation with normalized pressure above 1 shows a mismatch with the measures. However, these signals above 1 have a low weight, and thus correspond to unlikely events, and have a low influence on the meta-model.

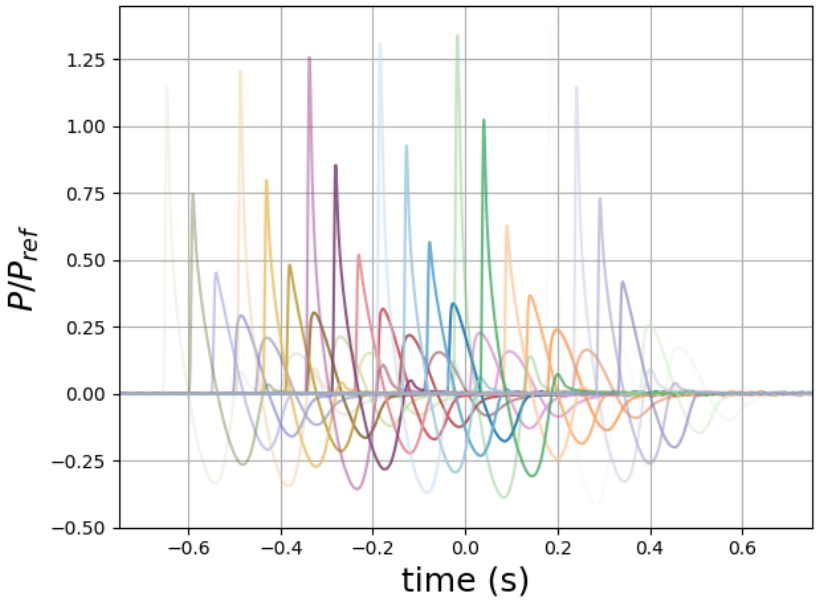

Figure 6.29: Simulated waveforms at the nodes, with the transparency depending of the weight of the node.

The meta-model of the propagation is used to obtain the ground pressure $p(t, cp_0, cp_1)$ after the propagation. The response surfaces of the 2 properties of the waveforms $p_2(cp_0, cp_1)/P_{ref}$ and $t_d(cp_0, cp_1)$ are traced on figure 6.30. The peak pressure is still influenced by both cp_0 and cp_1, with a higher influence of cp_1. For the positive phase duration, the variations come mainly from cp_1, but cp_0 has now a small effect.

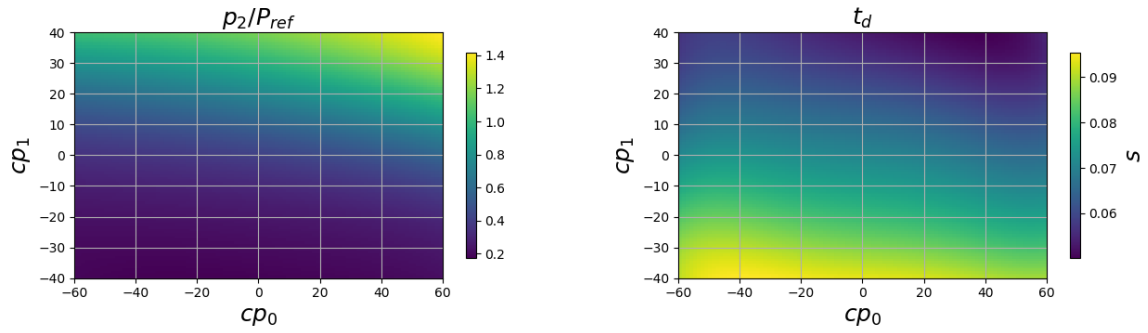

Figure 6.30: Response surface of the normalized pressure (left) and the positive phase duration (right) in function of the gPC parameters: the 2 main components of the PCA.

Knowing the probability distributions of cp_0 and cp_1, a Monte-Carlo analysis is performed, using the solver to compute 1000000 random realizations of the propagation. This analysis give us the probability distributions of the normalized peak pressure p_2/P_{ref} and the positive phase duration t_d. These distributions are plotted on figure 6.31. The shape of the distributions are similar to the upwind group, with the distribution of t_d being close to a normal distribution, and the distribution of the normalized p_2 being skewed to the lower values. However, the peak pressures are higher with more variations, while the positive phase durations are lower than for the upwind. These tendencies are also observed for the measured signals: upwind measured pressures are lower and upwind measured phase durations are longer than from the weak wind group. For p_2, 90 % of the normalized values are between 0.24 and 0.82. In comparison, the measured values are mainly between 0.2 and 0.4, with a single event above 0.8. The peak pressure values and variations are thus overestimated in this case. For t_d, 90 % of the values are between 0.06 and 0.08 s which is as before an underestimation of the positive phase duration, but the width of the variations is still comparable to the measurements. it is interesting to note that the probability distribution shows that the most likely normalized pressures are around 0.3, which is also observed in the measured signals.

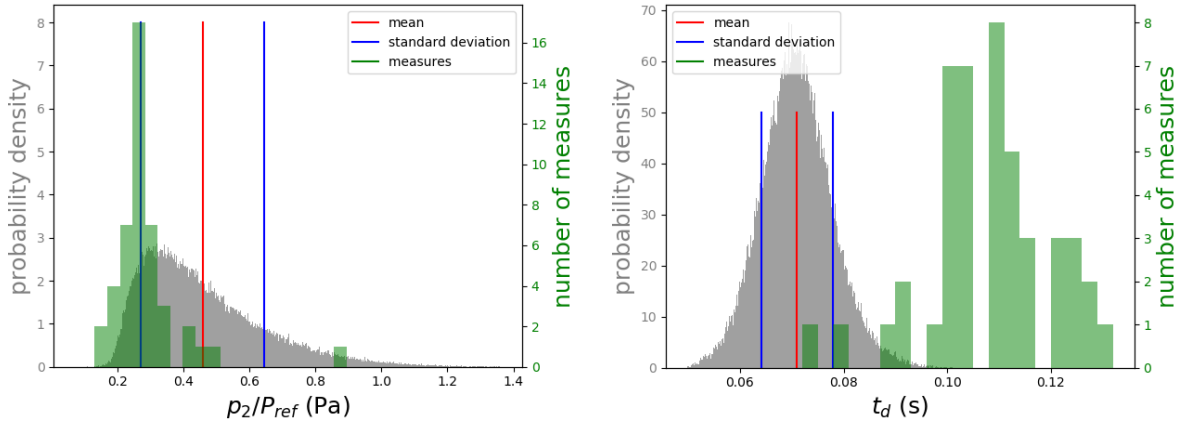

Figure 6.31: Probability density functions for the peak pressure p_2 and the positive phase duration t_d.

Finally, on figure 6.32 are plotted in red the experimental signals measured at the station MASR with an initial charge $W > 480\,\text{kg}$ equivalent TNT and without confinement, and in blue the signals produced by the meta-model, for the couples (cp_0, cp_1) corresponding to the meteorological profiles closest in time to the measures for each of the 8 Arome positions. The lower simulated pressures are comparable to the experimental ones, with normalized pressures between 0.2 and 0.4, but higher pressure are obtained with the simulation, which are not attained in the measures (with 1 exception). These higher pressures correspond to profiles with positive wind speeds forwards. As before, the positive phase durations are lower for the measurements.

This time, the waveforms obtained thanks to the simulations and the meta-model are less realistic than before, with pressures too high and positive phase durations to low. These differences with the measures should mainly be caused by the coupling between the relief and the meteorological conditions. For p_2, the uncertainty observed with the gPC method is also higher than the measured one.

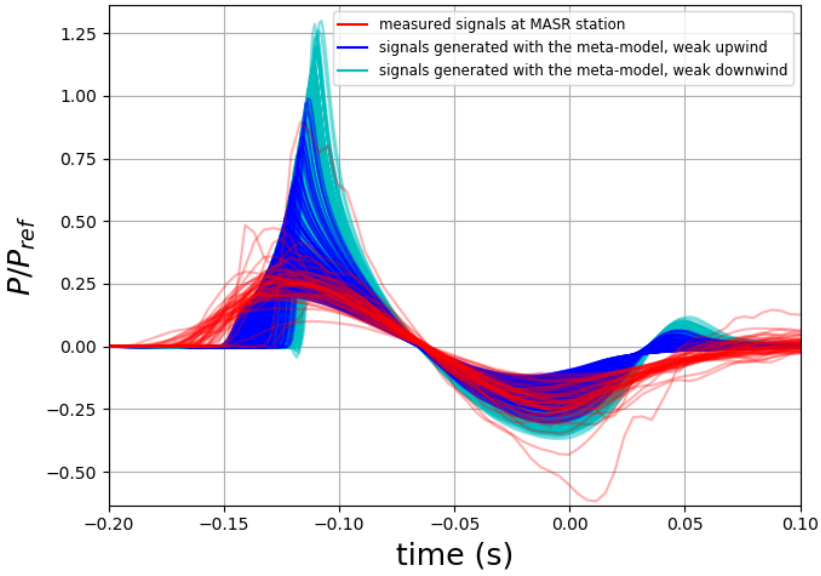

Figure 6.32: Signals measured at the MASR station for the weak wind meteorological conditions, with an initial charge $W > 480\,\text{kg}$ equivalent TNT and without confinement (red) and signals generated with the meta-model, for the variables (cp_0, cp_1) corresponding to the profiles closest to the times of the measured waveforms, for each of the 8 Arome positions, with positive ground upwind (cyan) and negative ground upwind (blue).

Downwind meteorological conditions

Finally, the gPC method is applied on the propagation for the strong downwind conditions, with the 2 principal components of the PCA as variables. These components are still called cp_0 and cp_1, but are not the same variables as previously. The order for the gPC method is now 9, because the waveforms for the upwind conditions are more complex. The profiles are plotted on figure 6.33. This time, the effect of the variables on the stratifications is not as clear as previously: the variations in the temperature profile are still caused by cp_0, but both cp_0 and cp_1 have a strong effect on the wind speed forward profile. Wind speed on the ground have values between -2 and 13 m/s, and can vary between -10 and 40 m/s in altitude.

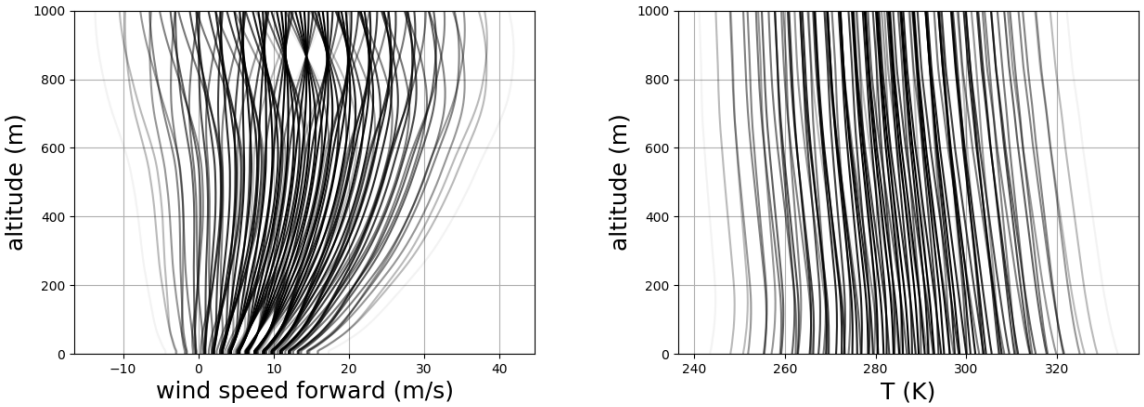

Figure 6.33: Wind and temperature profiles at the nodes of the gPC study, with the transparency depending of the weight of the node.

On figure 6.34 are plotted the simulated waveforms after 4 km of propagation, with the previous meteorological profiles. A lot of the waveforms have a normalized peak pressure above 1, which corresponds to the maximal measured peak pressure. There are still some low signals, with normalized peak pressures around 0.3, but they are not likely. For some signals, which mainly correspond to high cp_0, a second peak appear on the waveforms, which means that the atmospheric profile caused a second arrival of the signal. 2D configurations with 1 and 2 peaks are shown on figure 6.35, and their atmospheric profiles are shown figure 6.36. As expected, a waveguide is present for the 2 pics configuration, which causes the second arrival of the signal.

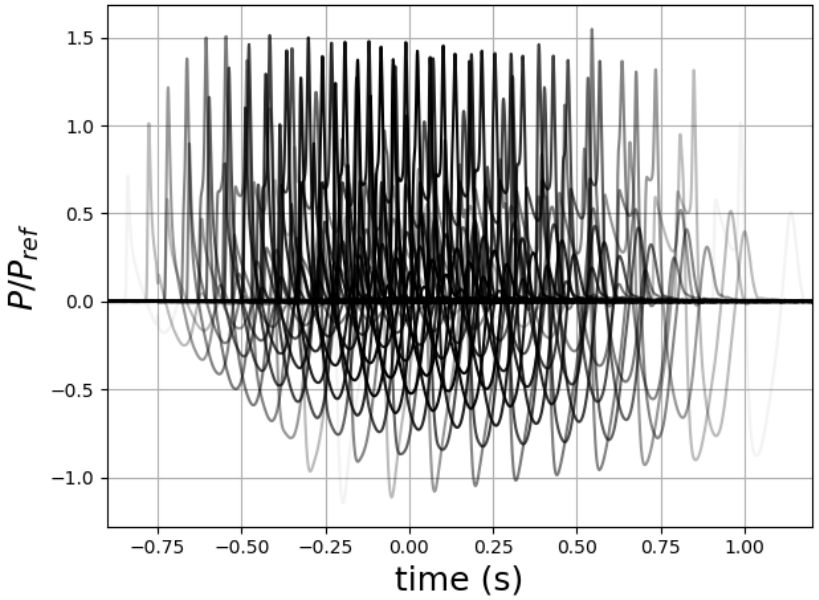

Figure 6.34: Simulated waveforms at the nodes, with the transparency depending of the weight of the node, for the downwind group.

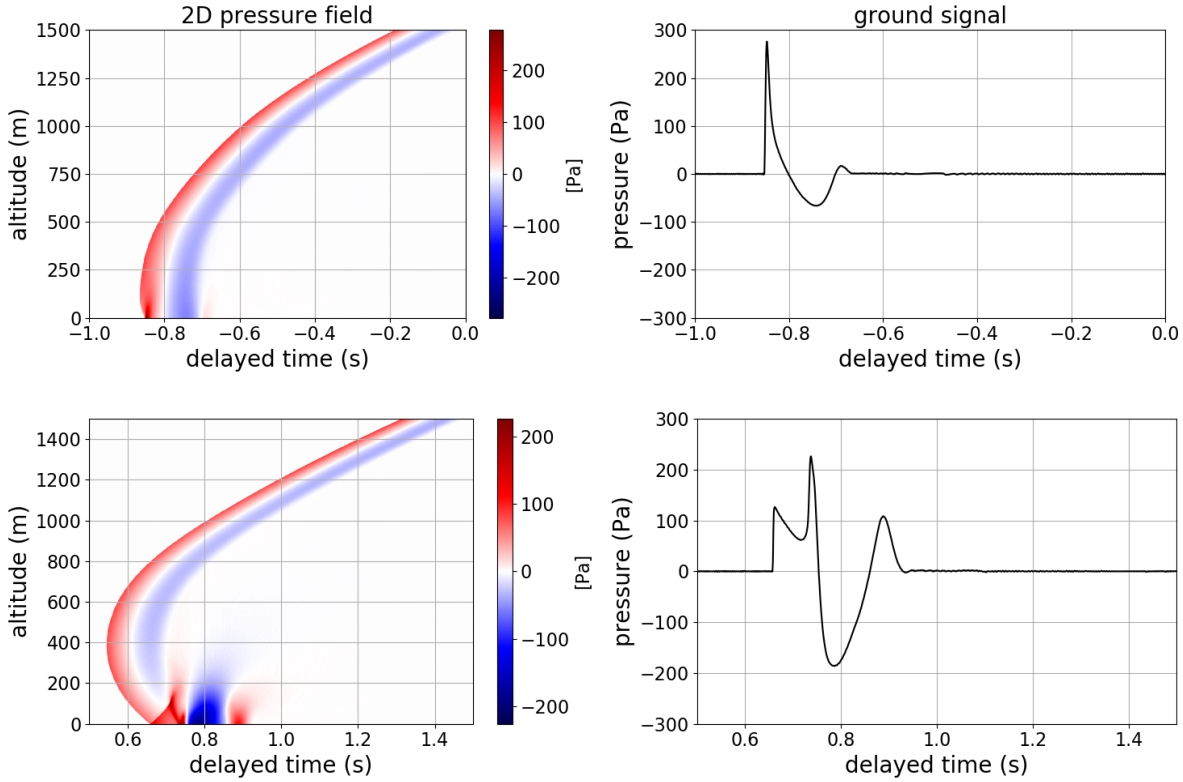

Figure 6.35: 2D pressure field (left) and ground signals (right) after propagation for a case with a low cp_0 (up) and a high cp_0 (down).

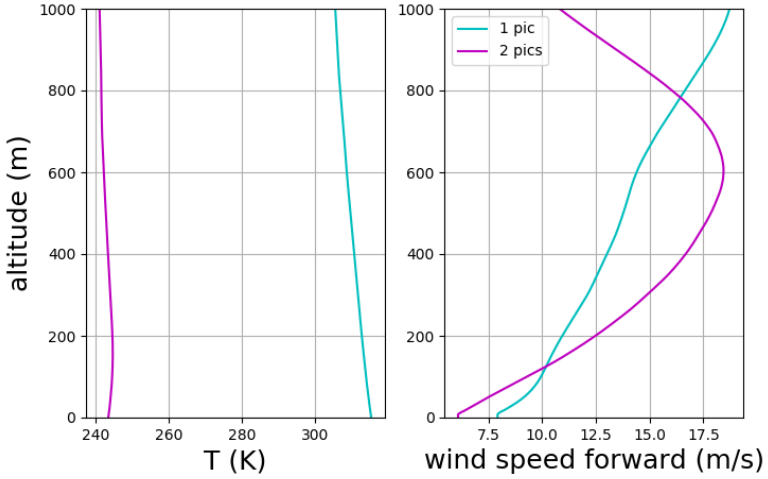

Figure 6.36: Temperature (left) and wind speed forward (right) profiles for the 2 configurations figure 6.35.

The meta-model of the propagation is used to obtain the ground pressure $p(t, cp_0, cp_1)$ after the propagation. The response surfaces of the 2 properties of the waveforms $p_2(cp_0, cp_1)/P_{ref}$ and $t_d(cp_0, cp_1)$ are traced on figure 6.37. The normalized peak pressure is still mainly

influenced by cp_1, but has small variations with values around 1.5 for $cp_1 > 0$. For the positive phase duration, the variations come mainly from cp_1. These response surfaces are more complex than previously and the variations on the boundaries are a potential sign of problems with the method.

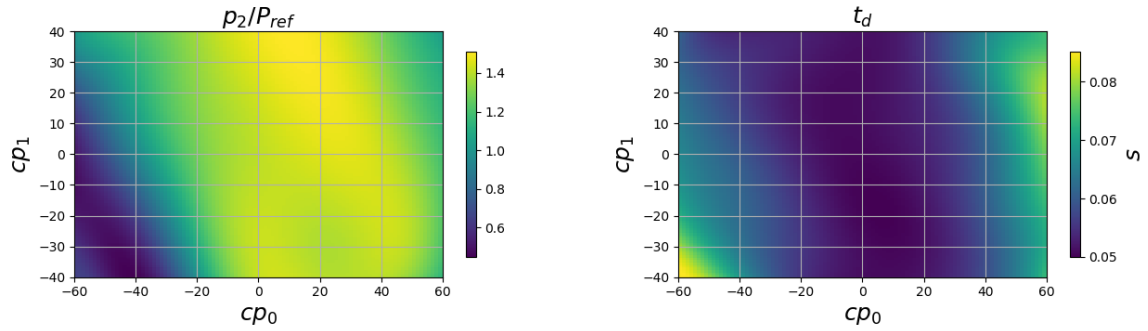

Figure 6.37: Response surface of the normalized pressure (left) and the positive phase duration (right) in function of the gPC parameters: the 2 main components of the PCA.

Knowing the probability distributions of cp_0 and cp_1, a Monte-Carlo analysis is performed, using the gPC solver to compute 1000000 random realizations of the propagation. This analysis gives us the probability distributions of the normalized peak pressure p_2/P_{ref} and the positive phase duration t_d. These distributions are plotted on figure 6.38. This time, the distributions are highly different from before: The normalized peak pressure distribution is strongly skewed towards the high pressures, and is extremely peaked at 1.4, while the positive phase duration is strongly skewed towards the low t_d, and are extremely peaked around 0.050 s. These distributions seem less realistic than before. The mean of the normalized peak pressure is above 1.3, considerably higher than the maximal measured peak pressure, while the mean of t_d is around 0.053, lower than for the other 2 groups. The measured peak pressures are also higher and the measured positive phase durations also lower than the other 2 groups, but with a smaller difference than for the simulations.

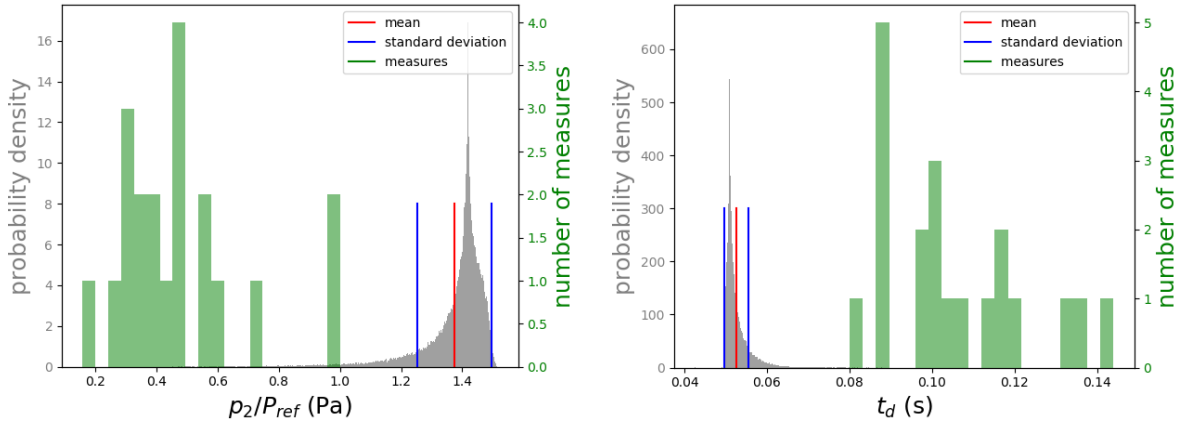

Figure 6.38: Probability density functions for the peak pressure p_2 and the positive phase duration t_d.

Finally, on figure 6.39 are traced in red the experimental signals measured at the station MASR with an initial charge $W > 480\,\text{kg}$ equivalent TNT and without confinement, and in blue the signals produced by the meta-model, for the couples (cp_0, cp_1) corresponding to the meteorological profiles closest in time to the measures for each of the 8 Arome positions. This time, the differences between the measured and simulated peak pressures, as well as in the positive phase durations are very important. In this situation, the coupling between the relief and the meteorological conditions make it difficult to predict the waveforms.

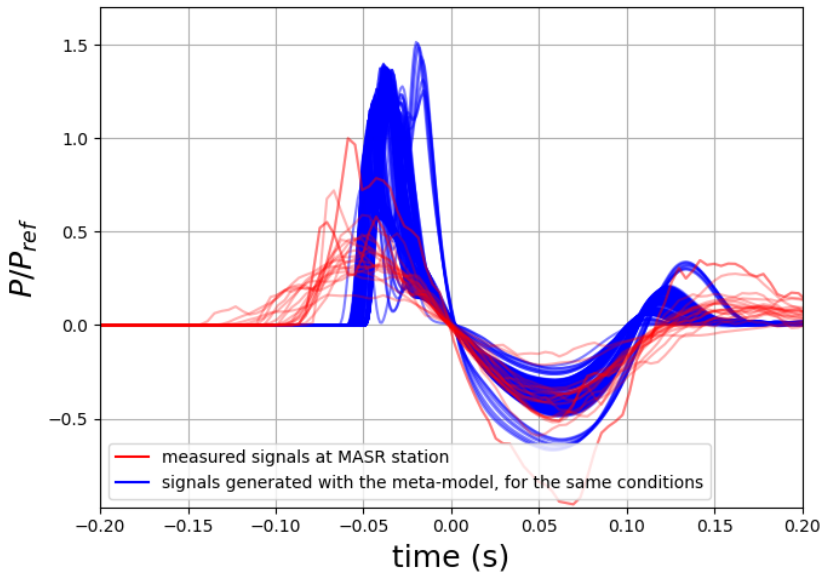

Figure 6.39: Signals measured at the MASR station for the strong downwind meteorological conditions, with an initial charge $W > 480\,\text{kg}$ equivalent TNT and no confinement (red) and signals generated with the meta-model, for the variables (cp_0, cp_1) corresponding to the profiles closest to the times of the measured waveforms, for each of the 8 Arome positions (blue).

6.3.3 Influence of the wind conditions on the propagation over a flat ground

With the meta-models, we can more precisely compare the 3 meteorological groups. The distributions of the peak pressure p_2 and the positive phase duration t_d for the 3 groups are shown on the upper part of figure 6.40. The distributions shows that, as observed in the deterministic study, pressures are lower for the upwind conditions and higher for the downwind conditions, and that its the opposite for the positive phase duration. The weak wind group also shows a higher range of variations than the other groups for the pressure, while for the positive phase duration, there are more variations in the upwind group. Waveforms computed with the meta-model are also plotted in the lower part of figure 6.40. As before, the upwind group has very rounded waveforms, the weak wind group has both rounded and peaked waveforms, while the downwind group has peaked waveforms, and sometimes more than one peak, which is the sign of a second arrival of the signal. Note that the confidence in the results for the strong downwind is low.

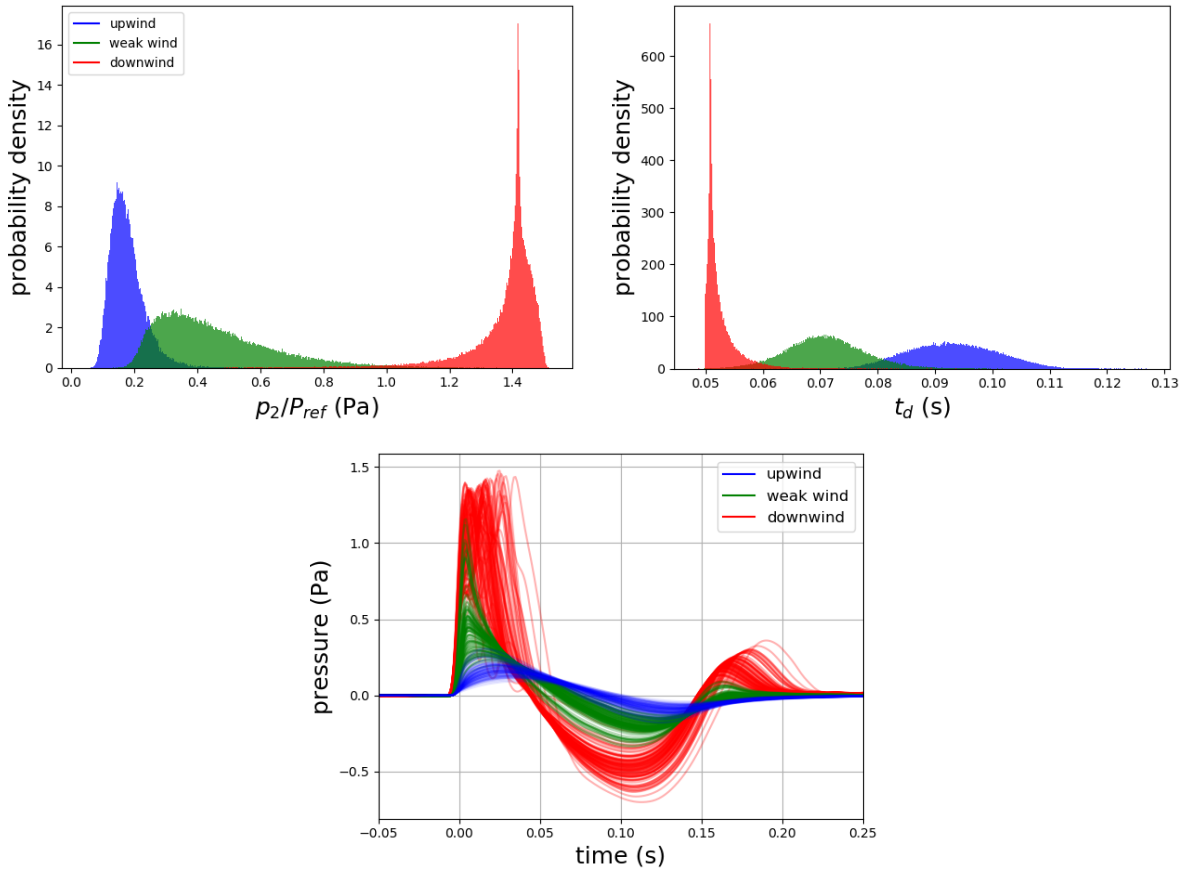

Figure 6.40: Probability densities of the normalized peak pressure (upper left) and the positive phase duration (right), and waveforms generated with the meta-model solver, with random variables following the probability distributions as inputs, for the 3 meteorological groups (with 100 waveforms per group) (down).

6.4 Conclusion

In this chapter, a study of the propagation of shock waves on the pyrotechnical site of Rivesaltes has been carried out. Deterministic simulations has been computed for these 3 groups. The positive phase duration is always underestimated by the simulations. This is supposed to be caused by the absence of topography in the FLHOWARD3D model. For the upwind group, the measured and simulated signals have a good similarity, while there are a lot of differences for the downwind group. The weak wind group has good results for weak upwind profiles, and worse results for weak downwind profiles. For each group, a principal components analysis has been performed on the available profiles, in order to characterize a group with a small number of variables. In each case, 2 variables, which explain around 90 % of the variations are selected.

Then a gPC method is performed with these 2 variables, and meta-models of the propagation are obtained, and used to determine the uncertainty of the propagated signals. As expected, positive phase durations are always underestimated, but the width of the variations is consistent with the measured values for the upwind and weak wind groups. For upwind, the measured peak pressures are well contained within the uncertainty of the model, while the weak wind group overestimate the peak pressure and the width of its variation. However, the most likely pressure is well approximated. Finally, as expected from the deterministic study, the downwind groups gives values and waveforms far from the experimental ones, probably because of combined effects of meteorological properties and relief, which is not taken into account in this study, as well as the complexity of the waveforms, which make it more difficult to have good results with the gPC method. A comparison between the meteorological groups is done for the propagation over a flat ground, which showed that upwind condition induce lower pressures and higher positives phases durations.

In conclusion, the uncertainty caused by the propagation has been well obtained in case of upwind conditions, but the absence of the influence of the relief in the numerical solver makes it difficult to obtain reliable results for the downwind conditions. It would be interesting to reproduce this study with a numerical solver taking into account the relief of the propagation medium, or include the relief in the FLHOWARD3D code, in order to have better results for the downwind conditions.

Chapter 7

Conclusion and Outlooks

7.1 Conclusion

In this thesis, the propagation of shock waves generated by supersonic aircraft and by explosions is studied, and the uncertainty of the results caused by atmospheric effects at different scales are investigated.

In chapter 2, the propagation code is described. The code FLHOWARD3D is based on a scalar wave equation considering diffraction without angle restriction, heterogeneities, absorption, relaxation and non-linearities. This makes it a high-fidelity solver since it includes numerous physical effects. It can simulate various configurations and has been especially designed for plane and cylindrical shock waves. Thanks to adaptations made during this thesis, it is now possible to mimic the spherical spreading in two-dimensional simulations and to downgrade the FLHOWARD3D solver into a KZK one, thus enabling a comparison between these two different approaches.

Chapter 3 is devoted to the numerical simulation of the propagation of classical and low boom signatures through turbulence. Optimal spatial and temporal samplings are determined by convergence studies. It is found that the spatial scale to use for the turbulence model should include structures whose sizes are greater than around one fifth of the characteristic wavelength of the incoming sonic boom. This result is essential to optimize the parameters required for the synthetic turbulence generation. Two models are introduced to account for the turbulence in the planetary boundary layer. They both use spectral methods with a von Kármán spectrum. The first one is homogeneous and does not consider temperature turbulence (only kinetic turbulence), while the second one is stratified with altitude for both temperature and wind turbulence. Comparisons between these two turbulence models and also test flight data from the literature, show that there are no significant differences between the two from the acoustical point of view. Using the optimal numerical parameters and the homogeneous von Kármán model, we have been able to simulate challenging 3D configurations for different kinds of signatures. For comparable peak pressures, classical booms tend to have higher pressures than low-boom signatures. Comparisons between 2D and 3D configurations with experimental measurements show that the statistical results are very close to one another: 2D propagation results are shown to be accurate for 98 % of cases compared to data, while 3D outputs are accurate for 99.8 % of the cases. Therefore, the whole numerical methodology is shown valid to simulate the propagation of sonic booms through kinetic turbulence, even with a

two-dimensional computational domain. This opens the way to a statistical treatment.

Chapter 4 focuses on this stochastic study. In this chapter, the atmosphere turbulence is considered as uncertain. It is parameterized by two physical parameters of the von Kármán model, the amplitude of the turbulence σ and its characteristic length L_0. The third parameter, the random vector $\underline{\mathrm{R}}$, which describes the inherent randomness of the turbulence, is fixed for a given study. A meta-model of the propagation is built with a generalized Polynomial Chaos method (gPC). It makes available ground signatures for all values of physical parameters with very low computational resources (no further simulations are required once the metamodel is built). So, it is possible to get a large numerical database of signatures taking into account turbulence effects and to use them for statistics or other purposes such as perceptive studies. In particular, we use them to obtain the probability density function which is important in order to analyze the characteristics of the signatures and its associated metrics. Effects of σ and L_0 are located near the shocks while the global randomness (vector $\underline{R}$) changes the global waveform. We observe that the standard deviation increases with the distance (cumulative effects of turbulence) and also depends on the boom signature (the N-wave is more sensitive than the low-booms) and on the metrics. This is an encouraging result regarding the robustness of sonic boom mitigation.

Chapter 5 provides an analysis of blast wave signatures generated by an industrial process recorded at different distances (between 300 m and 20 km) from the pyrotechnic site of Rivesaltes (South of France). This database has been acquired by CEA and also includes the characteristics of the source, the topography, and meteorological parameters at different positions and altitudes. This database cover a period of about four years. Depending on the conditions of propagation, a large variety of signatures is observed at the different stations, showing the great variability induced in particular by the medium of propagation. Using clustering methods, meteorological data have been classified into three groups depending on the wind direction and speed. Considering the source parameters, they have been classified into four groups depending mainly on the kind of explosives and whether it is confined or not. It is found that the knowledge of the meteorological properties on the ground only is insufficient, and that the wind and the temperature profiles are required for a more accurate description. This analysis makes the database a valuable tool to investigate effects of the meteorological conditions on the propagation of weak shock waves and to validate numerical methods for outdoor propagation.

Finally, chapter 6 deals with the simulation of the propagation of blast waves for conditions close to the ones of the experimental database described in the previous chapter. The initial signature is supposed to be a reference waveform whose parameters are chosen to be representative for the experimental results. First a deterministic study is made. Following the classification of chapter 5, the propagation conditions are divided into three groups (upwind, weak wind and downwind). For each group, about 20 atmospheric profiles are selected for numerical simulations of propagation. The comparisons with the experimental data show a good agreement for upwind conditions and a less satisfying one for downwind conditions (with a strong overestimation of the pressure). The comparison is in between for the weak wind cluster. We assume that the poor comparison in downwind case is due to the fact that the influence of topography is not taken into account in FLHOWARD3D code, while it has a stronger influence on the waveforms. In a second part, to obtain a better statistical description of the different regimes, a stochastic study

is needed. For this purpose, the different propagation conditions are parameterized to get a reduced model of the medium of propagation. To minimize the number of random variables, a Principal Component Analysis (PCA) has been applied on the meteorological profiles. It is shown that two variables are sufficient to statistically describe the observed variations. These variables are then considered as random variables in the gPC method to get a meta model for each of the three groups. In the upwind case, the agreement between the metamodel and the data remains very satisfying for the peak pressure. This study therefore shows the relevance of the proposed methodology which is able to produce numerous signatures at various locations in a few seconds by using the metamodel, just knowing the meteorological profile. It is a powerful method to predict the sound levels in a context of industrial exploitation.

The ambition of this thesis was to show that it is relevant to couple a high fidelity acoustic solver like FLHOWARD3D with a non-intrusive uncertainty quantification method. The results demonstrate that that coupling is necessary for a better understanding of the physics of propagation in media with uncertain properties, and that it is also efficient to build predicting tools based on such metamodel. This study paves the way to a better statistical description of outdoor sound propagation, but could be improved following different suggestions discussed in the outlooks.

7.2 Outlooks

First, the metamodel relying on only one observation station (at around 4 km from the source) in chapter 6 could be reproduced at different distances so as to obtain a more exhaustive knowledge of the propagation. However, with the existing numerical tools, it would again face the issue of topography.

Therefore, besides the effects of diffraction, heterogeneities, absorption, relaxation and nonlinearities on shock wave propagation, the next step should be to consider topography, which can significantly influence shock wave propagation, especially for the blast wave case, as the source is located on the ground. For example, in chapter 6, the shorter positive phase duration for the simulation compared to the measurements was attributed to the lack of topography in the simulation. The pressure overestimation for downwind conditions also probably arises from an interaction between wind and relief. Considering topography would lead to more realistic results. However, it would imply an atmosphere description consistent with the land elevation, which implies in particular that the assumption of a stratified atmosphere is questionable.

Another improvement regarding the description of the atmosphere, could be to add turbulent wind fluctuations to the atmospheric model of chapters 5 and 6. Indeed, the study was achieved with wind and temperature profiles as the only meteorological effects, but turbulent wind fluctuations are likely important. The distribution of the turbulence parameters σ and L_0 introduced for sonic-boom could be obtained from meteorological simulations. This would give a finest understanding of the influence of the atmosphere on blast waves propagation. In the same way, for sonic boom, the atmospheric model could also include the temperature and wind profiles, even though the kinetic turbulence is expected to be dominant.

Further studies could also improve the source modeling. In chapter 6, the measured data close to the source are not incorporated because topographic effects induce distortions

on the signatures. Starting from measurements, more realistic source waveforms could be deduced, by means of CFD codes or even by machine learning [86].

The stochastic studies were realized for 2D media. This approximation has been validated only for the sonic boom case, even though 3D simulations are preferable. Thus, 3D stochastic studies would be useful to complement and confirm our 2D observations, especially for the blast wave case.

There are several ways to improve the metamodel, for instance by increasing its order or the number of input variables. For instance, in this work, the meteorological profiles are modeled by 2 random variables which represent around 90 % of the variance. Increasing their number would likely lead to a more accurate model. An even more desirable feature would be to be able to use independent probability functions for each random variable. For example, in the case of the parameterization of the upwind atmospheric profiles, it could be interesting to introduce a bi-modal law for cp_0 and a modal one for cp_1. Recent studies on quantification uncertainty show the feasibility of this approach which would be worth implementing in our framework [120, 128].

Finally, the waveforms database gathered in chapter 4 could also be used for future perceptive studies, because it provide a variety of pressure signatures with different shapes and rise times, caused by kinetic turbulence and close to measured ones.

Bibliography

[1] ISO 9613-1. Acoustics—attenuation of sound during propagation outdoors—part 1: Calculation of the absorption of sound by the atmosphere, 1993.

[2] White Sands Missile Range Museum Archives. http://www.wsmr-history.org/archives.htm, 2022.

[3] M. Averiyanov. *Propagation des ondes acoustiques à travers un milieu turbulent: Etudes théorique et expérimentale des effets de diffraction et des effets non linéaires*. PhD thesis, Ecully, Ecole centrale de Lyon, 2008.

[4] M. Averiyanov, P. Blanc-Benon, R. O Cleveland, and V. Khokhlova. Nonlinear and diffraction effects in propagation of N-waves in randomly inhomogeneous moving media. *The Journal of the Acoustical Society of America*, 129(4):1760–1772, 2011.

[5] M. Averiyanov, S. Ollivier, V. Khokhlova, and P. Blanc-Benon. Random focusing of nonlinear acoustic N-waves in fully developed turbulence: Laboratory scale experiment. *The Journal of the Acoustical Society of America*, 130(6):3595–3607, 2011.

[6] M.V. Averiyanov, V.A. Khokhlova, O.A. Sapozhnikov, P. Blanc-Benon, and R.O. Cleveland. Parabolic equation for nonlinear acoustic wave propagation in inhomogeneous moving media. *Acoustical Physics*, 52(6):623–632, 2006.

[7] D. G. Baize, P. G. Coen, L. P. Ozoroski, and K. Domack. A performance assessment of eight low-boom high-speed civil transport concepts. In *High-Speed Research: 1994 Sonic Boom Workshop*, page 149, 1999.

[8] M. Baudoin, F. Coulouvrat, and J.-L. Thomas. Sound, infrasound, and sonic boom absorption by atmospheric clouds. *The Journal of the Acoustical Society of America*, 130(3):1142–1153, 2011.

[9] A. B. Bauer and C.J. Bagley. Sonic boom modeling investigation of topographical and atmospheric effects. Technical report, Douglas aircraft co long beach CA, 1970.

[10] A. Bechmann, N. Sorensen, and J. Johansen. Atmospheric flow over terrain using hybrid RANS/LES. In *Proceedings of The European Wind Energy Conference and Exhibition (EWEC 2007), Milan, Italy*, 2007.

[11] M. V. Berry. Waves and thom's theorem. *Adv. Phys.*, 25:1–26, 1976.

[12] P. Blanc-Benon and D. Juvé. Intensity fluctuations of spherical acoustic waves propagating through thermal turbulence. *Waves in random media*, 3(2):71, 1993.

[13] P. Blanc-Benon, D. Juvé, V.E. Ostashev, and R. Wandelt. On the appearance of caustics for plane sound-wave propagation in moving random media. *Waves in Random media*, 5(2):183, 1995.

[14] P. Blanc-Benon, B. Lipkens, L. Dallois, M. F. Hamilton, and D. T. Blackstock. Propagation of finite amplitude sound through turbulence: Modeling with geometrical acoustics and the parabolic approximation. *The Journal of the Acoustical Society of America*, 111(1):487–498, 2002.

[15] R. Blumrich, F. Coulouvrat, and D. Heimann. Meteorologically induced variability of sonic-boom characteristics of supersonic aircraft in cruising flight. *The Journal of the Acoustical Society of America*, 118(2):707–722, 2005.

[16] R. Blumrich, F. Coulouvrat, and D. Heimann. Variability of focused sonic booms from accelerating supersonic aircraft in consideration of meteorological effects. *The Journal of the Acoustical Society of America*, 118(2):696–706, 2005.

[17] P. Boulanger, R. Raspet, and H.E. Bass. Sonic boom propagation through a realistic turbulent atmosphere. *The Journal of the Acoustical Society of America*, 98(6):3412–3417, 1995.

[18] K. Bradley, C. Hobbs, C. Wilmer, V. Sparrow, T. Stout, J. Morgenstern, K. Underwood, D. Maglieri, R. Cowart, Matthew T M. Collmar, H. Shen, and P. Blanc-Benon. Sonic booms in atmospheric turbulence (SONICBAT): The influence of turbulence on shaped sonic booms. Technical report, NASA/CR 2020 220509, 2020.

[19] H. L. Brode. Numerical solutions of spherical blast waves. *Journal of Applied physics*, 26(6):766–775, 1955.

[20] H. L. Brode. Blast wave from a spherical charge. *The Physics of Fluids*, 2(2):217–229, 1959.

[21] H.-J. Bungartz and M. Griebel. Sparse grids. *Acta numerica*, 13:147–269, 2004.

[22] A. Can, G. Guillaume, and B. Gauvreau. Noise indicators to diagnose urban sound environments at multiple spatial scales. *Acta Acustica united with Acustica*, 101(5):964–974, 2015.

[23] A. Can, S. Michel, B. De Coensel, C. Ribeiro, D. Botteldooren, and C. Lavandier. Comparison of noise indicators in an urban context. In *Inter-noise and Noise-con Congress and Conference Proceedings*, volume 253, pages 775–783. Institute of Noise Control Engineering, 2016.

[24] S. Cheinet, M. Cosnefroy, F. Königstein, W. Rickert, M. Christoph, S. L. Collier, A. Dagallier, L. Ehrhardt, V. E. Ostashev, A. Stefanovic, et al. An experimental study of the atmospheric-driven variability of impulse sounds. *The Journal of the Acoustical Society of America*, 144(2):822–840, 2018.

[25] S. Cheinet, L. Ehrhardt, D. Juvé, and P. Blanc-Benon. Unified modeling of turbulence effects on sound propagation. *The Journal of the Acoustical Society of America*, 132(4):2198–2209, 2012.

[26] P. Chevret, P. Blanc-Benon, and D. Juvé. A numerical model for sound propagation through a turbulent atmosphere near the ground. *The journal of the Acoustical Society of America*, 100(6):3587–3599, 1996.

[27] R. O. Cleveland. *Propagation of sonic booms through a real, stratified atmosphere*. PhD thesis, The University of Texas at Austin, 1995.

[28] F. Coulouvrat. Sonic boom in the shadow zone: A geometrical theory of diffraction. *The Journal of the Acoustical Society of America*, 111(1):499–508, 2002.

[29] F. Coulouvrat. The challenges of defining an acceptable sonic boom overland. In *15th AIAA/CEAS Aeroacoustics Conference (30th AIAA Aeroacoustics Conference)*, page 3384, 2009.

[30] F. Coulouvrat. A quasi-analytical shock solution for general nonlinear progressive waves. *Wave Motion*, 46(2):97–107, 2009.

[31] F. Coulouvrat. New equations for nonlinear acoustics in a low Mach number and weakly heterogeneous atmosphere. *Wave Motion*, 49:50–63, 2012.

[32] D. B. Creamer. On using polynomial chaos for modeling uncertainty in acoustic propagation. *The Journal of the Acoustical Society of America*, 119(4):1979–1994, 2006.

[33] S.C. Crow. Distortion of sonic bangs by atmospheric turbulence. *Journal of Fluid Mechanics*, 37(3):529–563, 1969.

[34] CTBT. Comprehensive nuclear-test-ban treaty organisation, 2022.

[35] I.G. Cullis. Blast waves and how they interact with structures. *BMJ Military Health*, 147(1):16–26, 2001.

[36] F. Dagrau, M. Rénier, R. Marchiano, and F. Coulouvrat. Acoustic shock wave propagation in a heterogeneous medium: A numerical simulation beyond the parabolic approximation. *The Journal of the Acoustical Society of America*, 130(1):20–32, 2011.

[37] G.A. Daigle, J.E. Piercy, and TFW Embleton. Line-of-sight propagation through atmospheric turbulence near the ground. *The Journal of the Acoustical Society of America*, 74(5):1505–1513, 1983.

[38] T. Davies, M.J.P. Cullen, A. J. Malcolm, M.H. Mawson, A. Staniforth, A.A. White, and N. Wood. A new dynamical core for the met office's global and regional modelling of the atmosphere. *Quarterly Journal of the Royal Meteorological Society: A journal of the atmospheric sciences, applied meteorology and physical oceanography*, 131(608):1759–1782, 2005.

[39] B. A. Davy and D. T. Blackstock. Measurements of the refraction and diffraction of a short N-wave by a gas-filled soap bubble. *The Journal of the Acoustical Society of America*, 49(3B):732–737, 1971.

[40] V. del Campo, D. Ragni, D. Micallef, F. J. Diez, and CJ S. Ferreira. Estimation of loads on a horizontal axis wind turbine operating in yawed flow conditions. *Wind Energy*, 18(11):1875–1891, 2015.

[41] S. Del Pino, B. Després, P. Havé, H. Jourdren, and P.F. Piserchia. 3D finite volume simulation of acoustic waves in the earth atmosphere. *Computers & Fluids*, 38(4):765–777, 2009.

[42] L. Ehrhardt, S. Cheinet, D. Juvé, and P. Blanc-Benon. Evaluating a linearized Euler equations model for strong turbulence effects on sound propagation. *The Journal of the Acoustical Society of America*, 133(4):1922–1933, 2013.

[43] A. Emmanuelli, D. Dragna, S. Ollivier, and P. Blanc-Benon. Characterization of topographic effects on sonic boom reflection by resolution of the Euler equations. *The Journal of the Acoustical Society of America*, 149(4):2437–2450, 2021.

[44] B.O. Enflo. Saturation of nonlinear spherical and cylindrical sound waves. *The Journal of the Acoustical Society of America*, 99(4):1960–1964, 1996.

[45] A. A. Few. Power spectrum of thunder. *Journal of Geophysical Research*, 74(28):6926–6934, 1969.

[46] A. A. Few. Acoustic radiations from lightning. In *Handbook of Atmospheric Electrodynamics, Volume II*, pages 1–31. CRC Press, 2017.

[47] S. Finette. A stochastic representation of environmental uncertainty and its coupling to acoustic wave propagation in ocean waveguides. *The journal of the acoustical society of America*, 120(5):2567–2579, 2006.

[48] G. Fishman. *Monte Carlo: concepts, algorithms, and applications*. Springer Science & Business Media, 2013.

[49] R. Frehlich, L. Cornman, and R. Sharman. Simulation of Three-Dimensional Turbulent Velocity Fields. *Journal of Applied Meteorology*, 40(2):246–258, 2001.

[50] O. Gainville. *Modélisation de la propagation atmosphérique des ondes infrasonores par une méthode de tracé de rayons non linéaire*. PhD thesis, Ecully, Ecole centrale de Lyon, 2008.

[51] O. Gainville. Outdoor blast wave propagation in real environment: statistical comparisons between simulations and measurements. In *Forum Acusticum*, pages 879–882, 2020.

[52] O. Gainville. Calcul de la charge effective. Technical report, ANR Prolonge, consulté à Bruyères-le Chatel, 2021.

[53] O. Gainville. Caractéristiques des capteurs. Technical report, Internal Report, 2021.

[54] L-J Gallin, M. Rénier, E. Gaudard, T. Farges, R. Marchiano, and F. Coulouvrat. One-way approximation for the simulation of weak shock wave propagation in atmospheric flows. *The Journal of the Acoustical Society of America*, 135(5):2559–2570, 2014.

[55] L. Ganjehi, R. Marchiano, F. Coulouvrat, and J.-L. Thomas. Evidence of wave front folding of sonic booms by a laboratory-scale deterministic experiment of shock waves in a heterogeneous medium. *The Journal of the Acoustical Society of America*, 124(1):57–71, 2008.

[56] I. E. Garrick and D. J. Maglieri. A summary of results on sonic boom pressure signature variations associated with atmospheric conditions. Technical report, NASA TN D-458, 1968.

[57] A.R. George and K. J. Plotkin. Propagation of sonic booms and other weak nonlinear waves through turbulence. *The Physics of Fluids*, 14(3):548–554, 1971.

[58] K. E. Gilbert, R. Raspet, and X. Di. Calculation of turbulence effects in an upward-refracting atmosphere. *The Journal of the Acoustical Society of America*, 87(6):2428–2437, 1990.

[59] S. Girimaji and K. Abdol-Hamid. Partially-averaged Navier Stokes model for turbulence: Implementation and validation. In *43rd AIAA Aerospace Sciences Meeting and Exhibit*, page 502, 2005.

[60] X. Guo, L. Zhang, D. Wang, Z. Lu, Y. Wang, and J. Zhang. Efficient computation and uncertainty analysis of underwater acoustic propagation based on kriging surrogate model. *DEStech Transactions on Computer Science and Engineering*, (csae), 2017.

[61] R.C. Haefeli, W.D. Hayes, and H.E. Kulsrud. Sonic boom propagation in a stratified atmosphere, with computer program. Technical report, NASA, 1969.

[62] M.F. Hamilton and D.T. Blackstock. Nonlinear Acoustics. Academic press, 1998.

[63] G. Harrison. Pressure anomalies from the january 2022 hunga tonga-hunga ha'apai eruption. *Weather*.

[64] C. R. Hart, D. K. Wilson, C. L. Pettit, and E. T. Nykaza. Machine-learning of long-range sound propagation through simulated atmospheric turbulence. *The Journal of the Acoustical Society of America*, 149(6):4384–4395, 2021.

[65] M. Henneton, O. Gainville, and F. Coulouvrat. Numerical simulation of sonic boom from hypersonic meteoroids. *AIAA Journal*, 53(9):2560–2570, 2015.

[66] L. Hesselink and B. Sturtevant. Propagation of weak shocks through a random medium. *Journal of Fluid Mechanics*, 196:513–553, 1988.

[67] D. A. Hilton, V. Huckel, and D. J. Maglieri. *Sonic-boom measurements during bomber training operations in the Chicago area*, volume 3655. National Aeronautics and Space Administration, 1966.

[68] J. Højstrup. Velocity spectra in the unstable planetary boundary layer. *Journal of Atmospheric Sciences*, 39(10):2239–2248, 1982.

[69] John C Houbolt, Roy Steiner, and Kermit G Pratt. *Dynamic response of airplanes to atmospheric turbulence including flight data on input and response*, volume 199. National Aeronautics and Space Administration, 1964.

[70] ICAO. Internationnal civil aviation organisation, 2022.

[71] N. N. Janenko. *The method of fractional steps*, volume 160. Springer, 1971.

[72] Y. Jing and R. O. Cleveland. Modeling the propagation of nonlinear three-dimensional acoustic beams in inhomogeneous media. *The Journal of the Acoustical Society of America*, 122(3):1352–1364, 2007.

[73] J. C. Kaimal and J. J. Finnigan. *Atmospheric boundary layer flows: their structure and measurement*. Oxford university press, 1994.

[74] G. Kamali and A.D. Pierce. Time dependence of variances of sonic boom waveform. *Nature*, 234(5323):30–31, 1971.

[75] M. Karweit, P. Blanc-Benon, D. Juvé, and G. Comte-Bellot. Simulation of the propagation of an acoustic wave through a turbulent velocity field: A study of phase variance. *The Journal of the Acoustical Society of America*, 89(1):52–62, 1991.

[76] Bill Kayser, Benoit Gauvreau, David Écotière, and Vivien Mallet. Wind turbine noise uncertainty quantification for downwind conditions using metamodeling. *The Journal of the Acoustical Society of America*, 151(1):390–401, 2022.

[77] M. Kelly, R. Raspet, and H. E. Bass. Scattering of sonic booms by anisotropic turbulence in the atmosphere. *The Journal of the Acoustical Society of America*, 107(6):3059–3064, 2000.

[78] S. Khazaie, X. Wang, D. Komatitsch, and P. Sagaut. Uncertainty quantification for acoustic wave propagation in a shallow water environment. *Wave Motion*, 91:102390, 2019.

[79] Y. Y. Khine, D. B Creamer, and S. Finette. Acoustic propagation in an uncertain waveguide environment using stochastic basis expansions. *Journal of Computational Acoustics*, 18(04):397–441, 2010.

[80] K. Kim and A. Rodgers. Influence of low-altitude meteorological conditions on local infrasound propagation investigated by 3-D full-waveform modeling. *Geophysical Journal International*, 210(2):1252–1263, 2017.

[81] K. D. Koper, T. C. Wallace, R. E. Reinke, and J. A. Leverette. Empirical scaling laws for truck bomb explosions based on seismic and acoustic data. *Bulletin of the Seismological Society of America*, 92(2):527–542, 2002.

[82] V.P. Korobeinikov. *Problems in the Theory of Point Explosion*. 1985.

[83] T. Kovacs-Coskun, B. Volgyi, and I. Sikari-Nagl. Investigation of aluminum-steel joint formed by explosion welding. In *journal of physics: Conference Series*, volume 602, page 012026. IOP Publishing, 2015.

[84] V. P. Kuznetsov. Equations of nonlinear acoustics. *Sov. Phys. Acoust.*, pages 467–470, 1970.

[85] A. Lacroix, F. Coulouvrat, R. Marchiano, T. Farges, and J.-F. Ripoll. Acoustical energy of return strokes: A comparison between a statistical model and measurements. *Geophysical Research Letters*, 46(20):11479–11489, 2019.

[86] H. Lamy. Utilisation d'auto-encodeurs variationnels pour l'analyse de chocs acoustiques. Mémoire de mastère, CEA, DAM, DIF, 2021.

[87] J. Le Meitour, D. Lucor, and J.-C. Chassaing. Prediction of stochastic limit cycle oscillations using an adaptive polynomial chaos method. *Journal of Aeroelasticity and Structural Dynamics*, 2(1), 2010.

[88] J. D. Leatherwood, B. M. Sullivan, K. P. Shepherd, D. A. McCurdy, and S. A. Brown. Summary of recent nasa studies of human response to sonic booms. *The Journal of the Acoustical Society of America*, 111(1):586–598, 2002.

[89] R.A. Lee and J.M. Downing. Sonic booms produced by United States Air Force and United States Navy aircraft: Measured data. Technical report, Armstrong Lab Brooks Afb tx, 1991.

[90] B. Lihoreau, B. Gauvreau, M. Bérengier, P. Blanc-Benon, and I. Calmet. Outdoor sound propagation modeling in realistic environments: Application of coupled parabolic and atmospheric models. *The Journal of the Acoustical Society of America*, 120(1):110–119, 2006.

[91] J. E. Lingeman, J. A. McAteer, E. Gnessin, and A. P. Evan. Shock wave lithotripsy: advances in technology and technique. *Nature Reviews Urology*, 6(12):660–670, 2009.

[92] B. Lipkens. Model experiment to study sonic boom propagation through turbulence. part iii: Validation of sonic boom propagation models. *The Journal of the Acoustical Society of America*, 111(1):509–519, 2002.

[93] B. Lipkens and D. T. Blackstock. Model experiment to study sonic boom propagation through turbulence. part i: General results. *The Journal of the Acoustical Society of America*, 103(1):148–158, 1998.

[94] B. Lipkens and D. T. Blackstock. Model experiment to study sonic boom propagation through turbulence. part ii. effect of turbulence intensity and propagation distance through turbulence. *The Journal of the Acoustical Society of America*, 104(3):1301–1309, 1998.

[95] Lance L Locey and Victor W Sparrow. Modeling atmospheric turbulence as a filter for sonic boom propagation. *Noise control engineering journal*, 55(6), 2007.

[96] A. Loubeau and F. Coulouvrat. Effects of meteorological variability on sonic boom propagation from hypersonic aircraft. *AIAA journal*, 47(11):2632–2641, 2009.

[97] A. Loubeau, Y. Naka, B. G. Cook, V. W. Sparrow, and J. M. Morgenstern. A new evaluation of noise metrics for sonic booms using existing data. In *AIP Conference Proceedings*, volume 1685, pages 090015(1–4), 2015.

[98] A. Loubeau and J. Page. Human perception of sonic booms from supersonic aircraft. *Acoust. Today*, 14(3):23–30, 2018.

[99] D. Luquet. *3D Simulation of acoustical shock waves propagation through a turbulent atmosphere. Application to sonic boom.* PhD thesis, Université Pierre et Marie Curie-Paris VI, 2016.

[100] D. Luquet, R. Marchiano, and F. Coulouvrat. Long range numerical simulation of acoustical shock waves in a 3D moving heterogeneous and absorbing medium. *Journal of Computational Physics*, 379:237–261, 2019.

[101] D. J. Maglieri. Sonic boom flight research: Some effects of airplane operations and the atmosphere on sonic boom. In *Sonic Boom Research: Proceedings*, volume 147, page 25. Scientific and Technical Information Division, NASA, 1967.

[102] D. J. Maglieri, P. J. Bobbitt, K. J. Plotkin, K. P Shepherd, P. G. Coen, and D. M. Richwine. *Sonic boom: Six decades of research.* NASA, 2014.

[103] D. J. Maglieri, V. Huckel, and H. R. Henderson. *Variability in Sonic Boom Signatures Measured Along an 8000-foot Linear Array*, volume 5040. National Aeronautics and Space Administration, 1969.

[104] O. Maimon and L. Rokach. Introduction to knowledge discovery and data mining. In *Data mining and knowledge discovery handbook*, pages 321–352. Springer, 2009.

[105] R. Marchiano, F. Coulouvrat, and R. Grenon. Numerical simulation of shock wave focusing at fold caustics, with application to sonic boom. *The Journal of the Acoustical Society of America*, 114(4):1758–1771, 2003.

[106] R. Marchiano, F. Coulouvrat, and J.-L. Thomas. Nonlinear focusing of acoustic shock waves at a caustic cusp. *The Journal of the Acoustical Society of America*, 117(2):566–577, 2005.

[107] F. Marmel, C. Fritz, L. Cretagne, L.-T. Thuong, C. G. Armijos, F. Ollivier, U. Muller, and F. Coulouvrat. Impact of low sonic boom exposure on psychophysical and cognitive performance. In *Forum Acusticum*, pages 999–1000, 2020.

[108] W. E. McBride, H. E. Bass, R. Raspet, and K. E. Gilbert. Scattering of sound by atmospheric turbulence: Predictions in a refractive shadow zone. *The Journal of the Acoustical Society of America*, 91(3):1336–1340, 1992.

[109] B. E. McDonald and W.A. Kuperman. Time-domain solution of the parabolic equation including nonlinearity. *Computers & Mathematics with Applications*, 11(7-8):843–851, 1985.

[110] M. D. McKay, R. J. Beckman, and W.J. Conover. A comparison of three methods for selecting values of input variables in the analysis of output from a computer code. *Technometrics*, 42(1):55–61, 2000.

[111] A. S. Monin and A. M. Obukhov. Basic laws of turbulent mixing in the surface layer of the atmosphere. *Contrib. Geophys. Inst. Acad. Sci. USSR*, 151(163):e187, 1954.

[112] W. J. Morokoff and R. E. Caflisch. Quasi-Monte Carlo integration. *Journal of Computational Physics*, 122(2):218–230, 1995.

[113] NASA. https://www.nasa.gov/centers/armstrong/features/supersonic-shockwave-interaction.html, 2019.

[114] T. S. Nemer. The beirut port explosion: A geoscience perspective, 2021.

[115] M. Nguyen-Dinh, O. Gainville, and N. Lardjane. Simulation of blast wave propagation from source to long distance with topography and atmospheric effects. In *AIP Conference Proceedings*, volume 1685, page 090009. AIP Publishing LLC, 2015.

[116] M. Nguyen-Dinh, O. Gainville, and N. Lardjane. A one-way coupled Euler and parabolic model for outdoor blast wave simulation in real environment. *Journal of Theoretical and Computational Acoustics*, 26(04):1850019, 2018.

[117] M. Nguyen-Dinh, N. Lardjane, C. Duchenne, and O. Gainville. Direct simulations of outdoor blast wave propagation from source to receiver. *Shock Waves*, 27(4):593–614, 2017.

[118] F. Nielsen. *Introduction to HPC with MPI for Data Science*. Springer, 2016.

[119] K. Noren-Cosgriff, I. Belyaev, and F. Løvholt. Building vibration induced by sonic boom-field test in russia. *Applied Acoustics*, 185:108422, 2022.

[120] S. Oladyshkin and W. Nowak. Data-driven uncertainty quantification using the arbitrary polynomial chaos expansion. *Reliability Engineering and System Safety*, 106:179–190, 2012.

[121] International Civil Aviation Organization. *Manual of the ICAO Standard Atmosphere: extended to 80 kilometres (262 500 feet)*, volume 7488. International Civil Aviation Organization, 1993.

[122] World Health Organization et al. *Burden of disease from environmental noise: Quantification of healthy life years lost in Europe*. World Health Organization. Regional Office for Europe, 2011.

[123] V. E. Ostashev, E. M. Salomons, S. F. Clifford, R. J. Lataitis, D. K. Wilson, P. Blanc-Benon, and D. Juvé. Sound propagation in a turbulent atmosphere near the ground: A parabolic equation approach. *The Journal of the Acoustical Society of America*, 109(5):1894–1908, 2001.

[124] V. E. Ostashev and D. K. Wilson. *Acoustics in Moving Inhomogeneous Media*, volume 5040. CRC, Bcao Raton FL, 2015.

[125] V.E. Ostashev, B. Brähler, V. Mellert, and G.H. Goedecke. Coherence functions of plane and spherical waves in a turbulent medium with the von Kármán spectrum of medium inhomogeneities. *The Journal of the Acoustical Society of America*, 104(2):727–737, 1998.

[126] V.E. Ostashev, V. Mellert, R. Wandelt, and F. Gerdes. Propagation of sound in a turbulent medium. i. plane waves. *The Journal of the Acoustical Society of America*, 102(5):2561–2570, 1997.

[127] M. A. Park and M. Nemec. Nearfield summary and statistical analysis of the second AIAA sonic boom prediction workshop. *Journal of Aircraft*, 56(3):851–875, 2019.

[128] A. Paulson, E. A. Buehler, and A. Mesbah. Arbitrary polynomial chaos for uncertainty propagation of correlated random variables in dynamic systems. *IFAC-PapersOnLine*, 50(1):3548–3553, 2017. 20th IFAC World Congress.

[129] F. Pedregosa, G. Varoquaux, A. Gramfort, V. Michel, B. Thirion, O. Grisel, M. Blondel, P. Prettenhofer, R. Weiss, V. Dubourg, J. Vanderplas, A. Passos, D. Cournapeau, M. Brucher, M. Perrot, and E. Duchesnay. Scikit-learn: Machine learning in Python. *Journal of Machine Learning Research*, 12:2825–2830, 2011.

[130] A. A. Piacsek. Atmospheric turbulence conditions leading to focused and folded sonic boom wave fronts. *The Journal of the Acoustical Society of America*, 111(1):520–529, 2002.

[131] A. D. Pierce. Spikes on sonic-boom pressure waveforms. *The Journal of the Acoustical Society of America*, 44(4):1052–1061, 1968.

[132] A. D. Pierce. Statistical theory of atmospheric turbulence effects on sonic-boom rise times. *The Journal of the Acoustical Society of America*, 49(3B):906–924, 1971.

[133] A. D. Pierce and D. J. Maglieri. Effects of atmospheric irregularities on sonic-boom propagation. *The Journal of the Acoustical Society of America*, 51(2C):702–721, 1972.

[134] M. Pinsky, M. Shapiro, A. Khain, and H. Wirzberger. A statistical model of strains in homogeneous and isotropic turbulence. *Physica D: Nonlinear Phenomena*, 191(3-4):297–313, 2004.

[135] K. J. Plotkin. The effect of turbulence on the loudness of minimized sonic boom signatures. *NASA CP*, 3172:77–95, 1992.

[136] K. J. Plotkin. State of the art of sonic boom modeling. *The Journal of the Acoustical Society of America*, 111(1):530–536, 2002.

[137] K. J. Plotkin and A.R. George. Propagation of weak shock waves through turbulence. *Journal of Fluid Mechanics*, 54(3):449–467, 1972.

[138] R. Raspet, H. E. Bass, L. Yao, P. Boulanger, and W. E. McBride. Statistical and numerical study of the relationship between turbulence and sonic boom characteristics. *The Journal of the Acoustical Society of America*, 96(6):3621–3626, 1994.

[139] J. W. Reed. Atmospheric attenuation of explosion waves. *The Journal of the Acoustical Society of America*, 61(1):39–47, 1977.

[140] D. O. ReVelle. On meteor-generated infrasound. *Journal of Geophysical Research*, 81(7):1217–1230, 1976.

[141] H.S. Ribner, P. J. Morris, and W.H. Chu. Laboratory simulation of development of superbooms by atmospheric turbulence. *The Journal of the Acoustical Society of America*, 53(3):926–928, 1973.

[142] L. Robert. Notice d'utilisation de la plateforme numérique de modélisation de la propagation des infrasons dans l'atmosphère. Technical report, LETMA, 2018.

[143] RUMBLE. https://rumble-project.eu, 2022.

[144] R. Sabatini and C. Bailly. Numerical algorithm for computing acoustic and vortical spatial instability waves. *AIAA Journal*, 53(3):692–702, 2015.

[145] J. A. Salamone, V. W. Sparrow, and K. J. Plotkin. Solution of the lossy nonlinear Tricomi equation applied to sonic boom focusing. *AIAA journal*, 51(7):1745–1754, 2013.

[146] E. M. Salomons, V. E. Ostashev, S. F. Clifford, and R. J. Lataitis. Sound propagation in a turbulent atmosphere near the ground: An approach based on the spectral representation of refractive-index fluctuations. *The Journal of the Acoustical Society of America*, 109(5):1881–1893, 2001.

[147] E. Salze, P. Yuldashev, S. Ollivier, V. Khokhlova, and P. Blanc-Benon. Laboratory-scale experiment to study nonlinear N-wave distortion by thermal turbulence. *The Journal of the Acoustical Society of America*, 136(2):556–566, 2014.

[148] A. Seifert, M. Baldauf, K. Stephan, U. Blahak, and K. Beheng. The challenge of convective-scale quantitative precipitation forecasting. In *15th Int. Conf. on Clouds and Precipitation*, 2008.

[149] Y. Seity, P. Brousseau, S. Malardel, G. Hello, P. Bénard, F. Bouttier, C. Lac, and V. Masson. The AROME-france convective-scale operational model. *Monthly Weather Review*, 139(3):976–991, 2011.

[150] K. Shimoyama, D. Ono, A. Hashimoto, S. Jeong, and S. Obayashi. Sonic boom analysis under atmospheric uncertainties by a non-intrusive polynomial chaos method. In *10th World Congress on Computational Mechanics*, pages 342–350, 2012.

[151] M. Siclari and C. Darden. CFD prediction of the near-field sonic boom environment for two low boom HSCT configurations. In *22nd Fluid Dynamics, Plasma Dynamics and Lasers Conference*, page 1631, 1991.

[152] I. M. Sobol. Global sensitivity indices for nonlinear mathematical models and their Monte Carlo estimates. *Mathematics and computers in simulation*, 55(1-3):271–280, 2001.

[153] S. S. Stevens. Perceived level of noise by Mark VII and decibels (E). *The Journal of the Acoustical Society of America*, 51(2B):575–601, 1972.

[154] T. A. Stout. *Simulation of N-wave and shaped supersonic signature turbulent variations*. The Pennsylvania State University, 2018.

[155] T. A. Stout and V. W. Sparrow. Nonlinear propagation of shaped supersonic signatures through turbulence. In *Proceedings of Meetings on Acoustics 21ISNA*, volume 34, page 045011. Acoustical Society of America, 2018.

[156] T.A. Stout, V.W. Sparrow, and P. Blanc-Benon. Evaluation of numerical predictions of sonic boom level variability due to atmospheric turbulence. *The Journal of the Acoustical Society of America*, 149(5):3250–3260, 2021.

[157] R. A. Strehlow and W. E. Baker. The characterization and evaluation of accidental explosions. *Progress in Energy and Combustion Science*, 2(1):27–60, 1976.

[158] G. I. Taylor. The formation of a blast wave by a very intense explosion i. theoretical discussion. *Proceedings of the Royal Society of London. Series A. Mathematical and Physical Sciences*, 201(1065):159–174, 1950.

[159] S. Töpken and S. van de Par. Loudness and short-term annoyance of sonic boom signatures at low levels. *The Journal of the Acoustical Society of America*, 149(3):2004–2015, 2021.

[160] P.E. Tubb. Measured effects of turbulence on the rise time of a weak shock. *Aeroacoustics: acoustic wave propagation; aircraft noise prediction; aeroacoustic instrumentation*, 43:17, 1976.

[161] D. Valente, L. M. Ronsse, L. Pater, M. J. White, R. Serwy, E. T. Nykaza, M. E. Swearingen, and D. G. Albert. Blast noise characteristics as a function of distance for temperate and desert climates. *The Journal of the Acoustical Society of America*, 132(1):216–227, 2012.

[162] M. West, K. Gilbert, and R.A. Sack. A tutorial on the parabolic equation (PE) model used for long range sound propagation in the atmosphere. *Applied Acoustics*, 37(1):31–49, 1992.

[163] T. K. West IV, K. N. Bretl, E. L. Walker, and J. T. Pinier. Sonic boom pressure signature uncertainty calculation and propagation to ground noise. In *53rd AIAA Aerospace Sciences Meeting*, pages 2015–1051, 2015.

[164] G. B. Whitham. The flow pattern of a supersonic projectile. *Communications on pure and applied mathematics*, 5(3):301–348, 1952.

[165] G. B. Whitham. *Linear and nonlinear waves*, volume 42. John Wiley & Sons, 2011.

[166] G.B. Whitham. On the propagation of weak shock waves. *Journal of Fluid Mechanics*, 1(3):290–318, 1956.

[167] G.B. Whitham. Linear and nonlinear waves john wiley & sons. *Inc., New York*, 1974.

[168] W. L. Willshire Jr and D. W. Devilbiss. Preliminary results from the White Sands missile range sonic boom propagation experiment. *High-speed research: sonic boom*, 1:137–149, 1992.

[169] D. K. Wilson. Performance bounds for acoustic direction-of-arrival arrays operating in atmospheric turbulence. *The Journal of the Acoustical Society of America*, 103(3):1306–1319, 1998.

[170] D. K. Wilson. Turbulence models and the synthesis of random fields for acoustic wave propagation calculations. Technical report, Army research lab Adelphi md, 1998.

[171] D. K. Wilson. Calculated coherence and extinction of sound waves propagating through anisotropic, shear-induced turbulent velocity fluctuations. *The Journal of the Acoustical Society of America*, 105(2):658–671, 1999.

[172] D. K. Wilson. A turbulence spectral model for sound propagation in the atmosphere that incorporates shear and buoyancy forcings. *The Journal of the Acoustical Society of America*, 108(5):2021–2038, 2000.

[173] D. K. Wilson. An alternative function for the wind and temperature gradients in unstable surface layers. *Boundary-layer meteorology*, 99(1):151–158, 2001.

[174] D. K. Wilson, E. L. Andreas, J. W. Weatherly, C. L. Pettit, E. G. Patton, and P. P. Sullivan. Characterization of uncertainty in outdoor sound propagation predictions. *The Journal of the Acoustical Society of America*, 121(5):EL177–EL183, 2007.

[175] D. K. Wilson, J. G. Brasseur, and K. E. Gilbert. Acoustic scattering and the spectrum of atmospheric turbulence. *The Journal of the Acoustical Society of America*, 105(1):30–34, 1999.

[176] D. K. Wilson and V. E. Ostashev. A reexamination of acoustic scattering in the atmosphere using an improved model for the turbulence spectrum. Technical report, New Mexico state univ Las Cruces, 1998.

[177] D. K. Wilson, V. E. Ostashev, and G. H. Goedecke. Sound-wave coherence in atmospheric turbulence with intrinsic and global intermittency. *The Journal of the Acoustical Society of America*, 124(2):743–757, 2008.

[178] D. K. Wilson, C. L. Pettit, and V. E. Ostashev. *Sound propagation in the atmospheric boundary layer*. Acoustical Society of America, 2015.

[179] D. K. Wilson, N. P. Symons, E. G. Patton, P. P. Sullivan, D. H. Marlin, D. F. Aldridge, V. E. Ostashev, S. A. Ketcham, E. L. Andreas, and S. L. Collier. Simulation of sound propagation through high-resolution atmospheric boundary layer

turbulence fields. In *Proceedings of the 16th American Meteorological Society Symposium on Boundary Layers and Turbulence, Portland, ME, 2004*, 2004.

[180] X. Wu, W. Zhang, S. Song, and Z. Ye. Sparse grid-based polynomial chaos expansion for aerodynamics of an airfoil with uncertainties. *Chinese Journal of Aeronautics*, 31(5):997–1011, 2018.

[181] D. Xiu. *Numerical methods for stochastic computations: a spectral method approach*. Princeton university press, 2010.

[182] H. Yamashita and S. Obayashi. Sonic boom variability due to homogeneous atmospheric turbulence. *Journal of Aircraft*, 46(6):1886–1893, 2009.

[183] R. Yamashita and K. Suzuki. Full-field simulation for sonic boom cutoff phenomena. *Transactions of the Japan Society for Aeronautical and Space Sciences*, 58(6):327–336, 2015.

[184] P.V. Yuldashev, M.M. Karzova, V.A. Khokhlova, and P. Blanc-Benon. Numerical simulation of a nonlinear parabolic equation for analyzing the perceived loudness statistics of sonic boom wave after propagation through atmospheric turbulent layer. *Acoustical Physics*, 67(1):26–37, 2021.

[185] A. Zelias, O. Gainville, and F. Coulouvrat. Complex ray analytical solutions for infrasound and sonic boom propagation into shadow zones. In *e-Forum Acusticum 2020-9th edition*, pages 965–971, 2020.